

**VIETNAM GENERAL CONFEDERATION OF LABOUR
TON DUC THANG UNIVERSITY
FACULTY OF ELECTRICAL AND ELECTRONIC ENGINEERING**



PHONG THANH TRAN

**LOAD FREQUENCY CONTROL IN
MULTI-AREA INTERCONNECTED
POWER SYSTEM USING SLIDING
MODE CONTROL**

**DOCTORAL DISSERTATION OF
ELECTRICAL ENGINEERING**

HO CHI MINH CITY, YEAR 2024

**VIETNAM GENERAL CONFEDERATION OF LABOUR
TON DUC THANG UNIVERSITY
FACULTY OF ELECTRICAL AND ELECTRONIC ENGINEERING**



PHONG THANH TRAN

**LOAD FREQUENCY CONTROL IN
MULTI-AREA INTERCONNECTED
POWER SYSTEM USING SLIDING
MODE CONTROL**

**DOCTORAL DISSERTATION OF
ELECTRICAL ENGINEERING**

Advised by

Dr. Huynh Van Van

Dr. Dong Si Thien Chau

HO CHI MINH CITY, YEAR 2024

ACKNOWLEDGEMENTS

Firstly, I am profoundly grateful to Buddha for his incredible gifts; without his blessing and assistance, this endeavor would not have been possible.

I would like to extend my sincere gratitude and appreciation to my advisor, Dr. Huynh Van Van, and co-advisor, Dr. Dong Si Thien Chau, for their unwavering support and guidance throughout my Ph.D. studies and research. Their patience, motivation, and extensive knowledge have been invaluable to my academic journey.

I would like to thank Ton Duc Thang University for its facility support of my PhD studies. I would like to thank all the lecturers and staff in the Faculty of Electrical Engineering, Ton Duc Thang University, especially Dr. Dinh Hoang Bach and Dr. Tran Dinh Cuong for his great and full support. I also wish to thank Assoc. Prof. Le Hong Phu, my lovely colleague and close boss, who always supports and encourages me.

Last but not least, I express my heartfelt gratitude to my parents, family, and friends for their unwavering support during the process of writing this thesis and throughout my life as a whole.

Ho Chi Minh City, May 10, 2024

Author

Phong Thanh Tran

This dissertation was carried out at Ton Duc Thang

University. Advisor: Dr Huynh Van Van

Dr. Dong Si Thien Chau (Co-Advisor)

This dissertation is defended at the Doctoral Dissertation Examination Committee which was held at Ton Duc Thang University on 07/01/2024 pursuant to Decision on

Members of the Doctoral Dissertation Examination Committee:

- | | |
|----|------------|
| 1. | Chairman |
| 2. | Examiner 1 |
| 3. | Examiner 2 |
| 4. | Member |
| 5. | Secretary |

Confirmation of the Chairman of the Doctoral Dissertation Examination Committee and the Dean of the faculty after receiving the modified dissertation (if any).

CHAIRMAN

DEAN OF FACULTY

.....

.....

DECLARATION OF AUTHORSHIP

I hereby declare that this dissertation was completed by me under the guidance and supervision of Dr. Huynh Van Van and Dr. Dong Si Thien Chau (Co-Advisor); and that the work contained and the results in it are true by author and have not violated research ethics. The data and figures presented in this dissertation are for analysis, comments, and evaluations from various resources by my own work and have been duly acknowledged in the reference part.

In addition, other comments, reviews, and data used by other authors, and organizations have been acknowledged, and explicitly cited.

I will take full responsibility for any fraud detected in my dissertation. Ton Duc Thang University is unrelated to any copyright infringement caused on my work (if any).

Ho Chi Minh City, May 10, 2024

Author

Phong Thanh Tran

ABSTRACT

Achieving and maintaining stable operation in power systems (PS) is a challenging task that aims to satisfy both consumers and suppliers. Control and stability in power systems involve addressing various challenges. To ensure stable operation, different control loops are implemented to regulate different parameters. For instance, Load Frequency Control (LFC) or Automatic Generation Control is utilized to keep the frequency close to its nominal values. In addition, that control loop has the charge of upholding the scheduled power exchange between interconnected control areas through tie-lines. Power systems also employ other control loops, such as the Automatic Voltage Regulator (AVR). The focus of this thesis is on addressing frequency deviation (FD) in PS and proposing diverse solutions depending on several hypotheses.

Firstly, the utilization of SMC in LFC of power network (PN) poses challenges as a result of the chattering phenomena connected to high-frequency switching. These chattering issues can be highly detrimental to actuators employed in PS. To address this problem, this research proposes an approach to continuous control that combines a second-order mode and integral sliding surface. The suggested approach, known as second-order integral sliding mode control (SOISMC), not only effectively eliminates chattering in the control input but also ensures the robustness of the multi-area PN. This robustness is particularly valuable in the presence of parametric uncertainties including fluctuations in loads and uncertainties related to parameter matching or mismatching. Simulation results demonstrate that the suggested controller satisfies quality requirements by effectively managing a wider range of operating conditions, rejecting disturbances, reducing transient frequency response, eliminating overshoot, and providing improved handling of load uncertainties compared to a few existing control approaches. Additionally, the results obtained from simulations highlight the suitability of the proposed SOISMC for practical implementation in multi-area PN, where it effectively mitigates high parameter

uncertainties and load disturbances, time-delay communication.

Secondly, in response to the escalating demand for electricity and the need to balance the total generated power, the concept of the multi-area power system (MAPS) has emerged. This MAPS incorporates various power sources such as gas, nuclear, hydro, thermal, etc., leading to implications for LFC. Addressing this, the LFC of the two-area gas-hydro-thermal power system (TAGHTPS) is presented through the application of a single-phase sliding mode control-based state observer (SPSMCBSO). This approach offers several notable contributions. Firstly, the TAGHTPS model accounts for uncertainties in both parameter and interconnected matrix states. Secondly, a state observer is utilized to determine the state variables, enhancing feedback control. Thirdly, the SPSMCBSO technique modifies the conventional SMC, thereby improving TAGHTPS performance in the context of overshoot and time for settling. Moreover, the SPSMCBSO design relies exclusively on the state observer, mitigating challenges related to state variable measurement. A stability evaluation of TAGHTPS is conducted using a novel linear matrix inequality (LMI) scheme based on the hypothesis of stability proposed by Lyapunov. Finally, the experiment's outcomes are presented and compared against reputable traditional control techniques, confirming the viability of SPSMCBSO for LFC within the MAMSPS.

Lastly, this research introduces a novel LFC approach tailored for a MASHPS under parameter uncertainty. The suggested technique employs a second order sliding mode control with double integrated sliding surfaces, aiming to enhance frequency regulation, tie-line power management, and overall system reliability of the MASHPS. Notably, this method not only enhances the asymptotic stability and dependability of the MASHPS but also mitigates the inherent presence of the chattering phenomenon in first order SMC. Additionally, the study employs a new LMI based on Lyapunov stability to comprehensively analyze the stabilization of the entire MASHPS. To assess the effectiveness of the suggested technique for LFC, a two-area steam-hydropower system (TASHPS) is investigated. Through simulations

involving parameter uncertainties and various load disturbances from different sources like households, commercial buildings, and industries, the efficacy of the suggested second-order SMC with double integral sliding surface (SOSDISS) is demonstrated. This approach exhibits robustness and notable improvements in MASHPS response concerning frequency regulation, tie-line power management, and system reliability compared to other existing methods with limited consideration of uncertainties. The efficiency of the method and reliability of the suggested control scheme are demonstrated through its rapid frequency responses and its resilience to factors such as parameter fluctuations, load disturbances, load variations, delay time, and the nonlinearity effects of governor dead band (GDB) and generation rate constraint (GRC), IEEE 39 bus on the PN. In conclusion, the outcomes highlight the practical feasibility of the novel approach for LFC in MASHPS and its positive impact on PS reliability.

KEYWORDS: Power system, Sliding mode control, Load frequency control, Multi-area power system, Automatic generation control, Time delay communication, Governor dead band (GRC), Generation rate constraint (GRB), Wind plant.

CONTENTS

LIST OF FIGURES	xi
LIST OF TABLES	xv
ABBREVIATIONS	xvi
NOMENCLATURE.....	xviii
CHAPTER 1. INTRODUCTION	1
1.1. The motivation	1
1.2. The objectives of the research.....	3
1.3. Scope of the research.....	5
1.4. Research methodology	6
1.5. New contributions of the research.....	7
1.6. Organization of the dissertation	8
CHAPTER 2: LITERATURE REVIEW.....	10
2.1. Power system.....	10
2.2. Types of frequency control in power systems	13
2.3. Frequency regulation in power networks.....	16
2.4. Modelling of frequency response and dynamic model	18
2.4.1 Primary control.....	21
2.4.2 Secondary control loop or load frequency control.....	23
2.4.3 Power system frequency regulation	24
2.4.4 Frequency control in an interconnected power system.....	26
2.5. Load frequency control based different power system models.....	30
2.5.1 Traditional power networks	30
2.5.2 Modern power systems.....	31
2.6. Control strategies.....	35
2.6.1 Centralized control approach	35
2.6.2 Decentralized control approach.....	36
2.7. Categories of LFC based on different control strategies.....	36

2.7.1	Classical control methods.....	37
2.7.2	The concept discussion of optimal and sub-optimal control.....	37
2.7.3	Adaptive control for LFC power network.....	38
2.7.4	Robust control	38
2.7.5	Artificial intelligence schemes	39
2.7.6	Sliding mode control approach	41
2.7.7	Alternative control methods for load frequency control	42
2.8.	Summary	42
CHAPTER 3: DESIGN OF A NEW SECOND ORDER SLIDING MODE		
CONTROL FOR POWER SYSTEM LOAD FREQUENCY CONTROL44		
3.1.	A mathematical model for interconnected multi-area PS.	45
3.2.	A novel second order sliding mode load frequency control design.....	47
3.2.1.	Introduction of LFC approach.....	47
3.2.2.	A scheme design of second order sliding load frequency control	48
3.3.	Simulation results and discussions.....	53
3.3.1.	Frequency control in practical power system.....	53
3.3.2.	Various cases of simulation results	55
3.4.	Conclusion of chapter 3	72
CHAPTER 4: DESIGNING AN ADVANCED SLIDING MODE OBSERVER		
FOR LOAD FREQUENCY CONTROL IN MULTI-AREA MULTI-SOURCE		
POWER SYSTEMS73		
4.1.	Mathematical model of the interconnected multi-area multi-source power system	75
4.2.	Designing the power system state estimator	79
4.3.	Design of the power system state estimator.....	80
4.4.	Design of a sliding mode controller with total output feedback	86
4.5.	Simulation results and discussions.....	89
4.5.1	Simulation 1	90
4.5.2	Simulation 2:	92

4.5.3 Simulation 3	96
4.5.4 Simulation 4	101
4.5.5 Simulation 5	103
4.6. Conclusion of chapter 4	107
CHAPTER 5: SLIDING SURFACE DESIGN FOR SLIDING MODE LOAD FREQUENCY CONTROL OF MULTI AREA MULTI SOURCE POWER SYSTEM.....	108
5.1. Dynamic model of multi-area steam-hydropower system	109
5.2. New double integral sliding surface design	111
5.3. Decentralized continuous control law.....	117
5.4. Case studies and simulation results.....	119
5.4.1. Measurement model	120
5.4.2. Simulation 2:	125
5.4.3. Simulation 3:	130
5.5. Conclusion of chapter 5.	132
CHAPTER 6: CONCLUSIONS AND RECOMMENDATIONS FOR FUTURE WORK.....	133
6.1. Conclusions and limitations	133
6.2. Recommendations for future work.....	135
LIST OF PUBLISHED PAPERS BY AUTHOR	137
REFERENCES.....	139

LIST OF FIGURES

Figure 1.1. The evolutionary process of the transition to a future smart grid.....	2
Figure 1.2. The evolutionary process of the transition to a future smart grid.....	5
Figure 2.1. Control loops for frequency regulation within a power system	11
Figure 2.2. Various temporal scales of transients in power systems.	11
Figure 2.3. Frequency control loops displaying activation times and patterns.....	12
Figure 2.4 The variations in frequency that occur after a loss of generation of up to 1800 MW	15
Figure 2.5. Illustration depicting in PS dynamics and controls at different time frames	16
Figure 2.6. Conventional single area power system	19
Figure 2.7. Block diagram representation of a synchronous generator with fundamental frequency control loops	20
Figure 2.8. Expression of the generator-load model in block diagram.....	21
Figure 2.9. Simplified block diagram derived from Figure 2.4.	21
Figure 2.10. Governor-turbine with primary frequency control loop	22
Figure 2.11. The diagram illustrating the entire primary loop consists of components such as speed governing, turbine, generator, and load.	23
Figure 2.12. Governor-turbine with primary frequency control loop.....	24
Figure 2.13. Primary frequency control model for PS	25
Figure 2.14. The equilibrium state frequency-power correlation within a turbine- governor control system	26
Figure 2.15. A schematic diagram of an N-area interconnected PS.	27
Figure 2.16. A simplified PS with an interconnected LFC controller	29
Figure 2.17. LFC system with various contributing elements and generating units in the region i.	30
Figure 3.1. The simplified block diagram depicting the i^{th} area within a multi-area PS.....	45
Figure 3.2. Basic single-line schematic for a system of electricity.	53
Figure 3.3. The simplified block diagram illustrates the connection between control areas 1 and 2.	55
Figure 3.4. Multi-area thermal system transfer function model without the advanced	

SMC controller.	56
Figure 3.5. Frequency variation [Hz] of both control areas without controller.	56
Figure 3.6. Transfer function model of multi area thermal system with SMC controller.	57
Figure 3.7. Frequency variation [Hz] of both control areas with matched disturbances.	58
Figure 3.8. Tie line power variation [p.u.MW] with matched disturbances.	59
Figure 3.9. Fluctuations in the load of areas 1 and 2 in the power system.	59
Figure 3.10. Frequency variations [Hz] of both control areas under matched disturbances.	60
Figure 3.11. Tie line power variation [p.u.MW] with matched disturbances.	60
Figure 3.12. Frequency variation [Hz] of both control areas with matched disturbances.	61
Figure 3.13. Tie-line power variation [p.u.MW] of both areas with matched disturbances.	62
Figure 3.14. Frequency [Hz] of both control areas under unmatched disturbances.	63
Figure 3.15. Tie-line power [p.u.MW] of both control areas under unmatched disturbances.	64
Figure 3.16. Deviation load of both areas of the power network.	65
Figure 3.17. The mismatch parameter uncertainty and control frequency [Hz] under load fluctuations	65
Figure 3.18. Tie-line power [p.u.MW] underload deviations and the unmatched uncertainty in the parameters.	66
Figure 3.19. Frequency [Hz] of control area 1 under matched disturbances.	66
Figure 3.20. Frequency [Hz] of control area 2 under matched disturbances.	67
Figure 3.21. The configuration of the i^{th} area within the of the LSPSwCD	68
Figure 3.22. The layout of the interconnected PN with time delays.	68
Figure 3.23. Frequency deviation of the PS.	69
Figure 3.24. Tie-line deviation of the PS.	69
Figure 3.25. Load deviation of the three areas power system.	71
Figure 3.26. Frequency change of the PS under random load.	71
Figure 3.27. Tie-line deviation of the PS under random load.	71
Figure 4.1. Schematic of TAMSPS's LFC blocks.	77

Figure 4.2. The visual representation depicting the SPSMCBSO approach as a flowchart.....	89
Figure 4.3. The frequency variation [Hz] with 1% to 2% step load in area 1.	90
Figure 4.4. The frequency variation [Hz] with 1% to 2% step load in area 2.	91
Figure 4.5. Tie line power deviation [p.u.MW].....	91
Figure 4.6. The frequency variation [Hz] with 1% step load in both areas.	93
Figure 4.7. Tie line power variation [p.u.MW].....	94
Figure 4.8. Random load deviation	94
Figure 4.9. Frequency deviation [Hz] in area 1	95
Figure 4.10. Frequency deviation [Hz] in area 2	95
Figure 4.11. Change in tie line power [p.u.MW]	95
Figure 4.12. Frequency variation [Hz] in area 1	96
Figure 4.13. Frequency deviation [Hz] in area 2	97
Figure 4.14. Tie line power variation [p.u.MW].....	97
Figure 4.15. Random load deviation	98
Figure 4.16. Frequency deviation [Hz] in area 1	98
Figure 4.17. Frequency deviation [Hz] in area 2	99
Figure 4.18. The tie line power variation [p.u.MW].....	99
Figure 2.19. Deviation in random load.	100
Figure 4.20. Frequency variations [Hz] in area-1 and area-2.	100
Figure 4.21. Change in tie-line power [p.u.MW].....	100
Figure 4.22. Frequency deviation [Hz] in four areas.	101
Figure 4.23. Changes in tie-line power [p.u.MW].....	102
Figure 4.24. Two-area PS blocks schematic linked to a tie line	103
Figure 4.25. Wind speed chart (m/s).....	104
Figure 4.26. The frequency deviations [Hz] with 1.5% step load in area 1 without and with wind speed variation.....	104
Figure 4.27. The frequency deviations [Hz] with 1.5% step load in area 2 without and with wind speed variation.....	104
Figure 4.28. Tie line power deviation [p.u.MW].....	105
Figure 4.29. Random load (p.u)	106
Figure 4.30. The frequency deviations [Hz] in area 1.	106

Figure 4.31. The frequency deviations [Hz] in area 2.	106
Figure 4.32. Tie-line power deviation.....	107
Figure 5.1. Schematic diagram of a 1-zone-2 sources included thermal power plants using heat recovery turbines & hydropower plant.	109
Figure 5.2. Simple diagram of traditional integral sliding surface.	115
Figure 5.3. Simple diagram of the double integral sliding surface.	117
Figure 5.4. Frequency [Hz] of control area 1 under matched disturbances.....	120
Figure 5.5. Frequency [Hz] of control area 2 under matched disturbances.....	121
Figure 5.6. Tie line power deviation [p.u.MW] with matched disturbances.	121
Figure 5.7. Daily load curve of commercial business buildings	122
Figure 5.8. Control area 1 and control area 2 frequency deviation.....	123
Figure 5.9. TASHPS tie line power deviation.	123
Figure 5.10. Load curve due to industrial activity-based frequency sensitive loads.	124
Figure 5.11. Area 1 and area 2 frequency deviation under mismatched conditions.	124
Figure 5.12. TASHPS tie line power deviation under mismatched conditions.	125
Figure 5.13. The block diagram of the New England 39 bus system	126
Figure 5.14. Random load variation.....	126
Figure 5.15. The dynamic responses of the frequency deviation	127
Figure 5.16. The dynamic responses of the tie-line power	127
Figure 5.17. Nonlinear governor model with dead band and Nonlinear turbine model with the GRC.....	128
Figure 5.18. The frequency responses of two areas with GRC and GRB.	129
Figure 5.19. Dynamic responses of the tie-line power with GRC and GRB	129
Figure 5.20. The dynamic responses of frequency change in three areas.....	130
Figure 5.21. The dynamic responses of the tie-line power	130
Figure 5.22. A three-area restructured PS with transmission time delay.....	131
Figure 5.23. Frequency deviation with time delay at $\tau = 5s$	131
Figure 5.24. Tie-line deviation with time delay at $\tau = 5s$	132

LIST OF TABLES

Table 1.1 The layout of the dissertation.....	8
Table 2.1 The policy aimed at containing and regulating the frequency.....	14
Table 2.2 Characteristics of the simplified power system	25
Table 3.1. The characteristics and parameters associated with control areas in PS. ..	57
Table 3.2. Parameters of the LFC scheme.	60
Table 3.3. Setting time T_s and Maximum overshoot calculation of SOISMC and different method.....	63
Table 3.4. The power system's three regions' parameters.....	68
Table 3.5. Comparing the suggested SOISMC approach with the earlier approach. .	70
Table 4.1. Setting time T_s [s] and maximum overshoot MOS[Hz] comparison.....	93
Table 4.2. Setting time T_s [s] and maximum overshoot MOS[Hz] comparison.....	97
Table 5.1. Setting time T_s [s] and Maximum overshoot MOS [Hz] comparison.	121

ABBREVIATIONS

ACE	Area control error
AVR	Automatic voltage regulator
AI	Artificial Intelligence
AC	Alternating current
ANN	Artificial Neural Networks
CA	Control area
DC	Direct current
DE	Differential evolution
FD	Frequency deviation
GRB	Generation rate constraint
GRC	Governor dead band
GWO	Grey wolf optimization
HVDC	High voltage direct current
IMAPS	Interconnected multi area power system
LDs	Load disturbances
LFC	Load frequency control
LF	Load frequency
LMI	Linear matrix inequality
MAPS	Multi area power system
MASHPS	Multi-area steam-hydropower system
OGC	Optimized generation control
PI	Proportional-integral

PID	Proportional-integral-differential
PN	Power network, Power networks
PS	Power system, Power systems
PSO	Particle swarm optimization
SCL	Secondary control loop
SM	Sliding manifold
SMC	Sliding mode control
SOISMC	Second-order integral sliding mode control
SOSDISS	Second order sliding mode control via double integral sliding
SPSMCBSO	Single-phase sliding mode control-based state observer
SF	System frequency
TASHPS	Two-area steam-hydropower system
TLBO	Teaching learning-based optimization

NOMENCLATURE

$\Delta f_i(t), \Delta f_j(t)$	Incremental changes in frequency of each control area
$\Delta P_{gi}(t)$	Incremental change in governor output command
$\Delta P_{gi}(t)$	Incremental change in governor valve position of each area
$\Delta P_{tie}^{ij}(t)$	Total tie line power change between control i th area and all other control areas
$\Delta P_{di}(t)$	Incremental change in local load of each area
$\frac{1}{K_{pi}} = D_i$	Equivalent system damping coefficient of control area
$\frac{T_{pi}}{K_{pi}} = M_i$	Equivalent inertia constant of control area
T_{ij}	Tie-line power coefficient between i th area and j th area
T_{gi}	Time constants of governor
T_{ti}	Steam turbine time constant
T_{pi}	Power system time constant
$K_{pi}, R_i, K_{Ei}, K_{Bi}$	Power system gain, droop coefficient of individual area, speed regulation coefficient and frequency bias factor

CHAPTER 1. INTRODUCTION

This document presents the study background, with a specific focus on load frequency control (LFC) matters. The initial section of the literature review will provide a brief overview of the conventional power system (PS) controls related to PS operations. Subsequently, the concept of load frequency regulation in PS will be examined. In addition, this section will cover the research motivation, problem statement, thesis structure, main objectives, and research scope of the current study. Moreover, the contribution of the present assignment will be elucidated and discussed. A synopsis of the following sections of this dissertation will then be given, highlighting the subjects that will be thoroughly addressed.

1.1. The motivation

The electrical PS, a vital component of modern society, ranks among the world's largest interconnected networks (Machowski Jan and Z. et al., 2020) (Eremia Mircea et al., 2013). It is a vast, dynamic, and intricate system comprised of numerous individual components linked together to generate, transmit, and distribute electrical power across extensive geographical regions. Nonetheless, ongoing transformations in grid configuration are driven by a blend of technological, political, and economic factors, prompting the exploration of innovative approaches to PS management.

Traditionally, within the vertically integrated paradigm, large power networks consisted of multiple energy companies, each responsible for all the controls and devices needed to ensure the security, efficiency, and reliability of their respective jurisdictions (Momoh James, 2012). The fundamental operational structure of the power system, largely still in use today, can be summarized as follows:

1. Large power plants produce electricity, which is then transmitted at elevated voltage levels.
2. Interconnected transmission lines transport this high-voltage electricity across extensive distances.
3. Transformers at distribution substations reduce these elevated voltages to

medium levels.

4. Within localized networks, the voltage is further reduced to lower levels appropriate for various categories of end-users.

The conventional electrical system was structured around this framework. Utility companies were responsible for the entire process of electricity generation, transmission, and distribution within their designated areas, known as balancing or control areas. Contracts and energy supply agreements were confined to these specific control areas. Consequently, the system's design and control needs were well-established and reasonably manageable in terms of complexity. The ongoing transformation within the PS is closely tied to advancements in information and communication technology. This progression is anticipated to shape a future power system characterized by several key attributes. These include the capacity to integrate emerging generation technologies, optimize the utilization of network assets, adapt to evolving market dynamics, prioritize environmental sustainability, and enhance overall grid efficiency, safety, and reliability. This shift in the power landscape, accompanied by the growing intricacies of the grid, is illustrated in Figure 1.1 (Alhelou Hassan Haes et al., 2018).

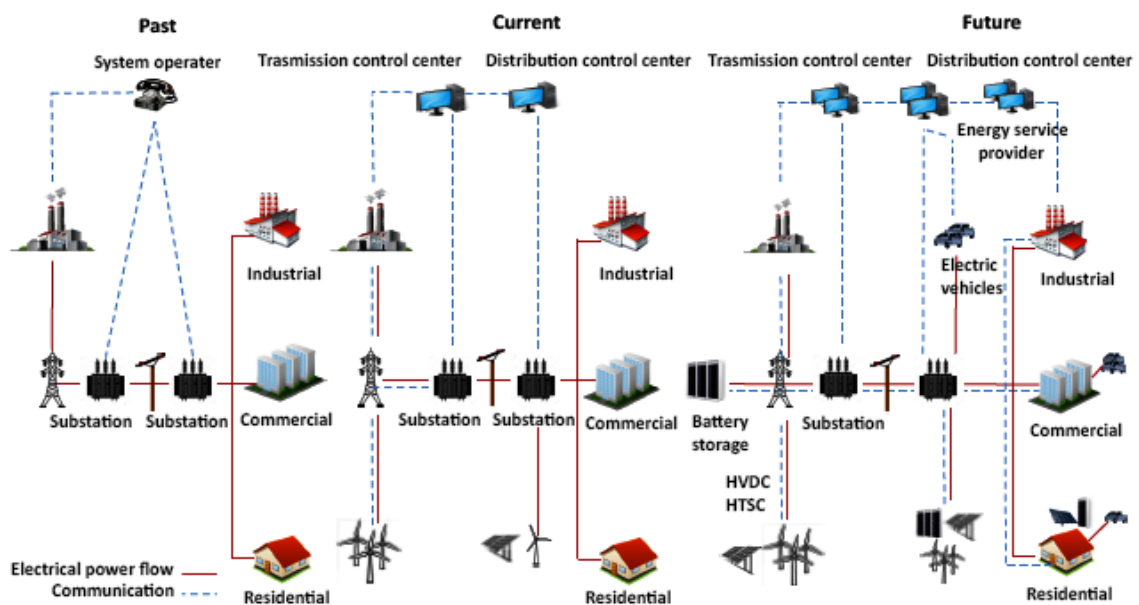


Figure 1.1. The evolutionary process of the transition to a future smart grid

To ensure the effective operation of the future grid, specific enabling technologies are essential (Edris, Abdel-A et al., 2017). These technologies encompass high-speed bidirectional adaptive communication networks, real-time decision-making capabilities for intelligent control and optimization, advanced computing infrastructure, and decentralized control systems. However, recent developments in the planning, operation, control, and regulatory landscape of the power industry have brought about significant changes. As the complexity continues to grow and nonlinearity of modern PS, driven by the growing capacity and reliance on diverse energy sources, various challenges arise. Among these challenges, frequency deviation stands out as a significant issue. The problem of frequency deviation stems from the ever-changing demand, which necessitates adjustments in generated power to maintain the frequency at its designated value. In PN, this control process is known as LFC (Khan Irfan Ahmed et al., 2023).

The primary goals of the LFC loop in PS are twofold. Firstly, it ensures the provision of required power from generation plants to meet fluctuating load demands. Secondly, it maintains the interchanged power at predetermined values among interconnected control areas (CA). By achieving these objectives, the LFC loop contributes to enhancing PS stability. It aims to eliminate steady-state errors in tie-line power deviation and frequency fluctuation (Kundur Prabha, 2022). Moreover, the LFC loop is responsible for dampening the oscillation over-shoot and under-switched power in a certain amount of time, which relies on the PS's capacity and the magnitude of the disturbance (Bevrani Hassan, 2014).

1.2. The objectives of the research

In this research, maintaining a constant frequency is essential for ensuring the efficient operation of a PS. Variations in frequency can have detrimental effects on PS performance, reliability, and efficiency. Substantial fluctuations in frequency can lead to equipment damage, degradation of load performance, overloading of transmission lines, and disruptions in system protection mechanisms. Frequency variations also have a negative influence the speed control and the operation of both

synchronous and inductive machinery.

Reduced motor speeds in power plant auxiliary systems, such as fans, pumps, and mills responsible for fuel, feedwater, and combustion air supply, can result in decreased plant output. Significant frequency drops can lead to elevated reactive electrical consumption by magnetizing currents in transformers and induction engines. In household appliances, lower power supply frequency can reduce the efficiency of refrigerators and increase the reactive power consumption of devices like televisions and air conditioners (Asghar Rafiq et al., 2023) (Sharma Jitendra et al., 2018). Substantial frequency deviations can eventually trigger a cascade of failures, potentially causing a complete system collapse. The power systems involve the interconnection of multiple control regions through tie lines. Within a control region, generators consistently adjust their speeds collectively (either speeding up or slowing down) to uphold frequency and the associated power angle at predetermined values in both static and dynamic conditions. Should an abrupt load change transpire within a control region of an interconnected PS, it will result in fluctuations in frequency and tie-line power. The objectives of this research are following:

1. To preserve the actual frequency and the specified control yield (megawatt) in the connected power frameworks.
2. To regulate the change in tie-line power between regulated regions.

Moreover, the recent increase in major power grid blackouts underscores the need for more vigilant consideration of various forms of control issues and PS instability in today's PS operations. Reports indicate that there have been instances of non-compliance with frequency control requirements have been a primary cause of multiple outages in the electricity grid (Asghar Rafiq et al., 2023), (Alkar Khaled et al. , 2019), (Falentina, Anna T. et al., 2019), (Haes Alhelou Hassan et al., 2019)

As a result, this dissertation is centered on proposing as explained in the next sections, three new control approaches based on various hypotheses of control were used to govern the frequency in two or three different multi-area multisource PS.

1.3. Scope of the research

In a connected power system, each generator is equipped with both load frequency control (LFC) and automatic voltage regulator (AVR) apparatus. Figure 1.2 (Alhelou Hassan Haes and M. et al., 2018) illustrates the schematic diagram of the LFC loop and the AVR loop. These controllers are configured for specific operating conditions and address minor fluctuations in load demand, ensuring that the frequency and voltage magnitude remain within predefined limits. Small variations in real power primarily hinge on changes in rotor angle and, consequently, the frequency. Reactive power, on the other hand, is predominantly influenced by the voltage magnitude, specifically the generator excitation. The excitation system's time constant is significantly smaller than that of the prime mover, and its transient decay is faster, having no significant impact on LFC dynamics. As a result, the cross-coupling between the LFC and AVR loops is minimal, allowing for independent analysis of load frequency and excitation voltage control.

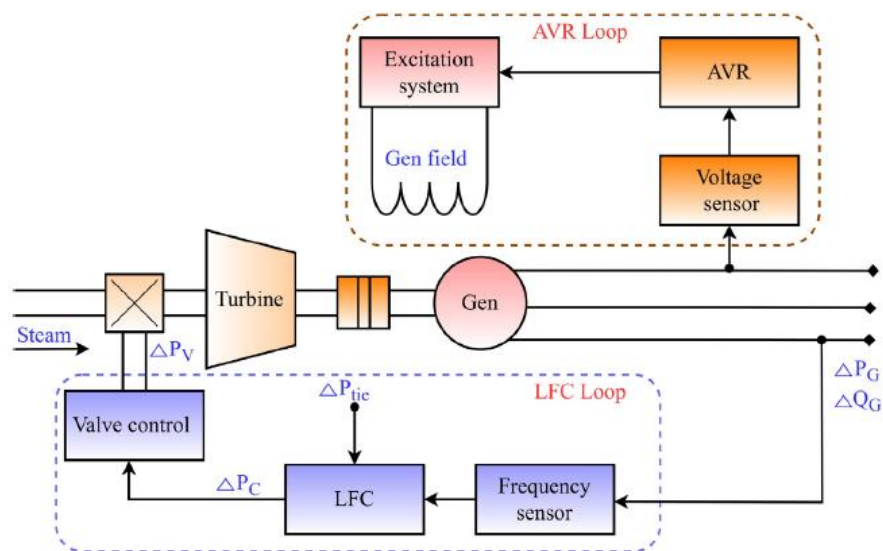


Figure 1.2. The evolutionary process of the transition to a future smart grid

Effectively managing large, interconnected PS in the face of increasing size, complexity, and unpredictable disturbances during operation is undeniably one of the most formidable challenges encountered in electric PS control. Furthermore, power

consumption from the demand side exhibits continuous and unforeseeable fluctuations, and any changes in load demand within specific control areas lead to transient deviations in frequency, generation, and tie-line power flow throughout the entire system. Consequently, the primary cause of these deviations is the mismatch between the sudden power demand and generation.

In the scope of this research, LFC is concentrated and investigated. In a stable, dependable, and secure PS, it's crucial to swiftly restore the frequency and tie-line power flow between interconnected regions to their predetermined values after a load disturbance and uncertainty. This is accomplished by synchronizing the generated power with the demand while considering losses. This control method, referred to as LFC, enables synchronous generators to adapt their output to meet load requirements, ensuring that fluctuations and discrepancies in area frequency and tie-line power converge to zero. The MATLAB/SIMULINK software serves as a valuable tool for optimizing the performance of controllers, particularly in simulation scenarios. This involves employing straightforward and effective optimization techniques to identify the ideal amounts for the recommended parameters of the controllers. Through simulation, these techniques help fine-tune controller settings, ensuring that the system operates at its best possible performance.

1.4. Research methodology

In a more comprehensive examination, to evaluate the efficacy and suitability of the proposed LFC systems, these methods are applied to various multi-area PS with multiple sources under diverse operating conditions. To attain the objective, the detailed following procedures are undertaken:

1. To perform an extensive examination of LFC, delve into the significant discoveries, current research areas, and potential problems, along with their corresponding solutions, pertaining to frequency fluctuations within contemporary PS.

2. To design and implement a new second-order integral sliding mode control (SOISMC) inside the streamlined multi-area PS, with filtered derivative reactions for

LFC and dual area interconnected PS, where it effectively mitigates high parameter uncertainties and load disturbances, time-delay communication.

3. To create new integral surface SMC control designs, specifically a single-phase sliding mode control-based state observer (SPSMCBSO), to effectively regulate frequency in the experiment involving a two-area multi-source PS, such as the gas-hydro-thermal PS, while ensuring power interchanges remain within predefined boundaries.

4. To introduce the suggestion of a new design for second order SMC with double integral sliding surface (SOSDISS) and provide a comprehensive mathematical derivation. This design is intended for use in multi-source system models, specifically those representing the two-area gas-hydro-thermal power system (TAGHTPS).

5. The stability of various power systems is investigated utilizing novel LMI techniques grounded in Lyapunov stability theory.

6. To figure out how to optimize the performance of the controllers such as the SOISM, SPSMCBSO, SOSDISS in simulation by using MATLAB/SIMULINK, the straightforward and effective optimization techniques, are used to determine the optimal values for the recommended parameters of controllers.

7. To conduct an in-depth evaluation of the resilience and effectiveness of the suggested control approaches, a thorough examination is performed. This involves subjecting the system to various operating conditions and subsequently comparing the outcomes with control techniques that have been previously recommended.

1.5. New contributions of the research

The objective of this thesis is to explore the possibility of creating robust LFC systems with the goal of enhancing the dynamic performance of multi-area PS. This involves ensuring that the frequency variation and tie-line power deviations remain within permissible bounds or limits, even in the event of disturbances.

The significant contributions or achievements of the research are as follows:

- To formulate and implement the novel control strategies referred to as

second-order integral sliding mode control (SOISMC) in the studied multi-area power models for LFC.

- To accomplish an innovative design and utilization of a single-phase sliding mode control-based state observer (SPSMCBSO) for the purpose of LFC in the context of a two-area gas-hydro-thermal power system (TAGHTPS).

- To employ the novel technique of a second order SMC with double integrated sliding surfaces, aiming to enhance frequency regulation, tie-line power management, and overall system reliability of the MASHPS. To put into practice a novel LFC approach tailored for a multi-area steam-hydropower system (MASHPS) under parameter uncertainty and various conditions.

1.6. Organization of the dissertation

Table 1.1 provides an overview of the arrangement and the primary focus of each chapter within this dissertation.

Table 1.1 The layout of the dissertation.

Number of Chapter	Summary of contents
Chapter 1	This part furnishes the background of the subject, research methodology, research goals, objectives, contributions, and the study's purpose, along with the problem statement.
Chapter 2	In this chapter, an extensive and current literature review is presented, covering various dimensions of LFC in PS, including considerations like system size, types, proposed LFC methods, and strategies. Each section within this chapter is assessed, and a concise summary is provided.
Chapter 3	This chapter proposes a continuous control scheme that combines a second-order mode and integral sliding surface. The suggested approach, known as second-order integral sliding mode control (SOISMC), not only effectively eliminates chattering in the control input but also ensures the flexibility of the multi-area PN. This robustness is particularly valuable in the existence of

	fluctuating loads and matched or unmatched parameter uncertainties, among other parametric uncertainties where it effectively mitigates the high parameter uncertainties and the load disturbances, time-delay.
Chapter 4	The load frequency control of the two-area gas-hydro-thermal power system (TAGHTPS) is introduced through the application of a single-phase sliding mode control-based state observer (SPSMCBSO). Moreover, the SPSMCBSO design relies exclusively on the state observer, mitigating challenges related to state variable measurement. TAGHTPS stability is investigated utilizing a novel LMI technique grounded in Lyapunov stability theory. Ultimately, simulation outcomes are showcased and juxtaposed with well-established classical control methods.
Chapter 5	In this chapter, this research introduces a novel LFC approach tailored for a MASHPS under parameter uncertainty. The proposed technique employs a second order sliding mode with double integrated sliding surfaces (SOSDISS), aiming to enhance frequency regulation, tie-line power management, and overall system reliability of the MASHPS. Through simulations, the effectiveness and reliability of the suggested control scheme are demonstrated through its rapid frequency responses and its resilience to factors such as parameter fluctuations, load disturbances, load variations, delay time, and the nonlinearity effects of GDB and GRC on the PN, IEEE 39 bus.
Chapter 6	This chapter offers a brief summary of the thesis, outlines its conclusion, and lays out a clear direction for future research endeavors.

CHAPTER 2: LITERATURE REVIEW

This chapter presents a comprehensive and current review of LFC in both traditional and modern PS. It begins with an overview of LFC and proceeds to explore the characteristics of different PS configurations. The chapter also examines various control strategies employed for LFC, including centralized and decentralized approaches. Furthermore, it discusses LFC schemes based on traditional, optimal, adaptive, robust, and soft computing methods using artificial intelligence.

2.1. Power system

In extensive PS, which consist of multiple interconnected control regions, the primary goal is to ensure the consistent generation and distribution of power while maintaining critical parameters like frequency and voltage within acceptable ranges (Alhelou Hassan Haes et al., 2018) (Ranjan Mrinal et al., 2022). Achieving this requires a delicate equilibrium between the power generated and the demand on the load side. However, because load demands are unpredictable and vary over time, they influence different operational aspects of the entire PS, leading to fluctuations in both frequency and the scheduled power exchange within the system. These fluctuations can result in unfavorable outcomes, potentially triggering instability within the system and the risk of a complete system blackout (Momoh James A. et al., 2017).

The most common approach to address frequency variations is hierarchical control, typically classified into three tiers: primary control, secondary control, and tertiary control levels (Bevrani Hassan, 2014). In cases where the frequency deviates significantly from its nominal value, there might also be a requirement for an emergency control loop to reestablish the PS's frequency (Gonzalez-Longatt et al., 2014). Under typical operating conditions, minor fluctuations in frequency are mitigated by primary control, which acts over a period of several seconds. In situations where there are more substantial deviations in frequency (during abnormal operation) and depending on the available reserve power, a secondary control loop, also referred to as LFC, is implemented to bring back the regularity of frequency. This process may take several minutes. Nevertheless, during situations characterized

by significant imbalances between power generation and load demand resulting from a major fault, the restoration of frequency to its nominal value using the LFC loop might not be achievable. During such occurrences, tertiary control mechanisms become essential. Additionally, emergency control services are utilized to alleviate or reduce the risk of cascading failures (see Figure 2.1) (Bevrani Hassan, 2014).

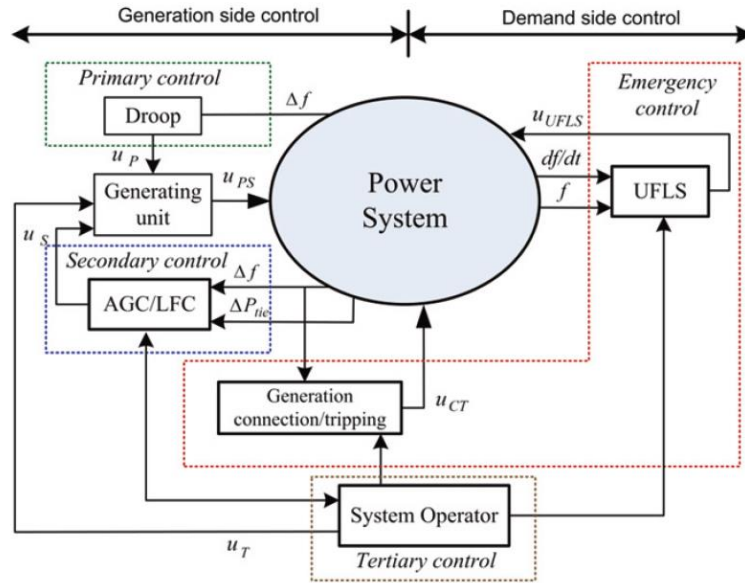


Figure 2.1. Control loops for frequency regulation within a power system

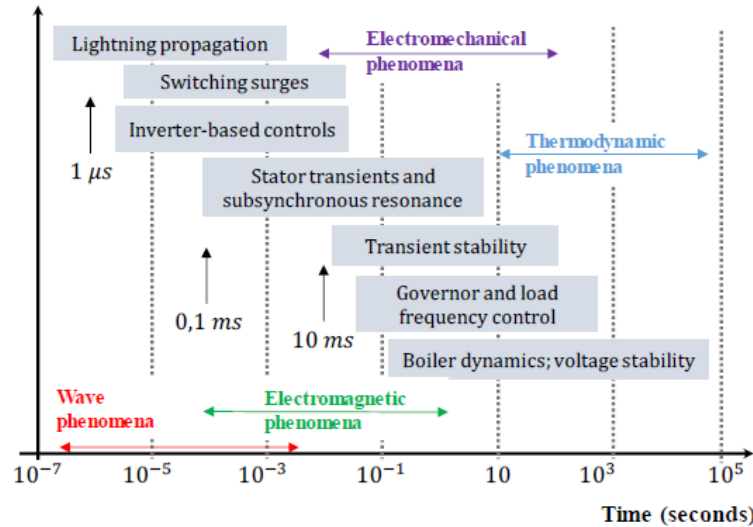


Figure 2.2. Various temporal scales of transients in power systems.

Building upon the preceding information, LFC or AGC emerges as a vital service crucial for ensuring the effective operation of PS (Bevrani Hassan et al., 2017). The entire control system exhibits complexity, but thanks to decoupling, it is

typically feasible to examine each control loop separately. Depending on the specific characteristics of each loop, including the necessary model, significant variables, uncertainties, and goals, various control schemes can be employed. A schematic diagram illustrating the distinct time scales relevant to PS controls and dynamics and controls of the PS is presented in Figure 2.2 (G. Andersson et al., 2009) (Vega-Herrera Jorge et al., 2020).

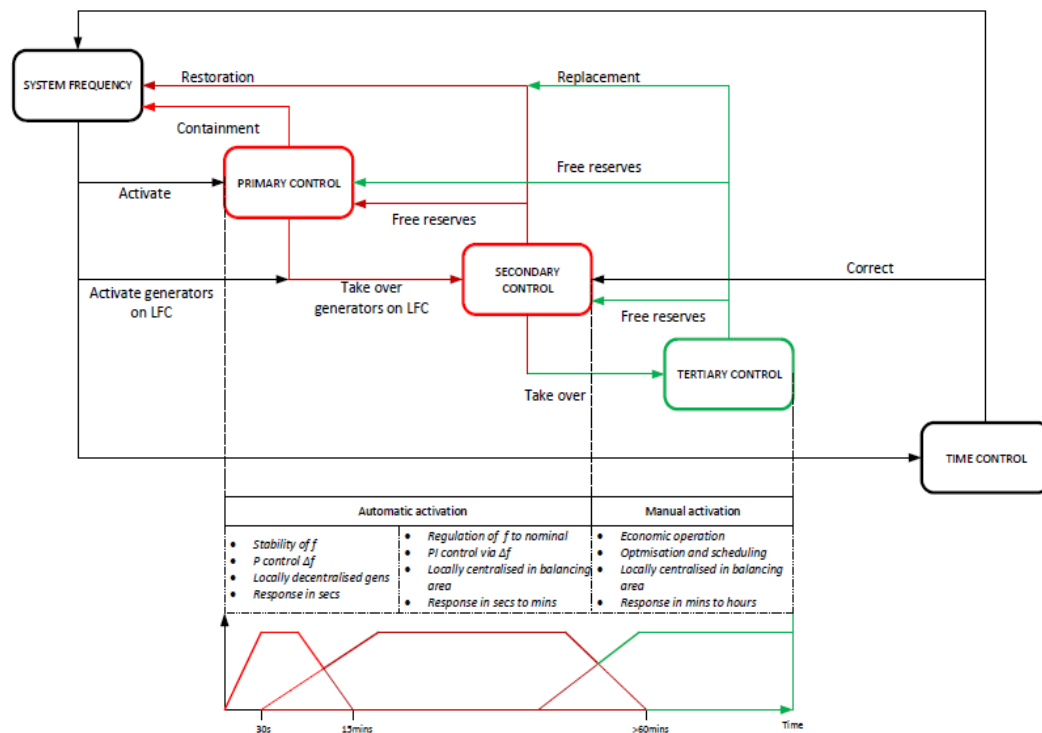


Figure 2.3. Frequency control loops displaying activation times and patterns.

The PS hierarchy consists of three distinct levels, each establishing independent frequency control loops within the system. By leveraging these dynamic variations in devices, which exhibit different decay rates during transients, it becomes feasible to decouple the various control loops (Bevrani Hassan, 2014) (Gonzalez-Longatt et al., 2014). These deviations in response speed are typically classified into three stability types: the quality of being stable of rotor angle, voltage, and frequency. Consequently, despite the PS's complexity, it is viable to analyze each control loop individually, as they are effectively separated due to their distinct timescales of operation. Figure 2.3 (Gonzalez-Longatt et al., 2014) illustrates all the frequency

control loops in a nested arrangement, demonstrating the stimulation pattern of every cycle after a disruption.

2.2. Types of frequency control in power systems

Ensuring a reliable and stable power supply is of utmost importance in PS operations, as it involves consistently delivering electricity of appropriate quality to customers. Maintaining a balance between energy supply and consumption is so essential. To achieve frequency control in PS, numerous control loops are employed comprising of primary, secondary, tertiary, and emergency controls, each providing a particular function (Bevrani Hassan, 2014). In a PS with a nominal frequency value of 50Hz, the dynamic power generation of the primary control loop reaches its maximum capacity within ten seconds, as a secondary control requires approximately thirty seconds to reach its maximum effectiveness (Machowski Jan et al., 2020).

Reserve services for frequencies can be categorized into dynamic services, which automatically respond to any frequency changes, and non-dynamic services, which are activated through load frequency relays. When there is an imbalance between generated power and demand, frequency deviations occur. These fluctuations must adhere to the quality of supply standards outlined in Clause 1, Article 15 of Decree No. 137/2013/ND-CP, which provides guidelines for the Electricity Law and its amendments. According to these standards, the voltage and frequency for electricity usage must stay within reasonable bounds, as specified in Table 2.1 (Machowski Jan et al., 2020) (Obaid Zeyad Assi et al., 2019).

- Regarding voltage, during normal operating conditions, the acceptable voltage deviation is typically within $\pm 5\%$ of the nominal voltage of the grid. The specific location for determining this deviation is typically at the site of the electricity metering equipment or as agreed upon by both parties involved. However, in the event of an unstable power grid following a fault, the permissible voltage deviation extends from $+5\%$ to -10% .

Table 2.1 The policy aimed at containing and regulating the frequency in the PS

Limitations on frequency	Analyses of the cases
±0.2 Hz	The frequency of the PS during normal operation and the allowable deviation of frequency in the event of a generation loss or connection of demand.
±0.5 Hz	The maximum frequency deviation observed when generation units exceeding 300 MW and up to 1320 MW experience a loss.

- In relation to frequency, typical conditions for operation, the acceptable deviation of the PS frequency is typically within ±0.2Hz of the nominal frequency of 50Hz. However, in the case of an unstable power grid following a single fault, the permissible frequency deviation expands to ±0.5Hz.

However, in the event of a significant frequency drop (below 49.2 Hz), low-frequency relays are employed to disconnect both the generators and the demand to maintain frequency control. Figure 2.4 (Teng Fei et al., 2017) illustrates the permissible frequency variations under normal typical conditions for operation and when a substantial generation loss occurs suddenly, such as from a significant nuclear generator (Teng Fei et al., 2017) (Greve Thomas et al., 2018).

Excitation control regulates voltage of the governor and output of reactive power in a power plant, while prime mover controls manage energy supply PS parameters such as temperatures, flows, pressures, and speed regulation. AGC is responsible for maintaining a balance between the total generation and load, including losses, to reach the initial SF range, which is generally 50 Hz, and fulfill the planned power exchange with nearby systems (Ullah Kaleem et al., 2021)

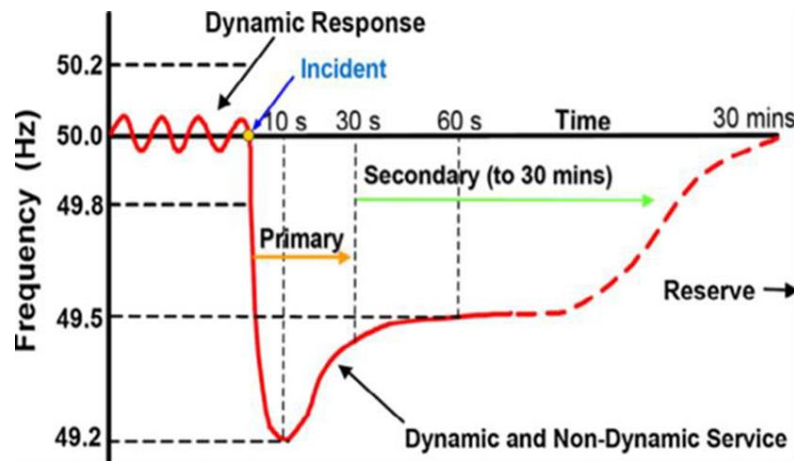


Figure 2.4 The variations in frequency that occur after a loss of generation of up to 1800 MW

In the context of dynamic examination, it is important to note that the timescale relevant for rotor angle research the stability in a transitory state (big disruption) generally, analysis of stability ranges from 3 to 10 seconds. In steady-state (small signal) studies, the timescale of interest is typically around 10 to 20 seconds. Rotor angle stability is considered a short-term stability issue. On the other hand, voltage stability may be classified as either a short-term or a long-term stability issue, with the timescale of interest varying from a short period of time, up to several minutes. While PS frequency stability is influenced by encompassing both the fast and slow dynamics of the timescale of concern generally falls within the range of several seconds to many minutes. Hence, it is regarded as a long-term issue of stability. Figure 2.5 provides a schematic diagram illustrating the key timescales associated with PS controls and dynamics. Currently, PS utilities utilize basic and conventional tuned controllers for frequency regulation tasks. The adjustment of parameters often relies on heuristic procedures conducted in the field. The existing parameters for frequency control are typically tuned using experiential, classical, and trial-and-error methods. However, these approaches lack the ability to deliver optimal dynamic performance across different operating conditions and load scenarios. Considering this, there is a pressing need for innovative modeling and robust control approaches that can strike a new balance in the relationship between market efficacy

and dynamics in the market.

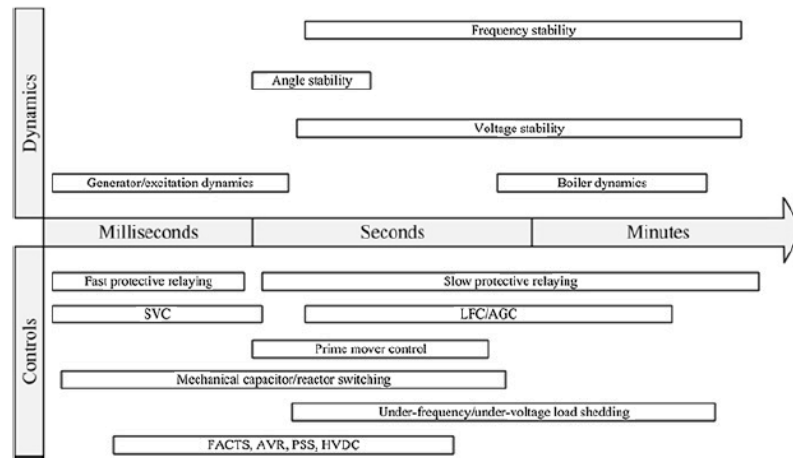


Figure 2.5. Illustration depicting in PS dynamics and controls at different time frames

In today's PS, the importance of frequency control has grown due to the expansion in size, evolving structure, and intricate nature of interconnected PS. The rising economic demands for efficiency and reliability in PS have necessitated the maintenance of SF and tie-line flows as close to their scheduled values as feasible (Parmar KP Singh et al., 2014). As a result, LFC provides a pivotal role in modern PS by serving as an ancillary service that supports power platforms and improves trading conditions for electricity.

2.3. Frequency regulation in power networks

Power systems in various countries comprise multiple generating and distribution subsystems. These extensive systems encompass interconnected power subsystems that span wide geographical CA (Yang Shengchun et al., 2017). Each subsystem possesses distinct generating capabilities, coupled with varying load demands. Power flow between these regions is regulated using tie-lines. Given the interconnected nature of these subsystems and CA, changes in load disturbance and demand within one area can trigger fluctuations in output frequencies across other interconnected regions, impacting power flow along the tie-line (Bevrani, 2014). In practice, real-world PS exhibit dynamic load behaviors, often associated with load changes, particularly in terms of their rate of change. LFCs are deployed to detect

such disturbances and address discrepancies by aligning the frequencies and active power on tie-lines across interconnected regions (Kumari, N., Malik, N., & Jha, A. N., 2019). Extensive research has been dedicated to the development of control algorithms and methodologies for LFCs. This ongoing effort aims to efficiently manage load perturbations, minimize steady-state errors, and adhere to various constraints. As a result, multiple techniques have been devised to address the challenges posed by the LFC problem (Asghar Rafiq et al., 2023). The interconnected PS is often described as one of the most extensive and intricate systems ever constructed by humans. While this statement may contain some exaggeration, it underscores the inherent truth of the system's complex interdependencies. Different parts of the system are interconnected in such a way that events occurring in geographically distant areas can have significant and unforeseen interactions (Guo Jianping, 2019).

In the past, electric PS were typically operated as separate units. However, as electricity generation and load centers are often located far apart, the connectivity and power control of flow have become necessary to supply power to these load centers. Moreover, the interconnection of PN allows for the integration and sharing of a significant quantity of energy from renewable sources, contributing to The decarbonization of the electric system. Areas with the highest potential for renewable energy are often located far from load centers, necessitating long-distance transmission interconnections. These interconnections help mitigate the variability of renewable energy sources by enabling the import and export of electricity between neighboring regions (Guo Jianping , 2021).

The integrated PS is made up of many places that are linked together via high-voltage AC (and occasionally DC) transmission tie-lines. Each control region is examined with a cohesive system comprising a group of generators and loads, with all generators reacting to changes in load or speed controller settings. The frequency changes measured in each area indicate variations in the power imbalance between generation and demand within that area and in interconnected areas. In an inter-

connected PS, LFC of PS has a critical role (Bevrani Hassan, 2014) (Dev Ark et al. , 2019). They not only ensure the desired real power output from generators to match load changes (by controlling the frequency) but also maintain power interchange between control areas through tie-lines at predetermined values. Furthermore, the concept of a multi-source PS involves interconnecting several lower-order subsystems within each area. Aside from the economic, resource, and environmental advantages, large-scale power network interconnections offer significant technological advantages. These include (Bevrani Hassan, 2014) a. Balancing supply and demand mismatches; b. Integration of intermittent renewable power; c. Access to remote energy resources.

The only potential disadvantage of interconnected PS is the possibility of fault propagation throughout the entire system, which can lead to system-wide instability. Proper management and control are essential to address these challenges effectively.

2.4. Modelling of frequency response and dynamic model

The PS's frequency is contingent on the balance of real power. Any alteration in real power demand within the network affects the entire system by causing a shift in frequency. Consequently, system frequency (SF) serves as a valuable indicator of the equilibrium between system generation and load. Any momentary disparity in energy balance causes an immediate shift in SF, as the disturbance is initially compensated for by the kinetic energy of the rotating machinery. A substantial loss in generation, without an appropriate system response, can lead to pronounced frequency deviations beyond the operational limits of the equipment (Weedy Birron Mathew et al., 2012) (Wakileh George J. , 2019).

Figure 2.6 illustrates a typical single-area power system. The primary parts are a speed changer, a speed governor, a hydraulic amplifier, and a control valve. A linking mechanism is used to join them. Figure 2.6 shows that A, B, and C are in one linkage mechanism, C, D, and E are in another linkage mechanism, and Pref is the turbine's steady-state output power. When A travels downhill, so does B; C moves upward; D moves upward, and E moves downward. This lets more steam into the

turbine, resulting in increased output production power. The pilot valve is controlled using high-pressure oil. The primary piston may move up and down according to E's location. A speed governor's output, ΔP_g , corresponds to the movement of ΔX_C in Figure 3.2. The speed governor has two inputs: the reference input (ΔP_{ref}) as indicated in Figure 3.2, and frequency deviation. The parameters ΔX_A , ΔX_B , ΔX_C , ΔX_D , ΔX_E represent the displacements of links A, B, C, D, and E. They go in vertical directions. The motions are measured in millimeters, but we characterize them as p u MW (per unit megawatts).

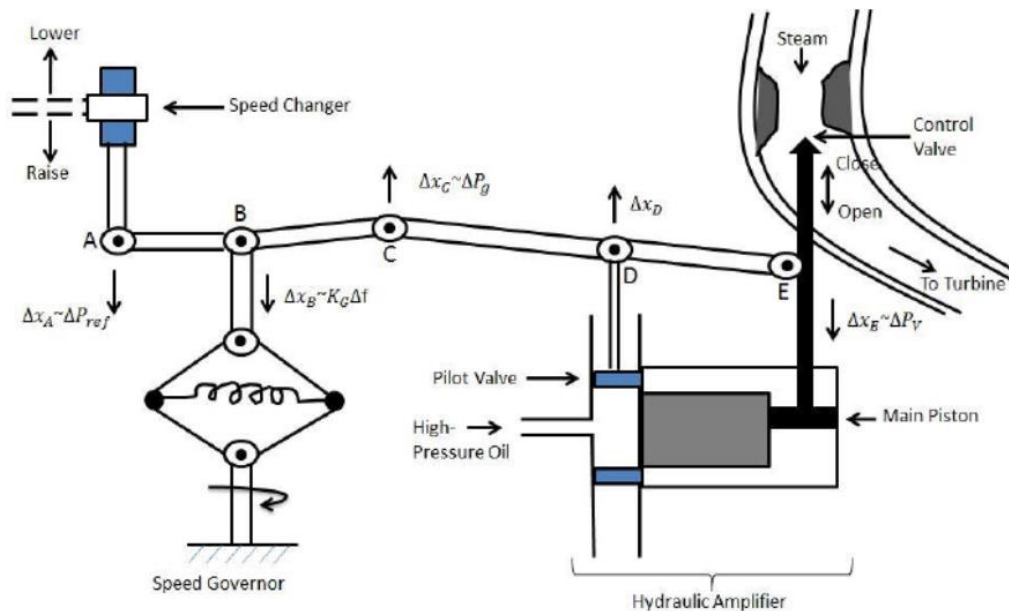


Figure 2.6. Conventional single area power system

The control of real power output from a generator is contingent upon the mechanical power generated by the prime mover, which can be a steam turbine, gas turbine, hydro turbine, or diesel engine, depending on the type of generation. In instances involving steam or hydro turbines, the adjustment of mechanical power is achieved by manipulating valves that regulate the intake of steam or water flow into the turbine. It is imperative to continually regulate the supply of steam (or water) to the generators to align it with the real power demand; otherwise, variations in machine speed will ensue, resulting in a shift in frequency. To guarantee the effective

operation of a PS, it is crucial to maintain a nearly constant frequency (P. M. Anderson and A. A. Fouad, 2008). Besides primary FC, many large synchronous generators are outfitted with a secondary frequency control loop (FCL). In Figure 2.7, the speed governor identifies alterations in speed (frequency) through both the primary and secondary control loop (SCL). The secondary loop employs feedback based on the frequency deviation, which is then incorporated into the primary control loop via a dynamic controller. The signal that results ΔP_c is employed to govern the system's frequency. As illustrated in Figure 2.7 (Bevrani Hassan, 2014), when there is a variation in load ΔP_L , the frequency undergoes a transient adjustment Δf . Consequently, the feedback mechanism becomes active, generating a suitable signal to ensure that the turbine aligns its generation ΔP_m with the load, thereby restoring the system's frequency (Bevrani Hassan, 2014).

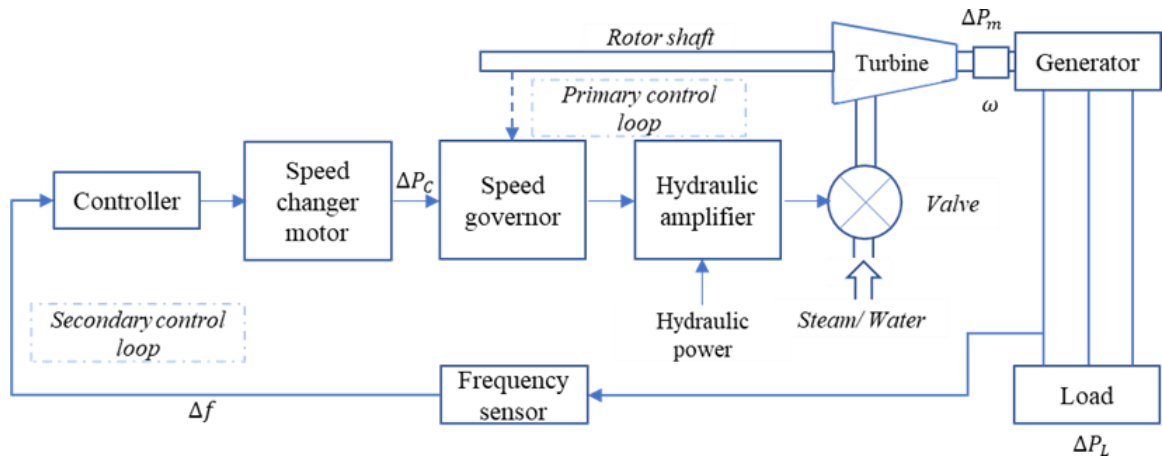


Figure 2.7. Block diagram representation of a synchronous generator with fundamental frequency control loops

Afterward, subsection will extend this model to encompass an interconnected multi-machine PS. The entire dynamic connection of the continuous mismatch energy $\Delta P_m - \Delta P_L$ and the frequency deviation Δf_i in the generator-load system can be mathematically expressed through a swing differential equation as follows:

$$\Delta P_m(t) - \Delta P_L(t) = 2H_{eq} \frac{d\Delta f_i(t)}{dt} + D\Delta f_i(t) \quad (2.1)$$

Here, Δf_i represents the FD, ΔP_m signifies the mechanical power change, ΔP_L denotes the load variation, H_{eq} stands for the inertia constant, and D represents the load damping coefficient. Typically, the damping coefficient is indicated as a percentage change in load resulting from a 1% change in frequency. For instance, a common value of 1.5 for D implies that a 1% alteration in frequency would lead to a 1.5% change in load (Bevrani Hassan, 2014). Employing the Laplace transform, Equation (2.1) can be expressed as follows:

$$\Delta P_m(s) - \Delta P_L(s) = 2H_{eq}(s)\Delta f_i(s) + D\Delta f_i(s) \quad (2.2)$$

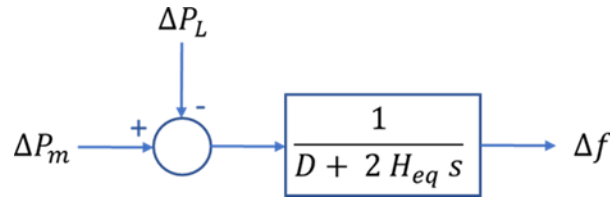


Figure 2.8. Expression of the generator-load model in block diagram

Equation (2.2) can be illustrated using a block schematic, as depicted in Figure 2.8.

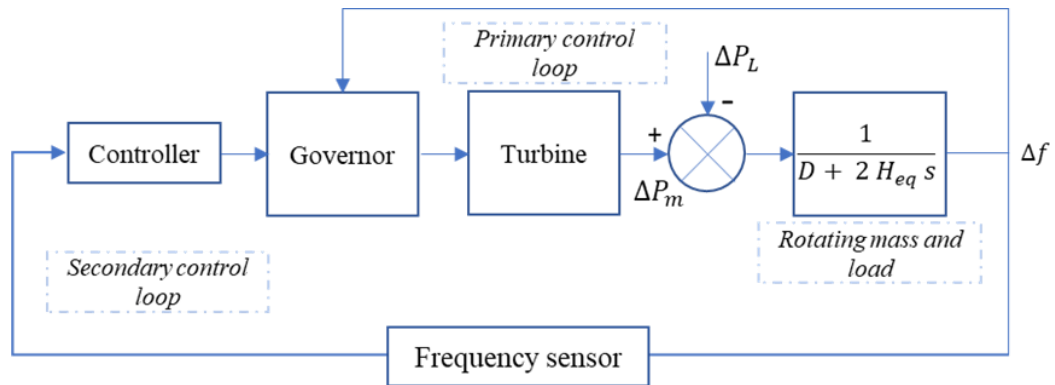


Figure 2.9. Simplified block diagram derived from Figure 2.4.

This generator-load model provides a simplified representation of the closed-loop synchronous generator's schematic block diagram (Figure 2.7), as demonstrated in Figure 2.9.

2.4.1 Primary control

According to the kind of manufacturing, the main mover, such as a steam, gas, hydro, or diesel engine, controls the actual generation of energy from a generator.

Steam turbines and hydraulic turbines both require open and closed valves to control the amount of steam or water that enters the turbine. To match the actual demand for energy, the generator's intake of steam (or water) must be continually regulated. If not, the machine's speed will vary in reaction to the frequency change. The frequency must be almost constant for the PS to function correctly. Figure 2.10 depicts how the primary control loop informs the governor of variations in speed (frequency). In reality, the principal control employs a local automated control that offers a reserve of energy to counteract frequency changes. A hydraulic amplifier and speed changer that provides a steady-state output power setting and the forces required to set the main valve against the turbine's high steam (or hydraulic) pressure, as depicted. Regardless of the minor positioning changes, all generating sets contribute to the overall shift in electrical power generation via the main speed control provided by speed regulators on each unit load via speed management. However, as previously noted, the primary control operations are frequently insufficient to restore the SF, particularly in linked PS, necessitating a second control loop to address the issue. Set the load reference using a variable-speed motor (Salgotra, A., 2012).

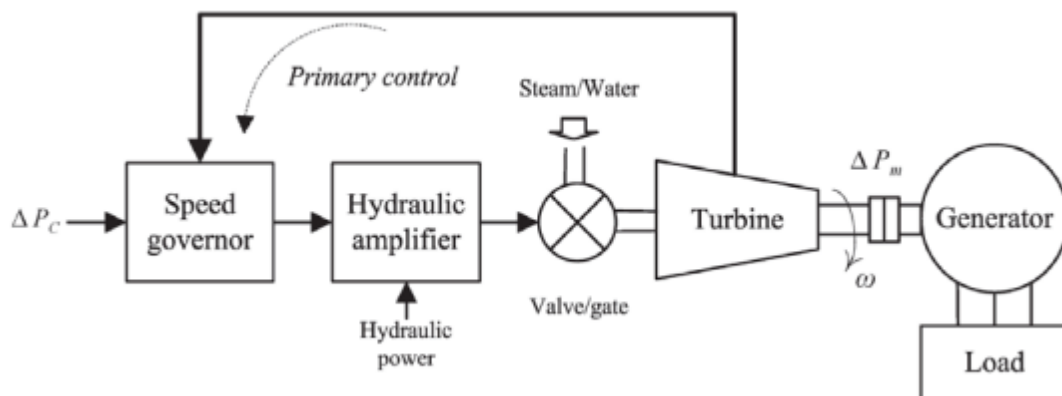


Figure 2.10. Governor-turbine with primary frequency control loop

The speed governing process of a synchronous generator involves considering a single generator initially supplying power to a local load. In this scenario, the net torque of the generator is determined as the difference between the mechanical and electrical torques. When these two torques are equal, the generator's speed remains constant and does not change. LFC analysis typically focuses on variations in load

demand, which is the approach adopted in this thesis. In a multi-generator system, the speed-droop characteristics of individual governors play a crucial role in determining the contribution of each generator to load balancing when a speed deviation occurs. This is accomplished through the additional loop around the integral controller shown in Figure 2.11, which serves to correct speed deviations.

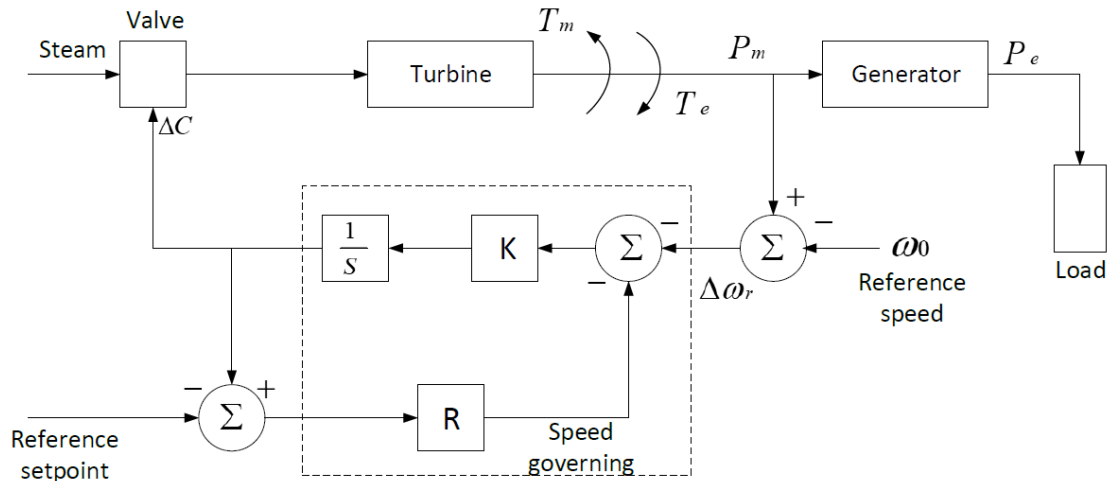


Figure 2.11. The diagram illustrating the entire primary loop consists of components such as speed governing, turbine, generator, and load.

2.4.2 Secondary control loop or load frequency control

The preceding section, which discusses speed governing, is typically referred to as the primary control loop. However, it does not restore a PN to its nominal frequency after a load disturbance. This limitation arises from the fact that speed governing merely adjusts the generator output in direct proportion to changes in speed, maintaining a fixed relationship. To modify this setting, a load reference set point is introduced, offering a means of regulating the output power of a generating unit. This adjustment is typically achieved through a speed changer, which results in a change in generator output. To facilitate frequency restoration, a supplementary control loop is incorporated into the governor and turbines.

Large synchronous generators can include a supplementary frequency control loop in addition to the primary control of frequency. The schematic block design for the generator depicts both the primary and secondary frequency regulation loops (Bevrani Hassan et al., 2017) (Bevrani Hassan, 2014). The supplemental loop adds

feedback to the primary control loop utilizing a dynamic control technique and provides feedback via frequency offset. The signal received is used to adjust the system's frequency. The dynamics control system in real-world PS is frequently a simple integral or proportional integral control. After a load shift, the feedback provides the turbine with the appropriate signal to supply (ΔP_m) load monitoring and restore SF in Figure 2.12 (Esmail M. et al., 2017).

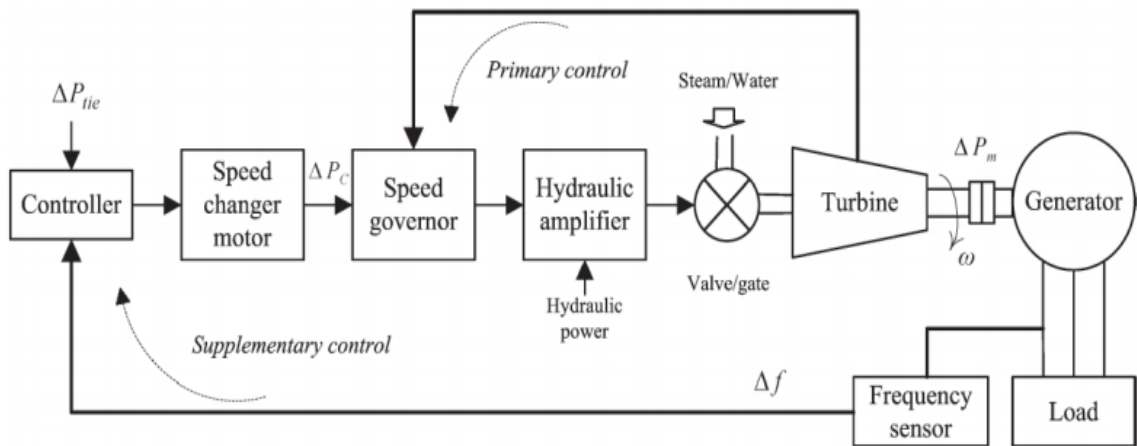


Figure 2.12. Governor-turbine with primary frequency control loop

2.4.3 Power system frequency regulation

In (Zhu Jianzhong et al., 2022) (Bevrani Hassan, 2014), a simplified governor-generator model for the single PS was established, as depicted in Figure 2.13. This model is employed for the analysis of PS frequency and the design of control strategies. It employs first-order transfer functions to represent the governor-turbine dynamics. The time constants of the governor and turbine (T_g , T_t , T_{tr} , and T_r) are presented in Table 2.2 (Zhu Jianzhong et al., 2022) (Bevrani Hassan, 2014) (Wood Allen J et al.)

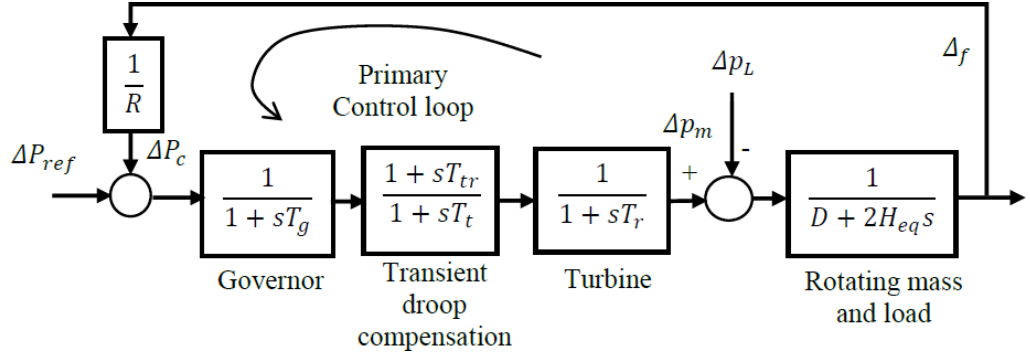


Figure 2.13. Primary frequency control model for PS

The droop gain R is determined by the ratio of frequency change $\Delta f(t)$ to the change in generator power output $\Delta P(t)$, as illustrated in Figure 2.13 (Bevrani Hassan et al., 2017). The primary goal of the turbine-governor control system is to maintain the system's desired frequency by regulating the mechanical power output of the turbine $\Delta P_m(t)$.

Table 2.2 Characteristics of the simplified power system

$1/R$	T_g	T_{tr}	T_t	T_r	H_{eq}	D
-0.09 pu	0.2 s	2 s	12 s	0.3 s	4.44 s	1 pu

Equation 2.3 depicts the connection between frequency and power in turbine-governor control:

$$\Delta P_c(t) = \Delta P_{ref}(t) - \frac{1}{R} \Delta f_i(t) \quad (2.3)$$

The term $\Delta P_c(t) - \Delta P_{ref}(t)$ is signified by $\Delta P(t)$, such that the droop gain is established.

$$-R = Slope = \frac{\Delta f(t)}{\Delta P(t)} \quad (2.4)$$

The governors employ droop control to regulate generator power output in response to changes in frequency. This process is referred to as primary frequency control and is automatically overseen by the governors. For instance, when there is a decrease in power demand (or a decrease in power generation) resulting in a frequency decrease, the governors automatically supply a low-frequency response. Conversely, in the case of reduced demand (resulting in a frequency increase), the

governors provide a high-frequency response (Muhssin Mazin et al., 2018).

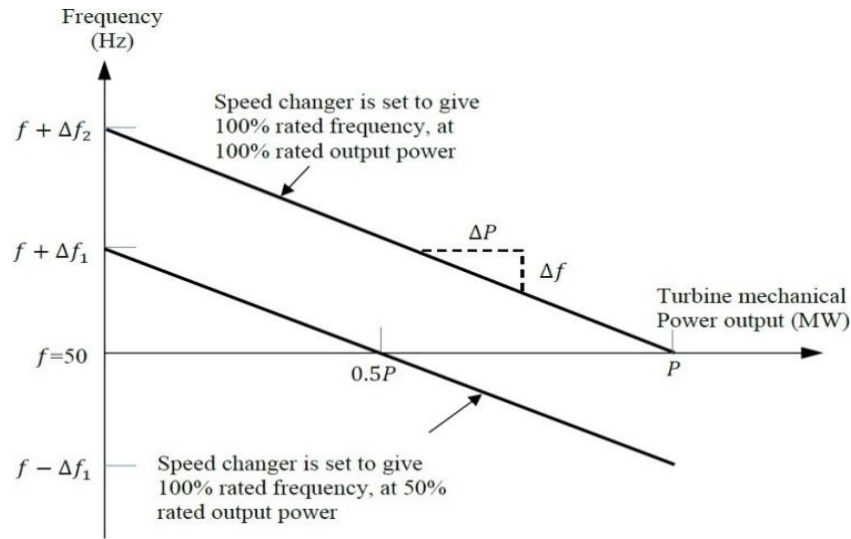


Figure 2.14. The equilibrium state frequency-power correlation within a turbine-governor control system

2.4.4 Frequency control in an interconnected power system

The assumption of coherence among a group of generators, where they collectively oscillate at a synchronized frequency, plays a significant role in defining CA. Generators within a CA work together to address disturbances within that specific region, operating as a unified entity managed by a Transmission System Operator (TSO) (Asghar Rafiq et al., 2023). There's also the possibility of grouping multiple control areas into a larger single control area, where these larger areas operate in coordination with one another. These individual control areas are interconnected by tie lines, allowing for the exchange of power between them, often based on predetermined agreements that consider the operating costs of the selling utility (Alhelou Hassan Haes et al., 2018).

A multi-area PS consists of regions linked together through high-voltage transmission lines or tie-lines. The frequency variations observed in each CA serve as indicators of the power imbalance trends in the interconnections, not just within each individual control area. In an interconnected or multi-area PS, the secondary frequency control or LFC system within each control area plays a crucial role in managing both the local frequency and the exchange of power with other control

areas. To illustrate this, refer to Figure 2.15, which illustrates a PS comprising N control areas:

Equation expresses the power flow over the tie-line from region 1 to region 2 (2.5).

$$P_{tie,12} = \frac{V_1 V_2}{X_{12}} \text{Sin}(\delta_1 - \delta_2) \quad (2.5)$$

In the provided equations, V_1 and V_2 represent the voltage values in per unit (p.u.) at the terminals of the equivalent machines in area 1 and area 2, respectively. Similarly, δ_1 and δ_2 stand for the power angles of the equivalent machines in area 1 and area 2, while X_{12} denotes the reactance of the tie line connecting area 1 and 2.

Using (2.5) as a linearization around an equilibrium point:

$$\Delta P_{tie,12} = T_{12} (\Delta \delta_1 - \Delta \delta_2) \quad (2.6)$$

where the synchronous force ratio T_{12} , as given by

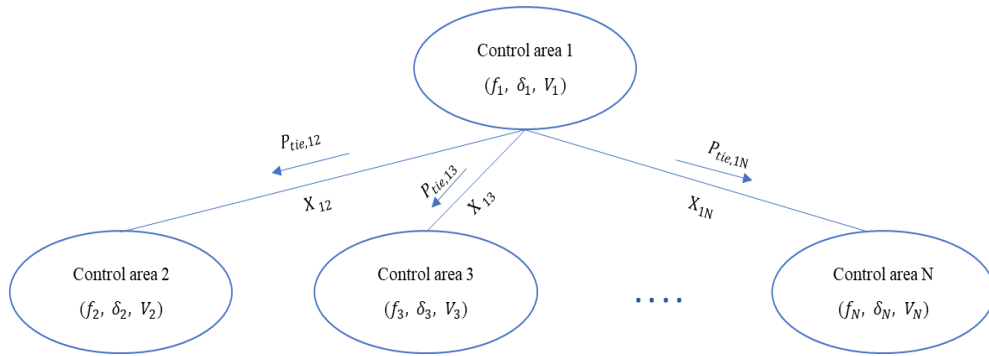


Figure 2.15. A schematic diagram of an N-area interconnected PS.

$$T_{12} = \frac{|V_1||V_2|}{X_{12}} \text{Cos}(\delta_1^0 - \delta_2^0) \quad (2.7)$$

Taking into account the connection between the power angle and frequency within the control areas, Equation (2.6) can be expressed as follows, where Δf_1 and Δf_2 represent frequency changes in area one and two, respectively. When we apply the Laplace transform to (2.8), it leads to Equation (2.9).

$$P_{tie,12} = 2\pi T_{12} (\int \Delta f_1 - \int \Delta f_2) \quad (2.8)$$

$$P_{tie,12}(s) = \frac{2\pi}{s} T_{12} \{ \Delta f_1(s) - \Delta f_2(s) \} \quad (2.9)$$

It seems like you're discussing the dynamics of power systems, particularly in the context of frequency control and the interaction between different control areas within a multiarea power system. The use of the CA concept helps to conceptualize and coordinate the response of generators and loads within a coherent area, ensuring that frequency remains stable across the entire system.

In an isolated power system, where there's no external tie-line connecting to other areas, the primary concern is restoring the system frequency to its nominal value. However, in a multiarea power system, where areas are interconnected via tie-lines, the frequency trend in each control area reflects the power exchange dynamics between different areas, not just within a single area.

In such interconnected systems, LFC systems in each control area need to manage not only the local frequency but also the interchange power with other control areas. This requires modifications to the dynamic LFC system model to incorporate signals from tie-lines, as depicted in Fig. 2.9, which represents a power system with multiple control areas (N-control areas).

By accounting for tie-line power signals, the LFC system can effectively regulate interchange power with other areas while maintaining stable frequency within each control area, ensuring overall system reliability and performance. Similar to this, Equation (2.10) provides the net power exchange between area 1 and area 3:

$$P_{tie,13}(s) = \frac{2\pi}{s} T_{13} \{ \Delta f_1(s) - \Delta f_{13}(s) \} \quad (2.10)$$

Taking into account equations (2.9) and (2.10), the total change in tie-line power between area 1 and the other areas can be computed using the formula presented in (2.11):

$$P_{tie,1}(s) = P_{tie,12} + P_{tie,13} = \frac{2\pi}{s} \left[\sum_{j=2,3} T_{1j} \Delta f_1 - \sum_{j=2,3} T_{1j} \Delta f_j \right] \quad (2.11)$$

According to Figure 2.15, the total tie-line power fluctuation between region 1 and the remaining areas for N-control regions is.

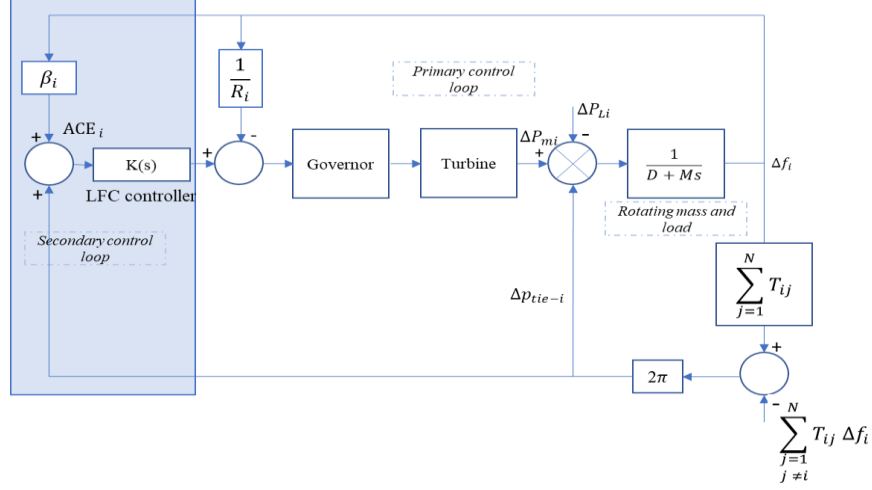


Figure 2.16. A simplified PS with an interconnected LFC controller

Equation (2.12) can be illustrated using a block diagram, which can be incorporated into the mechanical power mismatch $\Delta P_m - \Delta P_L$ as depicted in Figure 2.8. Consequently, the less complex block schematic of the linked PS is presented in Figure 2.15.

$$P_{tie,i}(s) = \sum_{\substack{j=1 \\ j \neq i}}^N \Delta P_{tie,ij} = \frac{2\pi}{s} \left[\sum_{\substack{j=1 \\ j \neq i}}^N T_{ij} \Delta f_i - \sum_{\substack{j=1 \\ j \neq i}}^N T_{ij} \Delta f_j \right] \quad (2.12)$$

In Figure 2.15, the shaded block denotes the secondary control loop when a tie-line is present. The alteration in tie-line power flow $\Delta P_{tie,i}$ is introduced to the frequency change Δf_i via a secondary feedback loop. Subsequently, the area control error ΔACE_i signal is calculated as described in Equation (2.13) and fed into the controller $K(s)$:

$$ACE_i = P_{tie,i} + \beta_i \Delta f_i \quad (2.13)$$

in which Equation (2.14) (Bevrani, 2014) may be used to determine the bias factor β_i

$$\beta_i = \frac{1}{R_i} + D_i \quad (2.14)$$

When there is a decrease in the area frequency, the LFC controller $K(s)$ will make adjustments to ACE_i (to bring it back to zero) and transmit the control signal to the governor.

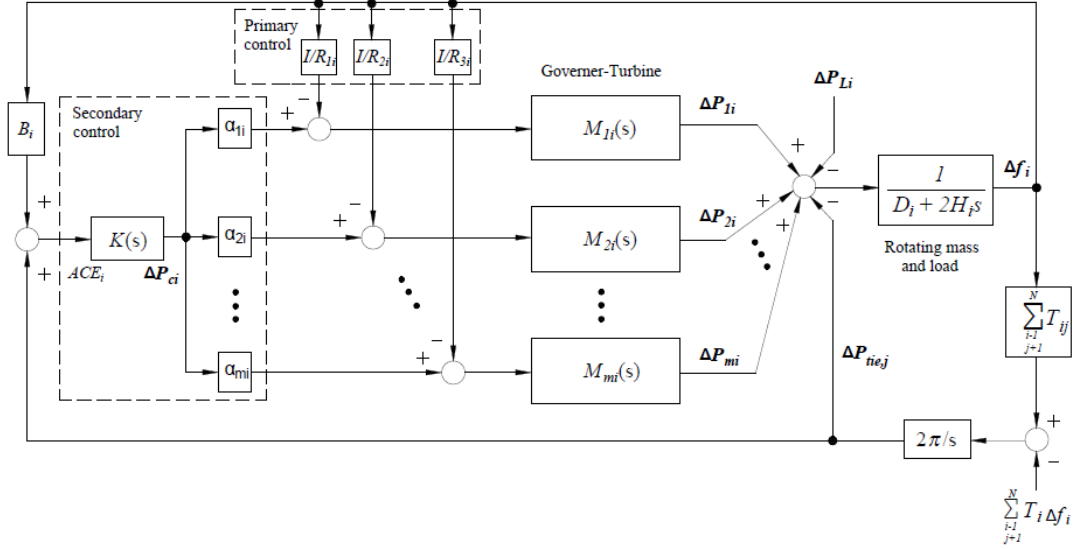


Figure 2.17. LFC system with various contributing elements and generating units in the region i.

This action aims to control the area frequency and uphold the scheduled level of net-interchange power. In each CA, numerous generators with diverse turbine-governor characteristics and power generation methods are present. Additionally, within this updated framework, generators may choose to partake or abstain from participating in the LFC process, and the degree of participation is not uniform among all contributing generators. To account for the diverse dynamics of power generation and the varying levels of involvement in secondary control, the dynamic model for control area i^{th} is depicted in Figure 2.17. There are many kinds of plants in power system such as Hydropower plants, Thermal power plants, Wind power plant, Solar power plant, Gas power plant and so on in Appendix 2.1 (Asghar Rafiq et al., 2023).

2.5. Load frequency control based different power system models.

2.5.1 Traditional power networks

For many years, traditional PS have relied predominantly on thermal, hydro,

and nuclear energy sources. These systems are typically categorized into four groups based on their size: single area, dual areas (which has received the most attention in research), three areas, and four areas PS (Ullah Kaleem et al., 2021). The supplemental AGC of a single area thermal PS with non-reheat turbines is proposed to be handled by a fractional order PID (FOPID) controller in this research (Ismayil C, 2014). In (Shiva Chandan Kumar et al., 2016), a single-area PS is examined to assess the effectiveness of a novel LFC method utilizing a unique quasi-oppositional harmony search algorithm. A comprehensive model is explored to illustrate the interconnection LFC loops, demonstrating the relationship between the control of reactive and active power in a single area PS (Morsali Javad et al., In 2020).

The difficulties related to LFC in the context of dual-area PS models have been extensively examined in (Gupta Neelesh Kumar et al., 2021) illustrates the development and utilization of PID and the two degree of freedom PID control approach for a two areas interconnected PS. Various optimization methods are applied to fine-tune the parameters of a PID control scheme based LFC system within a dual-area PS, and this study explores their effectiveness in mitigating wave energy disturbances in (Mostafa Elsaied Mohamed et al. , 2018). An attempt has been made to utilize a cascade integral double derivative and PID control approach for LFC in a three-area interconnected PN, and the dynamic performance is presented in (Sanajaoba Singh Sarangthem, 2022). The first attempt at LFC in a four-area hydropower system, which utilizes a comprehensive approach integrating systems with dual mode control, interrupted control, and changeable structure, is introduced in (Sahu Rabindra Kumar et al., 2015).

2.5.2 Modern power systems

In recent years, the PS has undergone significant expansion driven by continuous innovations and evolving concepts aimed at enhancing system stability. To meet the load demands of consumers in a reliable and cost-effective manner, PSs are interconnected to form multi-area control systems. Furthermore, traditional PS structures are being replaced by deregulated frameworks, aiming to improve power

quality and foster competition within the power sector. The diminishing availability of fossil fuels has prompted the emergence of considering distributed generating based on sustainable energy sources as a viable option to meeting rising energy need. Moreover, innovative concepts such as the smart grid, microgrid, and deregulation strategies have had a profound impact on the control and the stability of modern PS. These developments represent significant changes in the energy landscape and its management. To address the uncertainty and complexity inherent in modern PS, numerous novel control techniques have been introduced.

Power networks with HVDC links:

Interconnecting multiple electrical networks gives rise to several challenges, such as the requirement for network synchronization, losses incurred in lengthy transmission lines, elevated short-circuit currents, and potential reductions in network stability. A potential solution to address these limitations involves the deployment of HVDC transmission systems. These systems offer the promise of increased capacity, enhanced reliability, and improved efficiency in the power network (Plihal Kieran , 2019). This research investigates LFC in an uneven four-area thermal system incorporating an HVDC, the performance of controllers, including fractional-order PID, is assessed separately within the system in (Pahadasingh Sunita et al. , 2020).

Regulated and deregulated power networks:

A comprehensive review of critical research areas in various LFC methods is conducted within a deregulated PS context, considering both conventional and distributed power generation sources (Pappachen Abhijith et al., 2017). The complexity of PS performance in restructured environments has grown due to technical limitations and traditional demands in (Shahalami Seyed Hamid et al., 2018). In this research, (Esmail M et al. , 2017) examines a range of control methods for the design of AGC within a deregulated PS context. Additionally, the paper provides an analysis of the challenges and benefits associated with the reviewed control techniques and structures.

Distributed generation power networks:

For this study, (Pahadasingh Sunita et al. , 2021) outlines a methodology for developing and applying a distributed LFC approach in PS. The approach relies on a control law that provides feedback on the internal rotor angle deviation to each generator's governor. Consequently, the governors function as distributed controllers for regulating both frequency and transferred power, utilizing local measurements.

Micro grid power networks:

Frequency deviation is a significant issue in PN, especially in stand-alone hybrid microgrids that incorporate wind and solar systems with maximum power point tracking techniques. To address this problem, PID controllers have been employed to mitigate frequency deviations in the proposed stand-alone hybrid microgrid in (Nisha G. et al. , 2022). In this case, (Gnanam Nisha et al. , 2023) discusses a hybrid PS that integrates solar, wind, and battery sources. To tackle this issue, the paper shows the use of well-structured PID controllers for LFC in a stand-alone hybrid microgrid.

Smart grid power networks:

In (Vanitha, C. et al., 2023), a smart network is a high-tech electricity infrastructure that utilizes automation and energy management techniques to efficiently control various electronic operations and respond to energy demand. A smart grid is an intelligent electricity grid that leverages information and communication technologies to improve the production, distribution, and consumption of energy in (Daki Houda et al. , 2017). The smart grid is anticipated to transform the current electrical grid by enabling bidirectional communication, enhancing efficiency, reliability, cost-effectiveness, and sustainability in the generation, transmission, and distribution of electrical power in (Bari Ataul et al. , 2014).

Energy storage systems (ESSs) in power networks:

In this study, (Shankar Ravi , 2016) centers on the LFC mechanism in a deregulated power environment for a multi-generator, two-area interconnected PS

that includes an electricity system for storage. In the context of managing unwanted fluctuations in frequency and tie-line power, this study investigates the impact of an energy storage device on LFC performance in a dual-area interconnected PS that includes thermal and solar photovoltaic (PV) power sources in (Çelik Emre et al. , 2023).

Renewable energy in power network:

The light of the growing global awareness of climate change, there is a heightened priority placed on renewable energy systems over conventional energy systems (Gulzar Muhammad Majid et al. , 2022). Among these challenges, managing frequency changes is crucial for maintaining power quality in the grid (Tummala Ayyarao SLV et al. , 2018). The integration of electric vehicles into AC microgrids presents a crucial role in managing the challenges posed by the integration of the renewable energy sources, such as wind and solar farms (Jampeethong Phoompat et al. , 2020). The LFC problem becomes more challenging in systems with lower inertia and the stochastic behavior of solar radiation and wind speed, in contrast to conventional PS. (Ramesh Maloth et al. , 2021) explores the contributions of solar generators, wind turbine generators, energy storage systems, electric vehicles, and controllable loads to address and mitigate LFC issues in such systems. To address this issue, (Yang Minghui et al. , 2020) introduces a LFC approach that utilizes double equivalent-input-disturbance controllers researching and considering the impact of dynamic changes in SF on PV output power. It utilizes an artificial neural network with a radial basis function (ANN-RBF) to capture the nonlinear behavior of the PV power plant, taking into account frequency deviation as one of the input variables under various operating conditions in (Bakeer Abualkasim et al. , 2022). To offer a more pragmatic approach for regulating the frequency and the tie-line power flow within a MAIPS, (Huynh Van Van et al. , 2021) introduces a state observer based on SMC that operates with a second-order time derivative. In this study (Abazari Ahmadreza et al. , 2019), the authors present a model to analyze and simulate renewable power generation in two-area PS with a significant presence of wind farms.

To harness the stored kinetic energy from the rotating masses during abrupt load disturbances, a droop controller designed for a type 3 wind turbine is employed in (El-Bahay et al. , 2023).

Effects of nonlinear elements and time delays on ACG systems:

The critical factors impacting PS performance include time delay, GRC, and GDB nonlinearity. GDB refers to the range of speed change where there is no adjustment in valve position. GDB's impact is to amplify the perceived steady-state speed regulation in (Bevrani Hassan, 2014). In the research, the adjustable parameters of these controllers are optimized using an enhanced particle swarm optimization algorithm, incorporating chaotic parameters and a crossover operator, to achieve a globally optimal solution (Morsali Javad et al. , 2018). In this research, (Heidary Jalal et al. , 2022) introduces an innovative LFC method based on an optimized coefficient diagram method for a two-area thermal PS with consideration non-linearities under GDB and GRC.

This paper examines the effect of delay when communicating on load frequency regulation in an autonomous hybrid PS, particularly in the context of wide area monitoring and control applications where (Singh Vijay P. et al. , 2015). In this study, (Shangguan et al.) explores event triggered LFC in a PS with time delay and an open communication network. In this research, (Jain Shivam et al. , 2023) introduces an innovative control approach known as smith predictor generalized active disturbance rejection control) tailored to address communication delays in PS. Therefore, further research is required to investigate the effects of GRC, GDB, and delays in PS stability and LFC effectiveness to reduce the effect and enhance the whole effectiveness of the system.

2.6. Control strategies

2.6.1 Centralized control approach

Numerous studies have documented various LFC methods employing a centralized approach within diverse PS models. In traditional PS, LFC or AGC is achieved by employing PI controllers within steam turbine generator systems. In this

PI controller, the proportional component accounts for the governor's droop characteristics, while the integral component works to bring the frequency back to its nominal value by adjusting the load reference set point of the turbine valve in (Sagar P. et al. , 2016). LFC has been among the pioneering wide-area control applications within the power industry (Casavola et al. , 2023). The primary drawback of this approach lies in the requirement to exchange information between distinct control regions, which may not always be feasible or applicable.

2.6.2 Decentralized control approach

The decentralized scheme to LFC in PS was represented as a solution to overcome the limitations of the centralized method. This scheme is highly favored due to its simplicity and practicality, making it the preferred choice for LFC in large and complex PS. It alleviates the computational workload and communication complexity. In control scheme, intricate large-scale PSs are partitioned into multiple subsystems, each equipped with its own controller. An adaptive deadbeat control approach was created to assess its potential in delivering a rapid frequency response to an electrical PS. The control scheme in (Muhssin Mazin T. et al., 2017) was specifically designed to meet the criteria set forth in the national grid system operability framework. In (Arya Yogendra, 2018) a novel approach is introduced, involving an output scaling factor based fuzzy classical control approach, to improve the efficiency of AGC in two-area electrical PS. Despite its numerous advantages compared to the centralized approach, it's important to emphasize a key aspect of this approach. While it is widely adopted and extensively researched, it's not fully decentralized. This is because it relies on measuring the overall variation in the flow of power through tie lines that interconnect different areas. Since this measurement is not locally obtained, it introduces an element of centralization in an otherwise decentralized control scheme.

2.7. Categories of LFC based on different control strategies.

In the previous several decades, there has been a proliferation of control techniques proposed and developed to effectively address the issue of frequency

deviation. As PS has grown increasingly intricate, numerous control theories have emerged to confront the evolving challenges posed by modern PS. Consequently, a range of new hybrid techniques has been introduced to tackle these challenges effectively. In this subsection, we provide an up-to-date review that categorizes and investigates the various controllers proposed for LFC.

2.7.1 Classical control methods

Most investigations concerning the LFC field tend to focus on the utilization of typical control approaches. In traditional control techniques, techniques such as Bode plots, Nyquist diagrams, and root locus analysis are conventionally employed to determine the optimal controller gains and the phase margins. These well-established methods have been extensively applied in LFC research to design controllers that effectively regulate PS' frequency. The conventional LFC design scheme exhibits a destabilizing effect and unsatisfactory performance. As a result, (Saxena Sahaj , 2018) introduces an analytical and graphical approach for designing a PI controller tailored to address the challenges of a single-area LFC system with time system delays. The objective of (Celik Vedat et al., 2019) is to assess the impact of using a fractional order PI control scheme on the enhancement of delay margin in the management part of a single area LFC network with time delays as well. In the context of the high efficiency distributed PS, a three degrees of freedom PID control scheme has been developed and put into operation in (Guha Dipayan et al. , 2018). While this approach offers a broad array of advantages, there's a pressing need for more realistic techniques to fine-tune its parameter settings. Additionally, addressing the limitations of this approach in the face of system uncertainties is of utmost importance.

2.7.2 The concept discussion of optimal and sub-optimal control.

Optimal control principles are presented as a streamlined approach for addressing complex multivariable control problems. This controller relies on the state variable model and aims to minimize a cost function. In this research (Hamodat Zaid, 2021), a fuzzy PID controller optimized using a whale-inspired algorithm was

developed to oversee AGC in multi-area electrical energy systems operating under an availability-based tariff pricing scheme. (Hakimuddin et al. , 2020) investigates the AGC of a real-world, two-area multi-source PS including hydro, thermal, gas, and wind energy. The theoretical framework supporting these techniques operates on the assumption that it's possible to establish an aggregated CA model in (Patel Ragini et al. , 2019). Optimal controller approaches have demonstrated numerous advantages and may potentially play a prominent role in LFC in the future, provided that their design can incorporate the real-time dynamic states of the PS and effectively address potential cyber-attack challenges.

2.7.3 Adaptive control for LFC power network

Adaptive control has garnered significant attention from researchers over the past four decades. In (Mokhtar et al. , 2022), an adaptive controller is introduced with the aim of improving system performance, especially when dealing with load fluctuations. Furthermore, the proposed controller effectively mitigates disturbances arising from the inherent operation of energy from renewable sources, such as wave energy conversion systems and photovoltaic systems in (Gulzar Muhammad Majid et al. , 2022). Despite the significant advantages associated with this approach, it's important to note that it can be quite complex to implement. Moreover, achieving the ideal model following issues for the controlling plant is crucial for the successful application of this technique.

2.7.4 Robust control

Researchers have extensively explored LFC strategies grounded in the principles of robust control design. This preference is driven by the advantages that they bring in terms of enhancing system stability and fortifying it against uncertainties and fluctuations in plant parameters. In (Ahammad, F. U. A., & Mandal, S., 2016), we introduce the creation of robust controllers designed to address the challenges of frequency fluctuation reduction and tie line power error minimization in a MAPS experiencing various load disturbances. This control scheme considers system uncertainties and disturbances to ensure robust control performance in (Tabassum

Fariya et al. , 2020). A novel topological structure for the interconnected PS, incorporating the HESS, has been introduced in (Yan Wenxu et al. , 2018). In (Shangguan et al. , 2021), an innovative approach is introduced to enable the efficient design of a robust LFC scheme for large-scale PSs with time delays. Subsequently, they have implemented a novel control strategy known as the fractional-order global SMC scheme, which approaches in (Lv Xinxin , 2021) is aimed at enhancing the robustness of LFC.

This approach's benefits in managing parametric uncertainty have been validated. Nevertheless, it's important to note that designing a robust controller necessitates a deep understanding of the system under investigation, which is often unattainable in the case of many PS.

2.7.5 Artificial intelligence schemes

Recently, incorporating sustainable sources of energy has resulted in the expansion of PS, both in size and structural complexity. Typical or robust control techniques may no longer be sufficient to provide the appropriate degree of system accuracy. Soft computing approaches have become increasingly popular in answer to this difficulty. Based on optimizing methods, these techniques include ANN, FLC, and soft computing. Here is a summary of these approaches:

In this research, (Rajendran et al. , 2023) focuses on the study involves evaluating the performance of various controllers, including the controller for adaptive neuro fuzzy inference network, droop controller, FLC, ANN, and fractional order PID control scheme, within the context of the suggested AGC deregulated PS. (Sharma et al. , 2020) examines a two-area PS, which comprises non-reheat thermal turbines equipped with doubly fed induction generators and is parallel AC/DC tie-lines connected the systems together.

Fuzzy logic control is employed to address complicated and non-linear control issues that may not be effectively handled by typical control schemes. This approach has found extensive use in addressing various LFC challenges within PS. introduces an approach combining (Jalali Neda et al., 2020) the PI algorithm with fuzzy logic

techniques to design for two-area PS. This hybrid controller aims to implement the performance of LFC in the considered PS. In reference (Cam Ertugrul et al. , 2017), the authors put forth an innovative scheme to enhance the responsiveness and efficiency of a hybrid dual area PS. This improvement is realized by employing a well-coordinated approach that combines an optimized fuzzy fine-tuning method with the incorporation of gate-controlled series capacitors.

Over the past decade, numerous researchers have delved into the control and stability of PS, employing a variety of algorithms, including GA, FA, and TLBO. In many instances, (Bhagat S. et al. , 2014) introduces the utilization of a GA as an approach to attain an optimized value for the tuning parameter employed in the design of TDF-IMC controllers. Furthermore, genetic algorithm optimization is used to optimize the settings of the controlling agent (Daneshfar Fatheme et al. , 2010).

Kennedy and Eberhart presented the particle swarm optimization (PSO) method in 1995, and since then, it has garnered a lot of interest. In reference, (Soliman, Ahmed Mohammed Attiya et al. , 2023) introduces a robust secondary LFC for a two-area multi-source interconnected PS, where each area incorporates central solar park power plants. The study leverages heuristic methods, specifically particle swarm intelligence and fuzzy-based inferences, to efficiently determine the optimal gains for PID controllers. (Ogar Vincent N. et al. , 2023) highlights the utilization of a combined approach known as PSP-PID, which integrates PSO with PID controllers. This combination has shown promise in enhancing LFC system performance.

In this work (Ranjitha K. et al., 2021), a novel LFC, which has been optimized using the Firefly algorithm, is introduced for a PS that incorporates distributed generation. This system accommodates integrating sources that are renewable of power, such as solar PV systems and wind power to address the growing power demands. (Gorripotu et al. , 2017) presents a unique approach to LFC in a multi-area, multi-source system operating within a deregulated environment. The proposed method involves the use of a FA optimized hybrid fuzzy PID control scheme with a derivative filter. It considers various physical constraints, including the GRC and

GDB nonlinearity, to enhance the system's control system efficiency.

Numerous researchers have put forth various LFC techniques utilizing the DE algorithm as well as the TLBO method. In (Sahoo Dillip Kumar et al. , 2022), a new evolutionary differential evolution algorithm optimized Fuzzy PID control scheme is introduced for the purpose of LFC in an interconnected PS. This controller design considers the presence of nonlinearity within the system. In the context of a multi-source PS, (Gupta Deepak Kumar et al. , 2021)introduces an innovative hybrid optimization approach rooted in heuristics. Its primary aim is to attain the goal of automated LFC.

In addition to the methods mentioned, various other algorithms, including the Ant Lion Optimizer algorithm, Bacterial Foraging Optimization, Grey Wolf Optimizer algorithm, and Artificial Bee Colony, have been employed to optimize and adjust parameters of different controllers. These approaches have been utilized to address the complexities and challenges associated with LFC in diverse PS, as referenced in (Guo Chen et al. , 2021), (Paliwal Nikhil et al. , 2022).

Indeed, LFC techniques utilizing Artificial Intelligence (AI) methods have proven to be highly effective, showcasing exceptional ability to manage modelling uncertainties and system nonlinearities throughout a range of operational circumstances. One notable advantage of these AI-based approaches is their ability to operate without the strict requirement of an exact and precise system model.

2.7.6 Sliding mode control approach

Certainly, the SMC approach is fundamentally based on Variable Structure Control (VSC) principles, which originated in the early 1950s. Since its inception, this control concept has attracted considerable attention from researchers who have endeavored to apply it across a wide range of applications, harnessing its many advantages. Notably, SMC has proven to be highly valuable in addressing and mitigating the challenges associated with LFC in PS. (Kumar Anand and et al., 2021) presents a technique for crafting a SMC aimed at regulating the frequency within an interconnected PS. In reference (Cucuzzella Michele et al. , 2018), an alternative

approach to distributed SMC is introduced, with a specific focus on optimizing LFC. Reference (Yang Shengchun et al. , 2017) introduces a design that employs a sliding-mode perturbation observer-based SMC. In (Prasad Sheetla et al. , 2019) a different approach for LFC is developed, involving a nonlinear SMC capable of handling both matched and mismatched uncertainties. This approach is tested and validated in three control area PS. References (Mi Yang et al. , 2013) and (Prasad Sheetla et al. , 2017) describe a robust and potent nonlinear SMC method for LFC. This technique significantly enhances the performance of dynamic systems. Indeed, the SMC frequency controller mentioned earlier suffers from a notable drawback known as the “chattering phenomenon”. This problem emerges due to the use of a control signal in SMC that exhibits discontinuous behavior. Chattering can give rise to several unfavorable outcomes when applied to LFC systems within PS control areas. These repercussions encompass the risk of harming control actuators and the activation of unwanted unmodeled dynamics. Consequently, this chattering phenomenon can result in a decline in system performance and even the onset of instability.

2.7.7 Alternative control methods for load frequency control

In the research, a novel application of a linear quadratic regulator-based PI control approach is introduced for LFC on a two areas multi-source interconnected PS as a practical case study in (Prakash Abhineet et al. , 2020). In (Ali Hossam Hassan et al.), an optimal MPC strategy is fine-tuned employing a contemporary optimization algorithm referred to as the "Sooty Terns Optimization algorithm" employed in the design of an LFC system for renewable energy sources. (Singh Vijay P. et al., 2017) outlines an approach for calculating the best PID control scheme performance improvements, considering LMI constraints. The primary This design's subjective impression is to facilitate load frequency regulation in both single area and multi-area PS.

2.8. Summary

In the realm of PS, LFC plays a critical role in ensuring that customers receive an adequate and dependable supply of electrical power. This chapter provides an

extensive and current literature review on LFC within PS. The survey primarily focuses on LFC models designed for conventional PS, given their prominence in the field. However, the research also delves into recent advancements in LFC methodologies, addressing the unique aspects of modern PS, including deregulated PS, smart grids, microgrids, and PS integrated with renewable energy sources. Furthermore, this chapter offers a concise discussion of various control strategies. Finally, it reviews multiple control approaches applied to LFC in diverse PS. Each approach's benefits and possible drawbacks are extensively examined. Notably, the review highlights that LFC based on a decentralized scheme, utilizing soft computing techniques in conjunction with renewable energy resources, is a widely researched area that still requires further refinement, given its prevalence in modern PS.

In conclusion, this extensive literature review highlights a notable research gap in the realm of LFC systems, particularly in the application of soft computing techniques. Remarkably, no prior attempts have been documented in utilizing various schemes of SMC for the design of secondary frequency control in PS. The demonstrated effectiveness and superiority of various novel SMC as an optimization tool in diverse fields has prompted the author to explore this potent optimization techniques. In pursuit of the highest dynamic performance, various innovative SMC schemes were employed for optimization. These include: Firstly, the suggested approach, known as SOISMC, not only effectively eliminates chattering in the control input but also ensures the flexibility of the multi-area PN; Secondly, the load frequency control of the TAGHTPS is introduced through the application of a SPSMCBSO; Thirdly, the proposed technique employs a SOSDISS, aiming to enhance frequency regulation, tie-line power management, and overall system reliability of the MASHPS.

CHAPTER 3: DESIGN OF A NEW SECOND ORDER SLIDING MODE CONTROL FOR POWER SYSTEM LOAD FREQUENCY CONTROL

In this chapter, applying SMC to regulate the frequency of PN encounters challenges as a result of the chattering phenomena associated with high-frequency switching. This chattering issue poses a significant risk to actuators utilized in PS. To address this problem, this research introduces a continuous control strategy that combines a second-order mode with integral sliding surface, offering a potential solution. The suggested second-order integral sliding mode control (SOISMC) not only effectively mitigates chattering in control input but also enhances the robustness of the multi-area PN, making it more resilient to parametric uncertainties, including load variations and parameter mismatches. Additionally, simulation results demonstrate that the proposed controller maintains high-quality effectiveness under a variety of operational situations, effectively rejects disturbances, reduces transient frequency response, eliminates overshooting, and provides improved handling of load uncertainties compared to various prior control methods.

The chattering phenomenon arises due to the use of discontinuous control signals in SMC, and it has several adverse effects on LFC within PS control areas. Chattering has the potential to harm control actuators and activate undesired unmodeled dynamics, possibly leading to performance degradation and/or system instability. In this study, a continuous SMC strategy utilizing the second order integral sliding mode control (SOISMC) scheme is presented and formulated for LFC in an interconnected multi-area power network. This study's main contributions can be summarized as follows:

- ✓ A second order SMC utilizing an integral sliding surface is proposed to expedite the frequency's transient response and prevent overshooting.
- ✓ The PS's performance has been enhanced by mitigating chattering, as compared to employing the same SMC technique without the use of a

continuous controller. Consequently, this resolves the limitation associated with the strategy utilizing first order SMC described in (Guo Jianping, 2015) (Guo Jianping, 2019).

- ✓ A novel LMI technique is developed to ensure the overall system's stability through the application of Lyapunov theory.
- ✓ The simulation outcomes not only demonstrate but also conclusively verify the utility, efficiency, and resilience of the suggested SOISMIC approach in dealing with diverse disturbances, including matched and mismatched uncertainties, load fluctuations, and time-delayed communication. Moreover, in comparison to the prior control method involving the use of the differential games approach outlined in (Chen Haoyong, 2015). The results concentrate that the performance of the suggested SOISMIC scheme is notably superior.

3.1. A mathematical model for interconnected multi-area PS.

In this part, our primary objective is to introduce the mathematical model or dynamic model of the PN. The suggested LFC control law is tailored for an interconnected multi-area PS, as illustrated in Figure 3.1 (Guo Jianping, 2019), (Mi Yang et al., 2016), (Qian Dianwei , 2016), (Bui Le Ngoc Minh et al., 2018):

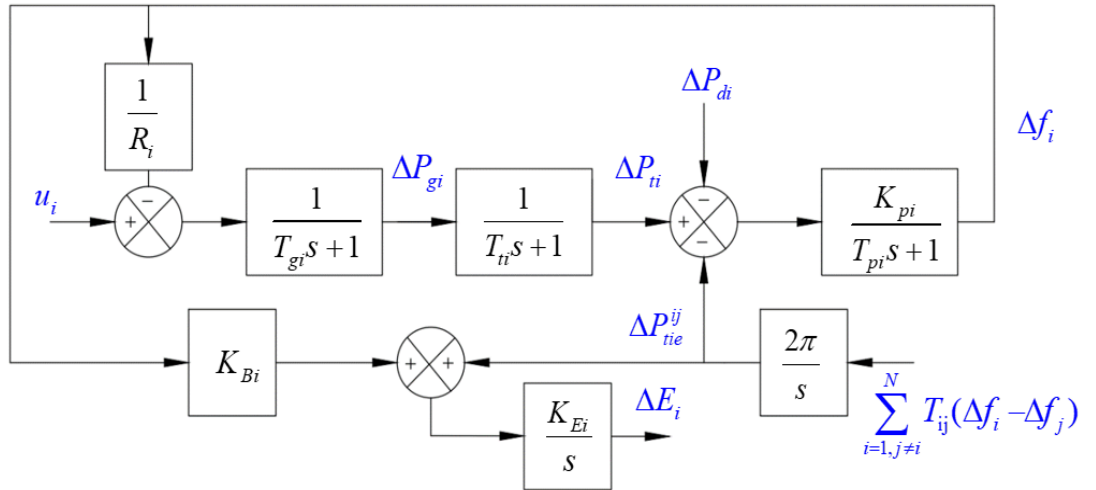


Figure 3.1. The simplified block diagram depicting the i^{th} area within a multi-area PS.

The detailed description of the frequency fluctuating actions in the i^{th} area, as provided in the part, can be applied in the subsequent the equation of differentiation:

$$\Delta \dot{f}_i(t) = -\frac{1}{T_{pi}} \Delta f_i(t) + \frac{K_{pi}}{T_{pi}} \Delta P_{ii}(t) - \frac{K_{pi}}{T_{pi}} \Delta P_{di}(t) - \frac{K_{pi}}{T_{pi}} \Delta P_{tie}^{ij}(t) \quad (3.1)$$

$$\Delta \dot{P}_{ii}(t) = -\frac{1}{T_{ii}} \Delta P_{ii}(t) + \frac{1}{T_{ii}} \Delta P_{gi}(t) \quad (3.2)$$

$$\Delta \dot{P}_{gi}(t) = -\frac{1}{R_i T_{gi}} \Delta f_i(t) - \frac{1}{T_{gi}} \Delta P_{gi}(t) + \frac{1}{T_{gi}} u_i(t) \quad (3.3)$$

$$\Delta \dot{E}_i = K_{Bi} K_{Ei} \Delta f_i + K_{Ei} \Delta P_{tie}^{ij} \quad (3.4)$$

$$\Delta \dot{P}_{tie}^{ij} = \sum_{\substack{j=1 \\ j \neq i}}^N 2\pi T_{ij} [\Delta f_i(t) - \Delta f_j(t)] \quad (3.5)$$

With i ranging from 1 to N , where N signifies the total count of control areas, $\Delta f_i(t)$ and $\Delta f_j(t)$ denote the incremental frequency changes for each respective control area (CA). Hence, the state-space representation of the i^{th} area in matrix form in Appendix 3.1, as depicted in the dynamic equations from (3.1) to (3.5), can be expressed as follows (3.6):

$$\dot{x}_i(t) = A_{mi} x_i(t) + B_{mi} u_i(t) + \sum_{\substack{j=1 \\ j \neq i}}^N H_{mij} x_j(t) + F_{mi} \Delta P_{mdi}(t) \quad (3.6)$$

$$\text{where, } x_i(t) = \begin{bmatrix} \Delta f_i(t) & \Delta P_{ii}(t) & \Delta P_{gi}(t) & \Delta E_i(t) & \Delta P_{tie}^{ij}(t) \end{bmatrix}^T$$

In practical PS, the operational state constantly fluctuates due to load disturbances and variations in available resources. When considering uncertainties and variations in parameters, the PS model can be described as follows:

$$\begin{aligned} \dot{x}_i(t) = & [A_{mi} + \Theta_{mi}(x_i, t)] x_i(t) + B_{mi} [u_i(t) + \xi_{mi}(x_i, t)] \\ & + \sum_{\substack{j=1 \\ j \neq i}}^N [H_{mij} + \Xi_{mij}(x_j, t)] x_j(t) + F_{mi} \Delta P_{mdi}(t) \end{aligned} \quad (3.7)$$

where, $\Theta_{mi}(x_i, t)$ refers to time-varying parameter uncertainties within the state matrix, $\Xi_{mij}(x_j, t)$ refers to the uncertainty in the linked matrix's time-varying parameters, and $\xi_{mi}(x_i, t)$ is the disturbance control input. Additionally, we can refer to the combined uncertainties, with the number of areas ranging from 1 to N :

$$\bar{L}_{mi}(x_i, t) = \Theta_{mi}(x_i, t)x_i(t) + B_{mi}\xi_{mi}(x_i, t) + \sum_{\substack{j=1 \\ j \neq i}}^N \Xi_{mij}(x_j, t)x_j(t) + F_{mi}\Delta P_{mdi}(t) \quad (3.8)$$

Therefore, the dynamic modeling (3.6) can be as well represented as:

$$\dot{x}_i(t) = A_{mi}x_i(t) + B_{mi}u_i(t) + \sum_{\substack{j=1 \\ j \neq i}}^N H_{mij}x_j(t) + \bar{L}_{mi}(x_i, t) \quad (3.9)$$

In this context, the term aggregated disturbance $\bar{L}_{mi}(x_i, t)$ encompasses uncertainties, comprising both the matched and mismatched components.

Assumption 3.1. The assumption is made that the aggregated disturbance $\bar{L}_{mi}(x_i, t)$ and the derivative of $\bar{L}_{mi}(x_i, t)$ is bounded, meaning that there exist known scalars γ_{mi} and $\bar{\gamma}_{mi}$ such that $\|\bar{L}_{mi}(x_i, t)\| \leq \gamma_{mi}$ and $\|\dot{\bar{L}}_{mi}(x_i, t)\| \leq \bar{\gamma}_{mi}$, where $\|\cdot\|$ is the matrix norm.

To demonstrate stability, we refer to the following lemma:

Lemma 3.1 (Kogan Mark Mikhailovich, 1999) Let $\bar{\mathbf{X}}$ and $\bar{\mathbf{Y}}$ are valid matrices with suitable dimensions, then for any scalar $\bar{\mu} > 0$, the matrix inequality that follows is valid:

$$\bar{\mathbf{X}}^T \bar{\mathbf{Y}} + \bar{\mathbf{Y}}^T \bar{\mathbf{X}} \leq \bar{\mu} \bar{\mathbf{X}}^T \bar{\mathbf{X}} + \bar{\mu}^{-1} \bar{\mathbf{Y}}^T \bar{\mathbf{Y}}. \quad (3.10)$$

Note 3.1: Assumption 3.1 and Lemma 3.1 establishes present conditions under which the sliding mode dynamics with matching and unmatched uncertainties are asymptotically stable. In the next part, a suggested SMC rule is created so that the system state is driven to and maintained on the sliding surface.

3.2. A novel second order sliding mode load frequency control design

3.2.1. Introduction of LFC approach

In this part, to be designed called SOISMC will be presented to address power networks facing challenges like parametric uncertainties and disturbances. Subsequently, we introduce the design of the second-order SMC law, relying on the Lyapunov stability theorem. This design showcases that the system's states converge to the sliding manifold and remain on it even in the presence of uncertainty in internal

parameters and external disruptions.

3.2.2. A scheme design of second order sliding load frequency control

Within this part, to present a novel approach, referred to as SOISMC, aimed at addressing the challenges encountered by PN dealing with issues like parametric uncertainties and disturbances. To address these challenges, the new scheme systematically outlines a step-by-step process for designing and implementing this innovative controller approach.

3.3.2.1 The integral sliding surface in the context of SMC.

To elaborate further, we initiate the process by proposing and constructing an integral sliding surface specifically designed for MAPS (3.9)

$$\sigma_{mi}[x_i(t)] = \bar{G}_{mi}x_i(t) - \int_0^t \bar{G}_{mi}(A_{mi} - B_{mi}K_{mi})x_i(\tau)d\tau \quad (3.11)$$

where, \bar{G}_{mi} is a continuous matrix and K_{mi} is the matrix of design, matrix \bar{G}_{mi} is selected to ensure that matrix $\bar{G}_{mi}B_{mi}$ is nonsingular. The matrix of design $K_{mi} \in R^{m_i \times n_i}$ chosen in such a way that it satisfies the inequality condition of the PS.

$$\text{Re}[\lambda_{\max}(A_{mi} - B_{mi}K_{mi})] < 0 \quad (3.12)$$

When combining (3.9) with the ability to identify and distinguish $\sigma_{mi}[x_i(t)]$ regarding time, then.

$$\begin{aligned} \dot{\sigma}_{mi}[x_i(t)] = & \bar{G}_{mi}[A_{mi}x_i(t) + B_{mi}u_i(t) + \sum_{\substack{j=1 \\ j \neq i}}^N H_{mij}x_j(t) + \bar{L}_{mi}(x_i, t) \\ & - \bar{G}_{mi}(A_{mi} - B_{mi}K_{mi})x_i(t)] \end{aligned} \quad (3.13)$$

Therefore, the configuration $\sigma_{mi}[x_i(t)] = \dot{\sigma}_{mi}[x_i(t)] = 0$, the equivalent control can be expressed as

$$\begin{aligned} u_i^{eq}(t) = & -(\bar{G}_{mi}B_{mi})^{-1}[\bar{G}_{mi}A_{mi}x_i(t) + \sum_{\substack{j=1 \\ j \neq i}}^N \bar{G}_{mi}H_{mij}x_j(t) + \bar{G}_{mi}\bar{L}_{mi}(x_i, t) \\ & - \bar{G}_{mi}(A_{mi} - B_{mi}K_{mi})x_i(t)] \end{aligned} \quad (3.14)$$

Alternating $u_i(t)$ with $u_i^{eq}(t)$ into the PS (3.9) gives the movement of sliding.

$$\begin{aligned} \dot{x}_i(t) &= (A_{mi} - B_{mi}K_{mi})x_i(t) + [I_i - B_{mi}(\bar{G}_{mi}B_{mi})^{-1}\bar{G}_{mi}]\bar{L}_{mi}(x_i, t) \\ &+ \sum_{\substack{j=1 \\ j \neq i}}^N [I_i - B_{mi}(\bar{G}_{mi}B_{mi})^{-1}\bar{G}_{mi}]H_{mij}x_j(t) \end{aligned} \quad (3.15)$$

The subsequent theorem establishes a condition under which the second order sliding mode dynamic Equation (3.15) demonstrates asymptotic stability.

3.2.2.2 Analysis of the MAPS's stability in sliding mode dynamics

Theorem 3.1. The sliding motion (3.15) is only asymptotically stable when a symmetric positive definite matrix is included P_{mi} , $i=1, 2, \dots, N$, and positive scalars $\hat{\epsilon}_{mi}$ and α_{mj} such that the following LMIs obtains.

$$\left[\begin{array}{cc} (A_{mi} - B_{mi}K_{mi})^T P_{mi} + P_{mi}(A_{mi} - B_{mi}K_{mi}) + \sum_{\substack{j=1 \\ j \neq i}}^N \alpha_j^{-1} H_{mji}^T H_{mji} & P_{mi}[I_i - B_{mi}(\bar{G}_{mi}B_{mi})^{-1}\bar{G}_{mi}] \\ [I_i - B_{mi}(\bar{G}_{mi}B_{mi})^{-1}\bar{G}_{mi}]^T P_{mi} & -\hat{\epsilon}_{mi}^{-1} \end{array} \right] < 0 \quad (3.16)$$

Proof 3.1. To investigate and analyze the stability of the sliding motion described in Equation (3.15), here's how we choose the Lyapunov function:

$$V = \sum_i^N x_i^T(t) P_{mi} x_i(t) \quad (3.17)$$

In this case, $P_{mi} > 0$ satisfies equation (3.17). By determining the equation's time derivative (3.17) and utilizing equation (3.15), we arrive at:

$$\begin{aligned} \dot{V} &= \sum_{i=1}^N \dot{x}_i^T(t) P_{mi} x_i(t) + x_i^T(t) P_{mi} \dot{x}_i(t) \\ &= \sum_{i=1}^N \{x_i^T(t) [(A_{mi} - B_{mi}K_{mi})^T P_{mi} + P_{mi}(A_{mi} - B_{mi}K_{mi})] x_i(t) + \sum_{\substack{j=1 \\ j \neq i}}^N x_j^T(t) H_{mij}^T [I_i - B_{mi}(\bar{G}_{mi}B_{mi})^{-1}\bar{G}_{mi}]^T P_{mi} x_i(t) \\ &+ \sum_{\substack{j=1 \\ j \neq i}}^N x_i^T(t) P_{mi} [I_i - B_{mi}(\bar{G}_{mi}B_{mi})^{-1}\bar{G}_{mi}] H_{mij} x_j(t) + x_i^T(t) P_{mi} [I_i - B_{mi}(\bar{G}_{mi}B_{mi})^{-1}\bar{G}_{mi}] \bar{L}_{mi}(x_i, t) \\ &+ \bar{L}_{mi}^T(x_i, t) [I_i - B_{mi}(\bar{G}_{mi}B_{mi})^{-1}\bar{G}_{mi}]^T P_{mi} x_i(t)\} \end{aligned} \quad (3.18)$$

Utilizing Lemma 3.1 for Equation (3.18), we obtain:

$$\begin{aligned}
\dot{V} \leq & \sum_{i=1}^N \{x_i^T(t) [(A_{mi} - B_{mi} K_{mi})^T P_{mi} + P_{mi} (A_{mi} - B_{mi} K_{mi})] x_i(t) + \sum_{\substack{j=1 \\ j \neq i}}^N x_j^T(t) \alpha_{mi}^{-1} H_{mij}^T H_{mij} x_j(t) \\
& + \sum_{\substack{j=1 \\ j \neq i}}^N x_i^T(t) \alpha_{mi} P_{mi} [I_i - B_{mi} (\bar{G}_{mi} B_{mi})^{-1} \bar{G}_{mi}] [I_i - B_{mi} (\bar{G}_{mi} B_{mi})^{-1} \bar{G}_{mi}]^T P_{mi} x_i(t) \\
& + x_i^T(t) \beta_{mi} P_{mi} [I_i - B_{mi} (\bar{G}_{mi} B_{mi})^{-1} \bar{G}_{mi}] [I_i - B_{mi} (\bar{G}_{mi} B_{mi})^{-1} \bar{G}_{mi}]^T P_{mi} x_i(t) + \beta_{mi}^{-1} \bar{L}_{mi}^T(x_i, t) \bar{L}_{mi}(x_i, t) \}
\end{aligned} \tag{3.19}$$

$$\text{Considering that } \sum_{i=1}^N \sum_{\substack{j=1 \\ j \neq i}}^N x_j^T(t) \alpha_{mi}^{-1} H_{mij}^T H_{mij} x_j(t) = \sum_{i=1}^N \sum_{\substack{j=1 \\ j \neq i}}^N x_i^T(t) \alpha_j^{-1} H_{mji}^T H_{mji} x_i(t) ,$$

this leads us to the result:

$$\begin{aligned}
\dot{V} \leq & \sum_{i=1}^N \{x_i^T(t) [(A_{mi} - B_{mi} K_{mi})^T P_{mi} + P_{mi} (A_{mi} - B_{mi} K_{mi}) + \hat{\varepsilon}_{mi} P_{mi} [I_i - B_{mi} (\bar{G}_{mi} B_{mi})^{-1} \bar{G}_{mi}] [I_i - B_{mi} (\bar{G}_{mi} B_{mi})^{-1} \bar{G}_{mi}]^T P_{mi} \\
& + \sum_{\substack{j=1 \\ j \neq i}}^N \alpha_j^{-1} H_{mji}^T H_{mji}] x_i(t) + \sum_{i=1}^N \mu_{mi}
\end{aligned} \tag{3.20}$$

$$\text{where } \hat{\varepsilon}_{mi} = \alpha_{mi} (N-1) + \beta_{mi} \text{ and } \mu_{mi} = \beta_{mi}^{-1} \gamma_{mi}^2 .$$

In addition, by the Schur complement of (Boyd, S.; Ghaoui, E.L.; Feron, E.; Balakrishna, V., 1994), LMIs (3.20) is equivalent to this inequality:

$$\begin{aligned}
& (A_{mi} - B_{mi} K_{mi})^T P_{mi} + P_{mi} (A_{mi} - B_{mi} K_{mi}) + \varepsilon_{mi} P_{mi} [I_i - B_{mi} (\bar{G}_{mi} B_{mi})^{-1} \bar{G}_{mi}] [I_i - B_{mi} (\bar{G}_{mi} B_{mi})^{-1} \bar{G}_{mi}]^T P_{mi} \\
& + \sum_{\substack{j=1 \\ j \neq i}}^N \alpha_{mj}^{-1} H_{mji}^T H_{mji} = -\Omega_{mi} < 0
\end{aligned} \tag{3.21}$$

Considering equations (3.20) and (3.21), we get.

$$\dot{V} \leq \sum_{i=1}^N [-\lambda_{\min}(\Omega_{mi}) \|x_i(t)\|^2 + \mu_{mi}] \tag{3.22}$$

Here, the constant value is denoted as μ_i and the eigenvalue is represented as $\lambda_{\min}(\Omega_i) > 0$. Consequently, we have $\lambda_{\min}(\Omega_{mi}) > 0$, which is achieved when

$$\|x_i(t)\| > \sqrt{\frac{\mu_{mi}}{\lambda_{\min}(\Omega_{mi})}} . \text{ Thus, the sliding motion of the system described in Equation}$$

(3.22) is asymptotically stable.

3.2.3. Load frequency control design

In the preceding step, we introduced and demonstrated that PN employing an

integral sliding surface (ISS) can achieve asymptotic stability and exhibit smooth behavior in the sliding mode, provided certain conditions are met. In the subsequent step, we introduce a novel SOISMC scheme for MAPS. This scheme is designed to mitigate the issues of chattering and oscillations associated with the ISS. The sliding manifold is defined and established in the following way $S_{mi}[x_i(t)]$ as

$$\bar{S}_{mi}[x_i(t)] = \dot{\sigma}_{mi}[x_i(t)] + \delta_i \sigma_{mi}[x_i(t)] \quad (3.23)$$

and

$$\dot{\bar{S}}_{mi}[x_i(t)] = \ddot{\sigma}_{mi}[x_i(t)] + \delta_{mi} \dot{\sigma}_{mi}[x_i(t)] \quad (3.24)$$

where $\delta_{mi} > 0$ is a positive constant. Referring to equation (3.9), equation (3.24) can be expressed as

$$\begin{aligned} \dot{\bar{S}}_{mi}[x_i(t)] = & \bar{G}_{mi}[A_{mi}\dot{x}_i(t) + B_{mi}\dot{u}_i(t) + \sum_{\substack{j=1 \\ j \neq i}}^N H_{mij}\dot{x}_j(t) + \dot{L}_{mi}(x_i, t)] \\ & - \bar{G}_{mi}(A_{mi} - B_{mi}K_{mi})\dot{x}_i(t) + \delta_{mi}\dot{\sigma}_{mi}[x_i(t)] \end{aligned} \quad (3.25)$$

Building upon the definitions of the sliding surface and sliding manifold, we can formulate the continuous decentralized second order sliding mode LFC for PN as follows:

$$\begin{aligned} \dot{u}_i(t) = & -(\bar{G}_{mi}B_{mi})^{-1}[\|\bar{G}_{mi}\| \|B_{mi}\| \|K_{mi}\| \|\dot{x}_i(t)\| + \sum_{\substack{j=1 \\ j \neq i}}^N \|\bar{G}_{mj}\| \|H_{mji}\| \|\dot{x}_j(t)\| + \delta_{mi} \|\dot{\sigma}_{mi}[x_i(t)]\| \\ & + \|\bar{G}_{mi}\| \bar{\gamma}_{mi} + \bar{\varepsilon}] \frac{S_{mi}[x_i(t)]}{\|S_{mi}[x_i(t)]\|} \end{aligned} \quad (3.26)$$

Now, we can present the following key findings:

Theorem 3.2. Analyzing the closed-loop dynamics of the PS as defined by Equation (3.15) and controlled using the continuous sliding mode controller (3.26), it becomes evident that each solution trajectory is oriented towards the sliding manifold $\bar{S}_{mi}[x_i(t)] = 0$. Moreover, once a trajectory intersects the sliding manifold $\bar{S}_{mi}[x_i(t)] = 0$, it remains confined to this sliding manifold throughout its entire course.

Proof 3.2. We introduce the Lyapunov function as follows:

$$\bar{V}(t) = \sum_{i=1}^N \|S_{mi}[x_i(t)]\| \quad (3.27)$$

Now, when we calculate the derivative of $\bar{V}(t)$, we get:

$$\begin{aligned} \dot{\bar{V}} &= \sum_{i=1}^N \frac{S_{mi}^T[x_i(t)]}{\|S_{mi}[x_i(t)]\|} \dot{S}_{mi}[x_i(t)] = \sum_{i=1}^N \frac{S_{mi}^T[x_i(t)]}{\|S_{mi}[x_i(t)]\|} \{ \bar{G}_{mi}[A_{mi}\dot{x}_i(t) + B_{mi}\dot{u}_i(t) + \sum_{\substack{j=1 \\ j \neq i}}^N H_{mij}\dot{x}_j(t) + \dot{\bar{L}}_{mi}(x_i, t)] \\ &\quad - \bar{G}_{mi}(A_{mi} - B_{mi}K_{mi})\dot{x}_i(t) + \delta_{mi}\dot{\sigma}_{mi}[x_i(t)] \} \end{aligned} \quad (3.28)$$

Using Equation (3.27) and property $\|AB\| \leq \|A\|\|B\|$, equation (3.28) conclude:

$$\begin{aligned} \dot{\bar{V}} &= \sum_{i=1}^N \{ \bar{G}_{mi}B_{mi}K_{mi}\dot{x}_i(t) + \delta_{mi}\dot{\sigma}_{mi}[x_i(t)] + \sum_{\substack{j=1 \\ j \neq i}}^N \bar{G}_{mi}H_{mij}\dot{x}_j(t) + \bar{G}_{mi}\dot{\bar{L}}_{mi}(x_i, t) \} \\ &+ \sum_{i=1}^N \frac{S_{mi}^T[x_i(t)]}{\|S_{mi}[x_i(t)]\|} \bar{G}_{mi}B_{mi}\dot{u}_i(t) \\ &\leq \sum_{i=1}^N \{ \|\bar{G}_{mi}\| \|B_{mi}\| \|K_{mi}\| \|\dot{x}_i(t)\| + \delta_{mi} \|\dot{\sigma}_{mi}[x_i(t)]\| + \sum_{\substack{j=1 \\ j \neq i}}^N \|\bar{G}_{mi}\| \|H_{mij}\| \|\dot{x}_j(t)\| + \|\bar{G}_{mi}\| \|\dot{\bar{L}}_{mi}(x_i, t)\| \} \\ &+ \sum_{i=1}^N \frac{S_{mi}^T[x_i(t)]}{\|S_{mi}[x_i(t)]\|} \bar{G}_{mi}B_{mi}\dot{u}_i(t) \end{aligned} \quad (3.29)$$

By applying Assumption 3.1, we obtain:

$$\begin{aligned} \dot{\bar{V}} &\leq \sum_{i=1}^N \{ \|\bar{G}_{mi}\| \|B_{mi}\| \|K_{mi}\| \|\dot{x}_i(t)\| + \delta_{mi} \|\dot{\sigma}_{mi}[x_i(t)]\| + \|\bar{G}_{mi}\| \bar{\gamma}_i + \sum_{\substack{j=1 \\ j \neq i}}^N \|\bar{G}_{mj}\| \|H_{mji}\| \|\dot{x}_j(t)\| \} \\ &+ \sum_{i=1}^N \frac{S_{mi}^T[x_i(t)]}{\|S_{mi}[x_i(t)]\|} \bar{G}_{mi}B_{mi}\dot{u}_i(t) \end{aligned} \quad (3.30)$$

Utilizing the control law (3.26) gives us:

$$\dot{\bar{V}} \leq - \sum_{i=1}^N \bar{\varepsilon}_{mi} \quad (3.31)$$

The inequality above implies that the state trajectories of the multi-area PS (3.31) reach the sliding manifold $S_{mi}[x_i(t)] = 0$ and remain on it thereafter.

Note 3.2: The smooth function $\dot{\bar{V}}$ in equation (3.31) is just one of the possible choices for the system. According to Lyapunov stability theory, any smooth function $\dot{\bar{V}}$ that ensures the derivative of the Lyapunov function is negative can be used.

3.3. Simulation results and discussions

3.3.1. Frequency control in practical power system

In practical PS, the primary goal is to provide high-quality, safe, and dependable electric power to households, industrial facilities, and commercial enterprises. A typical electrical PS configuration is depicted in Figure 3.2 (Steven, 2016). Large power generation stations are connected via high-voltage transmission lines to substations. These substations are equipped with transformers that step down the voltage levels for further distribution in sub-transmission and distribution systems.

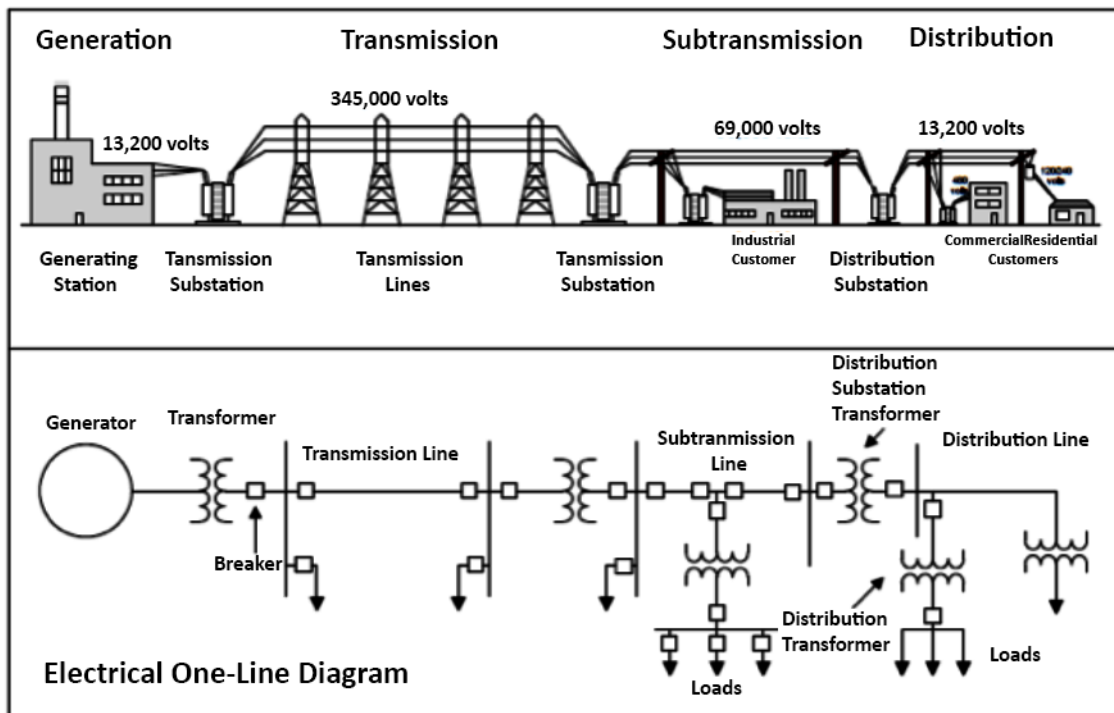


Figure 3.2. Basic single-line schematic for a system of electricity.

The electrical distribution system comprises elements such as substation transformers, both three-phase and single-phase distribution circuits, protective and switching devices, equipment for power factor correction, distribution transformers,

and service drops. Ensuring the protection of the electrical distribution system and coordinating the various components are paramount concerns for electric utility companies. Frequency deviation results from an imbalance between the electrical load and the power generated by interconnected generators. It functions as a crucial indicator, highlighting the mismatch between generation and load. Prolonged deviations from the standard frequency can have adverse consequences for PS functionality, security, dependability, and efficiency. These repercussions encompass equipment damage, degradation in load performance, overloads in transmission lines, and the activation of protective measures. Considering that the frequency within an electrical grid is intricately linked to the rotational speed of generators, managing frequency control can be likened to regulating the speed of the turbine-generator unit. This is initially tackled by integrating a governing mechanism that monitors the machine's speed and fine-tunes the input valve. This adjustment modulates the mechanical power output to accommodate fluctuations in load and restores the frequency to its designated value.

Hence, it is imperative to validate the suggested second order SMC, which relies on an integral sliding surface, to ascertain the reduction of frequency transient response duration and prevent overshooting. By doing so, we aim to enhance the performance of the PS, primarily by mitigating chattering in comparison to employing the same SMC technique. This evaluation is conducted on a two-area interconnected PS, as depicted in Figure 3.3.

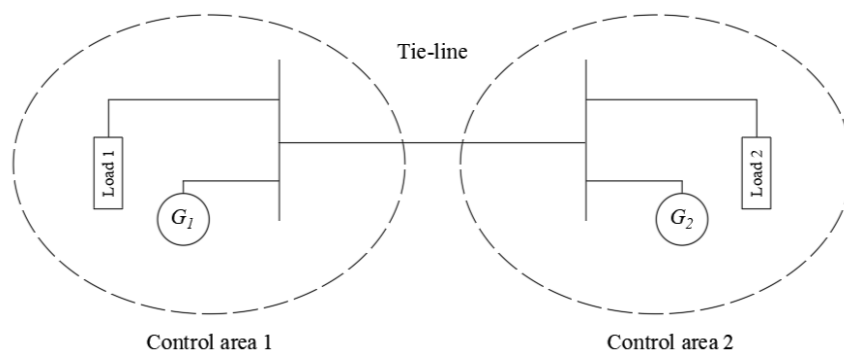


Figure 3.3. The simplified block diagram illustrates the connection between control areas 1 and 2.

3.3.2. Various cases of simulation results

In a power plant, The AGC balances total generation and load (including losses) to achieve the nominal frequency of the system (often 50 Hz) and planned power interchange with neighboring systems. The system parameters were acquired to analyze and assess the proposed SOISMIC technique for LFC in the two-area PN (Chen Haoyong, 2015), (Guo, J. , 2019).The theoretical proof and verification of the robust control performance of the proposed novel controller, specifically in achieving asymptotic convergence of incremental frequency deviation, are conducted through MATLAB/SIMULINK simulation. The reporting of various simulations is examined with their various operating circumstances outlined below:

LFC without the proposed controller:

In this section, we will illustrate the necessity of LFC for the operation of a PS. To do so, we will model a PS's LFC without the presence of a controller, as depicted in Figure 3.4. A step load disturbance of 0.01 (p.u.MW) will be applied for this demonstration.

The frequency deviation does not converge to zero, as observed in Figure 3.5. Maintaining the SF within the nominal range is essential to ensure power quality, as discussed in the previous chapter.

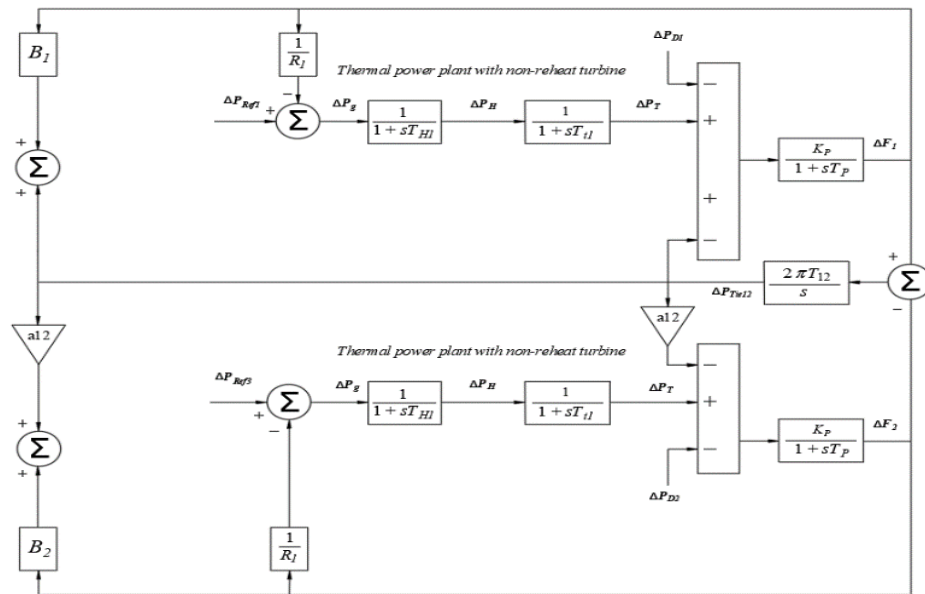


Figure 3.4. Multi-area thermal system transfer function model without the advanced SMC controller.

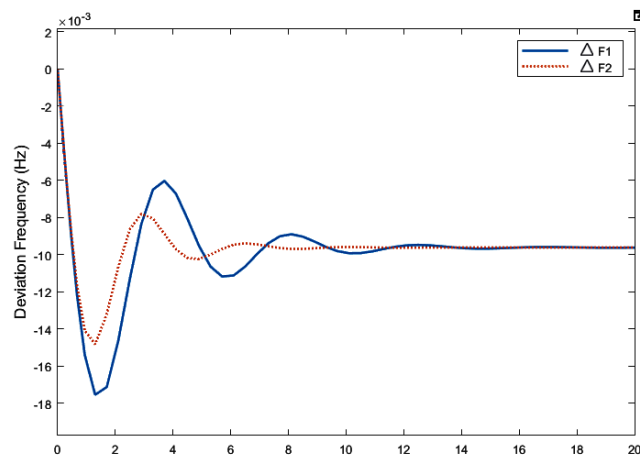


Figure 3.5. Frequency variation [Hz] of both control areas without controller.

Remark 3.1. The relationship between the frequency in an electrical network and the rotational speed of the generator means that addressing frequency control can be likened to managing the speed of the turbine-generator unit. Initially, this challenge is addressed by incorporating a governing mechanism that monitors the machine's speed. This mechanism then adjusts the input valve to modulate the mechanical power output. This modulation is designed to accommodate load variations and restore the frequency to its nominal value. Depending on the range of frequency deviation, different frequency control loops may be necessary to maintain

PS frequency stability. Without controllers in place for the PS, significant frequency deviations can lead to various issues, including equipment damage, degraded load performance, transmission line overloads, and interference with system protection schemes. Ultimately, this can result in an unstable condition for the PS. Hence, the presence of frequency controllers is essential for PS operation. Maintaining the nominal frequency of oscillation creates a stable environment, enabling the system and electrical equipment to operate efficiently.

LFC the proposed second order sliding mode controller:

In this study, we examine a standard two-area conventional PN in Figure 3.6. The purpose is to assess and analyze the proposed controller within this system, demonstrating its strength and efficiency, as outlined for the SOISM. The parameters pertaining to CA in PS were provided in the following sections (Chen Haoyong, 2015) as shown in Table 3.1.

Table 3.1. The characteristics and parameters associated with control areas in PS.

Parameter	T_{pi}	K_{pi}	T_{fi}	T_{gi}	R_i	T_{12}
Value for both areas	20	12	0.3	0.08	2.4	0.2545

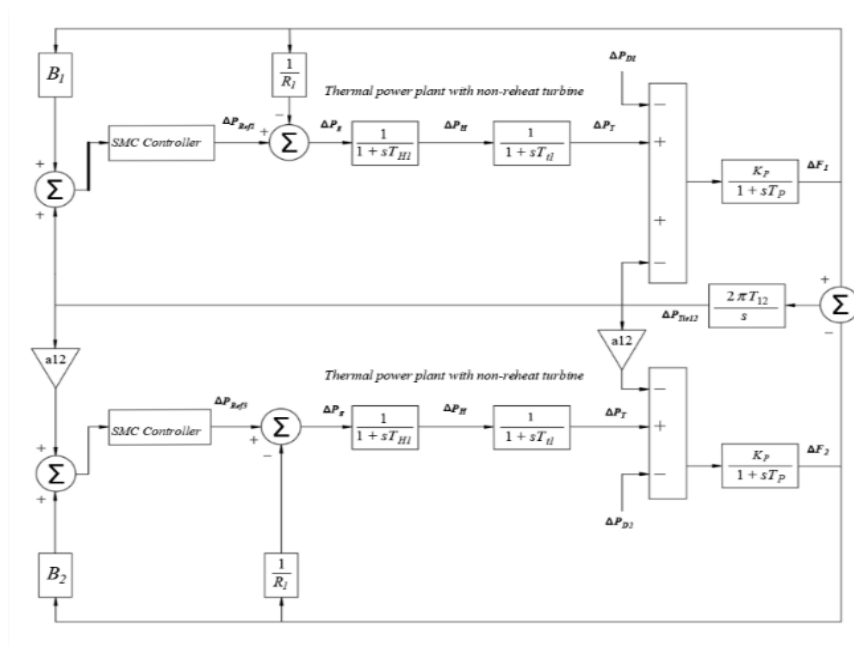


Figure 3.6. Transfer function model of multi area thermal system with SMC

controller.

Simulation 1:

Case 1: Initially, assumed to be at their nominal levels are the system parameters. The load disturbances impacting the system are $\Delta P_{d1} = 0.01$ p.u. at 5 seconds in area 1 and $\Delta P_{d2} = 0.03$ p.u. at seconds in area 2 of the PS. Figures 3.7 to 3.8 illustrate the frequency deviation in both area 1 and 2, tie-line power deviation. Notably, for the frequency variation to get closer to zero, the period of settling is approximately 3 seconds, which indicates a rapid response time for disturbance clearance compared to the 20-25 seconds response time mentioned in (Chen Haoyong, 2015). It's clear that the suggested SOISMIC yields a robust dynamic response. In summary, the proposed controller, utilizing a second-order control law, effectively reduces overshoot, oscillation, and system response re-equilibration.

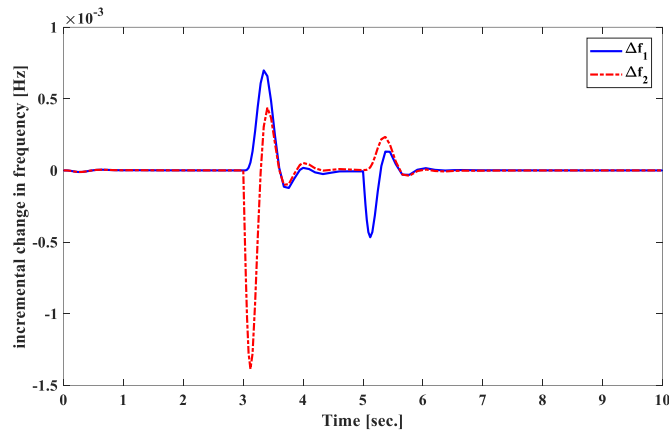


Figure 3.7. Frequency variation [Hz] of both control areas with matched disturbances.

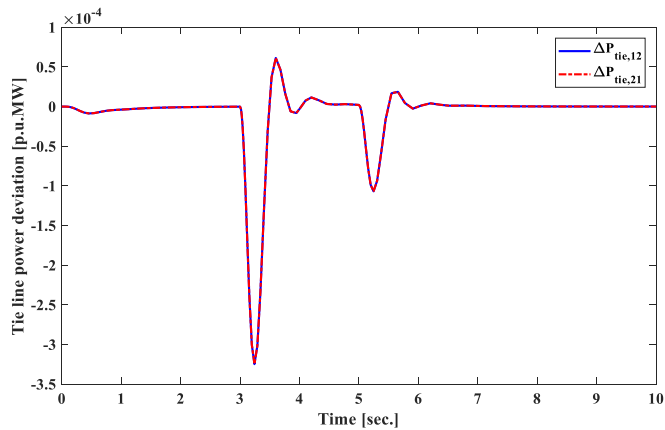


Figure 3.8. Tie line power variation [p.u.MW] with matched disturbances.

Figures 3.7 and 3.8 illustrate the switching surface function and the control law of the controller in Area 1 and Area 2 for this Case. The chosen switching coefficient gains are showcased in these figures.

$$\bar{K}_1 = [678.420504845789 \quad 29.8157000642646 \quad 3.52933333443281 \quad 600.949054250577 \quad 908.031410939919]$$

$$\bar{K}_2 = [678.420504845789 \quad 29.8157000642646 \quad 3.52933333443281 \quad 600.949054250577 \quad 908.031410939919]$$

$$\bar{G}_1 = [0.9 \quad 0.4 \quad 1/155 \quad 2.5 \quad 0.4]$$

$$\bar{G}_2 = [0.9 \quad 0.4 \quad 1/155 \quad 2.5 \quad 0.4]$$

Remark 3.2. The newly proposed controller exhibits superior performance in terms of robustness and rapid response to load disturbances compared to previous approaches, as demonstrated in (Chen Haoyong, 2015). Specifically, the controller effectively mitigates load disturbances, returning the system to a steady state within a short settling time and with minimal overshoot, highlighting the superior performance in mitigating the chattering problem within a finite frequency range.

Case 2. To implement the suggested SOISMIC scheme on the PS model depicted in Figure 3.1, we introduce mismatched uncertainty parameters and subject the system to random load variations to assess the controller's performance. To confirm the resilience of the suggested controller, we introduce random load disturbances, as illustrated in Figure 3.9, and incorporate parameter values with variations of up to $\pm 20\%$ into the system.

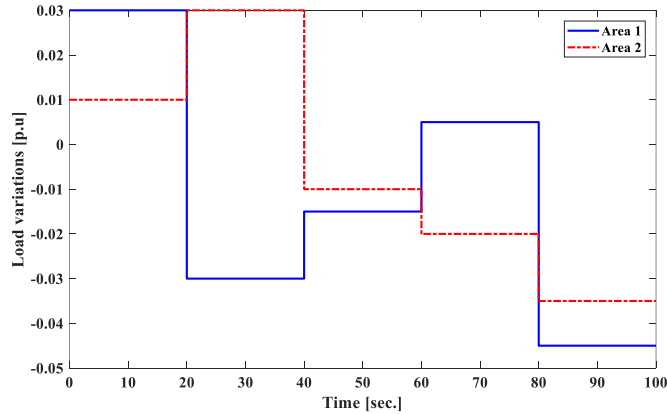


Figure 3.9. Fluctuations in the load of areas 1 and 2 in the power system.

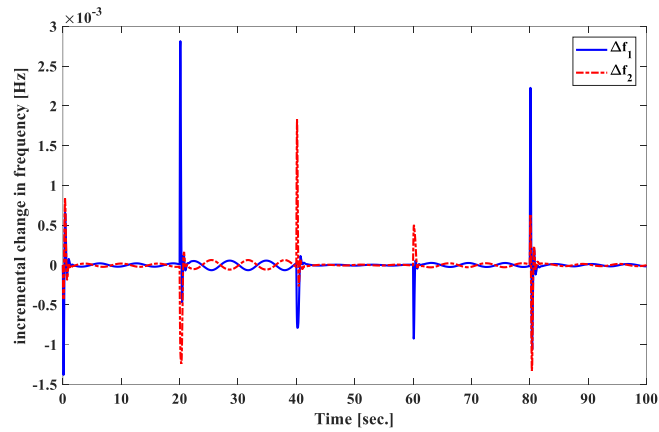


Figure 3.10. Frequency variations [Hz] of both control areas under matched disturbances.

The results displayed in Figure 3.10 showcase the response of the proposed controller to frequency variations in the first and second areas. Figure 3.11 presents the signal for tie-line power flow

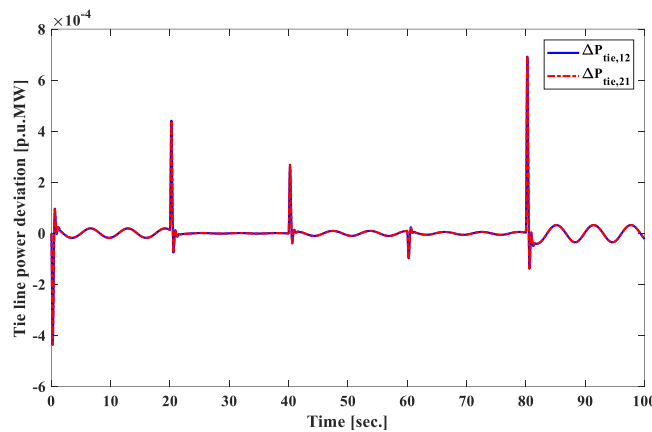


Figure 3.11. Tie line power variation [p.u.MW] with matched disturbances.

Simulation 2:

In this section, three different scenarios or cases are investigated. The PS parameters for the two-area PN are provided in the previous section. (Guo, J. , 2019) as shown Table 3.2.

Table 3.2. Parameters of the LFC scheme.

Parameter	T_{pi}	K_{pi}	T_{ti}	T_{gi}	R_i	T_{12}
Value for both areas	20	120	0.3	0.08	2.4	0.5450

Case 1. To proceed, let's once again assume that the system is operating with

nominal parameters. Load disturbances are introduced into the system at $\Delta P_{d1} = 0.01$ seconds for area 1 at $t_1 = 1$ s and $\Delta P_{d2} = 0.02$ seconds for area 2 at $t = 1$ s within the PN. As illustrated in Figure 3.14, the frequency deviation signals for control area 1 and 2 are shown. The proposed controller swiftly receives the frequency error signals from the sensors and efficiently manages the frequency deviation, bringing it to convergence around zero in roughly 3 seconds.

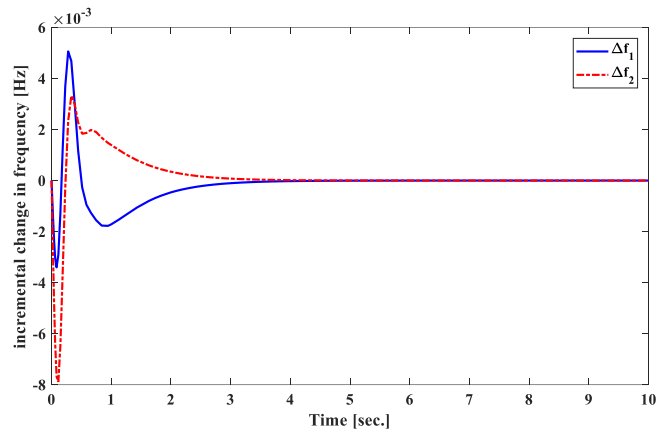


Figure 3.12. Frequency variation [Hz] of both control areas with matched disturbances.

Figure 3.12 presents the tie-line power flow signals for each area, while Figure 3.13 provides insight into the control signals for both areas. This novel control scheme, referred to as the SOISM law, is substantiated by the simulation results spanning from Figure 3.12 to Figure 3.13. These results emphasize the PS's swift and effective transient response in mitigating and eliminating the chattering issue. It is readily apparent that the frequency errors, tie-line power errors, and CA errors all converge to zero within a short timeframe, in stark contrast to previous control methodologies outlined in (Guo Jianping, 2019).

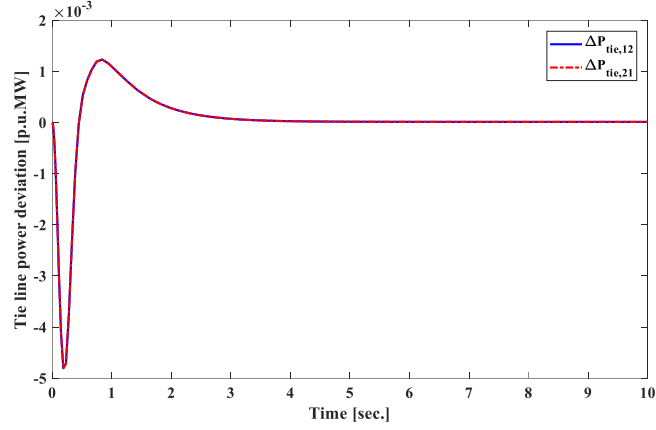


Figure 3.13. Tie-line power variation [p.u.MW] of both areas with matched disturbances.

Figures 3.12 and 3.13 depict both the switching surface function and the control law of the controller in Area 1 and Area 2 for Case 1 in simulation 2. The selected switching coefficient gains are highlighted in these visual representations.

$$\bar{K}_1 = [62.7741074068484 \quad 29.3456222825487 \quad 3.52933333324316 \quad 28.0626668071634 \quad 49.8871713116372]$$

$$\bar{K}_2 = [62.7741074068484 \quad 29.3456222825487 \quad 3.52933333324316 \quad 28.0626668071634 \quad 49.8871713116372]$$

$$\bar{G}_1 = [0.901 \quad 0.4 \quad 1/155 \quad 2.5 \quad 0.4]$$

$$\bar{G}_2 = [0.901 \quad 0.4 \quad 1/155 \quad 2.5 \quad 0.4]$$

Case 2. In the previous scenarios, to further investigate its robustness under different conditions, we introduced $\pm 20\%$ deviations from the nominal parameters and applied load disturbances of $\Delta P_{d1} = 0.02$ p.u. at $t_1 = 1$ s in area 1 and $\Delta P_{d2} = 0.03$ p.u. at $t_2 = 1$ s in area 2. This allowed us to assess the robustness and efficacy of the novel SOISM scheme. In the second case, we examined system responses related to generator frequencies and changes in tie-line power concerning load demand to evaluate the new scheme. Figure 3.14 illustrates the frequency deviation of generators, highlighting that the proposed second-order approach enables the PS to return to its nominal value within approximately 5–6 seconds after experiencing load disturbances. The scheduled values of tie-line power deviations are depicted in Figure 3.15. Results of a comparison between the proposed SOISM strategy and the prior method stated in (Guo Jianping, 2019) are summarized in Table 3.3. These results

demonstrate the superior transient response of the proposed method, with smaller transient deviations and shorter settling times in response to load disturbances.

Table 3.3. Setting time T_s and Maximum overshoot calculation of SOISMC and different method.

Kinds of controller	The suggested SOISMC		Different method for LFC	
	T_s [s]	Max.O.S (Hz)	T_s [s]	Max.O.S (Hz)
Δf_1	5	0.0090	105	0.0200
Δf_2	6	0.0070	110	0.0150

Source created by author.

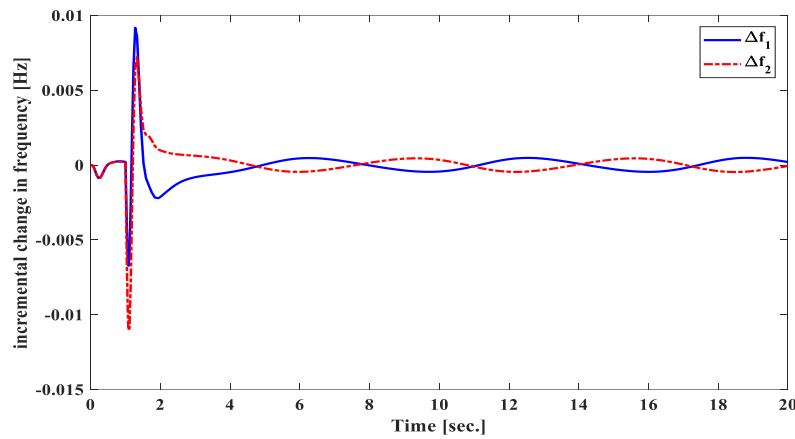


Figure 3.14. Frequency [Hz] of both control areas under unmatched disturbances.

In both control areas, the incremental changes in the actual tie-line power flow from control area-1 to 2 and the control input effort required to rapidly bring down the frequency using the proposed controller are depicted in Figures 3.14. In summary, the proposed control approach outperforms the one presented in (Guo Jianping, 2019) when subjected to varying load disturbances, demonstrating its superior performance, and chattering elimination capabilities.

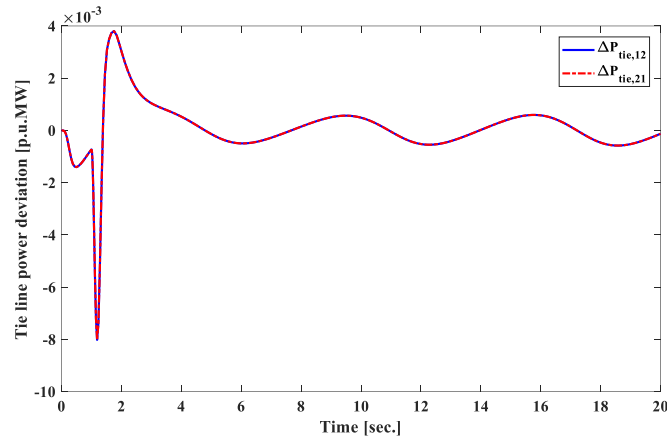
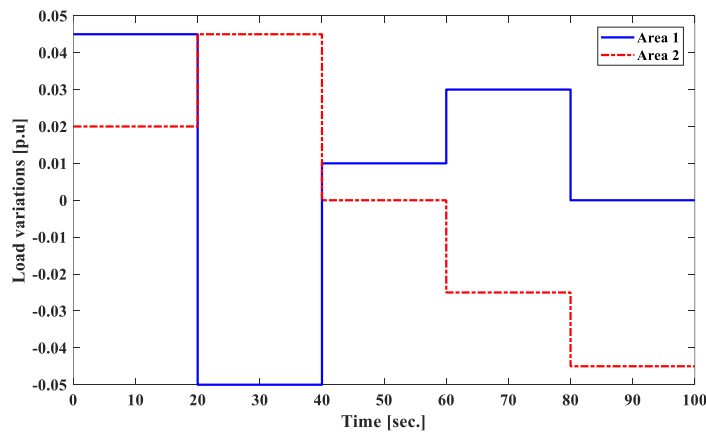


Figure 3.15. Tie-line power [p.u.MW] of both control-areas under unmatched disturbances.

Remark 3.3. The proposed approach represents a significant advancement in addressing the challenge of mismatched disturbances in PS. By implementing the second-order control law, it becomes feasible to achieve shorter settling times, smaller transient deviations, and reduced oscillations when dealing with load disturbances. This approach effectively resolves some limitations observed in other control strategies presented in the paper by (Guo Jianping, 2019), particularly in terms of decreasing chattering effects and enhancing transient response.

Case 3. In the final case, we examine the impact of load deviations and unmatched parameter uncertainties in a two-area PS. Random load variations are introduced into the PN under the same conditions as in case 2. To demonstrate the advantages of the suggested SOISMCM method, random load deviations are applied to the two-area PN in Figure 3.16. The simulation results, displayed in Figures 3.17 to 3.18, showcase the FD, tie-line power, providing a clear representation of



performance under different scenarios involving load deviations and unmatched parameter uncertainties.

Figure 3.16. Deviation load of both areas of the power network.

Consequently, the suggested controllers enable the PS to rapidly converge to the nominal frequency and reduce deviations in tie-line power, all while exhibiting a dynamic response that minimizes overshoots and shortens settling times when compared to the previous scheme presented in the paper (Guo Jianping, 2019).

Remark 3.4. Based on the two simulation results presented above, the novel second-order variable structure control scheme demonstrates effective response performance in diverse scenarios, including both matched and mismatched uncertainties, as well as load variations within the PN. The recommended approach to management is designed and refined to mitigate and counteract load disturbances within the PS, thereby restoring the system's performance to its nominal operating point and reducing the impact of load disturbances. The SOISMCM has been shown to be an effective strategy for mitigating chattering issues associated with SMC while achieving the desired system performance recovery.

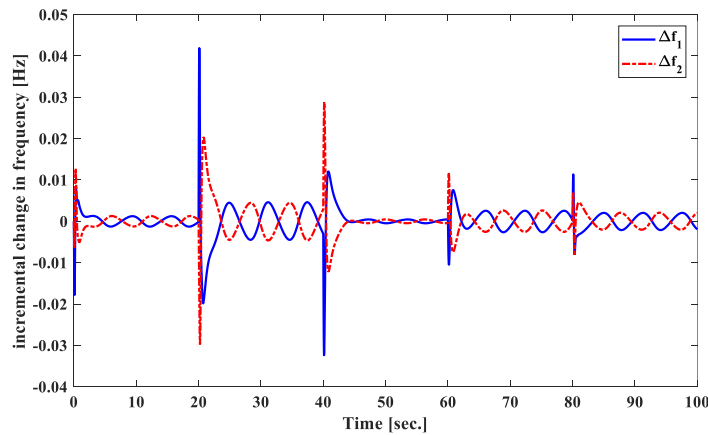


Figure 3.17. The mismatch parameter uncertainty and control frequency [Hz] under load fluctuations

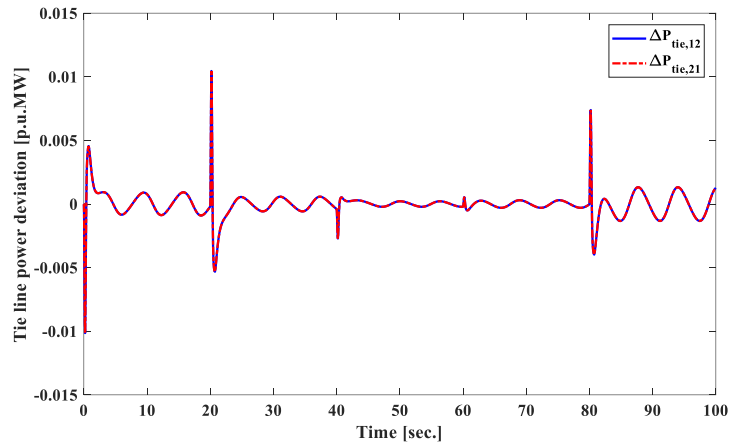


Figure 3.18. Tie-line power [p.u.MW] underload deviations and the unmatched uncertainty in the parameters.

Simulation 3:

In this simulation, the objective is to validate the suggested SOISMCMC by comparing it with the approach presented in (Guo Jianping , 2021). A step load disturbance of 0.01 p.u. is applied at $t = 0$ s in the first power CA, followed by another step load disturbance of 0.01 p.u. at $t = 0$ s in the second area. Additionally, it is believed that the two-area benchmarking system's unidentified variables change within 15% of their nominal values. The performance of the suggested SOISMCMC is thoroughly examined and compared with a new adaptive SMC method presented in (Guo Jianping , 2021).

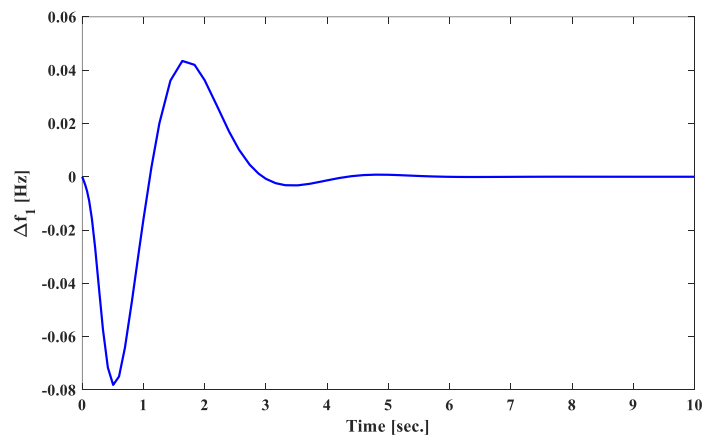


Figure 3.19. Frequency [Hz] of control area 1 under matched disturbances.

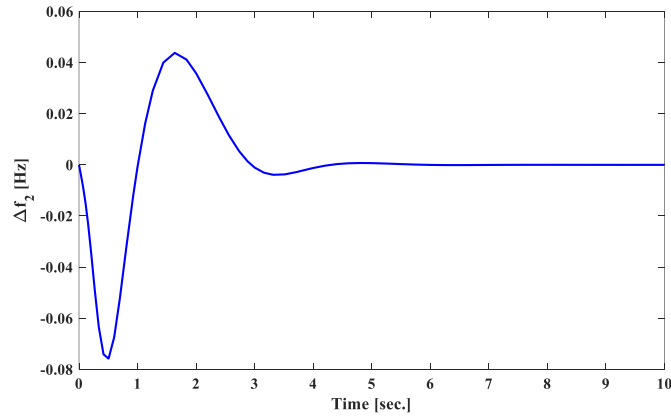


Figure 3.20. Frequency [Hz] of control area 2 under matched disturbances.

When there is an elevated demand for power at the nominal settings in the PS, it results in a deviation in the frequency, as evidenced by the undershoot or overshoot displayed in Figures 3.19 and 3.20. The system subsequently returns to its intended nominal frequency within approximately 4.5 seconds.

Remark 3.5. In simulation 3, we investigate the LFC problem in the PN while considering load variations and parameter uncertainties. As a result of employing the SOISMCM, this demonstrates the superior performance of the proposed SOISMCM, particularly in terms of reducing chattering, minimizing overshoot, and achieving faster response times when compared to the suggested SMC.

Simulation 4:

In contemporary PN, ensuring frequency stability is a crucial concern, especially in large-scale power systems (LSPS) that involve communication delays. In this study, Figure 3.21 depicts the component blocks schematic for the i^{th} area within the LSPS and Figure 3.22 shows the layout of the interconnected PN accounting for communication delays (Pradhan Subrat Kumar et al., 2020) (Fu Caifen et al., 2018). The model of the i^{th} area system comprises components such as A the governor, a non-reheat turbine, and an electrical generator. Additionally, the time delay of the Area Control Error (ACE) signal is taken into consideration in the PN.

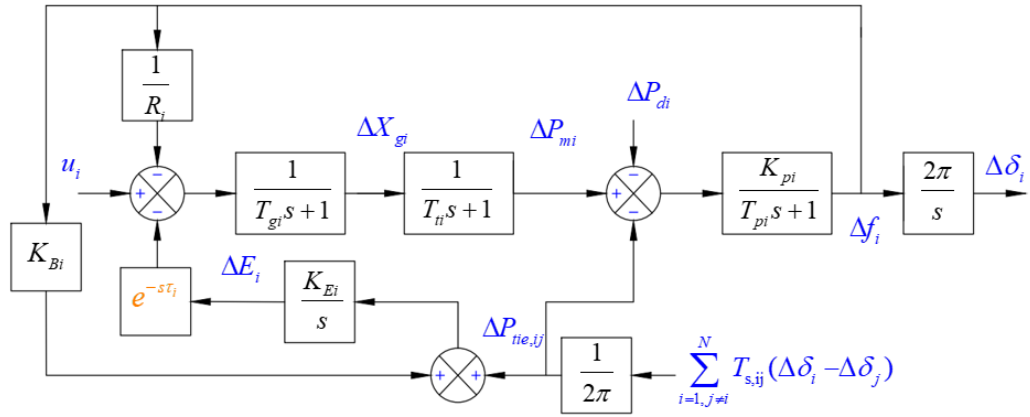


Figure 3.21. The configuration of the i^{th} area within the of the LSPSwCD

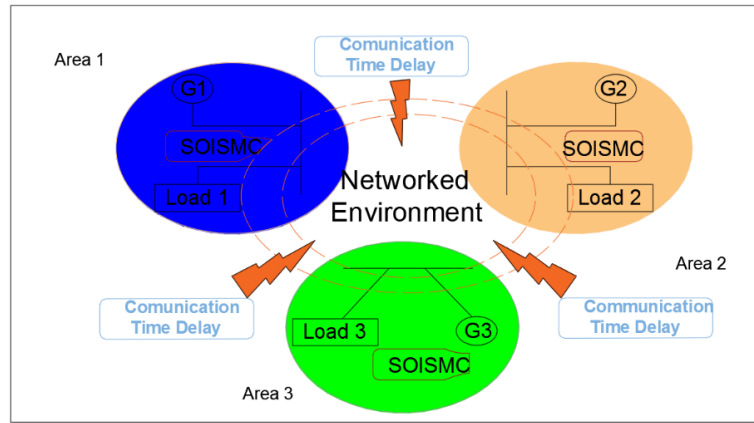


Figure 3.22. The layout of the interconnected PN with time delays.

In diverse scenarios and under various conditions, the efficiency and resilience of the suggested SOISM approach using an interconnected time-delay PN. The parameters for the large scale PS with communication delays (LSPSwCD) are extracted from (Sarkar Mrinal Kanti et al., 2018) and are comprehensively outlined in Table 3.4.

Table 3.4. The power system's three regions' parameters

Areas	T_{Pi}	K_{Pi}	T_{Ti}	T_{Gi}	R_i	K_{Ei}	K_{Bi}	K_{ij}
1	20	120.0	0.30	0.080	2.4	10.0	0.41	0.550
2	25	112.5	0.33	0.072	2.7	9.0	0.37	0.650
3	20	115.0	0.35	0.070	2.5	7.1	0.40	0.545

The objective of this analysis is to showcase the robustness and efficacy of the SOISMIC approach in handling diverse load disturbances and parameter variations.

Case 1: The LFC approach based on SOISMIC, as presented here, is subject to a comparative analysis with the traditional LFC approach detailed in (Sarkar Mrinal Kanti et al., 2018). In this specific case, load disturbances of magnitude (in per unit Megawatts) occur at time t in a three-area LSPS. The corresponding frequency deviations for the LSPS, which incorporates delay times of $\tau_i = 3$ s, are illustrated in Figure 3.23 to Figure 3.24.

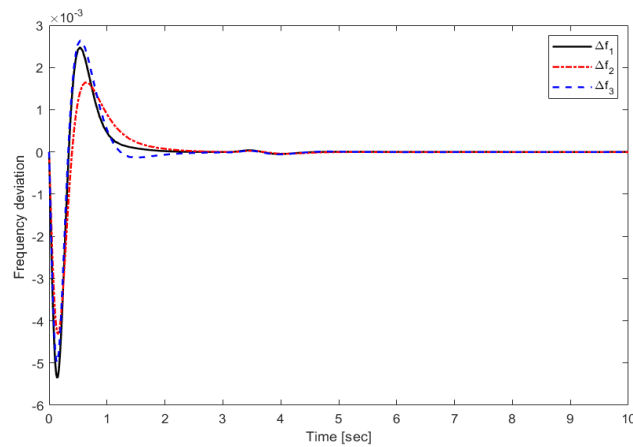


Figure 3.23. Frequency deviation of the PS.

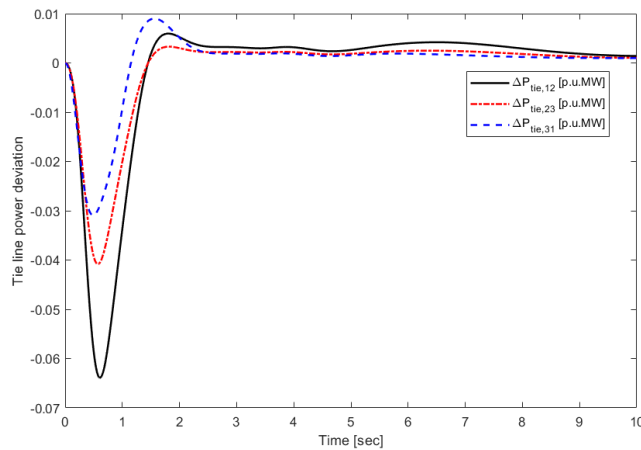


Figure 3.24. Tie-line deviation of the PS.

These figures also depict tie-line power deviations and control input signals for the three areas within the PS. From our analysis, it is evident that the transient responses achieved by the proposed LFC based on SOISMIC exhibit a faster settling time compared to the traditional controller described in (Sarkar Mrinal Kanti et al.,

2018). Additionally, the magnitude of overshoot percentage with the suggested recent controller is lower, highlighting its improved performance.

Table 3.5. Comparing the suggested SOISMIC approach with the earlier approach.

Kinds of controller	The SOISMIC approach		Previous load frequency controller	
	T_s (s)	Max.O. S (pu)	T_s (s)	Max.O. S (pu)
Δf_1	1	-3.8×10^{-3}	2	-3.8×10^{-3}
Δf_2	1	-2.1×10^{-3}	2	-2.1×10^{-3}
Δf_3	1	-1.9×10^{-3}	2	-2.0×10^{-3}

Source created by author.

Remark 3.6 As evident from Figure 3.23 to Figure 3.24, the outcomes of the simulation tests in this section have been tabulated in Table 3.5. This comprehensive presentation of results facilitates a meaningful comparison, especially when accounting for time-delay communication within the large-scale PN. Consequently, the performance of the proposed SOISMIC exhibits remarkable stability, with the frequency deviation converging towards zero, displaying minimal amplitude oscillation after 1 second.

Case 2: In this scenario, the PS with time delay parameters align with the references provided in (B. Le Ngoc Minh, V. V. Huynh, T. M. Nguyen, and Y. W. Tsai, 2018). The limited random parameter values for the PS with time delay undergo synchronized adjustments from their typical values. A delay time of 3 seconds is established, and Figure 3.25 illustrates the load variation. Notably, the deviations in both frequency and tie-line power profiles diminish swiftly, as evident in Figure 2.26 and Figure 3.27. It is crucial to underscore that the proposed control strategy effectively manages time delays and random load disruptions. This serves as evidence that the recommended PS system excels in mitigating disturbances with minimal control signal requirements, showcasing high quality and performance.

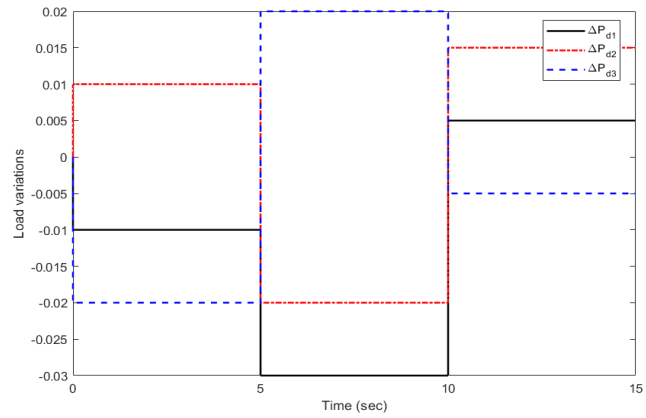


Figure 3.25. Load deviation of the three areas power system.

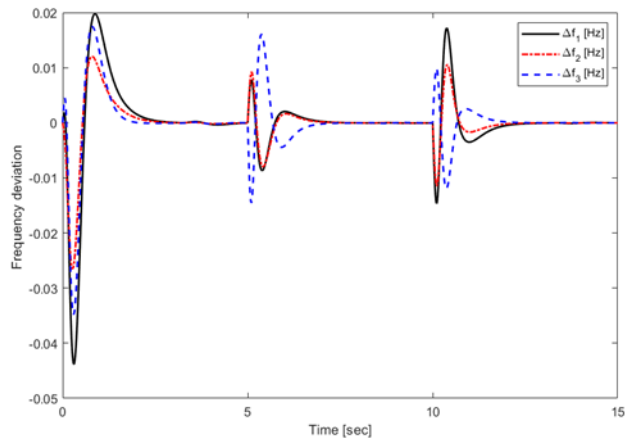


Figure 3.26. Frequency change of the PS under random load.

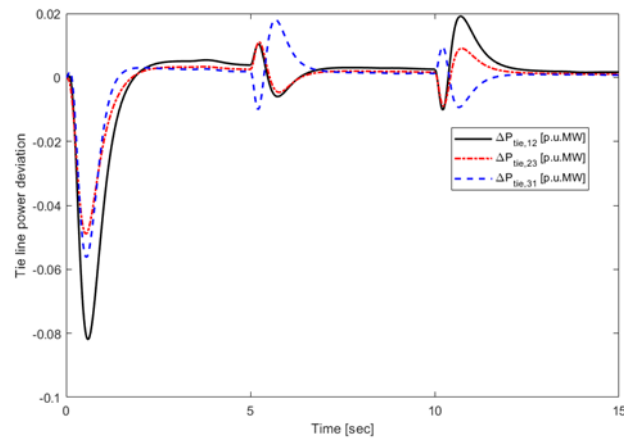


Figure 3.27. Tie-line deviation of the PS under random load.

Remark 3.7: In this setup, we have considered the influence of time-delay signals for the purpose of three areas MAPS under random load disturbance. It is evident that the SOISM based on the provided switching surface not only achieves superior response speed but also enhances transient performance, resulting in a

reduction within multi-area interconnected time-delay power grids.

3.4. Conclusion of chapter 3

In summary, this study introduces a novel SOISMCM scheme for effectively managing the active power balance in a MAPS. This is accomplished by prioritizing the active power balancing, minimizing excessive overshoot, and accelerating the frequency transient response with the use of an integrated sliding surface-based second order SMC. The solution of the chattering issue demonstrates the effectiveness of the MAPS and shows gains over earlier control techniques. Notably, in practical applications, the suggested SMC technique combined with the FLC approach provides a strong and efficient solution while removing chattering. By reducing chattering in the control input, the suggested control scheme supplies accurate signals to control mechanical inertia power, enabling it to effectively match load changes or demands. This capability makes it highly suitable for practical PS dealing with significant parameter uncertainties, load disturbances, communication delays in PS.

CHAPTER 4: DESIGNING AN ADVANCED SLIDING MODE OBSERVER FOR LOAD FREQUENCY CONTROL IN MULTI-AREA MULTI-SOURCE POWER SYSTEMS

In this session, the MAPS, which includes several power sources including gas, nuclear, hydro, thermal, etc., has recently been implemented to balance the rising demand for energy and the total power generated. This will influence the LFC. Thus, the single-phase sliding mode control-based state observer (SPSMCBSO) is used to introduce the LFC of the two areas gas-hydro-thermal power system (TAGHTPS). The uncertainty of the state's parameters and the linked matrix is considered for the first time in this scheme by the TAGHTPS model. Second, the state variables for feedback control are estimated using the state observer. Third, the SPSMCBSO is designed to alter the fundamental SMC to enhance TAGHTPS Effectiveness with regard to overshoot and time for settling. Furthermore, to resolve the challenge of measuring the state variable, the SPSMCBSO is designed to completely rely on the state observer. Fourth, a novel LMI scheme-Lyapunov stability theory is used to carry out the TAGHTPS stability study. Lastly, the SPSMCBSO choice of application for the LFC of the MAMSPS is validated by comparing simulation results to newly published conventional control techniques.

The primary objective of PS control is to maintain a balance between the total electrical power generated and the power demanded by the electrical load. This equilibrium is typically reflected in the system's frequency, which remains within acceptable limits under normal operating conditions. However, if the power demands of industries or other consumers increase, it can lead to a rise in the system's frequency. This, in turn, affects the balance between the total power generated and the power required to meet the increased demand. If all system state variables are monitored, those controllers were designed using a reduced observer control or a nonlinear disturbance observer to detect changes in load and maintain nominal frequency. However, this cannot be ensured for the actual execution of the controls

mentioned above if some MAPS state parameters are not measured or cannot be measured. Hence, the motivation behind the research is to develop a LFC system based on a novel SMC approach that fully integrates a state observer into the sliding surface, while employing a SPSMCBSO to address the concerns. The critical aspects of this design include the careful selection of switching strategies and sliding surfaces. The switching strategy plays a pivotal role in transitioning the system states and ensuring their convergence at a specific sliding surface.

As an outcome, a unique single-phase sliding surface has been devised, which ensures robustness during the reaching phase without the need for a predefined reaching time. Notably, this study marks the first instance of applying SPSMCBSO for the LFC of the TAGHTPS. The effectiveness of this approach is validated through a comparison with the classical methods mentioned earlier. In summary, the work's major contributions are as follows:

- ✓ The SPSMCBSO has been purposefully devised to be fully dependent on the state observer, rendering it highly efficient for LFC in MAMSPS, especially when certain variables are challenging to acquire.
- ✓ The innovative control system is designed to alter the essential SMC in a way that differs from the basic SMC, which relies on reaching time, in terms of the PS order, making the unique controller extremely resilient against disruption.
- ✓ The unique linear matrix inequality (LMI) technique, which is based on the stability of Lyapunov theoretical terms, is utilized to theoretically demonstrate entire system stabilization.
- ✓ Compared to recent LFC approaches such as those presented in (Hakimuddin Nizamuddin et al., 2020), (Sahu Rabindra Kumar et al., 2016), (Gupta Nidhi et al., 2022), (Sarkar Mrinal Kanti et al., 2018), (Dev Ark et al., 2021), (Patel Ragini et al., 2019), (Patel Ragini et al. , 2019), (Guha Dipayan et al., 2021), the new approach to SMC, which does not require reaching time, shows higher system efficiency as a result of settling time and overshoot, even when dealing with matched or mismatched disturbances and load variations and PS

integrated with renewable power generation sources.

4.1. Mathematical model of the interconnected multi-area multi-source power system

In this section, the MAPS includes many generators sets in each location, including nuclear, gas, hydro, and gas plants. But the nuclear plant doesn't relate to the LFC of MAPS because it's referred to be a base load system (Hakimuddin Nizamuddin et al., 2020), (Gupta Nidhi et al., 2022), (Sarkar Mrinal Kanti et al., 2018), (Dev Ark et al., 2021), (Patel Ragini et al., 2019), (Patel Ragini et al. , 2019), (Guha Dipayan et al., 2021). As a result, as seen in Figure 4.1, we take TAGHTPS into account in each region in this section. The modeling of PS is built in the differential equation in the following way, taking into consideration the effects of the load disturbance and the interconnection matrix from Equation (4.1) to Equation (4.13).

$$\begin{aligned} \Delta \dot{f}_i = & -\frac{\Delta f_i}{T_{PS_i}} + \frac{\Delta P_{pt_i} K_{PS_i} \alpha_{i1}}{T_{PS_i}} + \frac{\Delta P_{Gh_i} K_{PS_i} \alpha_{i2}}{T_{PS_i}} + \frac{\Delta P_{Gg_i} K_{PS_i} \alpha_{i3}}{T_{PS_i}} \\ & - \frac{K_{PS_i} a_{ij}}{T_{PS_i}} \Delta P_{tie_{ij}} - \frac{K_{PS_i}}{T_{PS_i}} \Delta P_{D_i} \end{aligned} \quad (4.1)$$

$$\Delta \dot{P}_{pt_i} = \frac{\Delta P_{Gt_i}}{T_{T_i}} - \frac{\Delta P_{pt_i}}{T_{T_i}} \quad (4.2)$$

$$\begin{aligned} \Delta \dot{P}_{Gt_i} = & -\frac{\Delta P_{Gt_i}}{T_{R_i}} + \frac{\Delta X_{Et_i}}{T_{R_i}} - \frac{\Delta X_{Et_i} K_{R_i}}{T_{SG_i}} - \frac{\Delta f_i K_{R_i}}{T_{SG_i} R_{i1}} \\ & + \frac{\Delta ACE_i K_{R_i}}{T_{SG_i}} + \frac{U_{i1} K_{R_i}}{T_{SG_i}} \end{aligned} \quad (4.3)$$

$$\Delta \dot{X}_{Et_i} = -\frac{\Delta X_{Et_i}}{T_{SG_i}} - \frac{\Delta f_i}{T_{SG_i} R_{i1}} + \frac{\Delta ACE_i}{T_{SG_i}} + \frac{U_{i1}}{T_{SG_i}} \quad (4.4)$$

$$\begin{aligned}\Delta\dot{P}_{Gh_i} = & \frac{2\Delta P_{Rh_i}}{T_{W_i}} - \frac{2\Delta P_{Gh_i}}{T_{W_i}} - \frac{2\Delta X_{Eh_i}}{T_{RH_i}} + \frac{2\Delta P_{Rh_i}}{T_{RH_i}} + \frac{2\Delta X_{Eh_i}T_{RS_i}}{T_{RH_i}T_{GH_i}} \\ & + \frac{2\Delta f_i T_{RS_i}}{R_{i2}T_{RH_i}T_{GH_i}} - \frac{2\Delta ACE_i T_{RS_i}}{T_{RH_i}T_{GH_i}} - \frac{2U_{i2}T_{RS_i}}{T_{RH_i}T_{GH_i}}\end{aligned}\quad (4.5)$$

$$\begin{aligned}\Delta\dot{P}_{Rh_i} = & \frac{\Delta X_{Eh_i}}{T_{RH_i}} - \frac{\Delta P_{Rh_i}}{T_{RH_i}} - \frac{\Delta X_{Eh_i}T_{RS_i}}{T_{RH_i}T_{GH_i}} - \frac{\Delta f_i T_{RS_i}}{R_{i2}T_{RH_i}T_{GH_i}} + \frac{\Delta ACE_i T_{RS_i}}{T_{RH_i}T_{GH_i}} \\ & + \frac{U_{i2}T_{RS_i}}{T_{RH_i}T_{GH_i}}\end{aligned}\quad (4.6)$$

$$\Delta\dot{X}_{Eh_i} = -\frac{\Delta X_{Eh_i}}{T_{GH_i}} - \frac{\Delta f_i}{T_{GH_i}R_{i2}} + \frac{\Delta ACE_i}{T_{GH_i}} + \frac{U_{i2}}{T_{GH_i}}\quad (4.7)$$

$$\Delta\dot{P}_{Gg_i} = -\frac{\Delta P_{Gg_i}}{T_{CD_i}} + \frac{\Delta P_{Rg_i}}{T_{CD_i}}\quad (4.8)$$

$$\begin{aligned}\Delta\dot{P}_{Rg_i} = & -\frac{\Delta P_{Rg_i}}{T_{F_i}} + \frac{\Delta X_{Vg_i}}{T_{F_i}} + \frac{\Delta X_{Vg_i}T_{CR_i}}{Y_{G_i}T_{F_i}} - \frac{\Delta X_{Eg_i}T_{CR_i}}{Y_{G_i}T_{F_i}} + \frac{\Delta X_{Eg_i}c_{g_i}X_{G_i}T_{CR_i}}{b_{g_i}Y_{G_i}T_{F_i}} \\ & + \frac{\Delta f_i X_{G_i}T_{CR_i}}{R_{i3}b_{g_i}Y_{G_i}T_{F_i}} - \frac{\Delta ACE_i X_{G_i}T_{CR_i}}{b_{g_i}Y_{G_i}T_{F_i}} - \frac{U_{i3}X_{G_i}T_{CR_i}}{b_{g_i}Y_{G_i}T_{F_i}}\end{aligned}\quad (4.9)$$

$$\begin{aligned}\Delta\dot{P}_{Vg_i} = & -\frac{\Delta P_{Vg_i}}{Y_{G_i}} + \frac{\Delta X_{Eg_i}}{Y_{G_i}} - \frac{\Delta X_{Eg_i}c_{g_i}X_{G_i}}{b_{g_i}Y_{G_i}} - \frac{\Delta f_i X_{G_i}}{R_{i3}b_{g_i}Y_{G_i}} \\ & + \frac{\Delta ACE_i X_{G_i}}{b_{g_i}Y_{G_i}} + \frac{U_{i3}X_{G_i}}{b_{g_i}Y_{G_i}}\end{aligned}\quad (4.10)$$

$$\Delta\dot{X}_{Eg_i} = -\frac{\Delta X_{Eg_i}c_{g_i}}{b_{g_i}} - \frac{\Delta f_i}{b_{g_i}R_{i3}} + \frac{\Delta ACE_i}{b_{g_i}} + \frac{U_{i3}}{b_{g_i}}\quad (4.11)$$

$$\Delta\dot{ACE}_i = B_i\Delta f_i + a_{ij}\Delta P_{tie_{ij}}\quad (4.12)$$

$$\Delta\dot{P}_{tie_{ij}} = \sum_{\substack{j=1 \\ j \neq i}}^L 2\pi T_{ij}(\Delta f_i - \Delta f_j)\quad (4.13)$$

where Δf_i and Δf_j is a gradual shift in each control area's frequency (Hz) and

$\Delta P_{tie_{ij}}$ is the real tie line power flow from controlling area to CA two that is changed incrementally (p.u.MW).

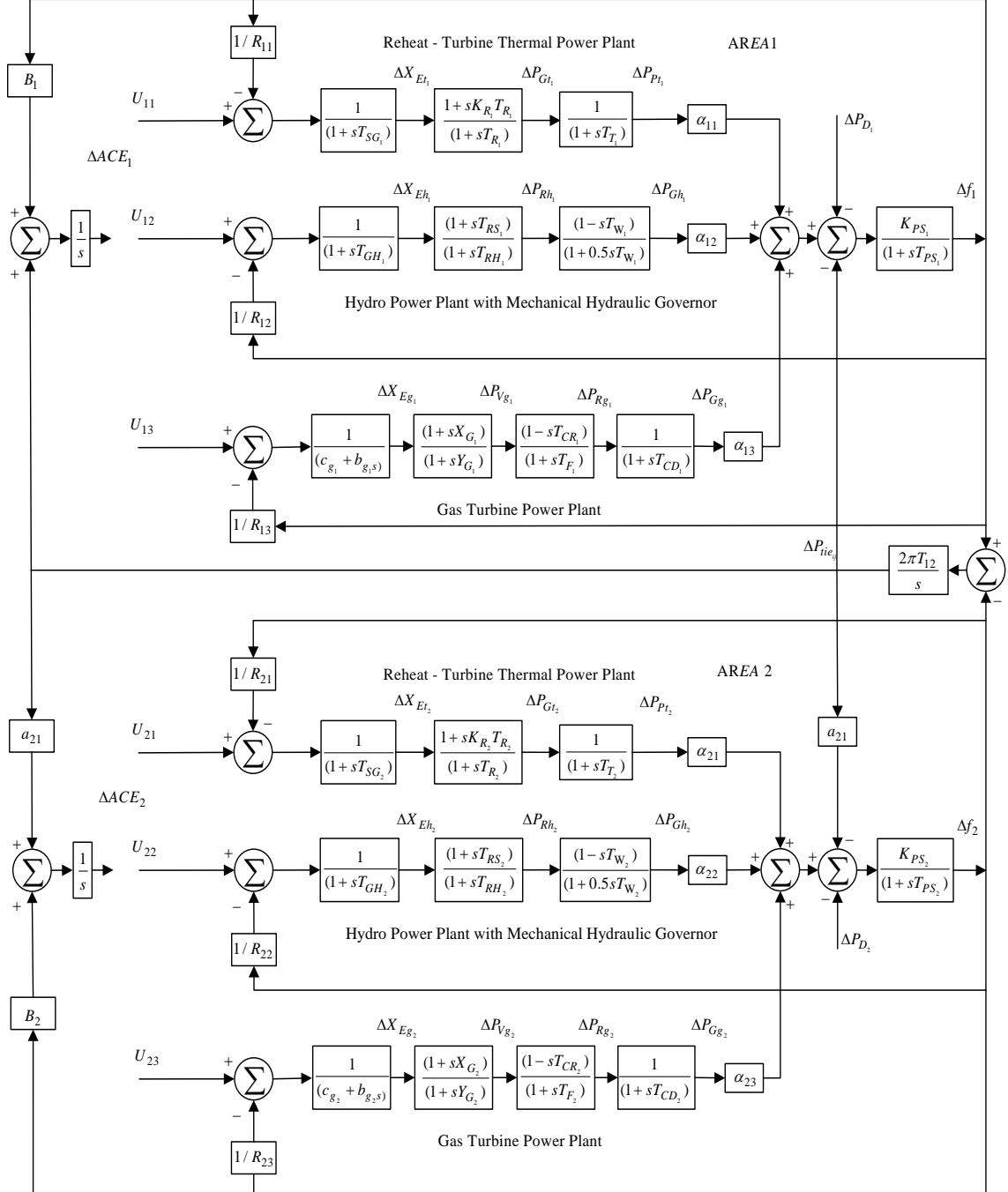


Figure 4.1. Schematic of TAMPSPS's LFC blocks.

The i^{th} region of the PS state space in the model is obtained by specifying the PS parameters and applying the dynamics expression from (4.1) to (4.13), which is

provided by (4.14).

$$\dot{x}_i(t) = A_{hi}x_i(t) + B_{hi}u_i(t) + \sum_{\substack{j=1 \\ j \neq i}}^L H_{hij} + \Delta H_{hij}x_j(t) + F_i\Delta P_{hdi}(t) \quad (4.14)$$

where the state space structure of the TAGHTPS is represented by formula (4.14)

$x_i(t) = \left[\Delta f_i \quad \Delta P_{pt_i} \quad \Delta P_{Gt_i} \quad \Delta X_{Et_i} \quad \Delta P_{Gh_i} \quad \Delta P_{Rh_i} \quad \Delta X_{Eh_i} \right. \\ \left. \Delta P_{Gg_i} \quad \Delta P_{Rg_i} \quad \Delta P_{Vg_i} \quad \Delta X_{Eg_i} \quad \Delta ACE_i \quad \Delta P_{tie_{ij}} \right]^T$ is the vector of states, $x_j(t)$ is the system's state vector of the linked system of $x_i(t)$, $u_i(t)$ is the vector of control, and $\Delta P_{hdi}(t)$ is the disturbance. A_{hi} , B_{hi} , H_{hij} and F_i are the system matrices listed in Appendix 4.1 exist.

In the practical MAMSPS, variations in operating conditions continually impact the dynamic load sources. Taking this factor into account, equation (4.14) can be reformulated as follows:

$$\dot{x}_i(t) = [A_{hi} + \Sigma_i(x_i, t)]x_i(t) + B_{hi}[u_i(t) + \psi_{hi}(x_i, t)] \\ + \sum_{\substack{j=1 \\ j \neq i}}^L [H_{hij} + \Xi_{hij}(x_j, t)]x_j(t) + F_i\Delta P_{hdi}(t) \quad (4.15)$$

where $\Sigma_{hi}(x_i, t)$, $\Xi_{hij}(x_j, t)$ are uncertainty caused by time-varying parameters and $B_{hi}\psi_{hi}(x_i, t)$ is the input disturbance. To put it differently, the total uncertainty can be expressed as:

$$\Phi_{hi}(x_i, t) = \Sigma_{hi}(x_i, t)x_i(t) + B_{hi}\psi_{hi}(x_i, t) + \sum_{\substack{j=1 \\ j \neq i}}^L \Xi_{hij}x_j(t) + F_i\Delta P_{hdi}(t) \quad (4.16)$$

Hence, the updated dynamic model can be represented as:

$$\dot{x}_i(t) = A_{hi}x_i(t) + B_{hi}u_i(t) + \sum_{\substack{j=1 \\ j \neq i}}^L H_{hij}x_j(t) + \Phi_{hi}(x_i, t) \quad (4.17)$$

$$y_i = C_{hi}x_i$$

where $\Phi_{hi}(x_i, t)$ expresses the uncertainty of the matched and unmatched parameters as a combined disturbance. In the context of the state space paradigm (4.17), the design of controllers $u_i(t)$ is critical. To create the novel $u_i(t)$, we first assume the things listed below and review the Lemmas.

Assumption 4.1: The matrix representing the system (A_{hi}, B_{hi}) is controllable and (A_{hi}, C_{hi}) is observable.

Assumption 4.2: Presumably, the load disturbance $\Phi_{hi}(x_i, t)$ is bounded, such that $\|\Phi_{hi}(x_i, t)\| \leq \gamma_{hi}$. Where γ_{hi} is the known scalar and $\|\cdot\|$ is the matrix norm.

Lemma 4.1. (Huynh Van Van et al., 2021), (Park Ju H et al., 2021): If \tilde{X} and \tilde{Y} are actual matrices with the appropriate size, then, for any scalar $\mu > 0$, the matrix inequality that follows is valid.

$$\tilde{X}^T \tilde{Y} + \tilde{Y}^T \tilde{X} \leq \mu \tilde{X}^T \tilde{X} + \mu^{-1} \tilde{Y}^T \tilde{Y}.$$

Lemma 4.2. (Huynh Van Van et al., 2021): Given a specific inequality.

$$\begin{bmatrix} \tilde{Q}(x) & \tilde{S}(x) \\ \tilde{S}(x)^T & \tilde{R}(x) \end{bmatrix} < 0 \quad (4.18)$$

where $\tilde{Q}(x) = \tilde{Q}(x)^T$ and $\tilde{R}(x) = \tilde{R}(x)^T$ such that $\tilde{S}(x)$ depend on the relationship with x , therefore, $\tilde{R}(x) < 0$ and $\tilde{Q}(x) - \tilde{S}(x)\tilde{R}(x)^{-1}\tilde{S}(x)^T < 0$.

4.2. Designing the power system state estimator

In the case of PS, when some state variables are difficult to address, few publications have used observer approaches to solve the LFC. Because of the above, we use the observer approach to recreate the original TAGHTPS (4.17) framework in the manner shown below.

$$\dot{\hat{x}}_i(t) = A_{hi}\hat{x}_i(t) + B_{hi}u_i(t) + \sum_{\substack{j=1 \\ j \neq i}}^L H_{hij}\hat{x}_j(t) + \Gamma_{hi}(y_i - \hat{y}_i) \quad (4.19)$$

$$\hat{y}_i = C_{hi}\hat{x}_i$$

where Γ_{hi} is the observer gain, $\hat{x}_i(t)$ is the estimation of $x_i(t)$, y_i is the

output vector, \hat{y}_i is the result of the state observer, correspondingly. With the pole positioning approach, it may be computed. The state error changing is then examined, and the state error is reported as

$$\tilde{x}_i(t) = x_i(t) - \hat{x}_i(t) \quad (4.20)$$

Differentiating the error \tilde{x}_i we get

$$\dot{\tilde{x}}_i = (A_{hi} - \Gamma_{hi} C_{hi}) \tilde{x}_i + \sum_{\substack{j=1 \\ j \neq i}}^L H_{hij} \tilde{x}_j + \Phi_{hi}(x_i, t) \quad (4.21)$$

The convergence of the state error towards zero depends on the eigenvalues of $(A_{hi} - \Gamma_{hi} C_{hi})$.

Remark 4.1: In this approach, a full-order state observer is employed, which means that the observer is designed to estimate all state variables of the system, even if some of these variables are not directly measurable. The mathematical model of the observer closely resembles that of the actual plant, with the inclusion of an additional term accounting for estimation errors. This additional term is necessary to compensate for inaccuracies in matrices A_{hi} and B_i to correct for any initial errors in the estimation process.

4.3. Design of the power system state estimator

In practical scenarios, the LFC scheme needs to exhibit a high level of robustness against specific disturbances to ensure the stability of MAMSPS. To address this, we introduce the SPSMCBSO along with a sliding surface that does not require a reaching phase, defined as follows:

$$\eta_{hi}[\hat{x}_i(t)] = M_{hi} \hat{x}_i(t) - \int_0^t M_{hi} (A_{hi} - B_{hi} \Lambda_{hi}) \hat{x}_i(\tau) d\tau - M_{hi} \hat{x}_i(0) e^{-\delta t} \quad (4.22)$$

where, M_{hi} is chosen to guarantee that the matrix $M_{hi} B_{hi}$ is nonsingular.

The design matrix $\Lambda_{hi} \in R^{m_i \times n_i}$ is selected in order to meet the non-linearity requirement.

$$\operatorname{Re}[\lambda_{\max}(A_{hi} - B_{hi}\Lambda_{hi})] < 0 \quad (4.23)$$

if we take derivative of $\eta_i[\hat{x}_i(t)]$ in terms of time, we've got the items that follow.

$$\begin{aligned} \dot{\eta}_{hi}[\hat{x}_i(t)] &= [M_{hi}A_{hi}\hat{x}_i(t) + M_{hi}B_{hi}u_i(t) + \sum_{\substack{j=1 \\ j \neq i}}^L M_{hi}H_{hij}\hat{x}_j(t) + M_{hi}\Gamma_{hi}(y_i - \hat{y}_i)] \\ &\quad - M_{hi}(A_{hi} - B_{hi}\Lambda_{hi})\hat{x}_i(t) + \delta_{hi}M_{hi}\hat{x}_i(0)e^{-\delta_i t} \end{aligned} \quad (4.24)$$

As $\dot{\eta}_{hi}(t) = \eta_{hi}(t) = 0$, then, to express the equivalent control a

$$\begin{aligned} u_i^{eq}(t) &= -(M_{hi}B_{hi})^{-1}[M_{hi}A_{hi}\hat{x}_i(t) + \sum_{\substack{j=1 \\ j \neq i}}^L M_{hi}H_{hij}\hat{x}_j(t) + M_{hi}\Gamma_{hi}(y_i - \hat{y}_i) \\ &\quad - M_{hi}(A_{hi} - B_{hi}\Lambda_{hi})\hat{x}_i(t) + \delta_{hi}M_{hi}\hat{x}_i(0)e^{-\delta_i t}] \\ &= -(M_{hi}B_{hi})^{-1}[M_{hi}B_{hi}\Lambda_{hi}\hat{x}_i(t) + M_{hi}\Gamma_{hi}(y_i - \hat{y}_i) + \delta_{hi}M_{hi}\hat{x}_i(0)e^{-\delta_i t} \\ &\quad + \sum_{\substack{j=1 \\ j \neq i}}^L M_{hi}H_{hij}\hat{x}_j(t)] \end{aligned} \quad (4.25)$$

By completing the system's loop, we provide (4.25) into (4.17)

$$\begin{aligned} \dot{x}_i(t) &= (A_{hi} - B_{hi}\Lambda_{hi})x_i(t) + (B_{hi}\Lambda_{hi} - B_{hi}(M_{hi}B_{hi})^{-1}M_{hi}\Gamma_{hi}C_{hi})\tilde{x}_i(t) \\ &\quad + \sum_{\substack{j=1 \\ j \neq i}}^L [H_{hij} - B_{hi}(M_{hi}B_{hi})^{-1}M_{hi}H_{hij}]x_j(t) \\ &\quad + \sum_{\substack{j=1 \\ j \neq i}}^L B_{hi}(M_{hi}B_{hi})^{-1}M_{hi}H_{hij}\tilde{x}_j(t) + \Phi_{hi}(x_i, t) - \delta_{hi}B_{hi}(M_{hi}B_{hi})^{-1}M_{hi}\hat{x}_i(0)e^{-\delta_i t} \end{aligned} \quad (4.26)$$

To examine MAMSPS (4.17), we integrate equations (4.21) and (4.26) as follows.

$$\begin{aligned}
\begin{bmatrix} \dot{x}_i \\ \dot{\tilde{x}}_i \end{bmatrix} &= \begin{bmatrix} A_{hi} - B_{hi}\Lambda_{hi} & \Theta_{hi} \\ 0 & A_{hi} - \Gamma_{hi}C_{hi} \end{bmatrix} \begin{bmatrix} x_i \\ \tilde{x}_i \end{bmatrix} \\
&+ \sum_{\substack{j=1 \\ j \neq i}}^L \begin{bmatrix} H_{hij} - \Upsilon_{hi}H_{hij} & \Upsilon_{hi}H_{hij} \\ 0 & H_{hij} \end{bmatrix} \begin{bmatrix} x_j \\ \tilde{x}_j \end{bmatrix} \\
&+ \begin{bmatrix} \Phi_{hi}(x_i, t) \\ \Phi_{hi}(x_i, t) \end{bmatrix} + \begin{bmatrix} N_{hi}e^{-\delta_i t} \\ 0 \end{bmatrix}
\end{aligned} \tag{4.27}$$

where $\Theta_{hi} = B_{hi}\Lambda_{hi} - B_{hi}(M_{hi}B_{hi})^{-1}M_{hi}\Gamma_{hi}C_{hi}$,

$N_{hi} = -\delta_{hi}B_{hi}(M_{hi}B_{hi})^{-1}M_{hi}\hat{x}_i(0)$ and $\Upsilon_{hi} = B_{hi}(M_{hi}B_{hi})^{-1}M_{hi}$.

Equation (4.27) represents the dynamic system of the MAMSPS. Therefore, we proceed to assess the stability of this system using the novel LMI provided in (4.28), accompanied by the corresponding theorem as stated.

Theorem 4.1: Asymptotically stable is formula (4.27) provided that the symmetric definite positive matrix Π_i and $\bar{\Pi}_i$ where $i=1, 2, \dots, L$ and the positive scalars λ_i, ρ_i and $\hat{\gamma}_i$ assuming the specified conditions, we can establish that the new LMI below holds.

$$\begin{bmatrix} X_i & \Pi_i\Theta_i & \Pi_i & \Pi_i N_i & 0 \\ \Theta_i^T \Pi_i & \bar{X}_i & 0 & 0 & \bar{\Pi}_i \\ \Pi_i & 0 & -\lambda_i^{-1} & 0 & 0 \\ N_i^T \Pi_i & 0 & 0 & -\hat{\gamma}_i^{-1} & 0 \\ 0 & \bar{\Pi}_i & 0 & 0 & -\rho_i^{-1} \end{bmatrix} < 0 \tag{4.28}$$

where $X_i = \Pi_i(A_{hi} - B_{hi}\Lambda_{hi}) + (A_{hi} - B_{hi}\Lambda_{hi})^T \Pi_i$

$$+ \sum_{\substack{j=1 \\ j \neq i}}^L [\bar{\lambda}_j (H_{hji} - \Upsilon_j H_{hji})^T (H_{hji} - \Upsilon_j H_{hji})],$$

$$\bar{X}_i = \bar{\Pi}_i(A_{hi} - \Gamma_{hi}C_{hi}) + (A_{hi} - \Gamma_{hi}C_{hi})^T \bar{\Pi}_i + \sum_{\substack{j=1 \\ j \neq i}}^L [\bar{\lambda}_j^{-1} H_{hji}^T H_{hji}]$$

$$+ \sum_{\substack{j=1 \\ j \neq i}}^L [\hat{\lambda}_j (\Upsilon_j H_{hji})^T \Upsilon_j H_{hji}].$$

Proof of Theorem 4.1: The Lyapunov's function (Liao Kai and Yan Xu, , 2017), (K. Liao and Y. Xu, 2018), (Manikandan, S. et al., 2020) is selected.

$$V = \sum_{i=1}^L \begin{bmatrix} x_i \\ \tilde{x}_i \end{bmatrix}^T \begin{bmatrix} \Pi_i & 0 \\ 0 & \bar{\Pi}_i \end{bmatrix} \begin{bmatrix} x_i \\ \tilde{x}_i \end{bmatrix} \quad (4.29)$$

where $\Pi_i > 0$ and $\bar{\Pi}_i > 0$ satisfy (4.29) for $i = 1, 2, \dots, L$. Then, taking the derivative of time, we get

$$\begin{aligned} \dot{V} &= \sum_{i=1}^L \begin{bmatrix} \dot{x}_i \\ \dot{\tilde{x}}_i \end{bmatrix}^T \begin{bmatrix} \Pi_i & 0 \\ 0 & \bar{\Pi}_i \end{bmatrix} \begin{bmatrix} x_i \\ \tilde{x}_i \end{bmatrix} \\ &\quad + \sum_{i=1}^L \begin{bmatrix} x_i \\ \tilde{x}_i \end{bmatrix}^T \begin{bmatrix} \Pi_i & 0 \\ 0 & \bar{\Pi}_i \end{bmatrix} \begin{bmatrix} \dot{x}_i \\ \dot{\tilde{x}}_i \end{bmatrix} \\ &= \sum_{i=1}^L \left\{ \begin{bmatrix} x_i \\ \tilde{x}_i \end{bmatrix}^T \begin{bmatrix} \Pi_i (A_{hi} - B_{hi} \Lambda_{hi}) + (A_{hi} - B_{hi} \Lambda_{hi})^T \Pi_i & \Pi_i \Theta_{hi} \\ \Theta_{hi}^T \Pi_i & \bar{\Pi}_i (A_{hi} - \Gamma_{hi} C_{hi}) + (A_{hi} - \Gamma_{hi} C_{hi})^T \bar{\Pi}_i \end{bmatrix} \begin{bmatrix} x_i \\ \tilde{x}_i \end{bmatrix} \right\} \\ &\quad + \sum_{i=1}^L [x_i^T \Pi_i N_{hi} e^{-\delta t} + (e^{-\delta t})^T N_{hi}^T \Pi_i x_i] \\ &\quad + \sum_{i=1}^L \sum_{\substack{j=1 \\ j \neq i}}^L [x_j^T (H_{hij} - \Upsilon_i H_{hij})^T \Pi_i x_i + x_i^T \Pi_i (H_{hij} - \Upsilon_i H_{hij}) x_j] \\ &\quad + \sum_{i=1}^L \sum_{\substack{j=1 \\ j \neq i}}^L [\tilde{x}_j^T (\Upsilon_i H_{hij})^T \Pi_i x_i + x_i^T \Pi_i \Upsilon_i H_{hij} \tilde{x}_j] \\ &\quad + \sum_{i=1}^L \sum_{\substack{j=1 \\ j \neq i}}^L (\tilde{x}_i^T \bar{\Pi}_i H_{hij} \tilde{x}_j + \tilde{x}_j^T H_{hij}^T \bar{\Pi}_i \tilde{x}_i) + \sum_{i=1}^L [\tilde{x}_i^T \bar{\Pi}_i \Phi_i + x_i^T \Pi_i \Phi_i + \Phi_i^T \Pi_i x_i + \Phi_i^T \bar{\Pi}_i \tilde{x}_i] \end{aligned} \quad (4.30)$$

Introducing Lemma 4.1 into equation (4.30), we get

$$\begin{aligned}
\dot{V} \leq & \sum_{i=1}^L \left\{ \begin{bmatrix} x_i \\ \tilde{x}_i \end{bmatrix}^T \left[\begin{array}{c} \Pi_i (A_{hi} - B_{hi} \Lambda_{hi}) + (A_{hi} - B_{hi} \Lambda_{hi})^T \Pi_i \quad \Pi_i \Theta_i \\ \Theta_i^T \Pi_i \quad \bar{\Pi}_i (A_{hi} - \Gamma_{hi} C_{hi}) + (A_{hi} - \Gamma_{hi} C_{hi})^T \bar{\Pi}_i \end{array} \right] \begin{bmatrix} x_i \\ \tilde{x}_i \end{bmatrix} \right\} \\
& + \sum_{i=1}^L \sum_{\substack{j=1 \\ j \neq i}}^L [\bar{\lambda}_i x_j^T (H_{hij} - \Upsilon_i H_{hij})^T (H_{hij} - \Upsilon_i H_{hij}) x_j] \\
& + \sum_{i=1}^L \sum_{\substack{j=1 \\ j \neq i}}^L [\bar{\lambda}_i^{-1} x_i^T \Pi_i \Pi_i x_i + \hat{\lambda}_i \tilde{x}_j^T (\Upsilon_i H_{hij})^T \Upsilon_i H_{hij} \tilde{x}_j] \\
& + \sum_{i=1}^L \sum_{\substack{j=1 \\ j \neq i}}^L (\hat{\lambda}_i^{-1} x_i^T \Pi_i \Pi_i x_i + \tilde{\lambda}_i \tilde{x}_i^T \bar{\Pi}_i \bar{\Pi}_i \tilde{x}_i + \tilde{\lambda}_i^{-1} \tilde{x}_j^T H_{hij}^T H_{hij} \tilde{x}_j) \\
& + \sum_{i=1}^L [\bar{\gamma}_i \tilde{x}_i^T \bar{\Pi}_i \bar{\Pi}_i \tilde{x}_i + \bar{\gamma}_i^{-1} \Phi_i^T \Phi_i + \tilde{\gamma}_i x_i^T \Pi_i \Pi_i x_i + \tilde{\gamma}_i^{-1} \Phi_i^T \Phi_i] \\
& + \sum_{i=1}^L [\hat{\gamma}_i^{-1} x_i^T \Pi_i N_i N_i^T \Pi_i x_i + \hat{\gamma}_i (e^{-\delta t})^T e^{-\delta t}] \tag{4.31}
\end{aligned}$$

Since $\sum_{i=1}^L \sum_{\substack{j=1 \\ j \neq i}}^L \bar{\lambda}_i x_j^T (H_{hij} - \Upsilon_i H_{hij})^T (H_{hij} - \Upsilon_i H_{hij}) x_j$

$$\begin{aligned}
& = \sum_{i=1}^L \sum_{\substack{j=1 \\ j \neq i}}^L \bar{\lambda}_j x_i^T (H_{hji} - \Upsilon_j H_{hji})^T (H_{hji} - \Upsilon_j H_{hji}) x_i, \\
& \sum_{i=1}^L \sum_{\substack{j=1 \\ j \neq i}}^L \hat{\lambda}_i \tilde{x}_j^T (\Upsilon_i H_{hij})^T \Upsilon_i H_{hij} \tilde{x}_j = \sum_{i=1}^L \sum_{\substack{j=1 \\ j \neq i}}^L \hat{\lambda}_j \tilde{x}_i^T (\Upsilon_j H_{hji})^T \Upsilon_j H_{hji} \tilde{x}_i \text{ and} \\
& \sum_{i=1}^L \sum_{\substack{j=1 \\ j \neq i}}^L \tilde{\lambda}_i^{-1} \tilde{x}_j^T H_{hij}^T H_{hij} \tilde{x}_j = \sum_{i=1}^L \sum_{\substack{j=1 \\ j \neq i}}^L \tilde{\lambda}_j^{-1} \tilde{x}_i^T H_{hji}^T H_{hji} \tilde{x}_i, \text{ and then}
\end{aligned}$$

$$\begin{aligned}
\dot{V} &\leq \sum_{i=1}^L \left\{ \begin{bmatrix} x_i \\ \tilde{x}_i \end{bmatrix}^T \begin{bmatrix} \Pi_i(A_{hi} - B_{hi}\Lambda_{hi}) + (A_{hi} - B_{hi}\Lambda_{hi})^T \Pi_i & \Pi_i \Theta_{hi} \\ \Theta_{hi}^T \Pi_i & \bar{\Pi}_i(A_{hi} - \Gamma_{hi}C_{hi}) + (A_{hi} - \Gamma_{hi}C_{hi})^T \bar{\Pi}_i \end{bmatrix} \begin{bmatrix} x_i \\ \tilde{x}_i \end{bmatrix} \right\} \\
&+ \sum_{i=1}^L \sum_{\substack{j=1 \\ j \neq i}}^L [\bar{\lambda}_j x_i^T (H_{hji} - \Upsilon_j H_{hji})^T (H_{hji} - \Upsilon_j H_{hji}) x_i] \\
&+ \sum_{i=1}^L \sum_{\substack{j=1 \\ j \neq i}}^L [\bar{\lambda}_i^{-1} x_i^T \Pi_i \Pi_i x_i + \hat{\lambda}_j \tilde{x}_i^T (\Upsilon_j H_{hji})^T \Upsilon_j H_{hji} \tilde{x}_i] \\
&+ \sum_{i=1}^L \sum_{\substack{j=1 \\ j \neq i}}^L (\hat{\lambda}_i^{-1} x_i^T \Pi_i \Pi_i x_i + \tilde{\lambda}_j \tilde{x}_i^T \bar{\Pi}_i \bar{\Pi}_i \tilde{x}_i + \tilde{\lambda}_j^{-1} \tilde{x}_i^T H_{hji}^T H_{hji} \tilde{x}_i) \\
&+ \sum_{i=1}^L [\bar{\gamma}_i \tilde{x}_i^T \bar{\Pi}_i \bar{\Pi}_i \tilde{x}_i + \tilde{\gamma}_i x_i^T \Pi_i \Pi_i x_i + \bar{\gamma}_i^{-1} \Phi_i^T \Phi_i + \tilde{\gamma}_i^{-1} \Phi_i^T \Phi_i] \\
&+ \sum_{i=1}^L [\hat{\gamma}_i^{-1} x_i^T \Pi_i N_i N_i^T \Pi_i x_i + \hat{\gamma}_i (e^{-\delta t})^T e^{-\delta t}] \\
&\leq \sum_{i=1}^L \left\{ \begin{bmatrix} x_i \\ \tilde{x}_i \end{bmatrix}^T \begin{bmatrix} \Omega_i & \Pi_i \Theta_i \\ \Theta_i^T \Pi_i & \bar{\Omega}_i \end{bmatrix} \begin{bmatrix} x_i \\ \tilde{x}_i \end{bmatrix} \right\} \\
&+ \sum_{i=1}^L [(\bar{\gamma}_i^{-1} + \tilde{\gamma}_i^{-1}) \gamma_i^2] + \sum_{i=1}^L [\hat{\gamma}_i (e^{-\delta t})^T e^{-\delta t}]
\end{aligned} \tag{4.32}$$

where $\lambda_i = (N-1)(\bar{\lambda}_i^{-1} + \hat{\lambda}_i^{-1}) + \tilde{\gamma}_i$ and $\rho_i = \tilde{\lambda}_i(N-1) + \bar{\gamma}_i$,

$$\begin{aligned}
\Omega_{hi} &= \Pi_i(A_{hi} - B_{hi}\Lambda_{hi}) + (A_{hi} - B_{hi}\Lambda_{hi})^T \Pi_i + \hat{\gamma}_i^{-1} \Pi_i N_i N_i^T \Pi_i \\
&+ \lambda_i \Pi_i \Pi_i + \sum_{\substack{j=1 \\ j \neq i}}^L [\bar{\lambda}_j (H_{hji} - \Upsilon_j H_{hji})^T (H_{hji} - \Upsilon_j H_{hji})] \text{ and} \\
\bar{\Omega}_{hi} &= \bar{\Pi}_i(A_{hi} - \Gamma_{hi}C_{hi}) + (A_{hi} - \Gamma_{hi}C_{hi})^T \bar{\Pi}_i + \rho_i \bar{\Pi}_i \bar{\Pi}_i \\
&+ \sum_{\substack{j=1 \\ j \neq i}}^L [\tilde{\lambda}_j^{-1} H_{hji}^T H_{hji}] + \sum_{\substack{j=1 \\ j \neq i}}^L [\hat{\lambda}_j (\Upsilon_j H_{hji})^T \Upsilon_j H_{hji}]
\end{aligned}$$

Furthermore, by the Schur complement of (Park Ju H. et al., 2021), the LMI is similar to the following.

$$\Psi_{hi} = \begin{bmatrix} \Omega_{hi} & \Pi_i \Theta_{hi} \\ \Theta_{hi}^T \Pi_i & \bar{\Omega}_{hi} \end{bmatrix} < 0 \quad (4.33)$$

Combination of (4.32) and (4.33), we get.

$$\dot{V} \leq \sum_{i=1}^L (-\rho_{\min}(\Psi_i) \left\| \begin{bmatrix} x_i \\ \tilde{x}_i \end{bmatrix} \right\|^2 + \zeta_i + \hat{\gamma}_i e^{-2\delta_i t}) \quad (4.34)$$

where $\zeta_i = \sum_{i=1}^L [(\bar{\gamma}_i^{-1} + \tilde{\gamma}_i^{-1})\gamma_i^2]$ is the constant value and the eigenvalue

$\rho_{\min}(\Psi_i) > 0$. The term $\hat{\gamma}_i e^{-2\delta_i t}$ will be getting closer to 0 as the time gets closer

to infinity. Hence, $\dot{V} < 0$ is derived with $\left\| \begin{bmatrix} x_i \\ \tilde{x}_i \end{bmatrix} \right\| > \sqrt{\frac{\zeta_i}{\rho_{\min}(\Psi_i)}}$ proves that the system

is extremely stable in fact.

4.4. Design of a sliding mode controller with total output feedback

In this section, we develop the decentralized single phase sliding mode control scheme (DSPSMCS) for LFC in the context of the MAMSPS described by Equation (4.35).

$$\begin{aligned} u_i(t) = & -(M_{hi} B_{hi})^{-1} [\|M_{hi}\| \|B_{hi}\| \|\Lambda_{hi}\| \|\hat{x}_i(t)\| \\ & + \delta_i \|M_{hi}\| \|\hat{x}_i(0)\| e^{-\delta_i t} + \|M_{hi}\| \|\Gamma_{hi}\| \|(y_i - \hat{y}_i)\| \\ & + \sum_{\substack{j=1 \\ j \neq i}}^L \|M_{hj}\| \|H_{hj}\| \|\hat{x}_j(t)\| + \theta_i] \frac{\eta_{hi}[\hat{x}_i(t)]}{\|\eta_{hi}[\hat{x}_i(t)]\|}, \quad (4.35) \\ & i = 1, 2, \dots, L \end{aligned}$$

where θ_i is the positive scalar and $u_i(t)$ represents the decentralized single-phase SMC scheme. In this subsection, we also derive a proof of the system state variables' reachability, along with the Lyapunov function associated with the following theorem:

Theorem 4.2: The variable state trajectories of the system (4.19) are guaranteed to reach the single-phase sliding surface and remain on it at all times when

utilizing the SSWRP given by Equation (4.22) and the controller given by Equation (4.35).

Remark 4.2. The fundamental function of a single-phase SMC is to provide motion strength over the whole state space. In the sliding mode, the size of the state space is according to the order of the motion equation. As such, the resilience of intricately linked PS may be guaranteed over the duration of the system's reaction, beginning at the first-time instance.

Proof of Theorem 4.2: The Lyapunov function (K. Liao and Y. Xu, 2018), (Manikandan, S. et al., 2020) is given.

$$V_1 = \sum_{i=1}^L (\|\eta_{hi}[\hat{x}_i(t)]\|) \quad (4.36)$$

Applying the term derivative of V_1 , we as a species acquire

$$\dot{V}_1 = \sum_{i=1}^L \left(\frac{\eta_{hi}^T[\hat{x}_i(t)]}{\|\eta_{hi}[\hat{x}_i(t)]\|} \dot{\eta}_{hi}[\hat{x}_i(t)] \right) \quad (4.37)$$

substituting Equation (4.24) into Equation (4.37), we obtain the following result:

$$\begin{aligned} \dot{V}_1 = & \sum_{i=1}^L \frac{\eta_{hi}^T[\hat{x}_i(t)]}{\|\eta_{hi}[\hat{x}_i(t)]\|} [M_{hi}A_{hi}\hat{x}_i(t) - M_{hi}(A_{hi} - B_{hi}\Lambda_{hi})\hat{x}_i(t) \\ & + \delta_i M_{hi}\hat{x}_i(0)e^{-\delta_i t} + M_{hi}\Gamma_{hi}(y_i - \hat{y}_i)] \\ & + \sum_{i=1}^L \frac{\eta_{hi}^T[\hat{x}_i(t)]}{\|\eta_{hi}[\hat{x}_i(t)]\|} M_{hi}B_{hi}u_i(t) \\ & + \sum_{i=1}^L \sum_{\substack{j=1 \\ j \neq i}}^L \left[\frac{\eta_{hi}^T[\hat{x}_i(t)]}{\|\eta_{hi}[\hat{x}_i(t)]\|} M_{hi}H_{hij}\hat{x}_j(t) \right] \end{aligned} \quad (4.38)$$

According to equation (4.38), property $\|AB\| \leq \|A\|\|B\|$ and

$$\sum_{i=1}^L \sum_{\substack{j=1 \\ j \neq i}}^L [\|M_{hi}\| \|H_{hij}\| \|\hat{x}_j(t)\|] = \sum_{i=1}^L \sum_{\substack{j=1 \\ j \neq i}}^L [\|M_{hj}\| \|H_{hji}\| \|\hat{x}_i(t)\|], \text{ it generates.}$$

$$\begin{aligned}
\dot{V}_1 = & \sum_{i=1}^L [\|M_{hi}\| \|B_{hi}\| \|\Lambda_{hi}\| \|\hat{x}_i(t)\| + \delta_i \|M_{hi}\| \|\hat{x}_i(0)\| e^{-\delta_i t}] \\
& + \sum_{i=1}^L [\|M_{hi}\| \|\Gamma_{hi}\| \|(y_i - \hat{y}_i)\|] \\
& + \sum_{i=1}^L \sum_{\substack{j=1 \\ j \neq i}}^L [\|M_{hj}\| \|H_{hji}\| \|\hat{x}_i(t)\|] \\
& + \sum_{i=1}^L \frac{\eta_{hi}^T [\hat{x}_i(t)]}{\|\eta_{hi} [\hat{x}_i(t)]\|} M_{hi} B_{hi} u_i(t)
\end{aligned} \tag{4.39}$$

Through the substitution of $u_i(t)$ into Equation (4.39), we attain the following outcome.

$$\dot{V}_1 \leq -\sum_{i=1}^L \theta_i < 0. \tag{4.40}$$

The derivative of the Lyapunov's function (4.40) is negative, demonstrating the successful achievement of the reachability proof. Subsequently, Figure 4.2 illustrates the flowchart representing the proposed single-phase SMC observer technique.

Remark 4.3. The stability of the LFC in a PS using the LMI technique is demonstrated in Paper (K. Liao and Y. Xu, 2018), (Manikandan, S. et al., 2020). Nevertheless, the previously indicated approach necessitates the identification of four positive matrices in the LMI equations in Appendix 4.2. This means that the proposed approach simplifies the search for a workable solution in LMI equations by requiring the identification of only two positive matrices.

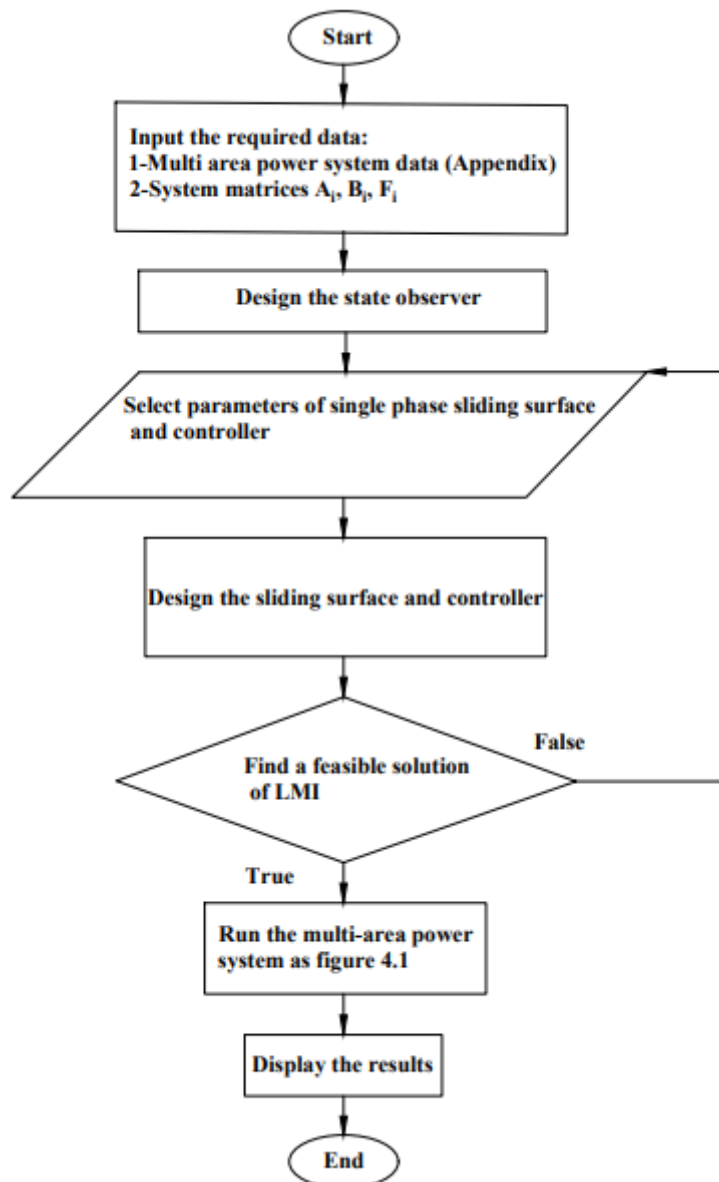


Figure 4.2. The visual representation depicting the SPSMCBSO approach as a flowchart.

4.5. Simulation results and discussions

The proposed new method is evaluated against conventional sliding mode LFC and robust LFC using MATLAB software. The simulation results indicate that the designed LFC exhibits a quicker response speed and superior robust performance compared to the conventional sliding mode and robust LFC approaches. In the presence of random and step load disturbances as well as parameter uncertainties, the efficiency of the suggested SPSMCBSO for the LFC of the TAGHTPS is

demonstrated in three simulations in the present session, which tests the effectiveness and resilience of the suggested control approach. As can be shown in (Hakimuddin Nizamuddin et al., 2020), (Gupta Nidhi et al., 2022), (Sarkar Mrinal Kanti et al., 2018), (Dev Ark et al., 2021), (Patel Ragini et al., 2019), (Patel Ragini et al., 2019), (Guha Dipayan et al., 2021), the simulation findings of the study are contrasted with the latest control technique results.

4.5.1 Simulation 1

Traditional control techniques have traditionally been employed for LFC in MAMSPS when facing step load disturbances. However, a recent development involves the utilization of the bacterial foraging algorithm (BFA) for designing and implementing a generation-based PID-Structured AGC algorithm, specifically tailored for investigating LFC in the context of the TAGHTPS (Hakimuddin Nizamuddin et al., 2020). In this particular case study, we put the suggested controller of the test, subjecting it to step load changes ranging from 1% to 2%, while maintaining the nominal parameters unchanged, as outlined in (Hakimuddin Nizamuddin et al., 2020). The results in terms of FD in both power areas are graphically depicted in Figure 4.3 to Figure 4.4, while Figure 4.5 illustrates the tie line power deviation (TLPD). When evaluating the act of performing of the TAGHTPS in terms of settling time and overshoot, a direct comparison is made with the findings presented in (Hakimuddin Nizamuddin et al., 2020).

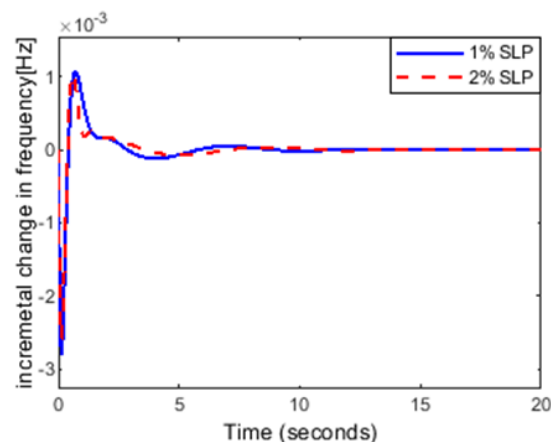


Figure 4.3. The frequency variation [Hz] with 1% to 2% step load in area 1.

It is evident that both controllers exhibit smaller frequency overshoot, thereby

ensuring that the operating frequency remains within the permissible range. However, the novel approach demonstrates a significantly shorter settling time (8 seconds) in comparison to the settling time reported in (Hakimuddin Nizamuddin et al., 2020), (Gupta Nidhi et al., 2022), (Sarkar Mrinal Kanti et al., 2018), (Dev Ark et al., 2021), (Patel Ragini et al., 2019), (Patel Ragini et al. , 2019). This indicates a notable optimized system speed of response with the suggested approach.

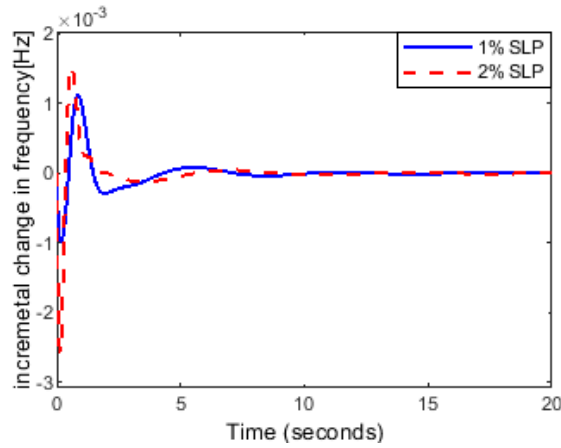


Figure 4.4. The frequency variation [Hz] with 1% to 2% step load in area 2.

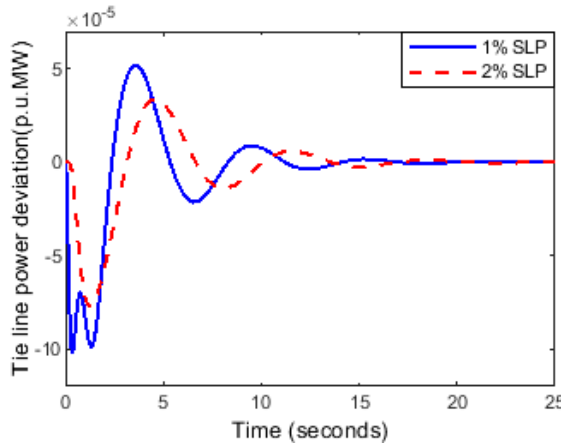


Figure 4.5. Tie line power deviation [p.u.MW].

Figures 4.4 and 4.5 portray the switching surface function and the control law of the controller in Area 1 and Area 2 for Case 1. The highlighted features in these visual representations include the selected switching coefficient gains and observer gain.

$$\bar{K}_1 = \begin{bmatrix} 0.0033 & 0.0018 & 0.0003 & 0.0043 & 0.0018 & 0.0000 & 0.0004 & 0.0018 \\ 0.0434 & 0.0112 & 0.0008 & 0.0025 & -0.0081 & 0.0010 & -1.4529 & 0.1544 \end{bmatrix}$$

$$\bar{K}_2 = \begin{bmatrix} 0.0033 & 0.0018 & 0.0003 & 0.0043 & 0.0018 & 0.0000 & 0.0004 & 0.0018 \\ 0.0434 & 0.0112 & 0.0008 & 0.0025 & -0.0081 & 0.0010 & -1.4529 & 0.1544 \end{bmatrix}$$

$$\bar{L}_1 = \begin{bmatrix} 12.7318 & 0.0002 & -0.1312 & 0.2169 & -0.5555 & 0.0509 & 0.0032 & 4.7421 \\ 0.0244 & 0.1584 & 0.0265 & -0.1143 & 0.1756 & -0.0166 & -0.0014 & -2.2491 \\ -13.1215 & 0.0265 & 0.2042 & -0.1692 & 0.3846 & -0.0360 & -0.0047 & -7.1637 \\ 21.6894 & -0.1143 & -0.1692 & 0.7309 & -1.9819 & 0.1779 & 0.0034 & 4.8805 \\ -55.5508 & 0.1756 & 0.3846 & -1.9819 & 8.9705 & -0.0477 & -0.0066 & -9.4244 \\ 5.0938 & -0.0166 & -0.0360 & 0.1779 & -0.0477 & 0.8118 & 0.0006 & 0.8744 \\ 0.3172 & -0.0014 & -0.0047 & 0.0034 & -0.0066 & 0.0006 & 1.0002 & 0.2443 \\ 4.7421 & -0.0225 & -0.0716 & 0.0488 & -0.0942 & 0.0087 & 0.0024 & 6.0337 \end{bmatrix}$$

$$\bar{L}_1 = \begin{bmatrix} 12.7318 & 0.0002 & -0.1312 & 0.2169 & -0.5555 & 0.0509 & 0.0032 & 4.7421 \\ 0.0244 & 0.1584 & 0.0265 & -0.1143 & 0.1756 & -0.0166 & -0.0014 & -2.2491 \\ -13.1215 & 0.0265 & 0.2042 & -0.1692 & 0.3846 & -0.0360 & -0.0047 & -7.1637 \\ 21.6894 & -0.1143 & -0.1692 & 0.7309 & -1.9819 & 0.1779 & 0.0034 & 4.8805 \\ -55.5508 & 0.1756 & 0.3846 & -1.9819 & 8.9705 & -0.0477 & -0.0066 & -9.4244 \\ 5.0938 & -0.0166 & -0.0360 & 0.1779 & -0.0477 & 0.8118 & 0.0006 & 0.8744 \\ 0.3172 & -0.0014 & -0.0047 & 0.0034 & -0.0066 & 0.0006 & 1.0002 & 0.2443 \\ 4.7421 & -0.0225 & -0.0716 & 0.0488 & -0.0942 & 0.0087 & 0.0024 & 6.0337 \end{bmatrix}$$

Remark 4.4. Through this comparison with references (Hakimuddin Nizamuddin et al., 2020), (Gupta Nidhi et al., 2022), (Sarkar Mrinal Kanti et al., 2018), (Dev Ark et al., 2021), (Patel Ragini et al., 2019), (Patel Ragini et al. , 2019), it becomes evident that the newly proposed SPSMCBSO controller for LFC in MAMSP exhibits greater robustness and responsiveness when facing load disturbances in comparison to previous techniques. The impact of load disturbance is clearly discernible, yet the system swiftly returns to a stable state with notably reduced overshoots.

4.5.2 Simulation 2:

Case 1: Once more, the TAGHTPS was modeled using a recently designed Teaching Learning Based Optimization (TLBO) method with a 2-Degree Freedom of Proportional–Integral–Derivative (2-DOF PID) controller, with nominal parameters provided as shown in (Sahu, R. Kumar, P. Sidhartha, Rout, U. Kumar, Sahoo, D.

Kumar, 2016) and a load disturbance of 0.01 p.u.MW in each region. We suggest SPSMCBSO to analyze PS performance, and we use the suggested technique to simulate the TAGHTPS response in a similar fashion to (Sahu Rabindra Kumar et al., 2016).

Table 4.1. Setting time T_s [s] and maximum overshoot MOS[Hz] comparison.

Controller	The suggested scheme		The recently approach	
Parameter	T_s [s]	MOS [Hz]	T_s [s]	MOS [Hz]
Δf_1	7	0.004	13	0.019
Δf_2	7	0.0012	13	0.017

Source: created by author

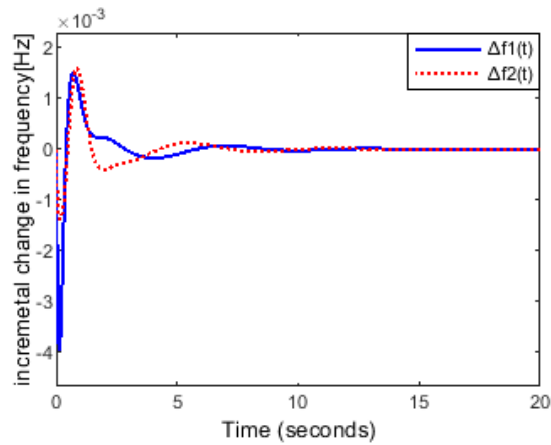


Figure 4.6. The frequency variation [Hz] with 1% step load in both areas.

Figure 4.6 shows the frequency fluctuation in both areas. In accordance, the TLPD is shown in Figure 4.7. The two controllers are thoroughly compared in Table 4.1. This indicates that because it is less difficult and easier to implement, the suggested approach is a better choice.

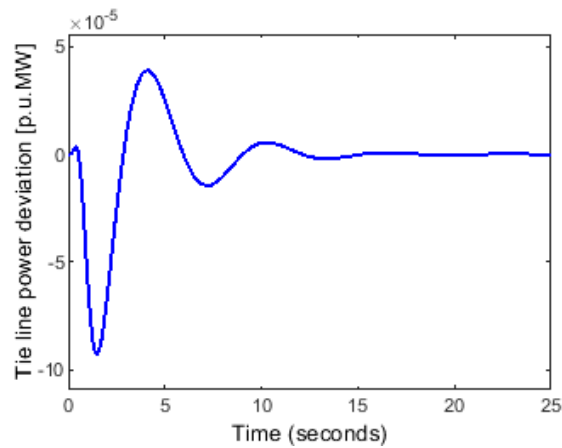


Figure 4.7. Tie line power variation [p.u.MW].

Case 2: As industrial activities continue to grow, the electricity requirements from nearby industries, hospitals, households, and various other types of loads also witness a rise. Conversely, MAMSPS are tasked with satisfying these escalating demands while ensuring that the SF remains within acceptable limits. Consequently, we consider these electricity demands as random load disturbances affecting each area of the TAGHTPS, as illustrated in Figure 4.8. For the purposes of this simulation, the subsystem parameters are presumed to be at their nominal values, akin to those in Case 1.

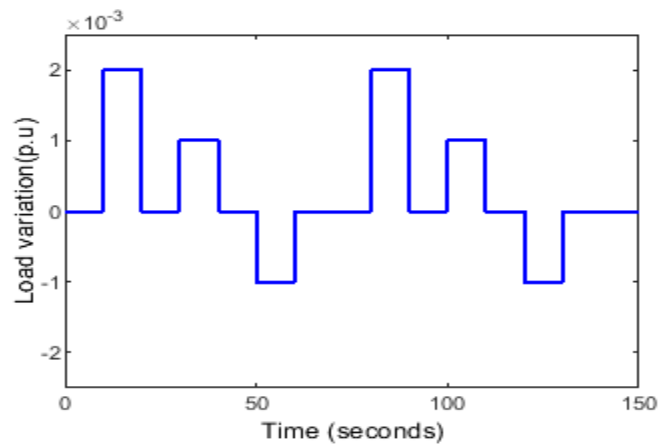


Figure 4.8. Random load deviation

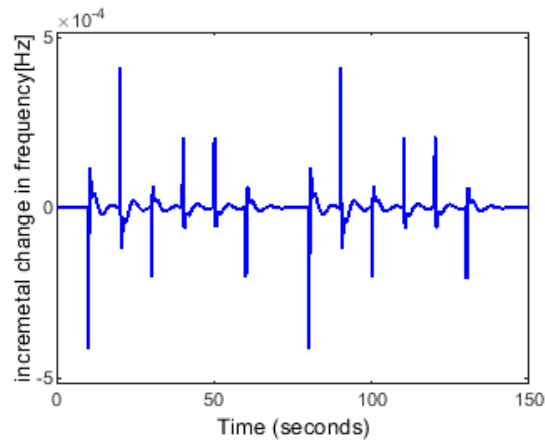


Figure 4.9. Frequency deviation [Hz] in area 1

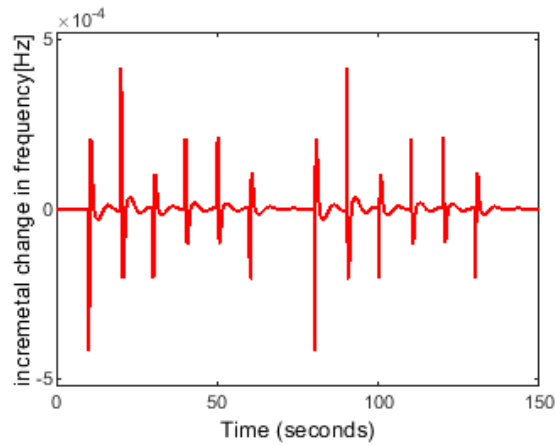


Figure 4.10. Frequency deviation [Hz] in area 2

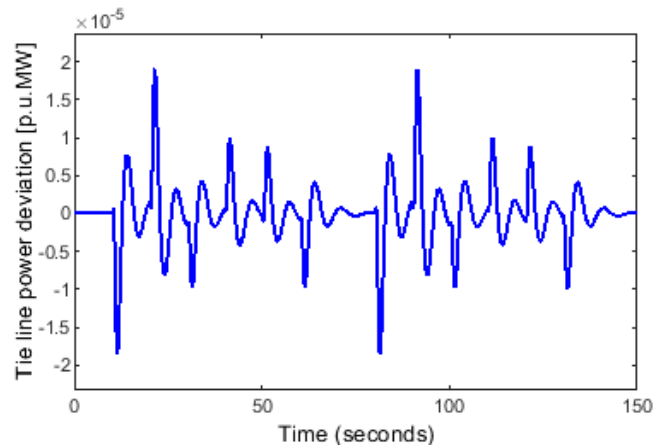


Figure 4.11. Change in tie line power [p.u.MW]

Figures 4.9 to 4.10 depict the frequency deviation in both regions, while Figure 4.11 shows the TLPD. Under random load variations, the frequency response in Figure 4.9 to 4.10 has improved. Once more, during operation, the frequency is

maintained at a manageable level, supporting the suggested SPSMCBSO for the LFC of MAMSPS.

Remark 4.5: As may be seen in (Sahu Rabindra Kumar et al., 2016), TAGHTPS was implemented with merely a step load disruption from client requests. Since load needs really fluctuate on a regular basis, this requirement is thought to be a random variation in load that is controlled by the PS. Under the TAGHTPS's random load situation, the suggested SPSMCBSO shows to be highly beneficial for the PS's stability, improving the MAMSPS's LFC.

4.5.3 Simulation 3

Case1: Utilizing the subsystem parameter from (Gupta Nidhi et al., 2022) and a step load disturbance of 1%, the TAGHTPS response was once more simulated using the Jaya approach to create PID structured regulators for the Optimized Generation Control (OGC) approach. The metaheuristic technique was utilized above to maximize the control parameter search for PS. It could be difficult to use this method for the LFC of MAMSPS, though. To sum up, the metaheuristic method is both time-consuming and very complicated. To put it another way, we re-proposed the easier-to-implement SPSMCBSO. Using the suggested method, we mimic the TAGHTPS response in this instance, using conditions akin to those reported in (Gupta Nidhi et al., 2022).

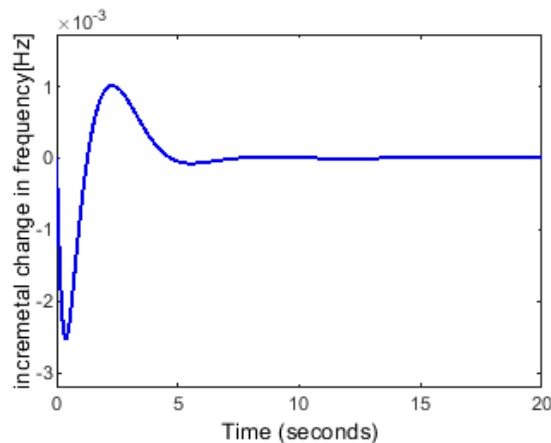


Figure 4.12. Frequency variation [Hz] in area 1

In Figure 4.12, the frequency variation in region one is displayed; in Figure 4.13, the FD in area two is displayed. Figure 4.14 provides the TLPD, in that order.

Better overshoot is observed for both controllers; nevertheless, the 5 s settling time with the suggested method is once more much less than the 8 s settling duration with the controller described in (Gupta Nidhi et al., 2022).

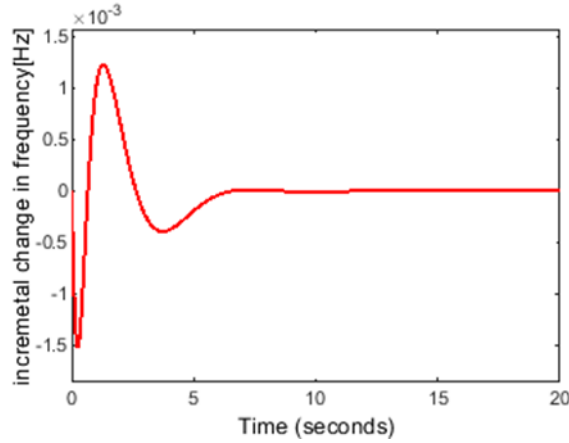


Figure 4.13. Frequency deviation [Hz] in area 2

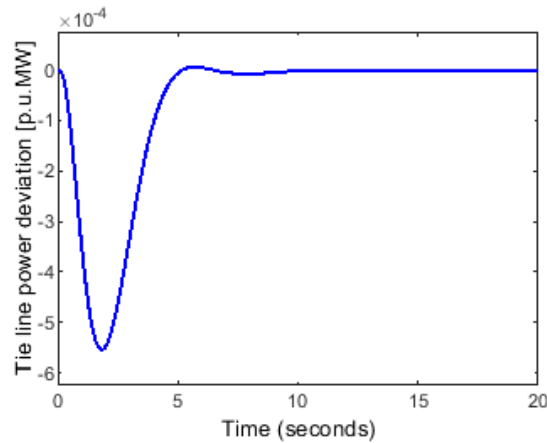


Figure 4.14. Tie line power variation [p.u.MW]

Table 4.2. Setting time T_s [s] and maximum overshoot MOS[Hz] comparison.

Controller	The suggested Method		The recent scheme	
	T_s [s]	MOS [Hz]	T_s [s]	MOS [Hz]
Δf_1	5	0.0025	8	0.007
Δf_2	6.25	0.0015	8	0.003

Source: created by author

Table 4.2 provides a thorough analysis of the two controllers. This further

suggests that the simpler and less demanding to execute suggested system is a superior option for the MAMSPS LFC.

Case 2: The requirement for electricity from nearby businesses, hospitals, homes, and other forms of load increases along with industrial activity. On the other hand, MAMSPS must satisfy the requirements at a frequency that stays within reasonable bounds. Consequently, we handle electrical demands as a random load disturbance delivered to each TAGHTPS sector, as shown in Figure 4.15.

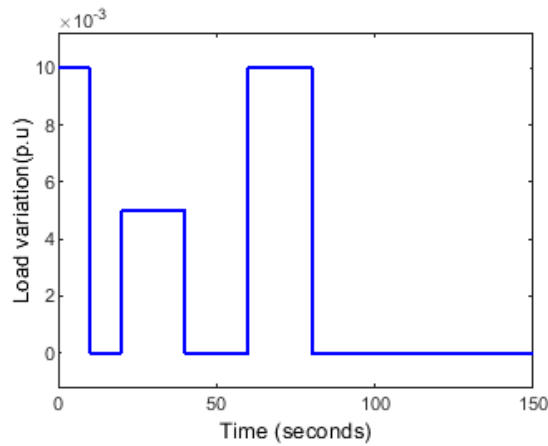


Figure 4.15. Random load deviation

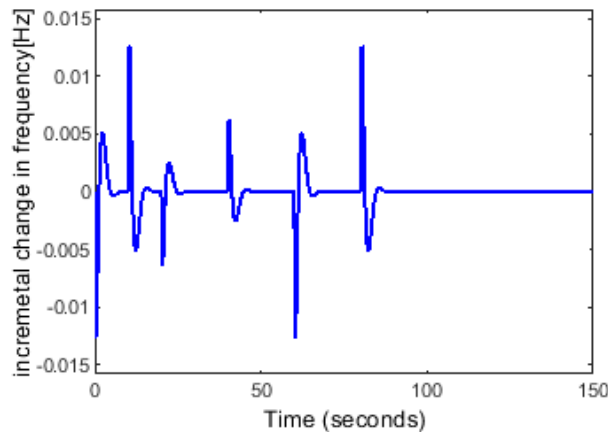


Figure 4.16. Frequency deviation [Hz] in area 1

Figures 4.16 to 4.17 illustrate the oscillations in frequency at both locations, while Figure 4.18 displays the TLPD. When subjected to random load fluctuations, the frequency response depicted in Figures 4.16 and 4.17 shows noticeable improvement. The frequency is effectively maintained within acceptable levels during system operation, thereby validating the effectiveness of the proposed

SPSMCBSO for LFC in the MAMSPS.

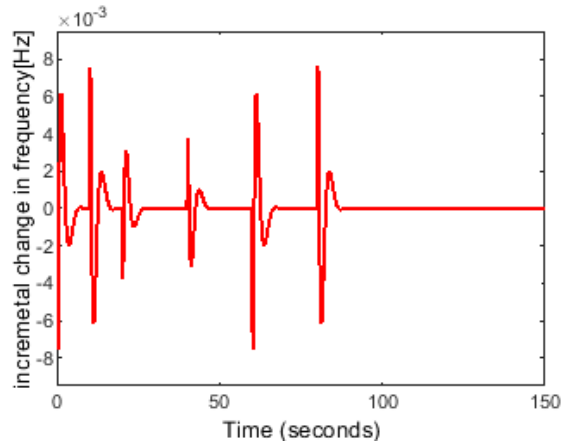


Figure 4.17. Frequency deviation [Hz] in area 2

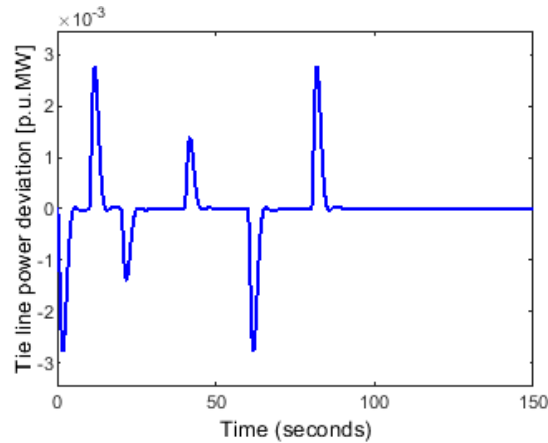


Figure 4.18. The tie line power variation [p.u.MW]

Case 3: To enhance the realism and achieve superior LFC for MAMSPS, it is imperative for the controller to exhibit robustness against various disturbances, including random load fluctuations, parameter uncertainties, and deviations in subsystem parameters. In this particular case, our simulation involves subjecting the TAGHTPS to a response analysis in the presence of random load disturbances, as depicted in Figure 4.19. Additionally, we introduce a $\pm 20\%$ deviation in the subsystem parameters. Moreover, we account for mismatched uncertainties in the system state matrix due to changes in valve positions within the TAGHTPS. These uncertainties are represented by a cosine function, which adds another layer of complexity to the analysis.

As we've established $\Delta A_1 = \Delta A_2 = [\Delta A_{11} \quad \Delta A_{12}]$ where in Appendix 4.3.

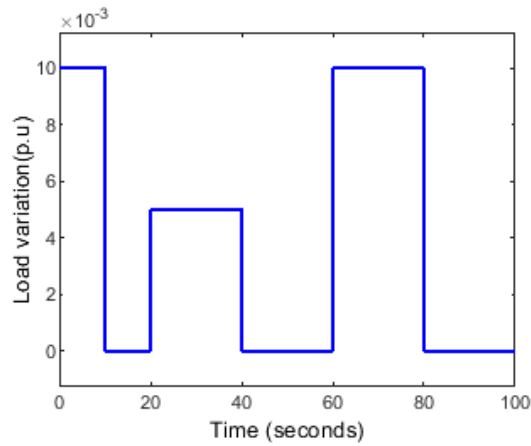


Figure 2.19. Deviation in random load.

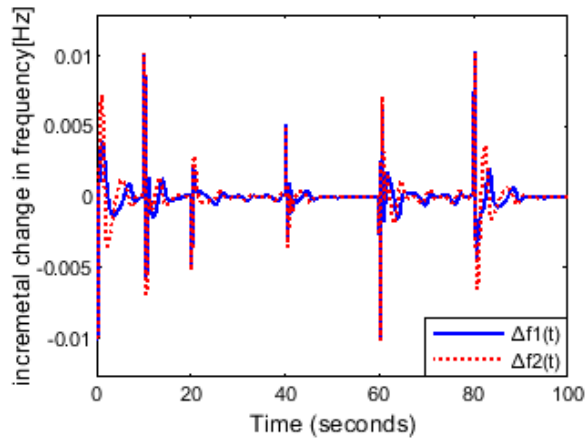


Figure 4.20. Frequency variations [Hz] in area-1 and area-2.

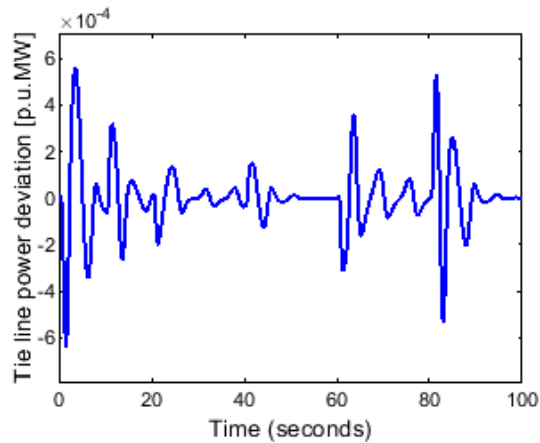


Figure 4.21. Change in tie-line power [p.u.MW].

Figure 4.20 shows the frequency variation in both locations, while Figure 4.21 shows the TLPD. By rejecting different disturbances and maintaining their frequency at the operating acceptable point while also effectively managing the TLPD, the

suggested SPSMCBSO was able to retain better resilience.

Remark 4.6. The response of the TAGHTPS has been subjected to simulations involving step load disturbances and random load variations, with the purpose of comparing it to the optimal controller presented in (Gupta Nidhi et al., 2022). The results of these simulations have demonstrated improvements. Nevertheless, LFC schemes are expected to exhibit robustness across a diverse range of disturbances. To address this requirement, the proposed SPSMCBSO scheme has been simulated under various challenging conditions. The results of these simulations affirm the robustness of the SPSMCBSO scheme as it effectively rejects these disturbances and maintains the stability of the TAGHTPS.

4.5.4 Simulation 4

To assess the computational efficiency of the SPSMCBSO scheme, the study has been extended to a more complex and realistic system, specifically a four-area multi-source PS. Each of these four areas (area-1, area-2, area-3, and area-4) is comprised of a combination of thermal, hydro, and gas power plants. The transfer function model for this test system is provided in Figure 4.1, with i equal to 4. In Figure 4.22 to 4.23, we present the comparative transient responses of the test simulation 4 following a 1% step load disturbance.

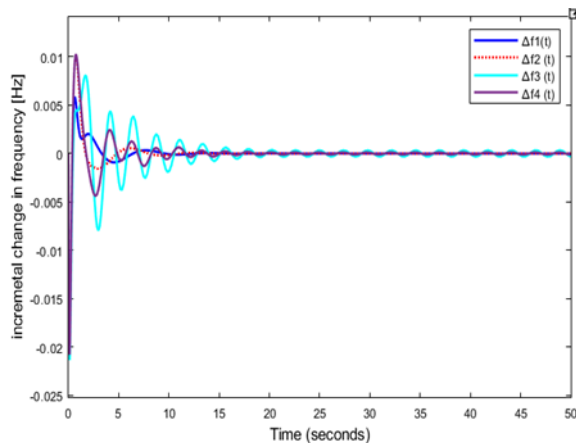


Figure 4.22. Frequency deviation [Hz] in four areas.

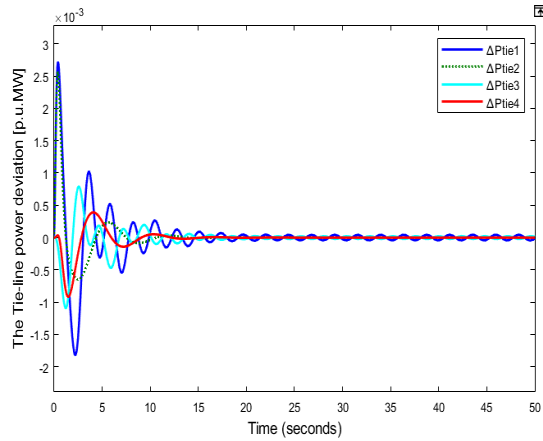


Figure 4.23. Changes in tie-line power [p.u.MW].

The optimal controller parameters, obtained through the proposed approach, are illustrated in Figure 4.22, showcasing the frequency variations across all four areas. Figure 4.23, on the other hand, displays the changes in tie-line power, providing insights into the system's response to the disturbance. Specifically, we take careful note of the typical transient criteria, such as peak undershoot and settling time of system oscillations, to effectively oversee and maintain the frequency within the permissible operating range. Additionally, we ensure that changes in the tie-line power are appropriately regulated in accordance with the suggested control scheme.

Remark 4.7: A sensitivity analysis spanning from simulation 1 to simulation 4 has been conducted to assess the advantages of the proposed SPSMCBSO scheme for LFC. In each case, settling times and the minimum under/overshoot values have been evaluated under both normal and varied conditions for the relevant PS. The results clearly demonstrate that performance values remain within acceptable limits and are nearly identical to the respective values obtained under nominal conditions. Therefore, it can be deduced that the benefits of the proposed controller are resilient to matched and mismatched disturbances, parameter variations, and it performs satisfactorily even when subjected to significant changes in both load conditions and system parameters. This performance outshines that observed in the prior studies (N. Hakimuddin, I. Nasiruddin, T.S. Hota, 2020) (Sahu, R. Kumar, P. Sidhartha, Rout, U. Kumar, Sahoo, D. Kumar, 2016) (G. Nidhi, K. Narendra, B. Chitti, 2019), (A. Dev, S. Anand, M.K Sarkar, 2021) (V. Patel, D. Guha, S. Purwar., 2020) (D. Guha,

P. K. Roy, S. Banerjee, , 2021).

4.5.5 Simulation 5

In this section, we conduct two separate simulations and subsequently analyze and compare the obtained results with recent findings from other studies. The FD arising from unmatched parameter uncertainties, including those associated with renewable energy sources as wind and varying load disturbances, a sliding mode LFC has been devised. This controller is designed by carefully choosing the suitable switching surfaces and defining the reaching law condition.

Case 1: In this scenario, we focus exclusively on the PS's response to step load disturbances and varying parameter values. To assess the PS's behavior when subjected to the new algorithm, we introduce step load changes with magnitudes of 0.015 per unit (p.u) for both area 1 and area 2, in conjunction with wind speed variations as depicted in Figure 4.24.

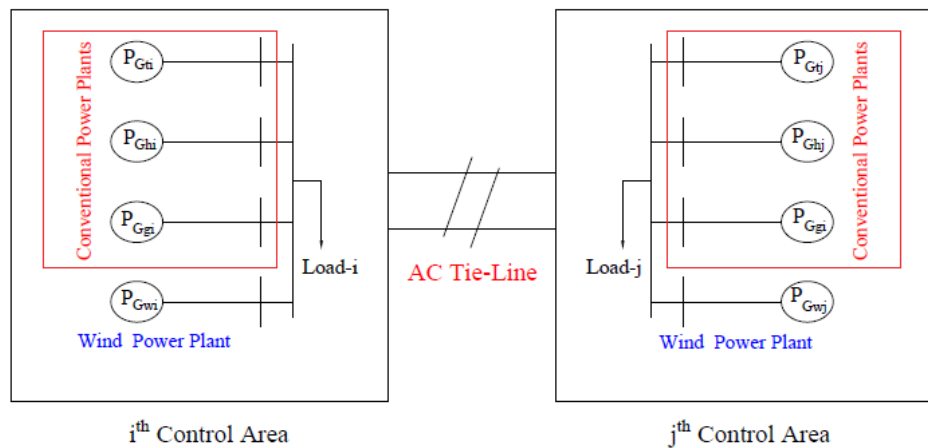


Figure 4.24. Two-area PS blocks schematic linked to a tie line

The proportion of wind energy in PS is on the rise that wind speed chart is displayed in Figures 4.25. However, the inherent fluctuations in renewable energy sources and variations in load can pose challenges for LFC.

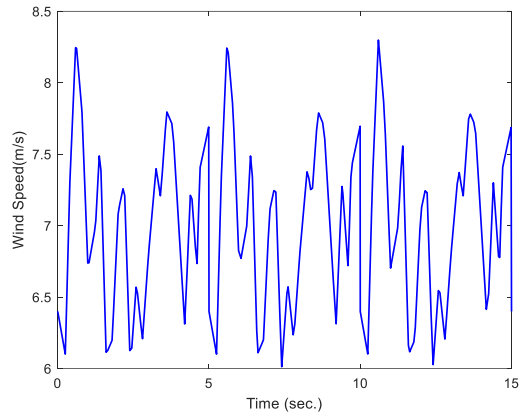


Figure 4.25. Wind speed chart (m/s).

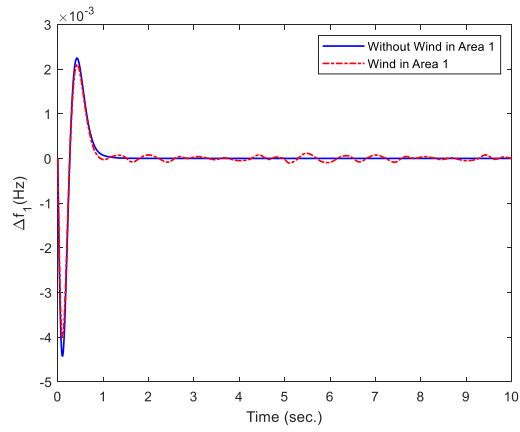


Figure 4.26. The frequency deviations [Hz] with 1.5% step load in area 1 without and with wind speed variation.

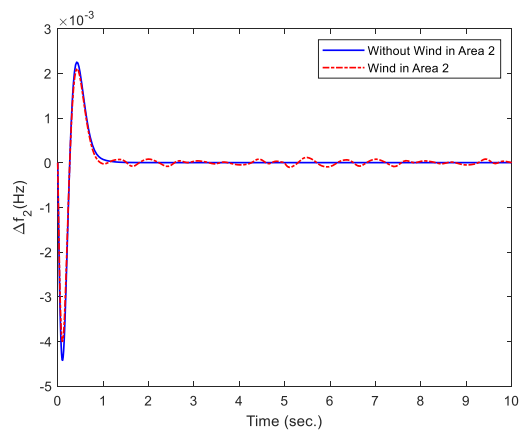


Figure 4.27. The frequency deviations [Hz] with 1.5% step load in area 2 without and with wind speed variation.

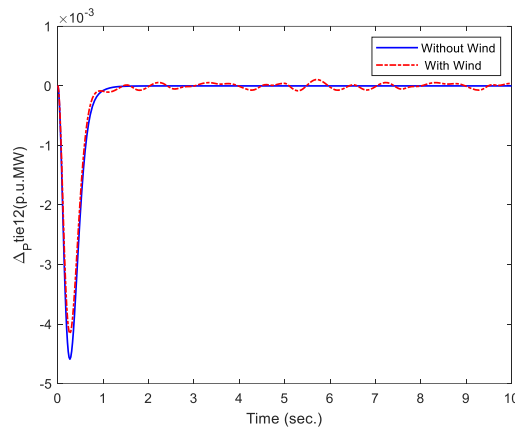


Figure 4.28. Tie line power deviation [p.u.MW].

In this case, the wind power generation model is added to the PS. Both wind power generation model output power and load are uncertain. The SPSMCBSO is tested by simulations of Figure 4.26, Figure 4.27 and 4.28 in both areas without and with wind speed variation, respectively. The wind speed model is shown in Figure 4.25. Figures 4.26 and 4.27 show that the system FD of the SPSMCBSO can be reduced. So, it can be concluded that the fluctuation is caused by renewable energy and load disturbances. But by making use of the designed disturbance observer, the chattering of the SMLFC can be reduced. So, it can be concluded that the fluctuation caused by renewable energy and load disturbances can be compensated effect through the designed SPSMCBSO.

Remark 4.8. The PS's response has shown notable improvements in terms of reduced overshoot and shorter settling times when subjected to step load disturbances and wind power variations. The simulation results affirm that the designed controller exhibits a faster response and enhanced stability. It is also more robust, effectively curbing FD.

Case 2: In real-world scenarios, continuous load demands from industries, households, and other sources are constant. Therefore, we introduced random load variations at 5 second intervals, as illustrated in Figure 4.29. When we conducted the simulation under these conditions, the incremental frequency, and tie-flow fluctuations for the two areas were analyzed, and the results are presented in Figure 4.30, Figure 4.31, and Figure 4.32, respectively. The outcomes of these simulations

confirm that the new controller maintains robustness and consistently corrects errors to zero at every interval without compromising control accuracy.

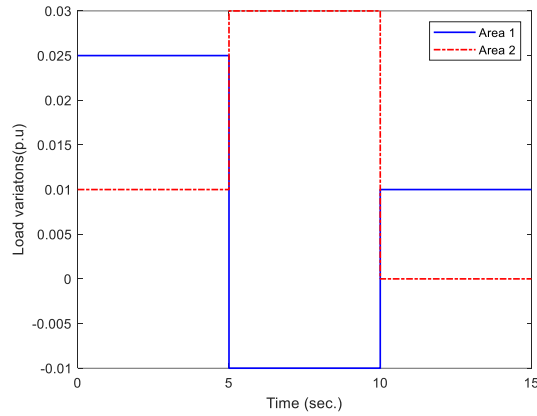


Figure 4.29. Random load (p.u) .

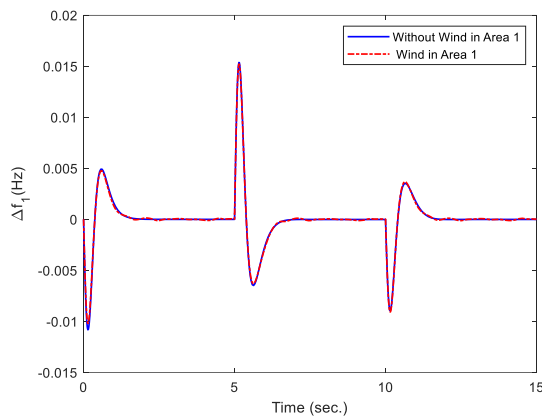


Figure 4.30. The frequency deviations [Hz] in area 1.

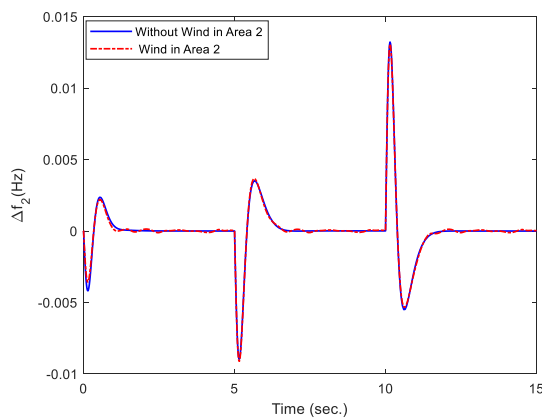


Figure 4.31. The frequency deviations [Hz] in area 2.

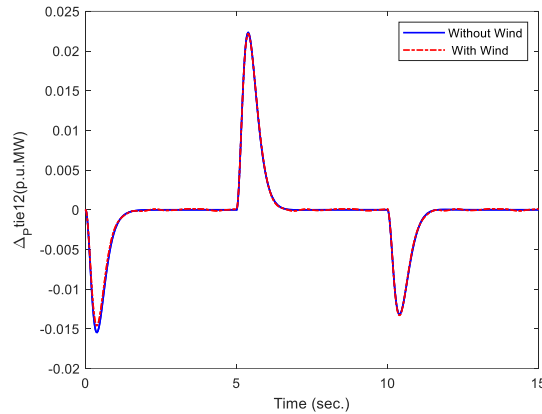


Figure 4.32. Tie-line power deviation.

Remark 4.10. The robustness of the new controller has been successfully demonstrated in the face of random load fluctuations and varying wind speeds. Furthermore, its practical applicability to real PS is evident from the reduced overshoots observed. These overshoots are small enough not to exert any significant effects that might lead to wear and tear of the actuator valve, thereby reinforcing the controller's effectiveness.

4.6. Conclusion of chapter 4

This chapter introduces a novel approach called the SPSMCBSO for LFC in MAMSPS. The practicality and effectiveness of the SPSMCBSO technique are evaluated using the TAGHTPS model, which incorporates uncertainties in both state variables and interconnected parameters. The stability of the TAGHTPS system is rigorously established through a novel LMI approach based on Lyapunov theory. Comparative analysis of simulation results against recent methods demonstrates the superior performance of the SPSMCBSO approach. It is evident that the application of the proposed SPSMCBSO technique significantly enhances TAGHTPS's performance, surpassing the outcomes of previously utilized methods. Moreover, the SPSMCBSO method displays robustness, remaining resilient in the face of subsystem parameter deviations, random load disturbances, and uncertainties in state variables and interconnected matrices, wind. Thus, by using MATLAB/SIMULINK simulation, the SPSMCBSO approach proves to be a highly valuable and effective tool for LFC in MAMSPS.

CHAPTER 5: SLIDING SURFACE DESIGN FOR SLIDING MODE LOAD FREQUENCY CONTROL OF MULTI AREA MULTI SOURCE POWER SYSTEM

In this chapter, a new LFC technique for a MASHPS with parameter uncertainty is proposed in this research. A second-order SMC via double integrated sliding surface is meant to improve MASHPS frequency regulation, tie-line power management, and dependability. This method not only develop the asymptotic stability and dependability of MASHPS, but it also reduces the chattering problem that is inherent in first order SMC. Furthermore, the new LMI based on Lyapunov stability is used to analyze the entire MASHPS stabilization. For the LFC study, the effective performance of the suggested technique is investigated in a two-area steam-hydropower system (TASHPS). Under parameter uncertainties and various assumed load disturbances (LDs) from households, commercial buildings, and industries, the proposed second-order SMC via double integral sliding surface (SOSDISS) proves to be highly robust and improves the MASHPS response in terms of frequency regulation, tie-line power management, and system reliability when compared to other existing proposed methods with less uncertainty consideration. Overall, the results indicate that the novel approach is feasible for MASHPS LFC and PS reliability.

To study a new LFC of a two-area steam-hydropower system (TASHPS), the principle of a double-integral sliding mode controller (DISMC) is used in a stand-alone photovoltaic system. A double integral SMC eliminates steady-state error by using the double integral of the tracking voltage error term on its sliding surface, in addition to offering robust control actions in the face of system uncertainties. Nevertheless, increased chattering and slower transient reaction remain a challenge with DISMC. The choice of the sliding surface in the first order has a substantial influence on the functioning of an SMC (Pradhan Raseswari et al., 2015). Therefore, the new LFC is approached with a proposed second-order SMC via double integral

sliding surface. The following are the research's significant contributions for the new double integral sliding surface is designed for the MASHPS's sliding mode LFC as follows:

- The proposed SOSDISS proves to be highly robust and improves the MASHPS response in terms of frequency regulation, tie-line power management, and system reliability of the MASHPS.
- The stability of the MASHPS is guaranteed under the new construction of sliding mode dynamic theory and Lyapunov stability theory.
- In comparison to the recent SMC approach, the PS performance has improved in terms of reduced chattering.
- The proposed control strategy's performance is effective and reliable, as evidenced by its fast frequency responses and insensitivity to parameter changes, load disturbance, load variation, delay time, and the GDB and GRC nonlinearity effects on power network, IEEE 39 bus.

5.1. Dynamic model of multi-area steam-hydropower system

To improve the stability and reliability of a multi-area steam-hydropower system (MASHPS), an LFC is needed. The LFC of the i^{th} area multi-source PS, which includes a reheated thermal power plant and a hydroelectric power plant and is presented in Figure 5.1. Both PS components are modelled and represented in their transfer functions together with the closed-loop LFC.

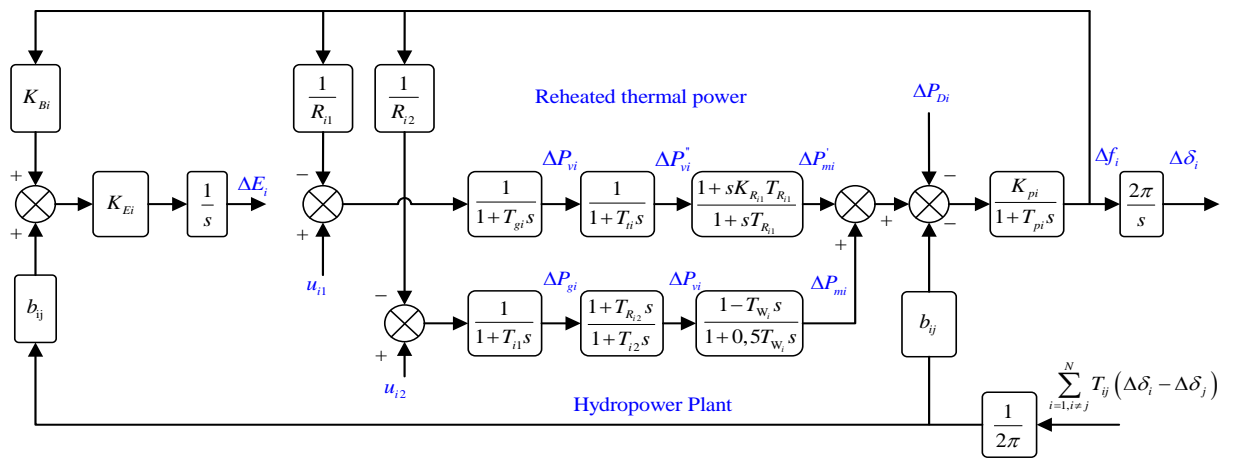


Figure 5.1. Schematic diagram of a 1-zone-2 sources included thermal power plants using heat recovery turbines & hydropower plant.

The PS is modeled in the state-space form by the first representing the system dynamics as follows Equation (5.1) to Equation (5.9) in Appendix 5.1. Therefore, we can represent the above dynamics in the state-space form below.

$$\dot{x}_i(t) = \bar{A}_{ki}x_i(t) + \bar{B}_{ki}u_i(t) + \sum_{\substack{i=1 \\ j \neq i}}^N \bar{H}_{kij}x_j + \bar{F}_i\Delta\bar{P}_{Dki}(t) \quad (5.10)$$

Where $x_i(t) = [\Delta f_i(t) \ \Delta P_{mi}(t) \ \Delta P_{vi}(t) \ \Delta P_{gi}(t) \ \Delta E_i(t) \ \Delta \delta_i(t) \ \Delta P'_{mi}(t) \ \Delta P''_{vi}(t) \ \Delta P'_{vi}(t)]^T$ and $x_i(t) \in R^{n_i}$ is the vector of state, $u_i(t) \in R^{m_i}$ is the input control vector, $x_j(t) \in R^{n_j}$ is the neighboring state vector of $x_i(t)$, n_i is the area's total number of state variables. of i^{th} area, m_i is the area's total number of controls the input variables of the i^{th} area. $A_{ki} \in R^{n_i \times n_i}$, $B_{ki} \in R^{n_i \times m_i}$, $F_i \in R^{n_i \times k_i}$ and H_{kij} are the nominal parameter system matrices in Appendix 5.2.

In practical PN, uncertainties can be experienced either in the difference of rotor angle change of each generator which impact on the system inertia time constant of the PS. These are considered and represented in the system matrices and the control input, as shown bellowing as

$$\begin{aligned} \dot{x}_i(t) = & [\bar{A}_{ki} + \Theta_{ki}(x_i, t)]x_i(t) + \bar{B}_{ki}[u_i(t) + \xi_{ki}(x_i, t)] + \sum_{\substack{j=1 \\ j \neq i}}^N [\bar{H}_{kij} + \Xi_{kij}(x_j, t)]x_j(t) \\ & + \bar{F}_i\Delta\bar{P}_{Dki}(t) \end{aligned} \quad (5.11)$$

where $\Theta_{ki}(x_i, t)$ is the time varying parameter uncertainty in the state matrix, $\Xi_{kij}(x_j, t)$ is the interconnected matrix's time-varying parameter uncertainty and $\xi_{ki}(x_i, t)$ is the disturbance input. If we simply uncertainties in equation (5.11), we can get that:

$$L_{ki}(x_i, t) = \Theta_{ki}(x_i, t)x_i(t) + \bar{B}_{ki}\xi_{ki}(x_i, t) + \sum_{\substack{j=1 \\ j \neq i}}^N \Xi_{kij}(x_j, t)x_j(t) + \bar{F}_i\Delta\bar{P}_{kDi}(t) \quad (5.12)$$

So, the state-space form of (5.12) can then be rewritten as

$$\dot{x}_i(t) = \bar{A}_{ki}x_i(t) + \bar{B}_{ki}u_i(t) + \sum_{\substack{j=1 \\ j \neq i}}^N \bar{H}_{kij}x_j(t) + \bar{L}_{ki}(x_i, t) \quad (5.13)$$

where $\bar{L}_{ki}(x_i, t)$ represents the aggregate uncertainties which consists of the matched and mismatched parts. An assumption is made and formulated coupled with a given Lemma to handle the aggregate uncertainties for the LFC of MASHPS (5.13) as follows.

Assumption 5.1: The assumption is aggregated disturbance $\bar{L}_{ki}(x_i, t)$ and the differential of $\dot{\bar{L}}_{ki}(x_i, t)$ is bounded such that $\|\bar{L}_{ki}(x_i, t)\| \leq \gamma_i$ and $\|\dot{\bar{L}}_{ki}(x_i, t)\| \leq \bar{\gamma}_i$.

Where γ_i and $\bar{\gamma}_i$ are the positive scalars and $\|\cdot\|$ is the matrix norm.

Lemma 5.1 (Huynh Van Van et al., 2021): Let $\tilde{\mathbf{X}}$ and $\tilde{\mathbf{Y}}$ are realistic, suitable-dimension matrices, then, for any scalar $\mu > 0$, the sequent matrix inequality obtains.

$$\tilde{\mathbf{X}}^T \tilde{\mathbf{Y}} + \tilde{\mathbf{Y}}^T \tilde{\mathbf{X}} \leq \mu \tilde{\mathbf{X}}^T \tilde{\mathbf{X}} + \mu^{-1} \tilde{\mathbf{Y}}^T \tilde{\mathbf{Y}} \quad (5.14)$$

Remark 5.1: The multi-area interconnection's current sliding mode control approach for LFC. The establishment of PS is predicated on the assumption that the standard would be followed. In (Mi Yang et al. , 2013), (Mi Yang et al., 2016), the majority of the aggregated uncertainty is confined by a positive constant.

5.2. New double integral sliding surface design

SMC based techniques have been applied for the LFC of IMAPS under a wide range of LDs given in (Su Xiaojie et al., 2017), (Mi Yang et al. , 2013), (Onyeka Adrian E et al. , 2020).The stability of the PS is determined by the sliding surface of the SMC (Huynh Van Van et al., 2021), (Alhelou Hassan Haes et al., 2018). Therefore, a new double integral sliding surface has been designed as given.

$$\begin{aligned} \sigma_{ki}[x_i(t)] &= P_{ki}x_i(t) \\ &- \int_0^t P_{ki}(\bar{A}_{ki} - \bar{B}_{ki}\Lambda_{ki})x_i(\tau)d\tau - \int_0^t \int_0^\tau P_{ki}(\bar{A}_{ki} - \bar{B}_{ki}\Lambda_{ki})x_i(\tau)d\tau d\tau \end{aligned} \quad (5.15)$$

where P_{ki} is the constant matrix and Λ_{ki} is the design matrix, matrix P_{ki} is

chosen in order to ensure that matrix $P_{ki} \bar{B}_{ki}$ is nonsingular. The design matrix $\Lambda_{ki} \in R^{m_i \times n_i}$ is chosen to satisfy the PS's inequality criterion (5.9).

$$\text{Re}[\lambda_{\max}(A_{ki} - B_{ki} \Lambda_{ki})] < 0 \quad (5.16)$$

To determine the equivalent control, we differentiate $\sigma_{ki}[x_i(t)]$ with respect to time as follows:

$$\begin{aligned} \dot{\sigma}_i[x_i(t)] = & P_i[\bar{A}_{ki}x_i(t) + \bar{B}_{ki}u_i(t) + \sum_{\substack{j=1 \\ j \neq i}}^N \bar{H}_{kij}x_j(t) + \bar{L}_{ki}(x_i, t)] - P_{ki}(\bar{A}_{ki} - \bar{B}_{ki}\Lambda_{ki})x_i(t) \\ & - \int_0^t P_{ki}(\bar{A}_{ki} - \bar{B}_{ki}\Lambda_{ki})x_i(\tau)d\tau \end{aligned} \quad (5.17)$$

So, by equating $\sigma_i[x_i(t)] = \dot{\sigma}_i[x_i(t)] = 0$. After that, the equivalent control is expressed by.

$$\begin{aligned} u_i^{eq}(t) = & -(P_{ki}\bar{B}_{ki})^{-1}[P_{ki}\bar{A}_{ki}x_i(t) + \sum_{\substack{j=1 \\ j \neq i}}^N P_{ki}\bar{H}_{kij}x_j(t) + P_{ki}\bar{L}_{ki}(x_i, t) \\ & - P_{ki}(\bar{A}_{ki} - \bar{B}_{ki}\Lambda_{ki})x_i(t) - \int_0^t P_{ki}(\bar{A}_{ki} - \bar{B}_{ki}\Lambda_{ki})x_i(\tau)d\tau] \end{aligned} \quad (5.18)$$

To close the loop system, we substitute $u_i^{eq}(t)$ into the equation (5.13) to yield the PS in the sliding motion with the following.

$$\begin{aligned} \dot{x}_i(t) = & (\bar{A}_{ki} - \bar{B}_{ki}\Lambda_{ki})x_i(t) + [I_i - \bar{B}_{ki}(P_{ki}B_{ki})^{-1}P_{ki}]\bar{L}_{ki}(t) + \sum_{\substack{j=1 \\ j \neq i}}^N [I_i - \bar{B}_{ki}(P_{ki}\bar{B}_{ki})^{-1}P_{ki}]\bar{H}_{kij}x_j(t) \\ & + \int_0^t \bar{B}_{ki}(P_{ki}\bar{B}_{ki})^{-1}P_{ki}(\bar{A}_{ki} - \bar{B}_{ki}\Lambda_{ki})x_i(\tau)d\tau \end{aligned} \quad (5.19)$$

Supporting that

$$\bar{z}_i(t) = \int_0^t x_i(\tau)d\tau; \quad \tilde{z}_i(t) = x_i(t) \quad (5.20)$$

To have

$$\dot{\tilde{z}}_i(t) = x_i(t) = \tilde{z}_i(t); \quad (5.21)$$

and

$$\begin{aligned}
\dot{\tilde{z}}_i(t) &= (\bar{A}_{ki} - \bar{B}_{ki}\Lambda_{ki})\tilde{z}_i(t) + [I_i - \bar{B}_{ki}(P_{ki}\bar{B}_{ki})^{-1}P_{ki}]\bar{L}_{ki}(t) \\
&+ \sum_{\substack{j=1 \\ j \neq i}}^N [I_i - \bar{B}_i(P_{ki}\bar{B}_{ki})^{-1}P_{ki}]\bar{H}_{kij}\tilde{z}_j(t) \\
&+ \bar{B}_{ki}(P_{ki}\bar{B}_{ki})^{-1}P_{ki}(\bar{A}_{ki} - \bar{B}_{ki}\Lambda_{ki})\bar{z}_i(t)
\end{aligned} \tag{5.22}$$

The above equation can be rewritten as

$$\begin{aligned}
\dot{\hat{z}}_i(t) &\equiv \begin{bmatrix} 0 & I \\ \bar{B}_{ki}(P_{ki}\bar{B}_{ki})^{-1}P_{ki}(\bar{A}_{ki} - \bar{B}_{ki}\Lambda_{ki}) & (\bar{A}_{ki} - \bar{B}_{ki}\Lambda_{ki}) \end{bmatrix} \hat{z}_i(t) + \begin{bmatrix} 0 \\ [I_i - \bar{B}_{ki}(P_{ki}\bar{B}_{ki})^{-1}P_{ki}] \end{bmatrix} \bar{L}_{ki}(t) \\
&+ \sum_{\substack{j=1 \\ j \neq i}}^N \begin{bmatrix} 0 & 0 \\ 0 & [I_i - B_{ki}(P_{ki}\bar{B}_{ki})^{-1}P_{ki}]\bar{H}_{kij} \end{bmatrix} \begin{bmatrix} \bar{z}_j(t) \\ \tilde{z}_j(t) \end{bmatrix}
\end{aligned} \tag{5.23}$$

and

$$\dot{\hat{z}}_i(t) = \tilde{A}_{ki}\hat{z}_i(t) + \tilde{F}_i\bar{L}_{ki}(t) + \sum_{\substack{j=1 \\ j \neq i}}^N \tilde{H}_{kij}\hat{z}_j(t) \tag{5.24}$$

$$\text{where } \hat{z}_i(t) = \begin{bmatrix} \bar{z}_i(t) \\ \tilde{z}_i(t) \end{bmatrix}, \tilde{F}_i = \begin{bmatrix} 0 \\ [I_i - B_{ki}(P_{ki}\bar{B}_{ki})^{-1}P_{ki}] \end{bmatrix},$$

$$\tilde{A}_{ki} = \begin{bmatrix} 0 & I \\ B_{ki}(P_{ki}\bar{B}_{ki})^{-1}P_{ki}(A_{ki} - B_{ki}\Lambda_{ki}) & (A_{ki} - B_{ki}\Lambda_{ki}) \end{bmatrix}, \text{ and}$$

$$\tilde{H}_{kij} = \begin{bmatrix} 0 & 0 \\ 0 & [I_i - B_{ki}(P_{ki}\bar{B}_{ki})^{-1}P_{ki}]H_{kij} \end{bmatrix}.$$

The above PS (5.24) is stable, which depends on the eigenvalue of the system matrices and the careful selection of the constant matrix gain P_i and design matrix gain Λ_i of the proposed equivalent control input. Furthermore, we analyze the stability of the PS using Lyapunov theory through LMI. To do this, we state the theorem as follows.

Theorem 5.1: The sliding motion (5.24) is asymptotically stable if and only if there are symmetric positive definite matrices $M_{ki}, i = 1, 2, \dots, N$, and positive scalars $\hat{\varepsilon}_i, \varepsilon_i, \delta_j$ and β_i and the following LMIs are obtained.

$$\begin{bmatrix} \tilde{A}_{ki}^T M_{ki} + M_{ki} \tilde{A}_{ki} + \sum_{\substack{j=1 \\ j \neq i}}^N \delta_j^{-1} \tilde{H}_{kji}^T \tilde{H}_{kji} & M_{ki} & M_{ki} \tilde{F}_i & M_{ki} \tilde{F}_i \\ & M_{ki} & -\hat{\varepsilon}_i^{-1} & 0 & 0 \\ & \tilde{F}_i^T M_{ki} & 0 & -\varepsilon_i & 0 \\ & \tilde{F}_i^T M_{ki} & 0 & 0 & -\beta_i \end{bmatrix} < 0 \quad (5.25)$$

Proof 5.1: To analyze the stability of (5.19), we apply Lyapunov stability theory so that the Lyapunov function is given as

$$V = \sum_{i=1}^N \hat{z}_i^T(t) M_{ki} \hat{z}_i(t) \quad (5.26)$$

where $M_{ki} > 0$ satisfies (5.26). Then, a time derivative of (5.26) and substitute equation (5.19), we have

$$\begin{aligned} \dot{V} &= \sum_{i=1}^N \dot{\hat{z}}_i^T(t) M_{ki} \hat{z}_i(t) + \hat{z}_i^T(t) M_{ki} \dot{\hat{z}}_i(t) \\ &= \sum_{i=1}^N \{ \hat{z}_i^T(t) [\tilde{A}_{ki}^T M_{ki} + M_{ki} \tilde{A}_{ki}] \hat{z}_i(t) + \sum_{\substack{j=1 \\ j \neq i}}^N \hat{z}_j^T(t) \tilde{H}_{kij}^T M_{ki} \hat{z}_i(t) \\ &\quad + \sum_{\substack{j=1 \\ j \neq i}}^N \hat{z}_i^T(t) M_{ki} \tilde{H}_{kij} \hat{z}_j(t) + \hat{z}_i^T(t) M_{ki} \tilde{F}_i \bar{L}_i(t) + \bar{L}_i^T(t) \tilde{F}_i^T M_{ki} \hat{z}_i(t) \} \end{aligned} \quad (5.27)$$

Using Lemma 5.1 to solve equation (5.27), we have.

$$\begin{aligned} \dot{V} &\leq \sum_{i=1}^N \{ \hat{z}_i^T(t) [\tilde{A}_{ki}^T M_{ki} + M_{ki} \tilde{A}_{ki}] \hat{z}_i(t) + \sum_{\substack{j=1 \\ j \neq i}}^N \hat{z}_j^T(t) \delta_i^{-1} \tilde{H}_{kij}^T \tilde{H}_{kij} \hat{z}_j(t) \\ &\quad + \sum_{\substack{j=1 \\ j \neq i}}^N \hat{z}_i^T(t) \delta_i M_{ki} M_{ki} \hat{z}_i(t) + \hat{z}_i^T(t) \beta_i^{-1} M_{ki} \tilde{F}_i \tilde{F}_i^T M_{ki} \hat{z}_i(t) \\ &\quad + \beta_i \bar{L}_i^T(x_i, t) \bar{L}_i(x_i, t) \} \end{aligned} \quad (5.28)$$

since

$$\sum_{i=1}^N \sum_{\substack{j=1 \\ j \neq i}}^N \hat{z}_j^T(t) \delta_i^{-1} \tilde{H}_{kij}^T \tilde{H}_{kij} \hat{z}_j(t) = \sum_{i=1}^N \sum_{\substack{j=1 \\ j \neq i}}^N \hat{z}_i^T(t) \delta_j^{-1} \tilde{H}_{kji}^T \tilde{H}_{kji} \hat{z}_i(t)$$

To be achieved that.

$$\begin{aligned} \dot{V} \leq & \sum_{i=1}^N \{ \hat{z}_i^T(t) [\tilde{A}_{ki}^T M_{ki} + M_{ki} \tilde{A}_{ki} + \hat{\varepsilon}_i M_{ki} M_{ki} \\ & + \beta_i^{-1} M_{ki} \tilde{F}_i \tilde{F}_i^T M_{ki} + \sum_{\substack{j=1 \\ j \neq i}}^N \delta_j^{-1} \tilde{H}_{kji}^T \tilde{H}_{kji}] \hat{z}_i(t) + \sum_{i=1}^N \varphi_i \end{aligned} \quad (5.29)$$

where $\hat{\varepsilon}_i = \delta_i(N-1)$ and $\varphi_i = \beta_i \gamma_i^2$.

Furthermore, the Schur complement, the LMIs (5.29) is equivalent to this inequality.

$$\begin{aligned} \dot{V} \leq & \sum_{i=1}^N \{ \hat{z}_i^T(t) [\tilde{A}_{ki}^T M_i + M_{ki} \tilde{A}_{ki} + \hat{\varepsilon}_i M_{ki} M_{ki} + \beta_i^{-1} M_{ki} \tilde{F}_i \tilde{F}_i^T M_{ki} \\ & + \sum_{\substack{j=1 \\ j \neq i}}^N \delta_j^{-1} \tilde{H}_{kji}^T \tilde{H}_{kji}] \hat{z}_i(t) + \sum_{i=1}^N \mu_i \end{aligned} \quad (5.30)$$

According to the equations (5.29) and (5.30), we obtain.

$$\dot{V} \leq \sum_{i=1}^N [-\lambda_{\min}(\Psi_{ii}) \|\hat{z}_i(t)\|^2 + \varphi_i] \quad (5.31)$$

where φ_i is the constant value and the eigenvalue $\lambda_{\min}(\Psi_i) > 0$. So, $\dot{V} < 0$ is made possible by $\|\hat{z}_i(t)\| > \sqrt{\frac{\varphi_i}{\lambda_{\min}(\Psi_i)}}$. As a result, the system's (5.19) sliding motion is asymptotically stable.

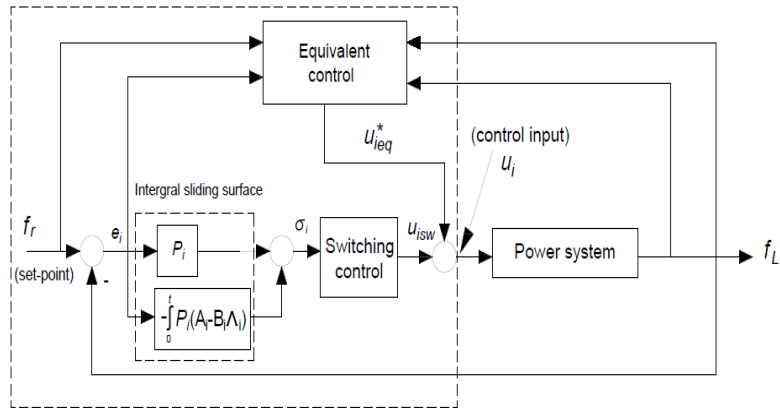


Figure 5.2. Simple diagram of traditional integral sliding surface.

Remark 5.2: The block diagrams of the aforesaid control techniques are shown in Figure 5.2 and Figure 5.3 to highlight the differences and improvements of

the control methods, which include classic integral SMC. The SMC using the traditional integral sliding surface results with the PI switching surface in (Guo Jianping, 2019), (Bui Le Ngoc Minh et al., 2018), (Liao Kai and Yan Xu. , 2017), (Mi Yang et al., 2016). First, a LFC for multi-area linked PS is created using a second-order double integral sliding mode control approach that overcomes the aforementioned constraint. Second, a double integral sliding surface-based second order sliding mode controller (SOSDISS) is presented to improve the closed-loop system's transient performance. However, in LFC techniques, the bound of the aggregated uncertainty of the MAPS is typically unknown in advance. As a result, determining the appropriate control parameter to keep the system state within the boundary layer is difficult. Furthermore, the above approaches have some limitations, such as the fact that disturbances are not truncated from the output points in steady state and controller gains are not set to be high to reduce disturbances of unknown boundaries and even parameter uncertainties or load variation. The SOSDISS prevents the system from fluctuating and may also reset the system to its set point.

Remark 5.3: Under matched uncertainties, SMC based on first-order double integral surfaces can be utilized to investigate the LFC of a PS in (Pradhan Raseswari et al., 2015). However, in a real power network, parametric uncertainties do not always meet the matching condition. As a result, certain major limitations are required to build the first-order SMC to correct for uncertainties, which can guarantee nominal frequency convergence and system stability, but system trajectories cannot reach the origin point. As a result, the second-order double sliding surface approach is presented as a way to push the system trajectory to an analogous point and improve transient performance.

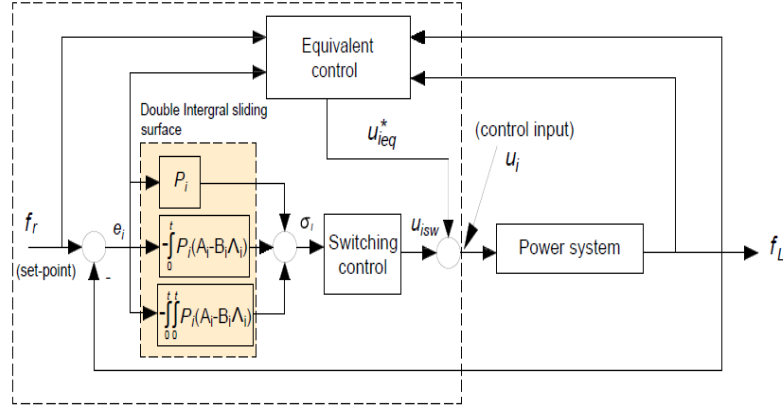


Figure 5.3. Simple diagram of the double integral sliding surface.

5.3. Decentralized continuous control law.

In this segment, the suggested decentralized second-order SMC law is suggested for LFC of the PS (5.19). The construction is done by simply making $\sigma_{ki}[x_i(t)]$ and $\dot{\sigma}_{ki}[x_i(t)]$ equal to zero (i.e., known as the sliding manifold) so that PS stability is improved.

In other words, the sliding manifold is defined and established $\Theta_{ki}[\hat{z}_i(t)]$ as

$$\Theta_{ki}(t) = \dot{\sigma}_{ki}[x_i(t)] + \gamma_i \sigma_{ki}[x_i(t)] \quad (5.32)$$

and

$$\dot{\Theta}_{ki}(t) = \ddot{\sigma}_{ki}[x_i(t)] + \gamma_i \dot{\sigma}_{ki}[x_i(t)] \quad (5.33)$$

where $\gamma_i > 0$ is a positive constant. According to the formula (5.13), the equation (5.33) can be rewritten as

$$\begin{aligned} \dot{\Theta}_{ki}(t) = & P_{ki}[\bar{A}_{ki}\dot{x}_i(t) + \bar{B}_{ki}\dot{u}_i(t) + \sum_{\substack{j=1 \\ j \neq i}}^N \bar{H}_{kij}\dot{x}_j(t) + \dot{L}_{ki}(x_i, t)] - P_{ki}(\bar{A}_{ki} - \bar{B}_{ki}\Lambda_{ki})\dot{x}_i(t) \\ & - P_{ki}(\bar{A}_{ki} - \bar{B}_{ki}\Lambda_{ki})x_i(t) + \gamma_i \dot{\sigma}_{ki}[x_i(t)] \end{aligned} \quad (5.34)$$

If the sliding manifold is made equal to zero, then the proposed decentralized SMC is given as

$$\begin{aligned}
\dot{u}_i(t) = & -(P_{ki}\bar{B}_{ki})^{-1} \{ \|P_{ki}\| \|\bar{A}_{ki}\| \|\dot{x}_i(t)\| + \sum_{\substack{j=1 \\ j \neq i}}^N \|P_{kj}\| \|\bar{H}_{kji}\| \|\dot{x}_i(t)\| \\
& + \|P_{ki}\| \|\bar{B}_{ki}\Lambda_{ki} - \bar{A}_{ki}\| \|\dot{x}_i(t)\| + \|P_{ki}\| \|\bar{B}_{ki}\Lambda_{ki} - \bar{A}_{ki}\| \|x_i(t)\| \\
& + \gamma_i \|\dot{\sigma}_{ki}[x_i(t)]\| + \|P_{ki}\| \|\bar{\gamma}_i + \nu_i\| \} \frac{\Theta_{ki}^T(t)}{\|\Theta_{ki}(t)\|}
\end{aligned} \tag{5.35}$$

To satisfy the above proposed control input (5.35), the system variables trajectories must be forcefully driven to the sliding manifold (SM) and remain therein at finite reaching time to ensure the PS's asymptotic stability (5.19) asymptotic stability. Therefore, we again analyze the stability of the system by the given theorem.

Theorem 5.2: Consider the PS's closed loop (5.19) with the controller for continuous sliding mode (5.35). Following that, each solution trajectory is pointed at the SM $\Theta_i(t) = 0$ and once the trajectory hits the SM $\Theta_i(t) = 0$ it remains on the SM thereafter.

Proof 5.2: As shown below, Lyapunov's function is introduced.

$$\bar{V}(t) = \sum_{i=1}^N \|\Theta_i(t)\| \tag{5.36}$$

Hence, using a derivation of $\bar{V}(t)$ then we get

$$\begin{aligned}
\dot{\bar{V}} &= \sum_{i=1}^N \frac{\Theta_i^T(t)}{\|\Theta_i(t)\|} \dot{\Theta}_i(t) \\
&= \sum_{i=1}^N \frac{\Theta_i^T(t)}{\|\Theta_i(t)\|} \{ P_i [A_i \dot{x}_i(t) + B_i \dot{u}_i(t) + \sum_{\substack{j=1 \\ j \neq i}}^N H_{ij} \dot{x}_j(t) \\
&\quad + \dot{L}_i(x_i, t)] - P_i (A_i - B_i \Lambda_i) \dot{x}_i(t) - P_i (A_i - B_i \Lambda_i) x_i(t) \\
&\quad + \gamma_i \dot{\sigma}_i[x_i(t)] \} \\
&= \sum_{i=1}^N \frac{\Theta_i^T(t)}{\|\Theta_i(t)\|} \{ P_i A_i \dot{x}_i(t) + P_i B_i \dot{u}_i(t) + \sum_{\substack{j=1 \\ j \neq i}}^N P_i H_{ij} \dot{x}_j(t) \\
&\quad + P_i \dot{L}_i(x_i, t) + P_i (B_i \Lambda_i - A_i) \dot{x}_i(t) + P_i (B_i \Lambda_i - A_i) x_i(t) \\
&\quad + \gamma_i \dot{\sigma}_i[x_i(t)] \}
\end{aligned} \tag{5.37}$$

According to the equation (5.29) as well as property $\|AB\| \leq \|A\| \|B\|$, it

produces.

$$\begin{aligned}
\dot{\bar{V}} \leq & \sum_{i=1}^N \{ \|P_i\| \|A_i\| \|\dot{x}_i(t)\| + \sum_{\substack{j=1 \\ j \neq i}}^N \|P_i\| \|H_{ij}\| \|\dot{x}_j(t)\| \\
& + \|P_i\| \|(B_i \Lambda_i - A_i)\| \|\dot{x}_i(t)\| + \|P_i\| \|(B_i \Lambda_i - A_i)\| \|x_i(t)\| \\
& + \gamma_i \|\dot{\sigma}_i[x_i(t)]\| + \|P_i\| \|\dot{L}_i(x_i, t)\| \} + \sum_{i=1}^N \frac{\Theta_i^T(t)}{\|\Theta_i(t)\|} P_i B_i \dot{u}_i(t)
\end{aligned} \tag{5.38}$$

$$\text{The term } \sum_{i=1}^N \sum_{\substack{j=1 \\ j \neq i}}^N \|P_i\| \|H_{ij}\| \|\dot{x}_j(t)\| = \sum_{i=1}^N \sum_{\substack{j=1 \\ j \neq i}}^N \|P_j\| \|H_{ji}\| \|\dot{x}_i(t)\|$$

and Assumption 5.1 we get.

$$\begin{aligned}
\dot{\bar{V}} \leq & \sum_{i=1}^N \{ \|P_i\| \|A_i\| \|\dot{x}_i(t)\| + \sum_{\substack{j=1 \\ j \neq i}}^N \|P_j\| \|H_{ji}\| \|\dot{x}_i(t)\| \\
& + \|P_i\| \|(B_i \Lambda_i - A_i)\| \|\dot{x}_i(t)\| + \|P_i\| \|(B_i \Lambda_i - A_i)\| \|x_i(t)\| \\
& + \gamma_i \|\dot{\sigma}_i[x_i(t)]\| + \|P_i\| \|\bar{\gamma}_i\| \} + \sum_{i=1}^N \frac{\Theta_i^T(t)}{\|\Theta_i(t)\|} P_i B_i \dot{u}_i(t)
\end{aligned} \tag{5.39}$$

When the control law (5.29) is applied, the following results are obtained:

$$\dot{\bar{V}} \leq -\sum_{i=1}^N \nu_i \tag{5.40}$$

The derivative of Lyapunov function (5.40) is less than or equal to zero, which implies that the system state variable trajectories are forcefully driven to the sliding manifold $S_i[x_i(t)] = 0$ to make the PS (5.19) to be asymptotically stable.

5.4. Case studies and simulation results.

In this part, the suggested second-order SMC via double integral sliding surface is put into practice for the LFC of a two-area steam-hydropower system (TASHPS) respectively. The LDs and aggregate uncertainties are included in the PS model for simulation. The effectiveness of the proposed method is assessed in comparison to conventional sliding mode LFC and robust LFC, utilizing MATLAB/SIMULINK software. The simulation results reveal that the designed LFC displays a faster response speed and superior robust performance when contrasted

with both the conventional sliding mode and robust LFC approaches. The objectives of the proposed approach for the LFC of TASHPS are to improve the stability of the PS, ensure the reliability of the power network and maintain the frequency at a tolerable point ± 0.5 Hz [17]. The proposed control strategy's performance is effective and reliable, as evidenced by its fast frequency responses and insensitivity to parameter changes, load disturbance, load variation, delay time, IEEE 39 bus and the GDB and GRC nonlinearity effects on power network. The proposed controller performance is validated when the simulation results are compared with recent methods, which are briefly discussed in three different simulations as follows.

5.4.1. Measurement model

Case 1: The LFC of TASHSP stability has been achieved by using different meta-heuristic optimization algorithms to optimize the fuzzy PID control parameters. A recent study was the application of grey wolf optimization (GWO) in (Srilekha J et al. , 2020). The proposed SMC is tested in a TASHPS with choosing the same step load disturbance and system parameters as in (Srilekha J et al. , 2020).

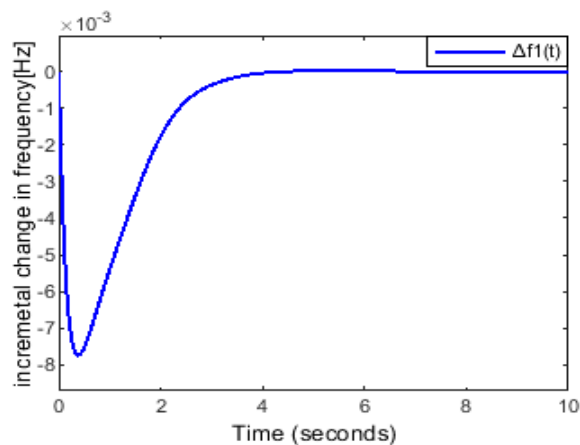


Figure 5.4. Frequency [Hz] of control area 1 under matched disturbances.

Figures 5.4 and 5.5 give the control area 1 and 2 frequency variations. The TASHPS tie-line power is shown in Figure 5.6. From the analysis of both results, both frequencies undershoot did not exceed the tolerable point of -0.5 Hz. Therefore, implies the proposed SMC is superior to the GWO based fuzzy PID method regarding control performance and Table 5.1 shows detailed summary of both controller's comparisons.

Table 5.1. Setting time T_s [s] and Maximum overshoot MOS [Hz] comparison.

Controller	The Proposed Method		Previous Method	
	T_s [s]	MOS [Hz]	T_s [s]	MOS [Hz]
Δf_1	4	0.0078	6	0.15
Δf_2	3.8	0.009	10	0.025

Source: created by author

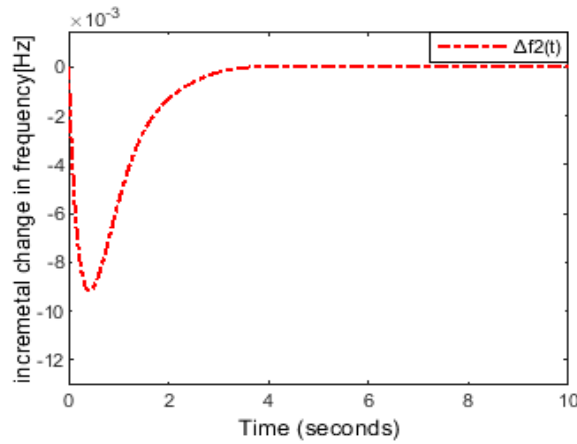


Figure 5.5. Frequency [Hz] of control area 2 under matched disturbances.

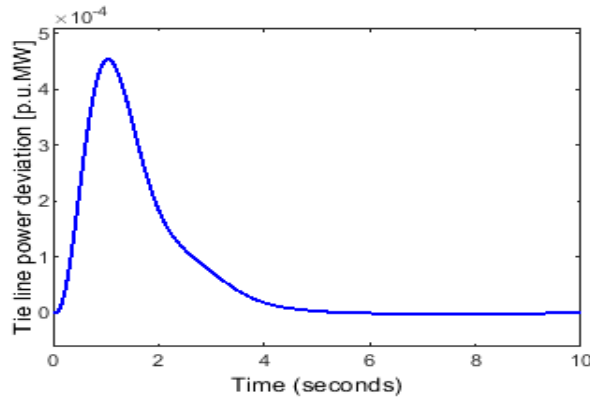


Figure 5.6. Tie line power deviation [p.u.MW] with matched disturbances.

The design gain matrices of the proposed SMC for area-1 and area-2 are used:

$$\Lambda_1 = \begin{bmatrix} 568 & 1004 & 1819 & 4876 & -248 & 549 & 1510 & 17 & 5 \\ 285 & 814 & 1531 & 13545 & 1655 & -2929 & 940 & 7 & 4 \end{bmatrix}$$

and

$$\Lambda_2 = \begin{bmatrix} 540 & 974 & 1786 & 4179 & 380 & -538 & 1473 & 16 & 5 \\ -89 & 186 & 419 & 10001 & -1857 & 3017 & 249 & 2 & 1 \end{bmatrix}$$

We design the constant gain matrix of the proposed SMC for each area as following below:

$$P_1 = \begin{bmatrix} 0 & 0 & 0 & 0 & 0 & 0 & 0 & 0 & 12.5000 \\ 0 & -0.7605 & 0.3802 & 0,0152 & 0 & 0 & 0 & 0 & 0 \end{bmatrix}$$

and

$$P_2 = \begin{bmatrix} 0 & 0 & 0 & 0 & 0 & 0 & 0 & 0 & 12.5000 \\ 0 & -0.7605 & 0.3802 & 0,0152 & 0 & 0 & 0 & 0 & 0 \end{bmatrix}$$

Remark 5.4: Notably, as can be seen in (J. Srilekha, C.N. Kalyan, G. Stanley, K. Suneetha, M.M. Thakreem, 2020), the new controller is more resilient to load disturbances and responds more quickly.

Case 2: Given this, we consider a change in the load demand from commercial business buildings in a metropolitan city. The commercial buildings load demand from control areas 1 and 2 of the TASHPS is given in (Srilekha J et al. , 2020). The demand curve is plotted and shown in Figure 5.7. As the demands change, as seen from the load curve, the dynamics responses of the TASHPS change.

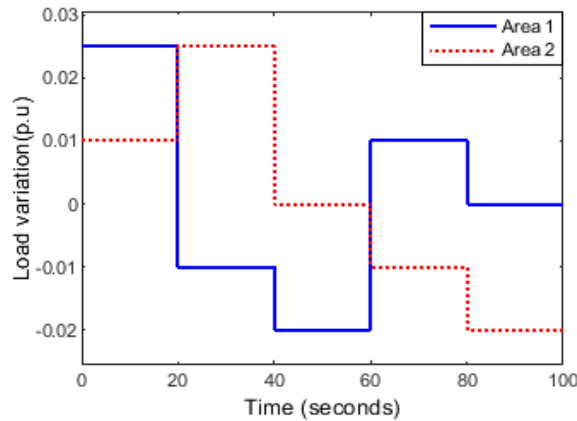


Figure 5.7. Daily load curve of commercial business buildings

Figure 5.8 shows the frequency variation of both control area 1 and control area 2 whereas Figure 5.7 illustrates the TASHPS tie-line power deviation. From the Figs, the TASHPS dynamics is improved with regard to far little under/overshoot and settling time, which did not exceed the tolerable point given in (Srilekha J et al. , 2020). This further makes the proposed method capable of handling LFC of large PS in order to keep the PS stable and reliable.

Remark 5.5: The SMC chattering issue is particularly harmful to the PS actuators. The suggested controller generates the correct signal and employs energy to make up for frequency damping in the primary control, which consists of a governor. As a consequence, the governor's droop control of speed will accurately activate the valve, supplying needed steam to the turbine to increase mechanical inertia power to match the load change or requirement. As a result, the setup time is short, and the overshoot is negligible.

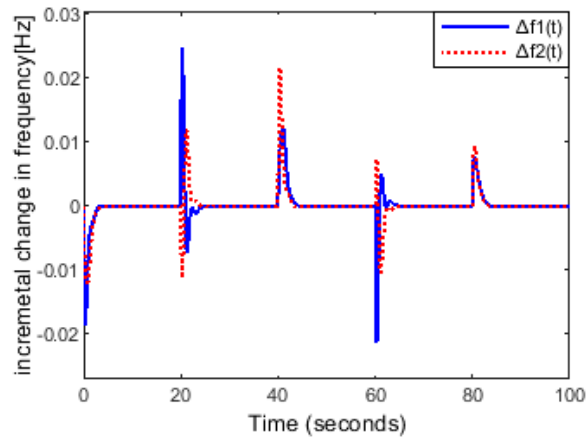


Figure 5.8. Control area 1 and control area 2 frequency deviation.

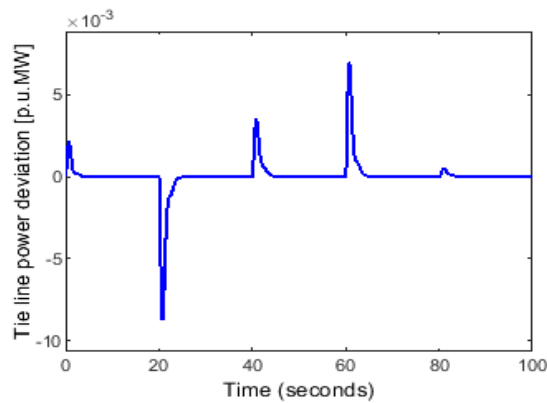


Figure 5.9. TASHPS tie line power deviation.

Case 3: Finally, we consider a more realistic problem in this case. The parameter uncertainties resulting from the different dynamic behaviors of the TASHPS which can impact the inertia time constant of the field gen sets are taken into account. The uncertainties with mismatch condition are represented in the state matrix of the PS as defined below with cosine functions given in (Huynh Van Van et al., 2021). Also, the variation in the demands of industrial activities is considered due

to frequency-sensitive loads. This industrial frequency sensitive load demand from area 1 and area 2 is conceptualized with practical knowledge and written in (Srilekha J et al. , 2020) and the load curve is shown as well in Figure 5.10, respectively. The proposed method parameter matrix gain is used in the same way as in the above cases discussed. We have the parameter uncertainties where in Appendix 5.2.

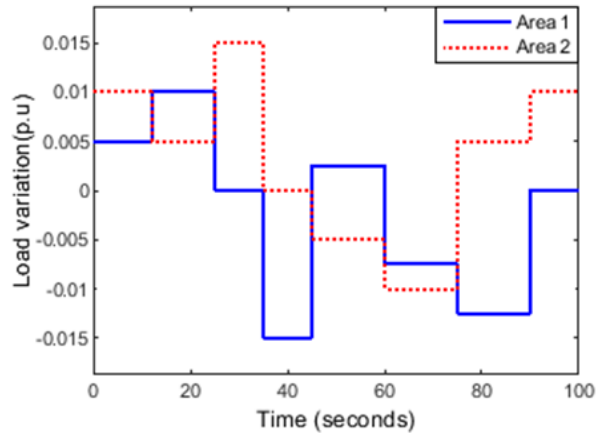


Figure 5.10. Load curve due to industrial activity-based frequency sensitive loads.

The frequency oscillation in control area 1 and control area 2 is shown in Fig. 11 while the tie-line power is presented in Figure 5.12.

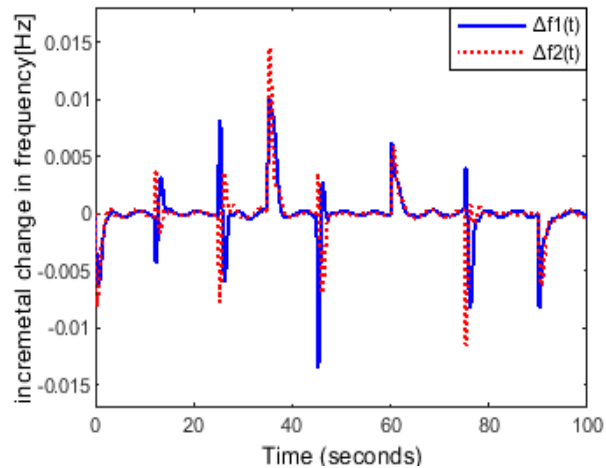


Figure 5.11. Area 1 and area 2 frequency deviation under mismatched conditions.

Fig11 demonstrates how the frequency variation did not exceed the tolerable level $\pm 0.5\text{Hz}$. The TASHPS tie-line power is properly managed within the schedule value as also seen in Figure 5.12. So, with the proposed method better control performance for the LFC of the TASHPS when compared with other methods, this

implies that it is very good for large power frequency regulation.

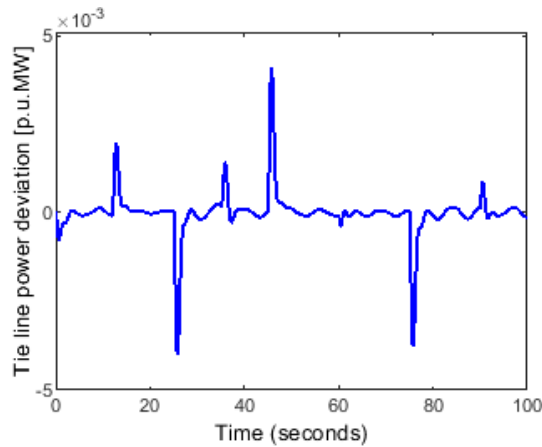


Figure 5.12. TASHPS tie line power deviation under mismatched conditions.

Remark 5.6: Using a double integral sliding surface based second order sliding mode controller, one of the most attainable goals in this proposed strategy is to finalize the mismatched disturbances and obtain a shorter settling time, lower transient deviation, and less oscillation in terms of LDs for the PS. As a result, various drawbacks of previous control systems discussed in journal paper (Srilekha J et al. , 2020) have been addressed, such as minimizing chattering and enhancing transient responsiveness.

5.4.2. Simulation 2:

Case 1: In this scenario, a larger and more realistic PS, the New England 10-generator 39-bus PS, is used to further evaluate the performance of the suggested LFC scheme. The New England test system consists of 10 generators, 39 buses, 09 loads, 34 lines for transmission, and twelve transformers. Fig. 14 depicts a single-line schematic of the test PS. The generator settings utilized in this work are taken from (Liao K. et al., 2018). All electrical generators include a speed governor. All electrical generators include a speed governor. In three control sections, the three generators (G3, G7, and G9) list the parameters of the IEEE 39-bus New-England test system in Appendix 5.3. In this instance, it is presumed that the LFC duty is carried out by a single generator in each region, which are G1 in region 1, G7 in Area 2, and G9 in Area 3. So, the load demands in a real PS fluctuate, we used a random load fluctuation

at each location, as seen in Fig.15. Fig. 16 depicts the frequency fluctuation of areas 1, 2, and 3, respectively, while Fig. 17 depicts the power deviation. Despite this, the system's state variables had not been monitored, the frequency fluctuation and tie-line power flow rapidly decreased to zero. As a result, in a huge power network where system state variables are hard to evaluate, this strategy is preferable for keeping frequency and tie-line power within a safe range. The simulation findings validate the higher dynamic performance and resilience of the suggested LFC scheme.

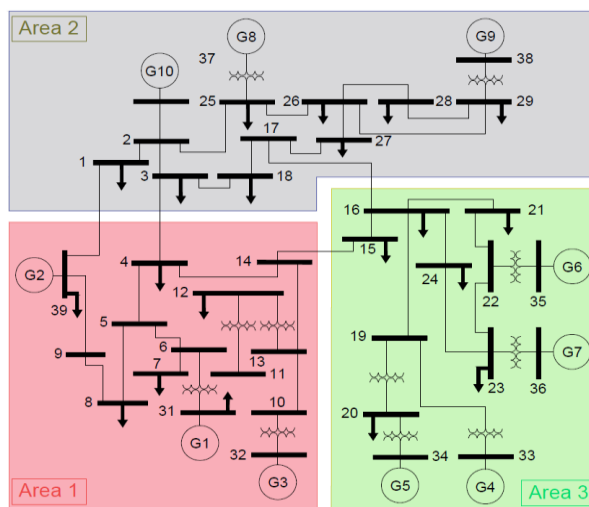


Figure 5.13. The block diagram of the New England 39 bus system

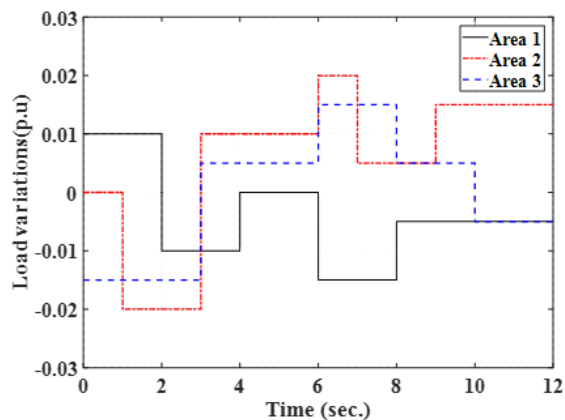


Figure 5.14. Random load variation

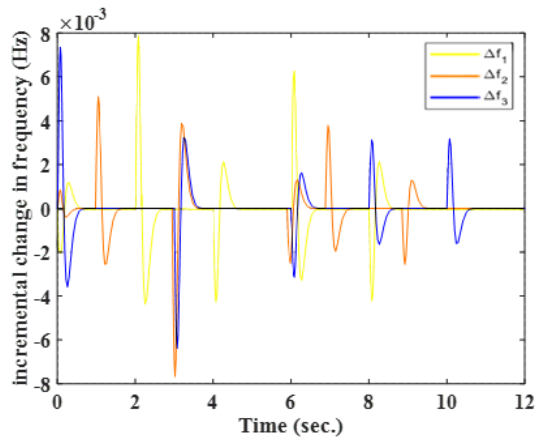


Figure 5.15. The dynamic responses of the frequency deviation

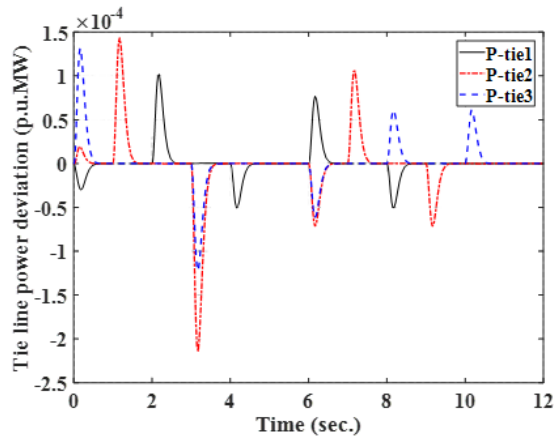


Figure 5.16. The dynamic responses of the tie-line power

Remark 5.7. In summary, the suggested novel technique provided higher control performance in terms of maintaining tie-line power and frequency at the approved point for the PS where system state variables are hard to quantify. The suggested approach is incredibly powerful, not only reducing chattering but also ensuring the MAPS's resilience.

Case 2: In particular, the generation rate constraint (GRC) is generally studied by adding a limiter and a hysteresis pattern to the governor-turbine system model. It is critical to address practical limits and natural circumstances such as the physical constraint of the GRC in paper (Liao K. et al., 2018). Due to its non-linearity, the GRC has a detrimental impact on power network performance. The GRC represents a realistic restriction on the ratio of variation in producing power due to physical constraints. Governor dead band (GDB) is a technique for power network frequency

regulation in the presence of disruptions. GDB has a distinct contour as the overall magnitude of a continuous speed shift with no consequent modification in the valve position. The use of grey wolf optimization (GWO) in (Srilekha J et al. , 2020) was a recent study. However, as observed in paper (Liao K. et al., 2018) the effects of GDB and GRC are not included in the power plant to assess the effective responsiveness of the proposed controller of power networks. In this scenario, we examine the dynamic models utilized in MAPS to represent the physical constraints of GDB and GRC. The proposed SMC is tested in a MAPS with the same step load disturbance and system parameters as in (Srilekha J et al. , 2020). Figure 5.17 depicts a nonlinear governor model with GDB and a nonlinear turbine model with GRC applied in the TASHSP.

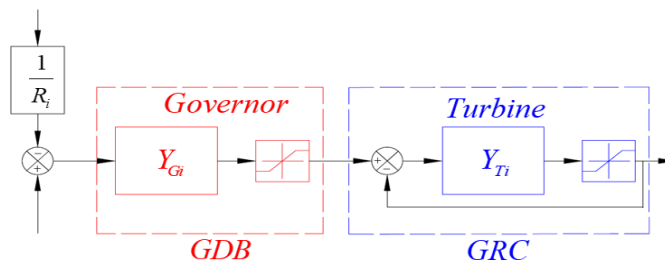


Figure 5.17. Nonlinear governor model with dead band and Nonlinear turbine model with the GRC.

Figures 5.18 and 5.19 show the frequency and tie-line power variations. As can be seen, with the suggested SOSDISS controllers, transient oscillations are determined for a longer time and with a bigger amplitude than in Case 1 in Simulation 1. In contrast to (Srilekha J et al. , 2020) and Simulation 1 with Case 1, the suggested control approach was found to be adequate even in the presence of GRC, GDB, and step LDs. In the transient performance of the proposed SOSDISS controller, the % overshoot and the settling time are greatly reduced under the GDB and GRC effects.

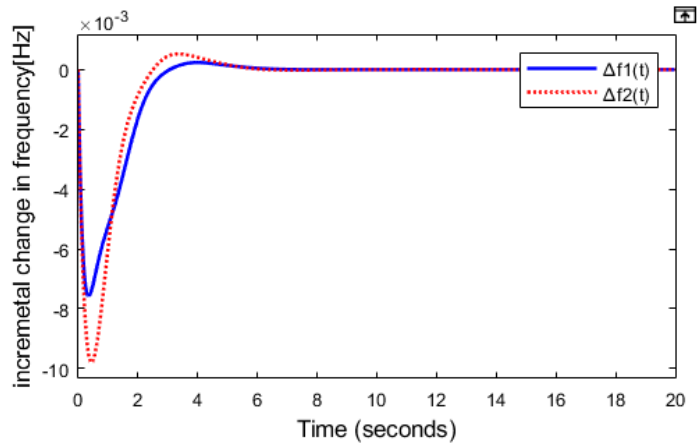


Figure 5.18. The frequency responses of two areas with GRC and GRB.

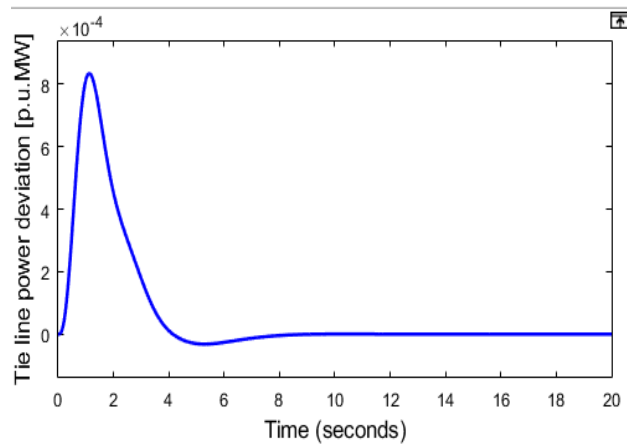


Figure 5.19. Dynamic responses of the tie-line power with GRC and GRB

Remark 5.8: The feedback signal of the linked power network is greatly influenced by GRC and GDB. The simulation results are used to compare Simulation 1 with Case 1 of considering or without considering the nonlinearity effects of GDB and GRC in to (Srilekha J et al. , 2020) to demonstrate the robustness of the proposed SOSDISS. In contrast to previous studies, the suggested SOSDISS controller clearly reveals that transient performance has changed with needed circumstances such as the setup time and under/overshoot under the GDB and GRC. As a result, the planned SOSDISS's tiny frequency fluctuations have less impact on plant reserve capacity and the electricity market.

Case 3: Because the same parameter uncertainty of the three regions MAPS is employed in Case 1 of Simulation 1, the nominal operating point is used to test the usefulness and resilience of the proposed controller to LDs. Figures 5.20 and 5.21

show the fast decrease of the tie-line power and FD.

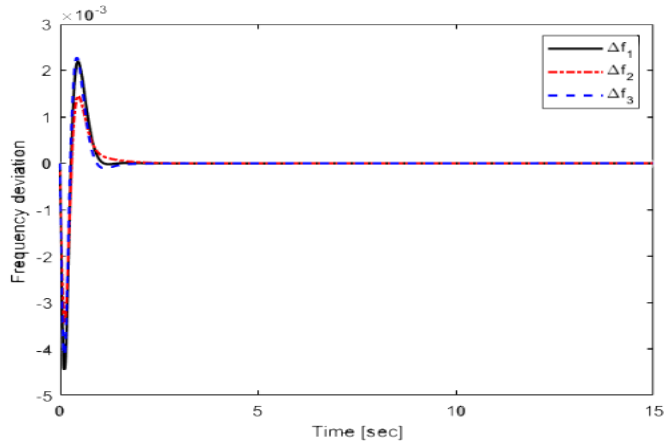


Figure 5.20. The dynamic responses of frequency change in three areas

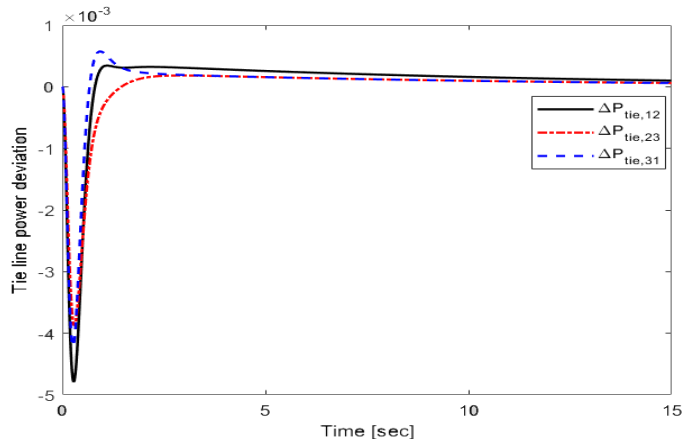


Figure 5.21. The dynamic responses of the tie-line power

As a result, the suggested SOSDISS controller is applied for three-area multisource multi-area PS. It also shows that the SOSDISS can stabilize the system in conjunction with the large system. When the simulation results are compared, the suggested double sliding switching surface and the planned SOSDISS can eliminate overshoot, improve reaction speed, and restrict frequency variation to zero. As a result, the developed controller is resilient and effective in controlling MAPS's parameter uncertainties.

5.4.3. Simulation 3:

The proposed LFC based on SOSDISS has been examined with different effects of step load disturbance on the MAPS with nominal parameter conditions in to (Srilekha J et al. , 2020) and time delay in (Mi Yang et al. , 2017)(Y. Mi, X. Hao,

Y. Liu, Y. Fu, C. Wang, P. Wang and P.C. Loh, 2017). The three-area restructured PS in Figure 5.22 has a transmission time delay. In this case, the load disturbances are $\Delta P_{d1} = 0.02$, $\Delta P_{d2} = 0.015$, and $\Delta P_{d3} = 0.01$ (p.u) at $t_1 = 0$ in three areas of the MASHPS. The FD of $\Delta f_1, \Delta f_2, \Delta f_3$ for the MASHPS with delay time as $\tau_i = 5s$ ($i = 1, 2, 3$) are displayed in Figure 5.23 to Figure 5.24 are the tie line power deviation and frequency change for three area power networks. To be clear in this study, the transient responses produced in the suggested LFC based on SOSDISS are as good as in terms of settling time and small magnitude of overshoot percentage.

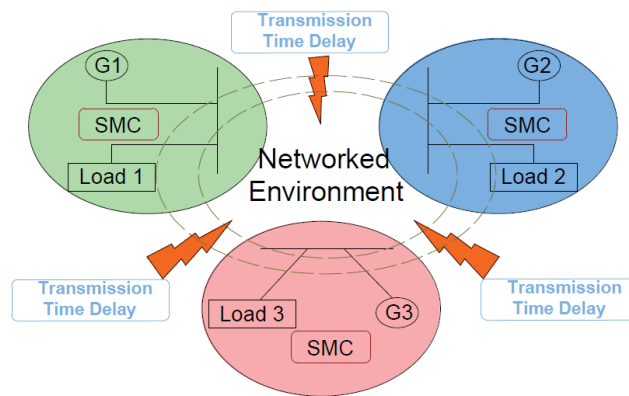


Figure 5.22. A three-area restructured PS with transmission time delay.

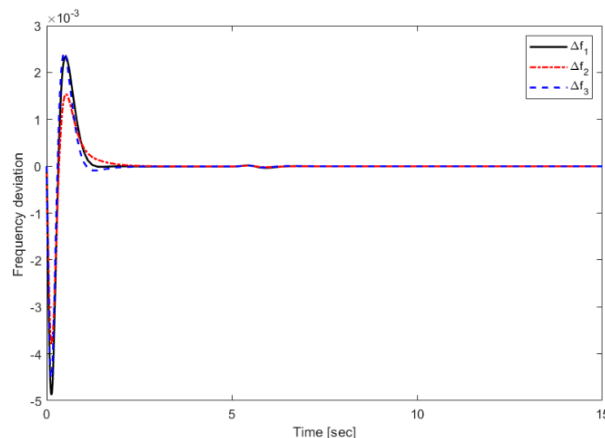


Figure 5.23. Frequency deviation with time delay at $\tau = 5s$

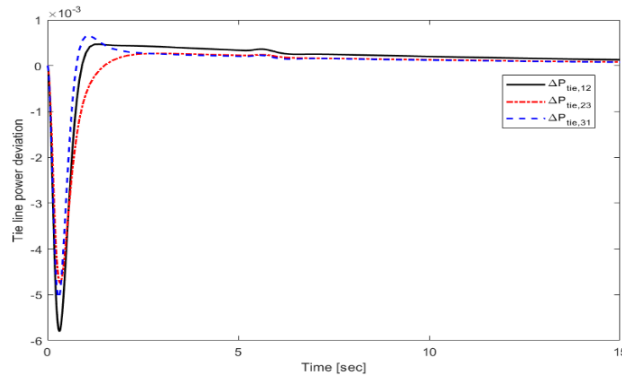


Figure 5.24. Tie-line deviation with time delay at $\tau = 5s$

Remark 5.9. The findings of the testing simulation are assigned in this section on Figures 5.23 to 5.24. Particularly when time-delay communication is considered for the large-scale power network, the report of findings can demonstrate in an effective comparison. As a result, the recommended SOSDISS's system performance is well balanced, and frequency variation is 0 after 1s.

5.5. Conclusion of chapter 5.

In conclusion, an LFC study has been achieved for TASHPS under load disturbance and parameter uncertainties. The proposed LFC method is developed with a SOSDISS. On the other hand, a decentralized SOSDISS is given with carefully selected matrices gains to improve the PS asymptotic stability and reduces chattering inherent in first-order SMC. The novel LMI based on Lyapunov theory, in which the derivative of the Lyapunov function is smaller than zero, is used to examine the asymptotic stability of the PS. To test large scale PS, the proposed second-order SMC appears to be capable of handling the PS's LFC, making it suitable for MASHPS frequency regulation and PS reliability. There are no assumptions about the distributions of the dynamics/bandwidth of the communication network with packet loss or the constraints of the controlled plants to evaluate the performance of SMC for disturbances with frequency domain specifications of networked control systems. In the future, we will focus on new SMCs for various disturbances with frequency domain requirements to evaluate the performance of the networked PS or will consider dynamics of the communication network considering the impact of packet loss.

CHAPTER 6: CONCLUSIONS AND RECOMMENDATIONS FOR FUTURE WORK

6.1. Conclusions and limitations

Multiple secondary frequency control strategies were developed based on different theories to ensure the maintenance of frequency within acceptable limits in two distinct testbed systems. In pursuit of the highest dynamic performance, various innovative SMC schemes were employed for optimization. These includes second-order integral sliding mode control (SOISMC), single-phase sliding mode control-based state observer (SPSMCBSO), and a second-order SMC approach using double integral sliding surfaces (SOSDISS). The key findings are as follows:

Firstly, this research introduces a novel SOISMC scheme for effectively managing the active power balance in a MAPS. The suggested method not only ensures the stability of the PN but also significantly mitigates the chattering problem in the PS. It achieves this using an integral sliding surface-based second order SMC to expedite the transient response of frequency, reduce excessive overshoot, and prioritize the active power balance. Importantly, the proposed SMC scheme, integrated with the FLC approach, offers a robust and effective solution while eliminating chattering in real-world applications. By reducing chattering in the control input, the suggested control method provides accurate signals to control mechanical inertia power, enabling it to effectively match load changes or demands. This capability makes it highly suitable for practical PS dealing with significant parameter uncertainties, load disturbances, communication delays in PS.

Secondly, this study introduces a novel approach called the single-phase sliding mode control-based state observer (SPSMCBSO) for LFC in MAMSPS. The stability of the TAGHTPS system is rigorously established through a novel linear matrix inequality approach based on Lyapunov theory. Comparative analysis of simulation results against recent methods demonstrates the superior performance of the SPSMCBSO approach. Moreover, the SPSMCBSO method displays robustness,

remaining resilient in the face of subsystem parameter deviations, random load disturbances, and uncertainties in state variables and interconnected matrices, wind. Thus, the SPSMCBSO approach proves to be a highly valuable and effective tool for LFC in MAMSPS.

Lastly, an LFC study is developed with a second-order SMC via double integral sliding surface (SOSDISS) for a two-area steam-hydroelectric system (TASHPS). On the other hand, a decentralized second double integral SMC is given with carefully selected matrices gains to improve the PS asymptotic stability and reduces chattering inherent in first-order SMC. The novel LMI based on Lyapunov theory, in which the derivative of the Lyapunov function is smaller than zero, is used to examine the asymptotic stability of the PS. To test large scale PS, the proposed second-order SMC appears to be capable of handling the PS's LFC, making it suitable for MASHPS frequency regulation and PS reliability. There are no assumptions about the distributions of the dynamics/bandwidth of the communication network with packet loss or the constraints of the controlled plants to evaluate the performance of SMC for disturbances with frequency domain specifications of networked control systems. In the future, we will focus on new SMCs for various disturbances with frequency domain requirements to evaluate the performance of the networked PS or will consider dynamics/bandwidth of the communication network considering the impact of packet loss.

The limitations of the proposed methods should be mentioned, especially in the practical application. SMC is a nonlinear and resilient control approach. The method's systematic design technique gives an easy answer for the control input. The approach has various advantages, including resistance to matching external shocks and unanticipated parameter alterations. Chattering, on the other hand, is a regular issue with the procedure. To address the chattering issue, certain ways have been offered in the literature. Traditional SMC (first order) procedures are evaluated experimentally, and their practical usefulness is studied. For speed tracking control and disturbance regulation concerns, an electromechanical system is used in

experiments. Based on time-domain analysis, the graphical findings are displayed, and the performance measures are tabulated. The experimental results show that the SMC is suitable for practical control systems, although with certain drawbacks. Due to the chattering phenomena of high-frequency switching, implementing the SMC for load frequency management of power networks becomes challenging. This SMC chattering issue is particularly hazardous to actuators used in power systems. This SMC chattering issue is extremely harmful to actuators used in power systems. The suggested controller generates the right signal and uses energy to compensate for frequency damping in the primary control, which is comprised of a governor. So that the governor's droop speed control appropriately actuates the valve to give needed steam to the turbine in order to boost mechanical inertia power to match the load shift or demand. Therefore, in the design of proposed SMC for practical applications, it is required to determine a proper sliding surface so that the tracking errors and output deviations can be reduced to a satisfactory level. The sliding-mode control, despite the advantages of simplicity and robustness, generally suffers from the well-known problem, called chattering, which is a very high-frequency oscillation of the sliding variable around the sliding manifold. The chattering is highly undesirable for the real systems and actuator since it may lead to actuator failure and unnecessarily large control signal. In practice, the presence of time delays in many industrial processes and the actuators, such as time lag, transportation lag, time delay, dead time and physical limitations, cannot switch at an infinite frequency along the sliding surface as demanded by the theory of SMC algorithms.

6.2. Recommendations for future work

As a result, these findings underscore the significance of emphasizing a growth mindset and fostering innovation capability within the realm of entrepreneurial studies. In line with these discoveries, it seems that the proposed relationship is positively influenced by the innovation capability approach. This study might be expanded in the following areas in future work:

1. In our current research, we operate under the assumption that PS control

areas comprise a diverse mix of power generation sources, including thermal, hydro, and gas resources within each area. However, to comprehensively assess the performance of the suggested controllers for LFC across power systems with a wide spectrum of potential configurations, future studies could broaden their scope. This expanded perspective might encompass the integration of diverse sources such as gas, wind, diesel, nuclear, energy storage systems, and other components within each control area of a multi-area multisource PS, restructured PS environment.

2. Given the rapid response provided by the suggested SMC, it would be prudent to conduct further investigations to assess the system's stability under varying operating conditions. It is well-established that an exceedingly fast response carries the risk of inducing system oscillations, making this an important aspect to examine.

3. Examining alternative artificial intelligence (AI) algorithms such as Differential Evolution, Bees Algorithm, and Cuckoo Search to fine-tune the suggested SMC controllers and evaluating their potential to enhance the dynamic performance of these controllers is a valuable direction for further research.

4. Continuing research into the development of combined fuzzy and SMC controllers, with the optimization of membership functions through advanced techniques, has the potential to greatly improve the overall performance of novel fuzzy logic controllers.

5. Demand-side frequency response represents another effective approach that warrants further investigation into controlling frequency within the PS. Therefore, delving deeper into this topic and offering novel solutions presents a promising avenue for frequency control research. These methods can potentially be extended to LFC studies of micro-grids, with the inclusion of various energy storage devices for enhanced control and stability.

LIST OF PUBLISHED PAPERS BY AUTHOR

1. Huynh, Van Van, **Phong, Thanh Tran***, Bui Le Ngoc Minh, Anh Tuan Tran, Dao Huy Tuan, Tam Minh Nguyen, and Phan-Tu Vu. "New second-order sliding mode control design for load frequency control of a power system." *Energies* 13, no. 24 (2020): 6509.

2. Huynh, Van Van, **Phong Thanh Tran***, Tien Minh Nguyen, Van-Duc Phan, and Viet-Thanh Pham. "Advanced Sliding Mode Observer Design for Load Frequency Control of Multiarea Multisource Power Systems." *International Transactions on Electrical Energy Systems* 2022.

3. Van Van Huynh, **Phong Thanh Tran***, and Chau Si Thien Dong, Bach Dinh Hoang, "Sliding Surface Design for Sliding Mode Load Frequency Control of Multi Area Multi Source Power System", *IEEE Transactions on Industrial Informatics*, 2024.

4. **Phong Thanh Tran**, Van Van Huynh and Chau Si Thien Dong, Bach Dinh Hoang, "Automatic Generation Control based Sliding Mode Observer Design for Multi-Area Multi-Source Power Systems", the 7th International Conference on Advanced Engineering – Theory and Applications, 2022.

5. **Phong Thanh Tran**, Van Van Huynh, Chau Thien Si Dong, and Bach Hoang Dinh. "Sliding Mode-Based Load Frequency Control of a Power System with Multi-Source Power Generation." In *2023 International Conference on System Science and Engineering (ICSSE)*, pp. 142-147. IEEE, 2023.

6. Tran, Anh-Tuan, Bui Le Ngoc Minh, **Phong, Thanh Tran**, Van Van Huynh, Van-Duc Phan, Viet-Thanh Pham, and Tam Minh Nguyen. "Adaptive integral second order sliding mode control design for load frequency control of large-scale power system with communication delays." *Complexity* 2021.

7. Van Huynh, Van, **Phong Thanh Tran**, Tuan Anh Tran, Dao Huy Tuan, and Van-Duc Phan. "Extended state observer-based load frequency controller for three

area interconnected power system." *TELKOMNIKA (Telecommunication Computing Electronics and Control)* 19, no. 3 (2021): 1001-1009.

8. Huynh, Van Van, Bui Le Ngoc Minh, Emmanuel Nduka Amaefule, Anh-Tuan Tran, and **Phong Thanh Tran**. "Highly robust observer sliding mode-based frequency control for multi area power systems with renewable power plants." *Electronics* 10, no. 3 (2021): 274.

9. Tran, Anh-Tuan, Bui Le Ngoc Minh, Van Van Huynh, **Phong Thanh Tran**, Emmanuel Nduka Amaefule, Van-Duc Phan, and Tam Minh Nguyen. "Load frequency regulator in interconnected power system using second order sliding mode control combined with state estimator." *Energies* 14, no. 4 (2021): 863.

10. Huynh, Van Van, Bui Le Ngoc Minh, Emmanuel Nduka Amaefule, Anh-Tuan Tran, **Phong Thanh Tran**, Van-Duc Phan, Viet-Thanh Pham, and Tam Minh Nguyen. "Load Frequency Control for Multi-Area Power Plants with Integrated Wind Resources." *Applied Sciences* 11, no. 7 (2021): 3051.

11. Tran Anh-Tuan, **Phong Thanh Tran**, and Van Van Huynh. "Load Frequency Control for Power System using Generalized Extended State Observer." *Journal of Advanced Engineering and Computation* 5, no. 1 (2021): 1-18.

REFERENCES

- Alhelou Hassan Haes and M. et al. (2018). Challenges and opportunities of load frequency control in conventional, modern and future smart power systems. *Energies*, 2497, <https://doi.org/10.3390/en11102497>.
- Alhelou Hassan Haes et al. (2018). Challenges and opportunities of load frequency control in conventional, modern and future smart power systems: A comprehensive review. *Energies*, 2497. Available at: <https://doi.org/10.3390/en11102497>.
- Ali Hossam Hassan et al. (n.d.). Multi-verse optimizer for model predictive load frequency control of hybrid multi-interconnected plants comprising renewable energy. *IEEE Access*, 114623-114642. Available at: <https://doi.org/10.1109/ACCESS.2020.3004299>.
- Alkar Khaled et al. . (2019). Performance evaluation of the blackout and power outages in Libyan power grid-Al-zawia combined cycle power plant case study. *In 2019 1st International Conference on Sustainable Renewable Energy Systems and Applications (ICSRESA)* (pp. pp. 1-6). IEEE, 2019. Available at: <https://doi.org/10.1109/ICSRESA49121.2019.9182337>.
- Andrade Diego Maldonado et al. (2020). Distributed load-frequency control in power systems. *In 2020 IEEE ANDESCON*, IEEE, pp. 1-6. Available at: <https://doi.org/10.1109/ANDESCON50619.2020.9272070>.
- Arya Yogendra. (2018). Automatic generation control of two-area electrical power systems via optimal fuzzy classical controller. *Journal of the Franklin Institute*, 2662-2688. Available at: <https://doi.org/10.1016/j.jfranklin.2018.02.004>.
- Asghar Rafiq et al. (2023). A Review of Load Frequency Control Schemes Deployed for Wind-Integrated Power Systems. *Sustainability* , 8380. Available at: <https://doi.org/10.3390/su15108380>.
- Bari Ataul et al. . (2014). Challenges in the smart grid applications: An overview. *International Journal of Distributed Sensor Networks* , 974682. Available at:

<https://doi.org/10.1155/2014/974682>.

- Bevrani Hassan. (2014). *Robust power system frequency control*. New York: Springer.
- Bevrani Hassan et al. (2017). *Intelligent automatic generation control*. CRC press.
- Bhagat S. et al. . (2014). GA based Internal Model Controller Design for Load Frequency Control in Power System via Reduced Order Model. *Int. J. Engg. Sci. Invention*, 17-26. .
- Bui Le Ngoc Minh et al. (2018). Decentralized Adaptive Double Integral Sliding Mode Controller for Multi-Area Power Systems. *Mathematical Problems in Engineering* , Available at: <https://doi.org/10.1155/2018/2672436>.
- Cam Ertugrul et al. . (2017). Use of the genetic algorithm-based fuzzy logic controller for load-frequency control in a two area interconnected power system. *Applied Sciences*, 308. Available at: <https://doi.org/10.3390/app7030308>.
- Casavola et al. . (2023). Centralized Supervision and Coordination of Load/Frequency Control Problems in Networked Multi-Area Power Systems. *Electric Transportation Systems in Smart Power Grids*, 275-423. Available at: <https://doi.org/10.1016/j.jfranklin.2011.02.009>.
- Çelik Emre et al. . (2023). Improved load frequency control of interconnected power systems using energy storage devices and a new cost function. *Neural Computing and Applications*, 681-697. Available at: <https://doi.org/10.1007/s00521-022-07813-1>.
- Celik Vedat et al. (2019). Effects of fractional-order PI controller on delay margin in single-area delayed load frequency control systems. *Journal of Modern Power Systems and Clean Energy*, 380-389. Available at: <https://doi.org/10.1007/s40565-018-0458-5>.
- Chen Haoyong. (2015). Cooperative control of power system load and frequency by using differential games. *IEEE Transactions on Control Systems Technology*, 882-897. Available at: <https://doi.org/10.1109/TCST.2014.2346996>.
- Cucuzzella Michele et al. . (2018). A robust consensus algorithm for current sharing

- and voltage regulation in DC microgrids. *IEEE Transactions on Control Systems Technology* , 1583-1595. Available at: <https://doi.org/10.1109/TCST.2018.2834878>.
- Daneshfar Fatheme et al. . (2010). Load–frequency control: a GA-based multi-agent reinforcement learning. *IET generation, transmission & distribution*, 13-26. Available at: <https://doi.org/10.1049/iet-gtd.2009.0168>.
- Dev Ark et al. (2021). Nonlinear disturbance observer based adaptive super twisting sliding mode load frequency control for nonlinear interconnected power network. *Asian Journal of Control*, 2484-2494. Available at: <https://doi.org/10.1002/asjc.2364>.
- Edris, Abdel-A et al. (2017). Transmission grid smart technologies. *Academic Press*, In The power grid, pp. 37-55.
- El-Bahay, M. H., Lotfy, M. E., & El-Hameed, M. A. . (2023). Effective participation of wind turbines in frequency control of a two-area power system using coot optimization. *Protection and Control of Modern Power Systems*, 1-15.
- Eremia Mircea et al. (2013). *Handbook of electrical power system dynamics: modeling, stability, and control*. and Mohammad Shahidehpour,: John Wiley & Sons.
- Esmail M et al. . (2017). Review of automatic generation control in deregulated environment. *IFAC-PapersOnLine* , 88-93: Available at: <http://dx.doi.org/10.3233/ATDE220776>.
- Esmail M. et al. (2017). Review of automatic generation control in deregulated environment. *IFAC-PapersOnLine* , 88-93. Available at: <https://doi.org/10.1016/j.ifacol.2017.12.016>.
- Esmail, M., Tzoneva, R., & Krishnamurthy, S. . (2017). Review of automatic generation control in deregulated environment. *IFAC-PapersOnLine*, 88-93.
- F. M. Gonzalez-Longatt and J. Luis Rueda, Eds. (2014). *Power Factory Applications for Power System Analysis*. Cham. Springer International Publishing.
- F. Teng, Y. M. (2017). Challenges on primary frequency control and potential

- solution from EVs in the future GB electricity system. *Applied Energy*, 353–362.
- Falentina, A. T., & Resosudarmo, B. P. (2019). The impact of blackouts on the performance of micro and small enterprises: Evidence from Indonesia. *World Development*, 104635.
- Falentina, Anna T. et al. (2019). The impact of blackouts on the performance of micro and small enterprises: Evidence from Indonesia. *The impact of blackouts on the performance of micro and small enterprises: Evidence from Indonesia*, 104635. Available at: <https://doi.org/10.1016/j.worlddev.2019.104635>.
- Farahani, M.; Ganjefar, S.; Alizadeh, M. (2012). PID controller adjustment using chaotic optimization algorithm for multi-area load frequency control. *IET Control. Theory Appl.*, 1984–1992.
- Fu, C., & Tan, W. . (2018). Decentralised load frequency control for power systems with communication delays via active disturbance rejection. *IET Generation, Transmission & Distribution*, 1397-1403.
- Fu, C., Wang, C., & Shi, D. (2020). An alternative method for mitigating impacts of communication delay on load frequency control. *International Journal of Electrical Power & Energy Systems*, 105924.
- Fu, C.; Tan, W. . (2018). Decentralized load frequency control for power systems with communication delays via active disturbance rejection. *IET Gener. Transm. Distrib.*, 1751–8687.
- G. Andersson et al.,. (2009). *Frequency and Voltage Control*. CRC Press, Boca Raton: Electric Energy Systems: Analysis and Operation.
- Gnanam Nisha et al. . (2023). Real-time frequency stabilization of standalone PV system with SMC. *International Journal of Innovative Research and Scientific Studies* , 38-48. Available at: <https://doi.org/10.53894/ijirss.v6i1.1080>.
- Gonzalez-Longatt et al. (2014). *Power Factory applications for power system analysis*. Springer.
- Gorripotu et al. . (2017). Firefly algorithm optimised PID controller for automatic

- generation control with redox flow battery . *International Journal of Computational Systems Engineering* , 48-57. Available at: <https://doi.org/10.1504/IJCSYSE.2017.083146>.
- Greve Thomas et al. (2018). A system operator's utility function for the frequency response market. *Applied Energy* , 562-569. Available at: <https://doi.org/10.1016/j.apenergy.2018.09.088>.
- Guo Chen et al. . (2021). A survey of bacterial foraging optimization. *Neurocomputing* , 728-746. Available at: <https://doi.org/10.1016/j.neucom.2020.06.142>.
- Guo Jianping . (2021). Application of a novel adaptive sliding mode control method to the load frequency control. *European Journal of Control*, 172-178. Available at: <https://doi.org/10.1016/j.ejcon.2020.03.007>.
- Guo Jianping . (2021). Application of a novel adaptive sliding mode control method to the load frequency control. *European Journal of Control* , 172-178. Available at: <https://doi.org/10.1016/j.ejcon.2020.03.007>.
- Guo Jianping. (2015). Load frequency control of a two area-power system with non-reheat turbines by SMC approach. *Journal of Energy and Power Engineering*, 566-573. Available at: <https://doi.org/10.17265/1934-8975%2F2015.06.008>.
- Guo Jianping. (2019). Application of full order sliding mode control based on different areas power system with load frequency control. *ISA transactions*, 23-34. Available at: <https://doi.org/10.1016/j.isatra.2019.01.036>.
- Guo, Jianping. (2020). Application of a novel adaptive sliding mode control method to the load frequency control. *European Journal of Control*, 172-178.
- Gupta Deepak Kumar et al. . (2021). Load frequency control using hybrid intelligent optimization technique for multi-source power systems. *Energies*, 1581. Available at: <https://doi.org/10.3390/en14061581>.
- Gupta Neelesh Kumar et al. (2021). Load Frequency Control of Two-Area Power System by Using 2 Degree of Freedom PID Controller Designed with the Help of Firefly Algorithm. *In Control Applications in Modern Power System: Select*

- Proceedings of EPREC 2020*, pp. 57-64. Springer Singapore, Available at: https://doi.org/10.1007/978-981-15-8815-0_5.
- Gupta Nidhi et al. (2022). JAYA optimized generation control strategy for interconnected diverse source power system with varying participation. *Energy Sources, Part A: Recovery, Utilization, and Environmental Effects*, 1813-1829. Available at: <https://doi.org/10.1080/15567036.2019.1646354>.
- Gupta Nidhi et al. (2022). JAYA optimized generation control strategy for interconnected diverse source power system with varying participation. *Energy Sources, Part A: Recovery, Utilization, and Environmental Effects*, 1813-1829. Available at: <https://doi.org/10.1080/15567036.2019.1646354>.
- Haes Alhelou Hassan et al. (2019). A survey on power system blackout and cascading events: Research motivations and challenges. *Energies* , 682. Available at: <https://doi.org/10.3390/en12040682>.
- Haes Alhelou, H., Hamedani-Golshan, M. E., Njenda, T. C., & Siano, P. (2019). A survey on power system blackout and cascading events: Research motivations and challenges. *Energies*, 682.
- Hakimuddin et al. . (2020). Optimal automatic generation control with hydro, thermal, gas, and wind power plants in 2-area interconnected power system. *Electric Power Components and Systems*, 558-571. Available at: <https://doi.org/10.1080/15325008.2020.1793829>.
- Hakimuddin Nizamuddin et al. (2020). Optimal automatic generation control with hydro, thermal, gas, and wind power plants in 2-area interconnected power system. *Electric Power Components and Systems*, 558-571. Available at: <https://doi.org/10.1080/15325008.2020.1793829>.
- Hamodat Zaid. (2021). Automated generation control of multiple-area electrical system with an availability-based tariff pricing scheme regulated by whale optimized fuzzy PID controller. *International Journal of Photoenergy* , 1-13. Available at: <https://doi.org/10.1155/2021/5596527>.
- Huynh Van Van et al. (2021). Highly robust observer sliding mode based frequency

- control for multi area power systems with renewable power plants. *Electronics*, 274. Available at: <https://doi.org/10.3390/electronics10030274>.
- Huynh Van Van et al. (2021). Load Frequency Control for Multi-Area Power Plants with Integrated Wind Resources. *Applied Sciences*, 3051. Available at: <https://doi.org/10.3390/app11073051>.
- Ismayil C. (2014). Automatic generation control of single area thermal power system with fractional order PID (PI λ D μ) controllers. *IFAC proceedings*, 552-557. Available at: <https://doi.org/10.3182/20140313-3-IN-3024.00025>.
- J. D. Glover, M. S. Sarma, and T. Overbye,. (2008). *Power Systems Analysis and Design*. Australia: Thomson.
- Jalali Neda et al. (2020). Optimized fuzzy self-tuning PID controller design based on Tribe-DE optimization algorithm and rule weight adjustment method for load frequency control of interconnected multi-area power systems. *Applied Soft Computing*, 106424. Available at: <https://doi.org/10.1016/j.asoc.2020.106424>.
- Jan Machowski, Z. et al. (2011). *Power system dynamics: stability and control*. UK: John Wiley & Sons.
- Jan Machowski, Zbigniew Lubosny, Janusz W. Bialek, James R. Bumby. (2020). *Power System Dynamics: Stability and Control, 3rd Edition*. John Wiley & Sons.
- Khan Irfan Ahmed et al. (2023). New trends and future directions in load frequency control and flexible power system: A comprehensive review. *Alexandria Engineering*, 263-308, <https://doi.org/10.1016/j.aej.2023.03.040>.
- Kogan Mark Mikhailovich. (1999). *Robust stabilization of uncertain linear systems."*. Differential Equations .
- Kumar Anand and et al. (2021). Sliding mode controller design for frequency regulation in an interconnected power system. *Protection and Control of Modern Power Systems*, 1-12. Available at: <http://dx.doi.org/10.1186/s41601-021-00183-1>.

- Kundur Prabha. (2022). *Power System Stability and Control*. McGraw Hill; 2nd edition .
- Liao K. et al. (2018). Robust load frequency control scheme for power systems based on second order sliding mode and extended disturbance observer. *IEEE Transactions on Industrial Informatics*, 3076-3086. Available at: <https://doi.org/10.1109/TII.2017.2771487>.
- Liao Kai and Yan Xu. . (2017). A robust load frequency control scheme for power systems based on second-order sliding mode and extended disturbance observer. *IEEE Transactions on Industrial Informatics*, 3076-3086. Available at: <https://doi.org/10.1109/TII.2017.2771487>.
- Machowski Jan and Z. et al. (2020). *Power system dynamics: stability and control*. John Wiley & Sons.
- Machowski Jan at al. (2020). *Power system dynamics: stability and control*. John Wiley & Sons.
- Machowski Jan et al. (2020). *Power system dynamics: stability and control*. John Wiley & Sons.
- Manikandan, S. et al. (2020). Stability analysis of load frequency control system with constant communication delays. *IFAC-PapersOnLine*, 338-343. Available at: <https://doi.org/10.1016/j.ifacol.2020.06.057>.
- Mi Yang et al. . (2013). Decentralized sliding mode load frequency control for multi-area power systems. *IEEE Transactions on Power Systems*, 4301-4309. Available at: <https://doi.org/10.1109/TPWRS.2013.2277131>.
- Mi Yang et al. . (2017). Sliding mode load frequency control for multi-area time-delay power system with wind power integration. *IET Generation, Transmission & Distribution* , 4644-4653. Available at: <https://doi.org/10.1049/iet-gtd.2017.0600>.
- Mi Yang et al. (2016). The sliding mode load frequency control for hybrid power system based on disturbance observer. *International Journal of Electrical Power & Energy Systems*, 446-452. Available at:

<https://doi.org/10.1016/j.ijepes.2015.07.014>.

- Momoh James. (2012). *Smart grid: fundamentals of design and analysis*. John Wiley & Sons.
- Momoh James A. et al. (2017). *Electric power system applications of optimization*. CRC press.
- Momoh, J. A. (2012). *Smart grid: fundamentals of design and analysis*. John Wiley & Sons.
- Morsali Javad et al. (In 2020). Proposing a new hybrid model for LFC and AVR loops to improve effectively frequency stability using coordinative CPSS. *28th Iranian conference on electrical engineering (ICEE)* (pp. pp. 1-7). IEEE. <https://doi.org/10.1109/ICEE50131.2020.9260695>.
- Mostafa Elsaied Mohamed et al. . (2018). Application of different optimization techniques to load frequency control with WECS in a multi-area system. *Electric Power Components and Systems*, 739-756. Available at: <https://doi.org/10.1080/15325008.2018.1509913>.
- Muhssin Mazin et al. (2018). *Adaptive control and dynamic demand response for the stabilization of grid frequency*. Cardiff University.
- Muhssin Mazin T. et al. (2017). A novel adaptive deadbeat-based control for load frequency control of low inertia system in interconnected zones north and south of Scotland. *International Journal of Electrical Power & Energy Systems*, 52-61. Available at: <https://doi.org/10.1016/j.ijepes.2016.12.005>.
- Nisha G. et al. . (2022). Frequency Stabilization of Stand-Alone Microgrid with Tuned PID Controller. *ECS Transactions*, 773. Available at: [10.1149/10701.0773ecst](https://doi.org/10.1149/10701.0773ecst).
- Nisha, G., & Jamuna, K. (2022). Frequency Stabilization of Stand-Alone Microgrid with Tuned PID Controller. *ECS Transactions*, 773.
- Obaid Zeyad Assi et al. (2019). Frequency control of future power systems: reviewing and evaluating challenges and new control methods. *Journal of Modern Power Systems and Clean Energy*, 9-25. Available at:

<https://doi.org/10.1007/s40565-018-0441-1>.

- Ogar Vincent N. et al. . (2023). Load Frequency Control Using the Particle Swarm Optimisation Algorithm and PID Controller for Effective Monitoring of Transmission Line. *Energies*, 5748. Available at: <https://doi.org/10.3390/en16155748>.
- Onyeka Adrian E et al. . (2020). Robust decentralised load frequency control for interconnected time delay power systems using sliding mode techniques. *IET Control Theory & Applications*, 470-48. Available at: <https://doi.org/10.1049/iet-cta.2019.0809>.
- Pahadasingh Sunita et al. . (2020). Load frequency control incorporating electric vehicles using FOPID controller with HVDC link. *Innovation in Electrical Power Engineering, Communication, and Computing Technology, Springer Singapore*, 181-203. Available at: https://doi.org/10.1007/978-981-15-2305-2_15.
- Pahadasingh Sunita et al. . (2021). Incorporation of distributed generation resources for three-area load frequency control optimized tilted integral derivative controller. *In Advances in Smart Grid and Renewable Energy: Select Proceedings of ETAEERE 2020, Springer Singapore*, pp. 57-68. Available at: https://doi.org/10.1007/978-981-15-7511-2_6.
- Paliwal Nikhil et al. . (2022). Application of grey wolf optimization algorithm for load frequency control in multi-source single area power system. *Evolutionary Intelligence* , 1-22. Available at: <https://link.springer.com/article/10.1007/s12065-020-00530-5>.
- Pappachen Abhijith et al. (2017). Critical research areas on load frequency control issues in a deregulated power system: A state-of-the-art-of-review. *Renewable and Sustainable Energy Reviews*, 163-177. A valaible at: <https://doi.org/10.1016/j.rser.2017.01.053>.
- Park Ju H et al. (2021). *Recent advances in control problems of dynamical systems and networks*. Berlin, Germany: Springer International Publishing.

- Parmar KP Singh et al. (2014). LFC of an interconnected power system with multi-source power generation in deregulated power environment. *International Journal of Electrical Power & Energy Systems* , 277-286. Available at: <https://doi.org/10.1016/J.IJEPES.2013.11.058>.
- Patel Ragini et al. . (2019). Enhancing optimal automatic generation control in a multi-area power system with diverse energy resources. *IEEE Transactions on Power Systems*, 3465-3475. <https://doi.org/10.1109/TPWRS.2019.2907614>.
- Patel Ragini et al. . (2019). Enhancing optimal automatic generation control in a multi-area power system with diverse energy resources. *IEEE Transactions on Power Systems*, 3465-3475. Available at: <https://doi.org/10.1109/TPWRS.2019.2907614>.
- Patel Ragini et al. (2019). Enhancing optimal automatic generation control in a multi-area power system with diverse energy resources. *IEEE Transactions on Power Systems*, 3465-3475. Available at: <https://doi.org/10.1109/TPWRS.2019.2907614>.
- Plihal Kieran . (2019). A study on the implementation of HVDC for Power system interconnection. *International Symposium on Electrical and Electronics Engineering (ISEEE)*, 1-6. Available at: <https://doi.org/10.1109/ISEEE48094.2019.9136144>.
- Prabha S. Kundur, O. M. (2022). *Power System Stability and Control, Second Edition*. McGraw Hill; 2nd edition .
- Pradhan Raseswari et al. (2015). Double integral sliding mode MPPT control of a photovoltaic system. *IEEE transactions on control systems technology*, 285-292. Available at: <https://doi.org/10.1109/TCST.2015.2420674>.
- Prakash Abhineet et al. . (2020). LQR based PI controller for load frequency control with distributed generations. *In 2020 21st National Power Systems Conference (NPSC)* (pp. pp. 1-5). IEEE.
- Prasad Sheetla et al. . (2017). Non-linear sliding mode load frequency control in multi-area power system. *Control Engineering Practice*, 81-92. Available at:

<https://doi.org/10.1016/j.conengprac.2017.02.001>.

- Prasad Sheetla et al. . (2019). Load frequency regulation using observer based non-linear sliding mode control. *International Journal of Electrical Power & Energy Systems*, 178-193. Available at: <https://doi.org/10.1016/j.ijepes.2018.06.035>.
- Qian Dianwei . (2016). Load frequency control by neural-network-based integral sliding mode for nonlinear power systems with wind turbines. *Neurocomputing*, 875-885: Available at: <https://doi.org/10.1016/j.neucom.2015.08.043>.
- Rajendran et al. . (2023). Performance Improvement of AGC Using Novel Controllers in a Multi-Area Solar Thermal System under Deregulated Environment. *Electric Power Components and Systems*, 1-16. Available at: <https://doi.org/10.1080/15325008.2023.2237007>.
- Ranjan Mrinal et al. (2022). A literature survey on load frequency control considering renewable energy integration in power system: Recent trends and future prospects. *Journal of Energy Storage*, 103717. Available at: <https://doi.org/10.1016/j.est.2021.103717>.
- Ranjitha K. et al. (2021). Firefly algorithm optimized load frequency controller for multi-source power system. *Emerging Trends in Industry, IEEE*, pp. 1-6. IEEE. Available at: <https://doi.org/10.1109/ETI4.051663.2021.9619304>.
- Sahoo Dillip Kumar et al. . (2022). Chaotic Harris hawks optimization based type-2 fractional order fuzzy PID controller for frequency regulation of power systems. *International Journal of Ambient Energy* 4, 3832. Available at: <https://doi.org/10.1080/01430750.2020.1860128>.
- Sahu Rabindra Kumar et al. (2015). A hybrid DE–PS algorithm for load frequency control under deregulated power system with UPFC and RFB. *Ain Shams Engineering Journal*, 893-911. Available at: <https://doi.org/10.1016/j.asej.2015.03.011>.
- Sahu Rabindra Kumar et al. (2016). Automatic generation control of multi-area

- power systems with diverse energy sources using teaching learning based optimization algorithm. *Engineering Science and Technology*, 113-134. Available at: <https://doi.org/10.1016/j.jestch.2015.07.011>.
- Sanajaoba Singh Sarangthem. (2022). Load frequency control of a three-area system with multiple-energy sources using exchange market algorithm optimized cascade IDD-PID controllers. *Electric Power Components and Systems*, 27-37. Available at: <https://doi.org/10.1080/15325008.2022.2135639>.
- Sarkar Mrinal Kanti et al. (2018). Chattering free robust adaptive integral higher order sliding mode control for load frequency problems in multi-area power systems. *IET Control Theory & Applications* , 1216-1227. Available at: <https://doi.org/10.1049/iet-cta.2017.0735>.
- Sarkar Mrinal Kanti et al. (2018). Chattering free robust adaptive integral higher order sliding mode control for load frequency problems in multi-area power systems. *IET Control Theory & Applications*, 1216-1227. Available at: <https://doi.org/10.1049/iet-cta.2017.0735>.
- Saxena Sahaj . (2018). PI controller based load frequency control approach for single-area power system having communication delay. *IFAC-PapersOnLine*, 622-626. Available at: <https://doi.org/10.1016/j.ifacol.2018.06.165>.
- Shahalami Seyed Hamid et al. (2018). Analysis of load frequency control in a restructured multi-area power system with the Kalman filter and the LQR controller. *AEU-International Journal of Electronics and Communications* , 25-46. Available at: <https://doi.org/10.1016/j.aeue.2018.01.011>.
- Shangguan et al. . (2021). Control performance standards-oriented event-triggered load frequency control for power systems under limited communication bandwidth. *IEEE Transactions on Control Systems Technology*, 860-868. Available at: <https://doi.org/10.1109/TCST.2021.3070861>.
- Shankar Ravi . (2016). Small-signal stability analysis for two-area interconnected power system with load frequency controller in coordination with FACTS and energy storage device. *Ain Shams Engineering Journal*, 603-612. Available at:

<https://doi.org/10.1016/j.asej.2015.06.009>.

Sharma et al. . (2020). Integrating layered recurrent ANN with robust control strategy for diverse operating conditions of AGC of the power system. *IET Generation, Transmission & Distribution*, 14. Available at: <https://doi.org/10.1049/iet-gtd.2019.0935>.

Sharma Jitendra et al. (2018). Robust PID load frequency controller design with specific gain and phase margin for multi-area power systems. *IFAC-PapersOnLine*,627-632. Available at: <https://doi.org/10.1016/j.ifacol.2018.06.166>.

Shiva Chandan Kumar et al. (2016). Automatic generation control of hydropower systems using a novel quasi-oppositional harmony search algorithm. *Electric Power Components and Systems*, 1478-1491. Available at: <https://doi.org/10.1080/15325008.2016.1147103>.

Singh Vijay P. et al. (2017). Improved load frequency control of power system using LMI based PID approach. *Journal of the Franklin Institute*, 6805-6830. Available at: <https://doi.org/10.1016/j.jfranklin.2017.08.031>.

Soliman, Ahmed Mohammed Attiya et al. . (2023). PSO tuned interval type-2 fuzzy logic for load frequency control of two-area multi-source interconnected power system. *Scientific Reports*, 8724. Available at: <https://doi.org/10.1038/s41598-023-35454-4>.

Srilekha J et al. . (2020). Load Frequency Control of Two Area Hydro-Thermal System considering GRCs and GDB Non Linearity's with Intelligent Controller. *International Journal of Recent Technology and Engineering (IJRTE)*, 2277. Available at: DOI:10.35940/ijrte.E6959.018520.

Su Xiaojie et al. (2017). Event-triggered sliding-mode control for multi-area power systems . *IEEE Transactions on Industrial Electronics*, 6732-6741. <https://doi.org/10.1109/TIE.2017.2677357>.

Tabassum Fariya et al. . (2020). Robust Control of Frequency for Multi-Area Power System. In *2020 IEEE Region 10 Symposium (TENSymp)*, pp. 86-89.

- Available at: <https://doi.org/10.1109/TENSYMP50017.2020.9230682>.
- Teng Fei et al. (2017). Challenges on primary frequency control and potential solution from EVs in the future GB electricity system. *Applied energy*, 353-362. Available at: <https://doi.org/10.1016/j.apenergy.2016.05.123>.
- Ullah Kaleem et al. (2021). Automatic generation control strategies in conventional and modern power systems: A comprehensive overview. *Energies*, 2376. Available at: 2021:i:9:p:2376-:d:541384.
- Vanitha, C. et al. (2023). Smart Grid-Overview, Challenges and Security Issues . *Smart Grids and Internet of Things: An Energy Perspective*, 67-90. Available at: <https://doi.org/10.1002/9781119812524.ch3>.
- Vanitha, C. N., Malathy, S., & Krishna, S. A. . (2023). Smart Grid-Overview, Challenges and Security Issues. Smart Grids and Internet of Things:.. *An Energy Perspective*, 67-90.
- Vega-Herrera Jorge et al. (2020). Analysis and application of quasi-static and dynamic phasor calculus for stability assessment of integrated power electric and electronic systems. *IEEE Transactions on Power Systems* , 1750-1760. Available at: <https://doi.org/10.1109/TPWRS.2020.3030225>.
- Weedy Birron Mathew et al. (2012). *Electric power systems*. John Wiley & Sons.
- Wood Allen J et al. (n.d.). Power generation, operation, and control. *John Wiley & Sons*, 2013.
- Yan Wenxu et al. . (2018). H_{∞} robust load frequency control for multi-area interconnected power system with hybrid energy storage system. *Applied Sciences*, 1748. Available at: <https://doi.org/10.3390/app8101748>.
- Yang Shengchun et al. . (2017). Load frequency control of interconnected power system via multi-agent system method. *Electric Power Components and Systems* , 839-851. Available at: <https://doi.org/10.1080/15325008.2015.1131764>.
- YouZhu Jianzhong et al. (2022). Model predictive control based control strategy for battery energy storage system integrated power plant meeting deep load peak

shaving demand. *Journal of Energy Storage*, 103811. Available at:
<https://doi.org/10.1016/j.est.2021.103811>.

APPENDIX

Appendix 2.1:

a. Hydropower plants

Introduction to hydropower plants in Figure 2.18: Hydroelectricity is a source of electricity generated by converting energy from water in the form of potential energy into mechanical energy to rotate turbines - generators to generate electricity to supply loads. However, during the operation of the load, there are always fluctuations such as: power grid failure, change in capacity, frequency and working mode of the unit and load leading to instability of the power system. The task of the hydroelectric power plant is to use the energy of the water flow to rotate the turbine, rigidly connect the turbine shaft to the generator and make the generator crank and generate electricity.



Figure 2.18. Hydroelectric power plant

b. Thermal power plants

Introduction to thermal power plants in Figure 2.19: General working principle of thermal power plants using backpressure turbines: Water is pumped from the reservoir to the boiler. The steam coming out of the boiler is saturated steam, and it is further heated by the heater into superheated steam and fed to the turbine which turns the generator. In addition to running the generator, the plant uses a counterpressure turbine to run the heat load. The steam after being used to run the heat load is also condensed by the condenser and pumped back to the storage tank.

Then from the tank that has not been filled with water, it is pumped to the boiler, continuing the process of generating steam, feeding it to the turbine and running the generator.



Figure 2.19. Thermal power plant model

c. Solar power plant

Introduction to solar power plants: Solar power is electricity converted from sunlight through solar panels. Based on the photoelectric effect of the semiconductors inside the solar panels, thereby converting the sun's light energy into electricity to provide for human activities and production, which is shown in Figure 2.20.



Figure 2.20. Solar power plant

d. Wind power plant

Introduction to wind power plants in Figure : When the wind hits the propeller, the propeller starts to rotate. The turbine rotor is connected to a high-speed gearbox.

The gearbox transforms the rotation of the rotor from low speed to high speed. The high-speed shaft from the gearbox is coupled to the rotor of the generator and thus the generator.



Figure 2.21. Wind power plant

The basic variable-speed wind turbine-generator system (VS-WTGS) is considered. The mechanical torque of WTGSs produced from wind energy is transmitted via the shaft to the generator rotor. The generator produces an electrical torque. Any difference between the mechanical torque and the electrical torque determines whether the mechanical system accelerates, decelerates, or remains at constant speed. Thus, the mechanical power is considered as net output power of wind system.

Building the dynamic equations of wind plant based on relationship of wind speed and mechanical output power. The output power of the turbine is given by the following equation.

$$P_m = C_p(\lambda, \beta) \frac{1}{2} \rho A V_{wind}^3 \quad (2.15)$$

P_m is mechanical output power of the turbine (W), C_p is performance coefficient of the turbine, λ is Tip speed ratio of the rotor blade tip speed to wind speed, β is Blade pitch angle (deg), ρ is Air density (kg/m^3), A is Turbine swept area (m^2), V_{wind} is Wind speed (m/s).

- Tip speed ratio (λ) of the rotor blade tip speed to wind speed is given by.

$$\lambda = \frac{\omega_r R_r}{V_w} \quad (2.16)$$

Where; R_r , ω_r are radius and spin speed of wind plant, respectively.

- Performance coefficient (C_p) of the turbine is given by.

$$C_p(\lambda, \beta) = c_1 \left(\frac{c_2}{\lambda_i} - c_3 \beta - c_4 \right) e^{\frac{-c_5}{\lambda_i}} + c_6 \lambda \quad (2.17)$$

with

$$\frac{1}{\lambda_i} = \frac{1}{\lambda + 0.08\beta} - \frac{0.035}{\beta^3 + 1} \quad (2.18)$$

where, the coefficients c_1 to c_6 are depends on wind plant.

Finally, we can present equation of wind plant via per unit (p.u) system given below.

$$P_{m_pu} = k_p \times C_{p_pu} \times V_{wind_pu}^3 \quad (2.19)$$

P_{m_pu} is mechanical power in per unit, $k_p \leq 1$ is amplified power factor, C_{p_pu} is the value per unit of the power factor CP, V_{wind_pu} is the value per unit of the basic wind speed and basic wind speed: is the value of expected wind speed in 1 year (m/s).

e. Gas power plant

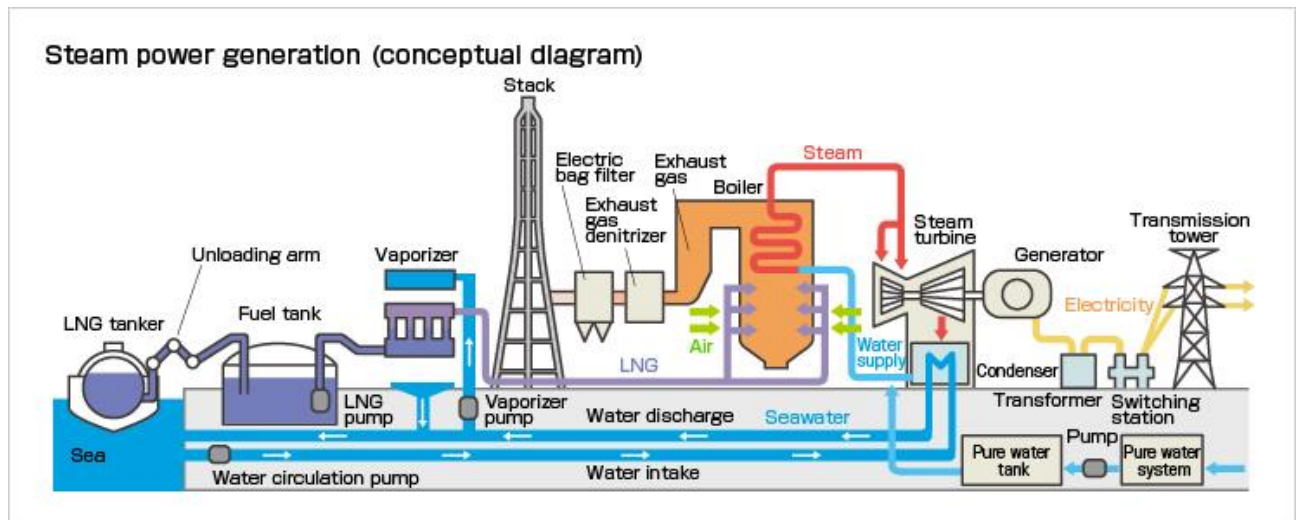


Figure 2.22. Gas power plant

Fuels such as heavy oil, LNG (liquefied natural gas) and coal are burned inside a boiler to generate steam at high temperature and high pressure. This steam is used to rotate the impeller of the steam turbine. This drives the power generators connected to the turbine that generate electricity. This system in Figure 2.22 has a thermal efficiency of around 42% to 46% and functions as a base-to-middle-load supply.

Appendix 3.1:

$$A_i = \begin{bmatrix} -\frac{1}{T_{pi}} & \frac{K_{pi}}{T_{pi}} & 0 & 0 & -\frac{K_{pi}}{T_{pi}} \\ 0 & -\frac{1}{T_{ti}} & \frac{1}{T_{ti}} & 0 & 0 \\ -\frac{1}{R_i T_{pi}} & 0 & -\frac{1}{T_{gi}} & 0 & 0 \\ K_{Bi} K_{Ei} & 0 & 0 & 0 & K_{Ei} \\ \sum_{\substack{j=1 \\ j \neq i}}^N 2\pi T_{ij} & 0 & 0 & 0 & 0 \end{bmatrix}, H_{ij} = \begin{bmatrix} 0 & 0 & 0 & 0 & 0 \\ 0 & 0 & 0 & 0 & 0 \\ 0 & 0 & 0 & 0 & 0 \\ 0 & 0 & 0 & 0 & 0 \\ \sum_{\substack{j=1 \\ j \neq i}}^N 2\pi T_{ij} & 0 & 0 & 0 & 0 \end{bmatrix}$$

$$B_i = \begin{bmatrix} 0 & 0 & \frac{1}{T_{gi}} & 0 & 0 \end{bmatrix}^T, F_i = \begin{bmatrix} -\frac{K_{pi}}{T_{pi}} & 0 & 0 & 0 & 0 \end{bmatrix}^T$$

and $x_i(t) \in R^{n_i}$ denotes the state of the vector $x_j(t) \in R^{n_j}$ denotes the neighboring state vector of $x_i(t)$, $u_i(t) \in R^{m_i}$ represents the control vector, $A_i \in R^{n_i \times n_i}$, $B_i \in R^{n_i \times m_i}$, $F_i \in R^{n_i \times k_i}$ refer to the matrices containing nominal parameters, n_i represents the count of state variables for the i^{th} area, m_i denotes the number of control input variables for the i^{th} area.

Appendix 4.1.

$$A_i = \begin{bmatrix} A_{i1} & A_{i2} \\ A_{i3} & A_{i4} \end{bmatrix},$$

$$A_{i1} = \begin{bmatrix} -\frac{1}{T_{PS_i}} & \frac{K_{PS_i}\alpha_{i1}}{T_{PS_i}} & 0 & 0 & \frac{K_{PS_i}\alpha_{i2}}{T_{PS_i}} & 0 & 0 \\ 0 & -\frac{1}{T_{T_i}} & \frac{1}{T_{T_i}} & 0 & 0 & 0 & 0 \\ -\frac{K_{R_i}}{T_{SG_i}R_{i1}} & 0 & -\frac{1}{T_{R_i}} & \frac{1}{T_{R_i}} - \frac{K_{R_i}}{T_{SG_i}} & 0 & 0 & 0 \\ -\frac{1}{T_{SG_i}R_{i1}} & 0 & 0 & -\frac{1}{T_{SG_i}} & 0 & 0 & 0 \\ \frac{2T_{RS_i}}{R_{i2}T_{RH_i}T_{GH_i}} & 0 & 0 & 0 & -\frac{2}{T_{W_i}} & \frac{2}{T_{W_i}} + \frac{2}{T_{RH_i}} & \frac{2T_{RS_i}}{T_{RH_i}T_{GH_i}} - \frac{2}{T_{RH_i}} \\ -\frac{T_{RS_i}}{R_{i2}T_{RH_i}T_{GH_i}} & 0 & 0 & 0 & 0 & -\frac{1}{T_{RH_i}} & \frac{1}{T_{RH_i}} - \frac{T_{RS_i}}{T_{RH_i}T_{GH_i}} \\ -\frac{1}{T_{GH_i}R_{i2}} & 0 & 0 & 0 & 0 & 0 & \frac{1}{T_{GH_i}} \end{bmatrix},$$

$$A_{i2} = \begin{bmatrix} \frac{K_{PS_i}\alpha_{i3}}{T_{PS_i}} & 0 & 0 & 0 & 0 & -\frac{K_{PS_i}a_{ij}}{T_{PS_i}} \\ 0 & 0 & 0 & 0 & 0 & 0 \\ 0 & 0 & 0 & 0 & 0 & 0 \\ 0 & 0 & 0 & 0 & 0 & 0 \\ 0 & 0 & 0 & 0 & 0 & 0 \\ 0 & 0 & 0 & 0 & 0 & 0 \\ 0 & 0 & 0 & 0 & 0 & 0 \end{bmatrix}, \quad A_{i3} = \begin{bmatrix} 0 & 0 & 0 & 0 & 0 & 0 & 0 \\ \frac{X_{G_i}T_{CR_i}}{R_{i3}b_{g_i}Y_{G_i}T_{F_i}} & 0 & 0 & 0 & 0 & 0 & 0 \\ -\frac{X_{G_i}}{R_{i3}b_{g_i}Y_{G_i}} & 0 & 0 & 0 & 0 & 0 & 0 \\ -\frac{1}{R_{i3}b_{g_i}} & 0 & 0 & 0 & 0 & 0 & 0 \\ B_i & 0 & 0 & 0 & 0 & 0 & 0 \\ \sum_{\substack{j=1 \\ j \neq i}}^L -2\pi T_{ij} & 0 & 0 & 0 & 0 & 0 & 0 \end{bmatrix},$$

Appendix 4.2:

Nominal system data A (N. Hakimuddin, I. Nasiruddin, T.S. Hota, 2020), (G. Nidhi, K. Narendra, B. Chitti., 2019).

$$T_{SG} = 0.08 \text{ s}, K_R = 0.3, T_R = 10, T_T = 0.3 \text{ s}, T_{GH} = 41.6 \text{ s}, T_{RS} = 5 \text{ s}, T_{RH} = 0.513 \text{ s}$$

$$T_W = 0.3 \text{ s}, C_g = 1, b_g = 1,$$

$$X_G = 0.6 \text{ s}, Y_G = 1, T_{CR} = 0.01 \text{ s}, T_F = 0.23 \text{ s}, T_{CD} = 0.2 \text{ s}, K_p = 120, T_p = 20 \text{ s},$$

$$T_{12} = 0.0433 \text{ puMW/rad}.$$

Nominal system data B (Sahu, R. Kumar, P. Sidhartha, Rout, U. Kumar, Sahoo, D. Kumar, 2016).

$$T_{SG} = 0.08 \text{ s}, K_R = 0.3, T_R = 10, T_T = 0.3 \text{ s}, T_{GH} = 28.75 \text{ s}, T_{RS} = 5 \text{ s},$$

$$T_{RH} = 0.2 \text{ s}, T_W = 1 \text{ s}, C_g = 1, b_g = 1, X_G = 0.6 \text{ s}, Y_G = 1, T_{CR} = 0.01 \text{ s},$$

$$T_F = 0.23 \text{ s}, T_{CD} = 0.2 \text{ s}, K_p = 68.9566 \text{ Hz/pu}, T_p = 11.49 \text{ s},$$

$$T_{12} = 0.0433 \text{ puMW/rad}$$

By solving LMI (4.28) it is easy to verify that conditions in Theorem 4.1 are satisfied with positive matrices:

$$\Pi_1 = \begin{bmatrix} 0.0138 & 0.0041 & 0.0021 & -0.0006 & 0.0033 & -0.0051 & 0.0020 & 0.0114 & 0.0026 & 0.0037 & -0.0021 & 0.0869 & -0.0208 \\ 0.0041 & 0.0021 & -0.0056 & 0.0017 & 0.0012 & 0.0006 & 0.0003 & 0.0041 & 0.0012 & -0.0002 & 0.0002 & 0.0226 & -0.0044 \\ 0.0021 & -0.0056 & 0.1624 & -0.0486 & -0.0052 & 0.2168 & -0.0394 & 0.0006 & -0.0034 & 0.0270 & -0.0164 & 0.0740 & -0.0416 \\ -0.0006 & 0.0017 & -0.0486 & 0.0146 & 0.0016 & -0.0648 & 0.0118 & -0.0002 & 0.0010 & -0.0081 & 0.0049 & -0.0220 & 0.0124 \\ 0.0033 & 0.0012 & -0.0052 & 0.0016 & 0.0013 & -0.0139 & 0.0028 & 0.0028 & 0.0007 & 0.0006 & -0.0004 & 0.0222 & -0.0049 \\ -0.0051 & 0.0006 & 0.2168 & -0.0648 & -0.0139 & 1.3665 & -0.2417 & -0.0036 & -0.0031 & 0.0179 & -0.0112 & -0.0024 & 0.0013 \\ 0.0020 & 0.0003 & -0.0394 & 0.0118 & 0.0028 & -0.2417 & 0.0429 & 0.0015 & 0.0007 & -0.0029 & 0.0018 & 0.0077 & -0.0018 \\ 0.0114 & 0.0041 & 0.0006 & -0.0002 & 0.0028 & -0.0036 & 0.0015 & 0.0136 & 0.0042 & -0.0087 & 0.0054 & 0.0696 & -0.0171 \\ 0.0026 & 0.0012 & -0.0034 & 0.0010 & 0.0007 & -0.0031 & 0.0007 & 0.0042 & 0.0037 & -0.0176 & 0.0107 & 0.0135 & -0.0024 \\ 0.0037 & -0.0002 & 0.0270 & -0.0081 & 0.0006 & 0.0179 & -0.0029 & -0.0087 & -0.0176 & 0.1240 & -0.0749 & 0.0382 & -0.0163 \\ -0.0021 & 0.0002 & -0.0164 & 0.0049 & -0.0004 & -0.0112 & 0.0018 & 0.0054 & 0.0107 & -0.0749 & 0.0452 & -0.0224 & 0.0097 \\ 0.0869 & 0.0226 & 0.0740 & -0.0220 & 0.0222 & -0.0024 & 0.0077 & 0.0696 & 0.0135 & 0.0382 & -0.0224 & 0.7435 & -0.2275 \\ -0.0208 & -0.0044 & -0.0416 & 0.0124 & -0.0049 & 0.0013 & -0.0018 & -0.0171 & -0.0024 & -0.0163 & 0.0097 & -0.2275 & 0.1241 \end{bmatrix}$$

$$\bar{\Pi}_1 = \begin{bmatrix} 64.7884 & -0.1475 & -1.6068 & -0.0044 & -0.9755 & -0.9224 & 0.0080 & -0.4101 & -0.0057 & -0.0062 & 0.0011 & -0.1122 & 0.3507 \\ -0.1475 & 0.1135 & -0.0062 & 0.0049 & -0.0039 & -0.0036 & -0.0037 & -0.0484 & -0.0026 & 0.0010 & 0.0042 & 0.0251 & 0.0103 \\ -1.6068 & -0.0062 & 15.3860 & 0.0557 & -13.6827 & -11.9157 & 0.0116 & -0.0158 & 0.0007 & 0.0006 & 0.0004 & 0.0174 & -0.0102 \\ -0.0044 & 0.0049 & 0.0557 & 0.8313 & -0.0498 & -0.0437 & -0.0066 & 0.0073 & 0.0001 & 0.0003 & 0.0002 & -0.0037 & -0.0014 \\ -0.9755 & -0.0039 & -13.6827 & -0.0498 & 28.2715 & -7.5486 & -0.0539 & -0.0099 & 0.0004 & 0.0003 & 0.0002 & 0.0107 & -0.0057 \\ -0.9224 & -0.0036 & -11.9157 & -0.0437 & -7.5486 & 30.3862 & 0.0361 & -0.0091 & 0.0003 & 0.0004 & 0.0002 & 0.0101 & -0.0057 \\ 0.0080 & -0.0037 & 0.0116 & -0.0066 & -0.0539 & 0.0361 & 0.2837 & -0.0044 & -0.0027 & 0.0035 & 0.0005 & 0.0021 & 0.0007 \\ -0.4101 & -0.0484 & -0.0158 & 0.0073 & -0.0099 & -0.0091 & -0.0044 & 0.1362 & -0.1001 & 0.0001 & 0.0064 & -0.0685 & -0.0226 \\ -0.0057 & -0.0026 & 0.0007 & 0.0001 & 0.0004 & 0.0003 & -0.0027 & -0.1001 & 0.2433 & -0.1489 & -0.0324 & 0.0514 & 0.0179 \\ -0.0062 & 0.0010 & 0.0006 & 0.0003 & 0.0003 & 0.0004 & 0.0035 & 0.0001 & -0.1489 & 0.1762 & 0.0408 & -0.0003 & 0.0002 \\ 0.0011 & 0.0042 & 0.0004 & 0.0002 & 0.0002 & 0.0002 & 0.0005 & 0.0064 & -0.0324 & 0.0408 & 1.3812 & -0.0033 & -0.0011 \\ -0.1122 & 0.0251 & 0.0174 & -0.0037 & 0.0107 & 0.0101 & 0.0021 & -0.0685 & 0.0514 & -0.0003 & -0.0033 & 24.8397 & -0.7063 \\ 0.3507 & 0.0103 & -0.0102 & -0.0014 & -0.0057 & -0.0057 & 0.0007 & -0.0226 & 0.0179 & 0.0002 & -0.0011 & -0.7063 & 39.6651 \end{bmatrix}$$

$$\Pi_2 = \begin{bmatrix} 0.0076 & 0.0023 & 0.0039 & -0.0012 & 0.0017 & -0.0022 & 0.0009 & 0.0064 & 0.0016 & 0.0015 & -0.0008 & 0.0494 & 0.0124 \\ 0.0023 & 0.0011 & -0.0010 & 0.0003 & 0.0006 & 0.0003 & 0.0001 & 0.0022 & 0.0007 & -0.0001 & 0.0001 & 0.0133 & 0.0030 \\ 0.0039 & -0.0010 & 0.0634 & -0.0190 & -0.0013 & 0.1258 & -0.0223 & 0.0024 & -0.0014 & 0.0159 & -0.0096 & 0.0473 & 0.0191 \\ -0.0012 & 0.0003 & -0.0190 & 0.0057 & 0.0004 & -0.0376 & 0.0067 & -0.0007 & 0.0004 & -0.0048 & 0.0029 & -0.0141 & -0.0057 \\ 0.0017 & 0.0006 & -0.0013 & 0.0004 & 0.0006 & -0.0077 & 0.0015 & 0.0014 & 0.0004 & 0.0002 & -0.0001 & 0.0122 & 0.0030 \\ -0.0022 & 0.0003 & 0.1258 & -0.0376 & -0.0077 & 0.7498 & -0.1326 & -0.0028 & -0.0021 & 0.0134 & -0.0083 & 0.0044 & 0.0017 \\ 0.0009 & 0.0001 & -0.0223 & 0.0067 & 0.0015 & -0.1326 & 0.0235 & 0.0009 & 0.0005 & -0.0023 & 0.0014 & 0.0032 & 0.0007 \\ 0.0064 & 0.0022 & 0.0024 & -0.0007 & 0.0014 & -0.0028 & 0.0009 & 0.0069 & 0.0022 & -0.0039 & 0.0024 & 0.0406 & 0.0102 \\ 0.0016 & 0.0007 & -0.0014 & 0.0004 & 0.0004 & -0.0021 & 0.0005 & 0.0022 & 0.0018 & -0.0083 & 0.0050 & 0.0082 & 0.0016 \\ 0.0015 & -0.0001 & 0.0159 & -0.0048 & 0.0002 & 0.0134 & -0.0023 & -0.0039 & -0.0083 & 0.0590 & -0.0356 & 0.0203 & 0.0089 \\ -0.0008 & 0.0001 & -0.0096 & 0.0029 & -0.0001 & -0.0083 & 0.0014 & 0.0024 & 0.0050 & -0.0356 & 0.0215 & -0.0119 & -0.0053 \\ 0.0494 & 0.0133 & 0.0473 & -0.0141 & 0.0122 & 0.0044 & 0.0032 & 0.0406 & 0.0082 & 0.0203 & -0.0119 & 0.4141 & 0.1260 \\ 0.0124 & 0.0030 & 0.0191 & -0.0057 & 0.0030 & 0.0017 & 0.0007 & 0.0102 & 0.0016 & 0.0089 & -0.0053 & 0.1260 & 0.0645 \end{bmatrix}$$

$$\bar{\Pi}_2 = \begin{bmatrix} 26.4556 & -0.0849 & -0.5551 & -0.0020 & -0.3222 & -0.3368 & -0.0013 & -0.2382 & -0.0044 & -0.0045 & -0.0004 & -0.0282 & -0.2007 \\ -0.0849 & 0.0768 & -0.0034 & 0.0033 & -0.0023 & -0.0021 & -0.0021 & -0.0329 & -0.0025 & 0.0004 & 0.0028 & 0.0113 & -0.0192 \\ -0.5551 & -0.0034 & 3.8551 & 0.0140 & -3.4083 & -2.9718 & 0.0027 & -0.0089 & 0.0004 & 0.0003 & 0.0002 & 0.0058 & 0.0003 \\ -0.0020 & 0.0033 & 0.0140 & 0.5542 & -0.0123 & -0.0114 & -0.0042 & 0.0048 & 0.0002 & 0.0002 & 0.0001 & -0.0017 & 0.0026 \\ -0.3222 & -0.0023 & -3.4083 & -0.0123 & 7.0583 & -1.8762 & -0.0134 & -0.0058 & 0.0002 & 0.0002 & 0.0001 & 0.0036 & -0.0002 \\ -0.3368 & -0.0021 & -2.9718 & -0.0114 & -1.8762 & 7.5944 & 0.0072 & -0.0051 & 0.0001 & 0.0002 & 0.0001 & 0.0031 & -0.0000 \\ -0.0013 & -0.0021 & 0.0027 & -0.0042 & -0.0134 & 0.0072 & 0.1911 & -0.0026 & -0.0022 & 0.0022 & 0.0002 & 0.0010 & -0.0013 \\ -0.2382 & -0.0329 & -0.0089 & 0.0048 & -0.0058 & -0.0051 & -0.0026 & 0.0887 & -0.0668 & 0.0003 & 0.0043 & -0.0295 & 0.0467 \\ -0.0044 & -0.0025 & 0.0004 & 0.0002 & 0.0002 & 0.0001 & -0.0022 & -0.0668 & 0.1626 & -0.0989 & -0.0216 & 0.0228 & -0.0363 \\ -0.0045 & 0.0004 & 0.0003 & 0.0002 & 0.0002 & 0.0002 & 0.0022 & 0.0003 & -0.0989 & 0.1171 & 0.0273 & -0.0000 & 0.0002 \\ -0.0004 & 0.0028 & 0.0002 & 0.0001 & 0.0001 & 0.0001 & 0.0002 & 0.0043 & -0.0216 & 0.0273 & 0.9202 & -0.0015 & 0.0023 \\ -0.0282 & 0.0113 & 0.0058 & -0.0017 & 0.0036 & 0.0031 & 0.0010 & -0.0295 & 0.0228 & -0.0000 & -0.0015 & 8.2364 & 3.0052 \\ -0.2007 & -0.0192 & 0.0003 & 0.0026 & -0.0002 & -0.0000 & -0.0013 & 0.0467 & -0.0363 & 0.0002 & 0.0023 & 3.0052 & 11.7695 \end{bmatrix}$$

and the scalars $\lambda_1 = 10$, $\rho_1 = 10$, $\hat{\gamma}_1 = 20$, $\lambda_2 = 20$, $\rho_2 = 20$, and $\hat{\gamma}_2 = 30$.

Appendix 4.3:

$$\Delta A_{11} = \begin{bmatrix} 0 & 0 & 0 & 0 & 0 & 0 & 0 \\ 0 & 0 & 0 & 0 & 0 & 0 & 0 \\ 4\cos(t) & 0 & 0 & 0 & 0 & 0 & 0 \\ 0.46\cos(t) & 0 & 0 & \cos(t) & 0 & 0 & 0 \\ \cos(t) & 0 & 0 & 0 & 0 & \cos(t) & 0 \\ \cos(t) & 0 & 0 & 0 & 0 & 0 & 0 \\ 0 & 0 & 0 & 0 & 0 & 0 & 0 \\ 0 & 0 & 0 & 0 & 0 & 0 & 0 \\ \cos(t) & 0 & 0 & 0 & 0 & 0 & 0 \\ \cos(t) & 0 & 0 & 0 & 0 & 0 & 0 \\ 0 & 0 & 0 & 0 & 0 & 1.6\cos(t) & 0 \\ 0 & 0 & 0 & 0 & 0 & 0 & 0 \\ 0 & 0 & 0 & 0 & 0 & 0 & 0 \end{bmatrix} \text{ and}$$

$$\Delta A_{12} = \begin{bmatrix} 0 & 0 & 0 & 0 & 0 & 0 \\ 0 & 0 & 0 & 0 & 0 & 0 \\ 0 & 0 & 0 & 0 & 0 & 0 \\ 0 & 0 & 0 & 0 & 0 & 0 \\ 0 & 0 & 0 & 0 & 0 & 0 \\ 0 & 0 & 0 & 0 & 0 & 0 \\ 0 & 0 & 0 & 0 & 0 & 6\cos(t) \\ 0 & 0 & 0 & 0 & 0 & 0 \\ 0 & 0 & 0 & \cos(t) & 0 & 0 \\ 0 & 0 & 0.2\cos(t) & \cos(t) & 0 & 0 \\ 0 & 0 & 0 & 0 & 0 & 0 \\ 0 & 0 & 0 & 0 & 0 & 0 \\ 0 & 0 & 0 & 0 & 0 & 0 \end{bmatrix}.$$

Appendix 5.1.

$A_i \in R^{n_i \times n_i}$, $B_i \in R^{n_i \times m_i}$, $F_i \in R^{n_i \times k_i}$ and H_{ij} are the nominal parameter system matrices

in

$$\bar{A}_i = \begin{bmatrix} \frac{-1}{T_{pi}} & \frac{K_{pi}}{T_{pi}} & 0 & 0 & 0 & -\frac{b_{ij}K_{pi}}{2\pi T_{pi}} \sum_{i=1, i \neq j}^N T_{ij} & \frac{K_{pi}}{T_{pi}} & 0 & 0 \\ \frac{2T_{Ri2}}{T_{i2}T_{i1}R_{i2}} & -\frac{2}{T_{Wi}} & \frac{2}{T_{Wi}} + \frac{2}{T_{i2}} & \frac{2T_{Ri2}}{T_{i2}T_{i1}} - \frac{2}{T_{i2}} & 0 & 0 & 0 & 0 & 0 \\ -\frac{T_{Ri2}}{T_{i2}T_{i1}R_{i2}} & 0 & -\frac{1}{T_{i2}} & \frac{1}{T_{i2}} - \frac{T_{Ri2}}{T_{i2}T_{i1}} & 0 & 0 & 0 & 0 & 0 \\ -\frac{1}{T_{i1}R_{i2}} & 0 & 0 & -\frac{1}{T_{i1}} & 0 & 0 & 0 & 0 & 0 \\ K_{Ei}K_{Bi} & 0 & 0 & 0 & 0 & \frac{K_{Ei}}{2\pi} b_{ij} \sum_{i=1, i \neq j}^N T_{ij} & 0 & 0 & 0 \\ 2\pi & 0 & 0 & 0 & 0 & 0 & 0 & 0 & 0 \\ 0 & 0 & 0 & 0 & 0 & 0 & -\frac{1}{T_{Ri1}} & \frac{1}{T_{Ri1}} - \frac{K_{Ri1}}{T_{Ri1}} & \frac{K_{Ri1}}{T_{Ri1}} \\ 0 & 0 & 0 & 0 & 0 & 0 & 0 & -\frac{1}{T_{i1}} & \frac{1}{T_{i1}} \\ -\frac{1}{T_{gi}R_{i1}} & 0 & 0 & 0 & 0 & 0 & 0 & 0 & -\frac{1}{T_{gi}} \end{bmatrix}$$

$$\bar{B}_i = \begin{bmatrix} 0 & 0 \\ 0 & -\frac{2T_{Ri2}}{T_{i2}T_{i1}} \\ 0 & \frac{T_{Ri2}}{T_{i2}T_{i1}} \\ 0 & \frac{1}{T_{i1}} \\ 0 & 0 \\ 0 & 0 \\ 0 & 0 \\ \frac{1}{T_{gi}} & 0 \end{bmatrix}, \quad \bar{F}_i = \begin{bmatrix} -\frac{K_{pi}}{T_{pi}} \\ 0 \\ 0 \\ 0 \\ 0 \\ 0 \\ 0 \\ 0 \end{bmatrix}, \quad \bar{H}_{ij} = \begin{bmatrix} 0 & 0 & 0 & 0 & 0 & \frac{b_{ij}K_{pi}}{2\pi T_{pi}} T_{ij} & 0 & 0 & 0 \\ 0 & 0 & 0 & 0 & 0 & 0 & 0 & 0 & 0 \\ 0 & 0 & 0 & 0 & 0 & 0 & 0 & 0 & 0 \\ 0 & 0 & 0 & 0 & 0 & 0 & 0 & 0 & 0 \\ 0 & 0 & 0 & 0 & 0 & -\frac{b_{ij}K_{Ei}T_{ij}}{2\pi} & 0 & 0 & 0 \\ 0 & 0 & 0 & 0 & 0 & 0 & 0 & 0 & 0 \\ 0 & 0 & 0 & 0 & 0 & 0 & 0 & 0 & 0 \\ 0 & 0 & 0 & 0 & 0 & 0 & 0 & 0 & 0 \end{bmatrix}$$

Appendix 5.2.

$$\begin{aligned} \Delta \dot{f}_i = & -\frac{1}{T_{pi}} \Delta f_i + \frac{K_{pi}}{T_{pi}} \Delta P_{mi} + \frac{K_{pi}}{T_{pi}} \Delta P'_{mi} - \frac{K_{pi}}{T_{pi}} \Delta P_{Di} \\ & - \frac{b_{ij} K_{pi}}{2\pi T_{pi}} \sum_{i=1, i \neq j}^N T_{ij} \{ \Delta \delta_i(t) - \Delta \delta_j(t) \} \end{aligned} \quad (5.1)$$

$$\begin{aligned} \Delta \dot{P}_{mi} = & \frac{2T_{Ri2}}{T_{i2} T_{i1} R_{i2}} \Delta f_i - \frac{2}{T_{Wi}} \Delta P_{mi} + \left(\frac{2}{T_{Wi}} + \frac{2}{T_{i2}} \right) \Delta P_{vi} + \left(\frac{2T_{Ri2}}{T_{i2} T_{i1}} - \frac{2}{T_{i2}} \right) \Delta P_{gi} \\ & - \frac{2T_{Ri2}}{T_{i2} T_{i1}} \Delta E_i - \frac{2T_{Ri2}}{T_{i2} T_{i1}} u_{i2} \end{aligned} \quad (5.2)$$

$$\Delta \dot{P}_{vi} = -\frac{T_{Ri2}}{T_{i2} T_{i1} R_{i2}} \Delta f_i - \frac{1}{T_{i2}} \Delta P_{vi} + \left(\frac{1}{T_{i2}} - \frac{T_{Ri2}}{T_{i2} T_{i1}} \right) \Delta P_{gi} + \frac{T_{Ri2}}{T_{i2} T_{i1}} \Delta E_i + \frac{T_{Ri2}}{T_{i2} T_{i1}} u_{i2} \quad (5.3)$$

$$\Delta \dot{P}_{gi} = -\frac{1}{T_{i1} R_{i2}} \Delta f_i - \frac{1}{T_{i1}} \Delta P_{gi} + \frac{1}{T_{i1}} \Delta E_i + \frac{1}{T_{i1}} u_{i2} \quad (5.4)$$

$$\Delta \dot{E}_i(t) = K_{Ei} K_{Bi} \Delta f_i(t) + K_{Ei} \frac{1}{2\pi} b_{ij} \sum_{i=1, i \neq j}^N T_{ij} \{ \Delta \delta_i(t) - \Delta \delta_j(t) \} \quad (5.5)$$

$$\Delta \dot{\delta}_i(t) = 2\pi \Delta f_i(t) \quad (5.6)$$

$$\begin{aligned} \Delta \dot{P}'_{mi} = & -\frac{1}{T_{Ri1}} \Delta P'_{mi} + \left(\frac{1}{T_{Ri1}} - \frac{K_{Ri1}}{T_{Ri1}} \right) \Delta P''_{vi} \\ & + \frac{K_{Ri1}}{T_{Ri1}} \Delta P_{vi} \end{aligned} \quad (5.7)$$

$$\Delta \dot{P}''_{vi} = -\frac{1}{T_{i1}} \Delta P''_{vi} + \frac{1}{T_{i1}} \Delta P'_{vi} \quad (5.8)$$

$$\Delta \dot{P}'_{vi} = -\frac{1}{T_{gi} R_{i1}} \Delta f_i - \frac{1}{T_{gi}} \Delta P_{vi} + \frac{1}{T_{gi}} \Delta E_i + \frac{1}{T_{gi}} u_{i1} \quad (5.9)$$

Appendix 5.2.

$$\Delta A_{11} = \begin{bmatrix} 0 & 0 & 2.6\cos(t) & 0 \\ 0 & \cos(t) & 0 & 0 \\ 0 & 0 & 0 & 0 \\ 0 & 0 & 0 & 0.24\cos(t) \\ \cos(t) & 0 & 0 & 0 \\ 0 & 0 & 0 & 0.14\cos(t) \\ 2.6\cos(t) & 0 & 0 & 0 \\ 0 & 0 & 0 & 0 \\ 0 & 0 & 0 & 0 \end{bmatrix},$$

$$\Delta A_{12} = \begin{bmatrix} 0 & 0 & 0 & 0 & 0 \\ 0 & 0 & 0 & 0 & 0 \\ 0 & 0.26\cos(t) & 0 & 0 & 0 \\ 0 & 0 & 0 & 0 & 0 \\ 0 & 0 & 0 & 0 & 0 \\ 0 & 0 & 0 & 0 & 0 \\ 0 & 0 & 0 & 0 & 0 \\ 0 & 0 & 0 & 0 & 0 \\ 0 & 0 & 1.26\cos(t) & 0 & 0 \\ 4.6\cos(t) & 0 & 0 & 0 & 0 \end{bmatrix}$$

Appendix 5.3. We have a detailed description of the system parameters described in this table. There are the nominal parameters for multi-area multi-source power system of IEEE 39-bus New-England

Generators	T_{gi}	T_{ti}	K_{Ri1}	T_{Ri1}	K_{pi}	T_{pi}	T_{i1}	T_{Ri2}	T_{i2}	T_{wi}	K_{Ei}	K_{Bi}	b_{ij}	T_{ij}	R_{i2}	R_{i1}
G3	0.08s	0.3s	0.5	10s	120 (Hz/puMW)	20s	48.7s	5s	0.513s	1s	1	0.425 (puMW/Hz)	-1	0.0433 (puMW/Hz)	2.4 (Hz/puMW)	2.4 (Hz/puMW)
G7	0.08s	0.3s	0.5	10s	120 (Hz/puMW)	20s	48.7s	5s	0.513s	1s	1	0.425 (puMW/Hz)	-1	0.0433 (Hz/puMW)	2.4 (Hz/puMW)	2.4 (Hz/puMW)
G9	0.08s	0.3s	0.5	10s	120 (Hz/puMW)	20s	48.7s	5s	0.513s	1s	1	0.425 (puMW/Hz)	-1	0.0433 (Hz/puMW)	2.4 (Hz/puMW)	2.4 (Hz/puMW)